Urban Materials and Evaporative Cooling for Heat Mitigation in Cities: Adapting Pavement-Watering to Different Parisian Pavements

Sophie Parison

Université de Paris

Ecole doctorale Physique en Ile de France 564

Laboratoire Interdisciplinaire des Energies de Demain UMR 8236

Urban Materials and Evaporative Cooling for Heat Mitigation in Cities

Adapting Pavement-Watering to Different Parisian Pavements

Thèse de Doctorat de Physique / Sciences pour l'Ingénieur

Dirigée par Laurent Royon

Réalisée par

Sophie Parison

Présentée et soutenue publiquement le 6 octobre 2020

Devant un jury composé de :

M. Stéphane Lassue	Professeur, Université d'Artois	Président du jury
M. Mat Santamouris	Professeur, University of New South Wales	Rapporteur
M. Valéry Masson	Ingénieur en chef, CNRM Météo-France	Rapporteur
Mme Marjorie Musy	Directrice de Recherche, Cerema Ouest	Examinatrice
M. Laurent Royon	Professeur, Université de Paris	Directeur
M. Martin Hendel	Maître de conférences, ESIEE Paris	Encadrant, Invité
Mme Kristine Jurski	Maître de conférences, Université de Paris	Encadrante, Invitée
Mme Agathe Cohen	STEA, DPE, Mairie de Paris	Invitée
M. Jérôme Lefebvre	LEP, DVD, Mairie de Paris	Invité

Foreword

Avant-propos

Title: Urban Materials and Evaporative Cooling for Heat Mitigation in Cities: Adapting Pavement-Watering to Different Parisian Pavements

Abstract: This manuscript examines the use of pavement-watering as a heat mitigation strategy and climate change adaptation tool for cities. The method is fine-tuned for traditional and cool paving materials in order to limit the water footprint of the technique.

The first Part of this research is based on field measurements gathered form watering campaigns in Paris from 2013 to 2018. A suited statistical analysis method is proposed in order to determine the microclimatic effects of watering, including effects on air temperature and pedestrian thermal stress using the Universal Thermal Climate Index. Two watering protocols are compared to determine the influence of the surface area being watered on the efficiency and duration of pavement-watering.

Secondly, a laboratory experiment is used to compare the thermal behaviour of realistic paving structures under heat-wave like conditions. The pavement undergoes a 24-h climate cycle and watering can be enabled at a fixed frequency. On the basis of surface and in-depth temperature and heat flux measurements, using the surface heat budget, the evaporative cooling flux is determined for each tested watering rate. Results obtained on an asphalt road structure with the lab protocol are compared to field results.

Finally, the lab protocol is applied to twelve traditional and cool pavements under dry and watered conditions. Watering is fine-tuned for each structure to maximize cooling and minimize the water consumption using two linear cooling regimes. Driving parameters influencing the optimization of the evaporative cooling versus the watering rate are determined. The surface heat budget and the partitioning of irradiance into conductive, convective, radiative and cooling fluxes are analysed for each paving structure. In the end, the benefits of each pavement, the efficiency of the method and the limitations of the lab protocol are discussed.

This research intends to provide useful information for decision-makers considering the use of pavement-watering or cool pavements as heat mitigation strategy. Future work should principally investigate the microclimatic effects of cool pavements combined with pavement-watering to confront lab results to field studies. Those should come with an adapted experimental design, while associated statistical procedures may also require improvements in the future.

Keywords: pavement-watering; urban materials; cool pavements; evaporative cooling; climate change adaptation.

Titre : Matériaux urbains et nouveaux usages de l'eau pour le rafraichissement des villes : stratégies d'arrosage de différents revêtements parisiens

Résumé : Ce manuscrit s'intéresse à l'arrosage urbain comme stratégie d'atténuation de la chaleur et d'adaptation au changement climatique. La méthode est optimisée pour des matériaux de voirie traditionnels et "frais" afin de limiter la consommation d'eau du procédé.

La première partie de ce manuscrit utilise des mesures de terrain recueillies lors de campagnes d'arrosage à Paris entre 2013 et 2018. Une méthode d'analyse statistique permet de déterminer les effets microclimatiques de l'arrosage sur la température de l'air et le stress thermique à l'aide de l'Indice Universel de Climat Thermique. Deux protocoles d'arrosage sont comparés afin de déterminer l'influence de la surface arrosée sur l'efficacité de la méthode.

Dans un second temps, une expérience de laboratoire est utilisée afin de comparer le comportement thermique de structures de voirie réalistes dans des conditions similaires à celles d'une vague de chaleur parisienne. L'échantillon subit un cycle climatique de 24 heures et son arrosage peut être activé à une fréquence fixe. A l'aide de mesures de température et de flux thermique en surface et en profondeur, le bilan thermique de surface permet de déterminer le flux rafraîchissant évaporatif pour chaque débit d'arrosage testé. Les résultats obtenus sur une structure de chaussée en asphalte sont comparés à ceux du terrain.

Enfin, le protocole est appliqué à douze revêtements traditionnels et "frais", avec et sans arrosage. L'arrosage est optimisé pour chaque structure afin de maximiser le rafraîchissement en minimisant la consommation d'eau. Pour ce faire, deux régimes de rafraîchissement sont employés. Les paramètres déterminants dans l'optimisation du flux rafraîchissant selon le débit sont identifiés. Le bilan thermique de la surface et le partitionnement de l'irradiance sont analysés pour chaque échantillon. L'efficacité de la méthode selon les structures ainsi que les limites du protocole de laboratoire sont discutées.

Ce travail vise à fournir des informations utiles aux décideurs qui envisagent l'emploi de l'arrosage urbain ou de revêtements "frais" dans leur stratégie d'atténuation de la chaleur. La recherche future devrait s'intéresser aux effets microclimatiques de revêtements "frais" en combinaison avec de l'arrosage afin de confronter les résultats de laboratoire à davantage d'études de terrain. Ces dernières devront proposer un plan expérimental adéquat, tandis que les méthodes d'analyse statistique associées pourront également faire l'objet de futures améliorations.

Mots-clés : arrosage urbain; matériaux urbains; revêtements frais; rafraîchissement évaporatif; adaptation au changement climatique.

Remerciements

Cette thèse constitue l'aboutissement de trois années de travail, riches d'apprentissages tant sur le plan scientifique que professionnel et humain. Je souhaiterais commencer ces quelques lignes en rappelant tout d'abord les circonstances dans lesquelles ce projet a vu le jour.

Initialement, à l'automne 2015, alors étudiante de Master 2, je n'envisageais pas encore pleinement la possibilité de faire une thèse. Presque par hasard, au fil de discussions passées avec Benjamin Thiria, responsable de mon Master, je compris que cette voie pourrait me plaire et me correspondre. C'est à l'occasion d'un projet de Master, portant sur les îlots de chaleur urbains et encadré par Martin Hendel et Laurent Royon, que l'opportunité de faire une thèse se présenta finalement. Ce projet m'aura permis de confirmer mon intérêt pour ces thématiques de recherche qui correspondaient déjà à mes sensibilités et mes attentes. Qui plus est, j'avais déjà eu l'opportunité de travailler avec Laurent Royon en stage de Master 1, ce qui me conforta dans mon envie de postuler à cette thèse au sein de l'équipe. La thèse proposée me permettait en outre d'intégrer la Ville de Paris par le biais du dispositif CIFRE, ce qui me satisfaisait complètement. Il eut fallu attendre décembre pour apprendre que ma candidature avait été retenue par Laurent et par Martin. Je tiens à les en remercier et à leur témoigner ma profonde gratitude pour la confiance qu'ils m'ont accordée. Puis, en avril 2016, vint la validation par le Conseil de Paris, et enfin en juin l'aval final et décisif de financement par l'ANRT, pour un début de thèse programmé en janvier 2017.

Je souhaite ici exprimer ma grande reconnaissance envers mon équipe d'encadrement de thèse. Je remercie en premier lieu mon directeur, Laurent Royon, pour son accompagnement tant scientifique qu'humain. Merci pour tes conseils et pour les discussions riches que nous avons eues, ainsi que pour tes commentaires pertinents sur mon travail. Je remercie également Martin Hendel, mon encadrant, pour m'avoir guidée et soutenue tout au long de cette thèse. Merci pour tes remarques, toujours très justes et constructives, et pour les très nombreuses réflexions communes que nous avons eues. Enfin, merci à vous deux pour votre bienveillance et votre grande prévenance à mon égard, dont la portée s'est même étendue au-delà du cadre de la thèse à diverses reprises (post-doc, enseignements, conférences, etc.). J'adresse aussi mes remerciements sincères à Agathe Cohen et Jérôme Lefebvre, mes encadrants Ville de Paris, pour leur aide logistique et pour leur écoute attentive, qui se sont avérées être essentielles à la réalisation pratique de mon travail de thèse. Merci également à Nicolas Londinsky et Damien Balland pour leur soutien managérial et opérationnel, ainsi qu'à Kristine Jurski pour son accompagnement tout au long de cette thèse. Merci enfin à Patricia Bordin et Brice Tréméac pour nos échanges et pour leur suivi au sein de mon comité de thèse.

Je remercie mes rapporteurs Mat Santamouris et Valéry Masson, ainsi que mes examinateurs, Marjorie Musy et Stéphane Lassue, pour avoir accepté de faire partie de mon jury, pour la relecture de mon manuscrit ainsi que pour leurs remarques constructives et les échanges que cela a nourri.

Je souhaite aussi adresser mes remerciements aux services de la Ville de Paris avec lesquels j'ai collaboré durant ma thèse. Merci aux équipes du STEA, en particulier à la SPE pour son accueil, mais également à la SAP, la DEI, la DII et au STPP. Je remercie en particulier les équipes

iv

opérationnelles ayant mis en œuvre l'arrosage l'été pour me permettre de mener ce projet à bien, ainsi que l'atelier Deleusseux pour son aide dans la pose et dépose de stations météo sur le terrain. Merci aux collègues de Commandeur pour les bons moments passés ensemble : Fenotte, Nathalie, Marlène, Michelle pour son accueil au 5eme, Khajin, Anastasia, Chantal, Marie-Claude, Daouda, Alain et Jean-Claude. Je salue aussi les membres du groupe de travail *Expérimentation de rafraîchissement de l'espace public par arrosage* que j'ai piloté durant ma thèse, mais également ceux du groupe *Ilots et parcours de fraîcheur* piloté par l'AEU, auquel j'ai eu le plaisir de contribuer. J'adresse également mes remerciements au LEP, qui m'a aussi accueillie durant cette thèse. Merci aux équipes opérationnelles pour leur accueil chaleureux, leur disponibilité et pour leur aide pratique, notamment dans la confection d'éprouvettes, essentielles à la réalisation du travail décrit dans ce document. Un grand merci à Didier, Isabelle, Khelil, Eric, Souazic, Jean-Luc, Céline, Laurent, Claude, Chantal et Patricia. Enfin, merci à Sophie Zuber de la DAE pour son écoute attentive et son accompagnement précieux pendant ces trois années.

Je tiens également à remercier les personnes avec qui j'ai eu l'occasion de collaborer à diverses reprises durant ces trois années. Je remercie tous les membres du projet *Life Cool & Low Noise Asphalt* auquel j'ai eu la chance de contribuer : merci à la DEVE et à l'AEU, à nouveau à la DPE et à la DVD, mais également à Colas, Eurovia et BruitParif. Je salue également Andrej et Marcos ainsi que tous les partenaires du projet *Lisière d'une Tierce Forêt*. Merci à SLG et à Captec pour leur aide précieuse concernant les instruments de mesure employés pendant ma thèse. Merci également aux membres du *Workshop Climat Urbain* pour les échanges que nous avons pu avoir. J'exprime enfin ma gratitude envers Valérie Douay, Emmanuelle Algré et Gaëlle Lissorgues pour leur chaleureux accueil à l'ESIEE à l'occasion de vacations d'enseignement, ainsi qu'à Kristine, à nouveau, en ce qui concerne les vacations à l'IUT de Paris-Diderot. Merci également aux stagiaires que j'ai encadrés et qui m'ont apporté une aide précieuse dans mon travail durant l'été : Eva, Param, et Maïlys, mais également Khadija, Lucas O, Lucas B, André et Antoine.

Je remercie aussi les anciens et actuels membres du LIED et du MSC ainsi que les techniciens, pour leur aide, pour nos discussions et pour le temps passé ensemble : Fred, José, Petros, Catherine, Xiao-Feng, Delphine, Insaaf, Melina, Wlad, Amir, Mathieu, Christophe, Eric, Sylvain, Cécilia, Florence, Gwenaëlle, et tous les autres. Un très grand merci à Arnaud pour son aide considérable dans la réalisation de l'expérimentation de laboratoire, ainsi que pour les bons moments passés ensemble. Je n'oublie pas les membres de la 544 A, Etienne, Sara, Nicolas et Darius, et remercie aussi Grégoire du MPQ, ainsi que Marion, Yann et Donatella du côté de l'APC.

Je souhaiterais faire part de mes sincères remerciements aux doctorants du LIED et du MSC aux côtés desquels j'ai eu la chance de réaliser ma thèse depuis son commencement (ou presque) : Marie-Cécile, Rémy, Souhil, Yohann, Joachim, Zejun et Chuanyu. Aussi, c'est avec beaucoup d'affection que je voudrais tout particulièrement remercier les doctorants de l'équipe CEMU. Au début de ma thèse, j'ai intégré cette équipe en tant que seule doctorante travaillant sur le rafraîchissement urbain. Il m'aura fallu patienter jusqu'à l'été 2018 avant de voir arriver des stagiaires au sein de l'équipe sur cette même thématique, qui comme moi se seront finalement transformés en "stagiaires longue durée", avant de progressivement devenir des amis.

Merci à vous, Maxime, Ghid, Maïlys et Maxime F, pour nos éclats de rire, nos discussions animées, nos pauses café, nos crises existentielles, nos instants "mezza", nos virées en triporteur (non sans risques !), nos verres après le travail, et pour tout le reste. Je t'adresse aussi un merci particulier Marie-Cécile, amie et "compagne de thèse" dès le début de celle-ci (bien que sur des sujets très différents), et ce jusqu'à nos soutenances respectives qui ont eu lieu à deux jours d'intervalle. J'en profite pour remercier Martin une fois encore, pour son initiation à la préparation et à la dégustation de café "digne de ce nom", ainsi que pour ses (très) nombreuses relectures indispensables de ce manuscrit. Merci à toute l'équipe pour sa préparation de la soutenance et son organisation du buffet qui a suivi, mais surtout, merci à vous tous pour votre bonne humeur quotidienne, pour tout ce que vous m'avez apporté humainement, et pour nos moments partagés, qui je l'espère perdureront bien au-delà du cadre de nos thèses.

Je voudrais aussi remercier mes amis pour leur soutien plus que nécessaire : Amina, Amandine, Anne-So, Céline, Julien, Gab, Thomas, Raph, Marion, Emma et tous les autres. Je remercie aussi toute ma famille pour sa présence et son soutien. Merci en particulier à mes deux sœurs adorées Marie et Claire, ainsi qu'à ma mère, à qui je dois pour beaucoup mon parcours universitaire. Merci également à toi Philippe, pour ta présence quotidienne à mes côtés depuis maintenant plusieurs années, dans les moments ordinaires comme dans les moments difficiles, mais aussi pour ton soutien scientifique et moral et pour la stabilité affective que tu continues de m'apporter chaque jour. Merci enfin à toutes les personnes que j'oublie et qui ont contribué de près ou de loin à la réussite de cette thèse.

Contents

List of Figures

List of Tables

Acronyms and Abbreviations

BACI	Before-After-Control-Impact
com.	combined
counter	countermeasure period (after countermeasure implementation)
exp.	experimental
FEM	fixed-effects model
GIS	geographic information system
HD	Humidex
HIP	heat island potential
IR	infrared
LCZ	local climate zone
LMM	linear mixed model
LW	longwave (3 - 100 μm)
MBACI	multiple Before-After-Control-Impact design
MCTP	mass convection transport problem
MEMI	Munich Energy Balance Model for Individuals
MRT	mean radiant temperature
NA	not available
NIR	near-infrared (0.74 - 3 μm)
NR	not relevant
num.	numerical
PCM	phase-change material
PET	Physiological Equivalent Temperature
PMV	Predicted Mean Vote
PPCC	pervious Portland-cement concrete
ref	reference period (before countermeasure implementation)

RH   relative humidity

SET*   Standard Equivalent Temperature
stat. sign.   statistically significant
SW   shortwave (0.3 - 3 μm)

TEB   Town Energy Balance

UHI   urban heat island
UTCI   Universal Thermal Climate Index

WBGT   Wet-Bulb Globe Temperature
WCI   Wind Chill Index
WMO   World Meteorological Organization

List of Symbols

A_{itx} local landscape effects for a weather type i, period t and location x, $[-]$

α albedo or shortwave reflectivity, $[-]$

a global surface absorptivity, $[-]$

C_{itx} "background" climate for a weather type i, period t and location x, $[-]$

c specific heat, $[J.kg^{-1}.K^{-1}]$

c_w specific heat of water: 4.18 kJ.kg^{-1}.K^{-1}

c_a specific heat of air: 1.005 kJ.kg^{-1}.K^{-1}

$\Delta H^{dry-wet}$ dry-wet difference in atmospheric convective heat flux, $[W.m^{-2}]$

ΔM_t interstation profile for the period t, $[-]$

ΔQ sensible heat absorption flux, $[W.m^{-2}]$

$\Delta R_n^{dry-wet}$ dry-wet difference in net radiation, $[W.m^{-2}]$

ΔT temperature reduction, $[°C]$

$\Delta V_0^{dry-wet}$ dry-wet difference in surface conductive heat flux, $[W.m^{-2}]$

E evaporation rate, $[mm/h]$

E^{max} maximum evaporation rate, $[mm/h]$

E_0 surface conduction energy density, $[kWh.m^{-2}]$

$E_{H,atm}$ atmospheric convection energy density, $[kWh.m^{-2}]$

ϵ surface material emissivity, $[-]$

ϵ_t deviation from the linear model, $[-]$

ϵ_w emissivity of water: 0.98

e thickness, $[m]$

H upwards atmospheric convective flux, $[W.m^{-2}]$

H/W canyon aspect ratio, $[-]$

h convective heat transfer coefficient, $[W.m^{-2}.K^{-1}]$

I_x countermeasure impact at location x, $[-]$

i weather type, $[-]$

K total number of datasets, $[-]$

k k-th dataset among the total number of datasets, $[-]$

L incident longwave radiation, $[W.m^{-2}]$

L_{up}	upwards longwave radiation, $[W.m^{-2}]$
λ	thermal conductivity, $[W.m^{-1}.K^{-1}]$
l	latent heat of vaporization of water: 2,260 kJ.kg^{-1}
M_{itx}	meteorological parameter for a weather type i, period t and location x, $[-]$
N_t	total number of observations for a given time period t, $[-]$
Φ	total pavement cooling flux, $[W.m^{-2}]$
Φ_{lat}	latent cooling flux, $[W.m^{-2}]$
Φ_{opti}	optimal pavement cooling flux, $[W.m^{-2}]$
$\Phi_{reg,lat}$	"latent" regime cooling flux, $[W.m^{-2}]$
$\Phi_{reg,sens}$	"sensible" regime cooling flux, $[W.m^{-2}]$
Φ_{sens}	sensible cooling flux, $[W.m^{-2}]$
φ_g	global surface heat flow, $[W.m^{-2}]$
φ_{rad}	radiative surface heat flow, $[W.m^{-2}]$
p_0	total air pressure, $[Pa]$
p_s	saturation vapour pressure, $[Pa]$
p_v	partial vapour pressure, $[Pa]$
Q	watering rate, $[mm/h]$
Q_A	heat advection, $[W.m^{-2}]$
Q_F	atmospheric anthropogenic heat release, $[W.m^{-2}]$
Q_{opti}	optimal watering rate, $[mm/h]$
$R_{intercept}$	random intercept, $[-]$
R_n	net radiation, $[W.m^{-2}]$
R_{slope}	random slope, $[-]$
ρ	density, $[kg.m^{-3}]$
ρ_w	water density: 1000 kg.m^{-3}
S	incident shortwave radiation, $[W.m^{-2}]$
S_{up}	reflected shortwave radiation, $[W.m^{-2}]$
σ	Stefan-Boltzmann constant: 5.67$\times$10^{-8} W.m^{-2}.K^{-4}
T_a	air temperature, $[°C]$
T_{dew}	dew point temperature, $[°C]$
T_g	globe temperature, $[°C]$
T_{mrt}	mean radiant temperature, $[°C]$
T_s	surface temperature, $[°C]$
T_w	water temperature, $[°C]$
$T_{wet-bulb}$	wet-bulb air temperature, $[°C]$
T_z	pavement temperature at depth z, $[°C]$
τ	in-depth heat transmission index, $[-]$
t	period of evaluation (before or after countermeasure implementation, $[-]$, or time, $[s]$
U_{itx}	effects of local urbanization for a weather type i, period t and location x, $[-]$

V	downwards conductive heat flux, $[W.m^{-2}]$
V_z	downwards conductive heat flux at depth z $[cm]$, $[W.m^{-2}]$
v	wind speed, $[m.s^{-1}]$
x_1	control site location, $[-]$
x_2	case site location, $[-]$
z	depth z, $[m]$

PART I

GENERAL INTRODUCTION

Introduction

The strong cooling benefits of water under the overwhelming heat of hot climates is a well-known fact. Arabic architecture took full advantage of it using *mashrabiyas*, decorative windows favouring ventilation, behind which porous clay jars filled with water were stored. Water evaporation cooled the passing air as it entered the house (Mohamed, 2015). Similarly, wealthy ancient Persian homes sometimes came with special rooms connected to *badgirs*, wind-catching towers that forced downwards air circulation, where cooling was often enhanced with a small water pond or an underground water channel called *qanat* (English, 1998). These provided a cool refuge during the afternoon in the harsh Iranian climate.

Examples of such vernacular designs or historical practices can be found abundantly all across the globe. In traditional Japan, the secular water-throwing ceremony of *uchimizu* (from *uchi*, to throw and *mizu*, water) plays a major cultural role in addition to cooling ground surfaces and the local atmosphere during summers. As well, ground- or roof-sprinkling with water has been employed for centuries as a customary practice in the Mediterranean region, although it is not limited to hot areas. For instance, in his novel *Au bonheur des dames* published in 1883, Emile Zola mentions its informal practice in Paris: "*Un lourd soleil chauffait les vitrages, et malgré les stores de toile grise, la chaleur tombait dans l'air immobile. Par moments, une haleine fraîche montait des parquets, que des garçons de magasin arrosaient d'un mince filet d'eau*[1]."

In Paris still, official traces of this practice by the municipal services can be found in the early 20th century. At that time, public spaces were regularly watered in order to placate dust clouds formed by passing horse-drawn carriages. If the modernization of transport has caused the gradual disappearance of this practice up to this day, local inhabitants of the time reported a sensation of cooling associated with watering (Girard, 1923). Street-cleaning with non-potable water was enabled thanks to the progressive modernization of the water supply and drainage infrastructures of the French capital. The latter is now a far cry from the Gallic Lutetia, which used to draw its water directly from the river, shortly before the first construction of the Roman aqueducts. From 1860, along with the important renovation of Paris driven by Baron Hauss-

---

[1]"*A warm sun was playing on the windows, and in spite of the grey linen blinds, the heat penetrated the stagnant air. Now and then a refreshing breath arose from the floor, which some assistants were gently watering.*" (translated from *The Ladies' Paradise*, Emile Zola, 1883)

mann and in accordance with the hygienist theories, the engineer Eugène Belgrand supervised the creation of the underground sewers, within which two twin water networks, potable and non-potable, were installed (Husson, 1996). Non-potable water, principally sourced from the Ourcq canal and to a lesser extent from the Seine, remains dedicated to public use today, supplying public fountains, parks and street-cleaning.

In the last couple of decades, pavement-watering has regained popularity across the globe, with scientific field studies and publications principally in Japan or France. Specifically, in Paris, the use of the non-potable water network for emergency cooling of public spaces during the summer has recently been of particular interest for the City Hall. Indeed, following a decision by the City Council in 2012, the non-potable water network has been given new impetus (Paris City Council, 2012). Ever since, it has been undergoing renovation work as well as a revaluation of its uses. In this context, its use to cool the city has been studied notably as part of a Ph.D. thesis which aimed to quantify the cooling effects of this technique (Hendel, 2015).

This initiative is part of a wider political movement driven by the City of Paris for several years in order to develop a wide range of climate change adaptation measures. This awareness rose in the wake of the major European heat-wave of 2003, shortly followed by Paris' first Climate Plan in 2007. Since then, the reinforcement of these measures is also motivated by predictions of an increase in the frequency, duration and intensity of heat-waves as a result of climate change in the years to come (Lemonsu et al., 2013). Awareness has been further strengthened by recent weather observations, which indicate that 2019, 2018 and 2014 were the hottest years on record in France (Météo-France, 2020). While the Climate Plan is updated every 5 years (Paris City Hall, 2017a), Adaptation and Resilience strategies have also been adopted in the meantime (Paris City Hall, 2015, 2017b). These milestones have laid a favourable ground for the emergence of various studies (Météo-France and CSTB, 2012) and urban planning projects all aiming at cooling public spaces via urban greening, reflective materials or new water uses such as pavement-watering.

In this context, cities are seeking guidance in the implementation of their cooling strategies at local territorial scale, taking into account the specificities of each site and using suited evaluation tools. The main goal of this dissertation is to provide elements to advise decision-makers on the procedure to favour, with a specific focus on pavement-watering and pavement materials. Many facets can be considered to tackle the problem. For instance, water availability, positive impacts on air pollution or soil cleanliness and other potential socio-economic side-effects are relevant when deploying a pavement-watering strategy and should not be overlooked. The use of appropriate paving structures, including cool materials, raises questions about mechanical resistance, adhesion, maintenance, ageing, reparability, availability or implementation procedures. Regardless of the solution considered, associated energy and financial costs as well as CO_2 emissions are also important. In order to narrow the area of research, we turn to the language associated with adaptation to heat-waves in Paris' Climate Plan (2017a). This brings us to focus on the extensive study of the microclimatic and thermal effects of cooling strategies through the prism of public-space intervention. The document prompts the development of specific areas "open to the public and cooler than the nearby environment" and solutions that help "reduce the temperature". Having defined these criteria, we first identify decision-makers' specific needs.

Practically speaking, whether for pavement-watering or other cooling strategies, the efficiency of the implemented solution needs to be quantitatively assessed. In order to do so, adapted tools and methods for *in situ* evaluation of their performance under real conditions must be developed. The field deployment of a pavement-watering strategy also requires knowing which surface area (whole street, pavement, sidewalk, etc.) needs to be treated in order to obtain satisfactory cooling benefits while limiting the method's water consumption. Assessing the cooling effects associated with a given treated street-portion also meets an operational need, as the potential presence of shops, terraces or pedestrians on Parisian sidewalks can prevent from implementing watering in a simple manner. Decision-makers therefore need to be aware of the performance associated with each possible strategy.

Finally, declining pavement-watering to different sites requires adapting the strategy to their specificities (type of materials in place, exposure, etc.), as those influence the optimal watering strategy to adopt in order to reduce the water consumption associated with pavement-watering. At the same time, urban-planning projects integrating innovative materials are emerging, as alternatives to traditional asphalt pavements inherited from the post-Haussmanian period. To answer this question without deploying costly and long-lasting field tests, a laboratory approach can be used, while validated against a limited number of field studies. Such an approach permits optimizing the watering strategy according to the pavement material, and studying the behaviour of each pavement material and its synergies with watering.

Our research question can therefore be stated as follows: how can a pavement-watering strategy be operationally adapted to the characteristics of different urban sites, in particular to the variety of paving materials composing the urban fabric and to the surface area available for watering? With which tools can the corresponding microclimatic effects be evaluated?

Before getting to the very heart of the matter, the following Chapters of Part I will present the scientific background of urban climate, thermal comfort and heat mitigation strategies. A brief state of the art of pavement-watering will be provided as well. These Chapters will help us identify more specific research questions that will guide this dissertation.

Scientific Background

2.1 The UHI Effect and the Urban Climate

Urban areas, through a combination of various mechanisms, display warmer air and surface temperatures than their surroundings. This phenomenon, known as the urban heat island (UHI) effect, is a tangible expression of the presence of cities and the human activities taking place within them. The UHI effect has long been observed in many cities around the globe. It was first described in the 1810's by Luke Howard, commonly referred to as the father of modern meteorology, who established a very thorough documentation of London's climate (Howard, 1833). Through temperature records outside and within London, Howard observed that "*the temperature of the city is not to be considered as that of the climate: it partakes too much of an artificial warmth, induced by its structure, by a crowded population and the consumption of great quantities of fuel in fires*". Emilien Renou, a French meteorologist, conducted a similar work for Paris during the mid-19th century (Renou, 1855). The phenomenon was named later on by analogy to the topographic patterns of the isotherms on a surface weather map, which appear as an island (Stull, 2012).

The UHI phenomenon is the most well-known feature of the urban climate. Lowry (1977) was the first to establish a framework choosing a site's past-atmospheric state as reference for explaining the "urban effect". Urban meteorological observations are seen as the "background climate" (the "flat-plane" climatological background for the region) on which the "local climate" (function of local natural features such as topography, shorelines, etc.) as well as "urbanization effects" are overlaid. The understanding of the physical mechanisms involved in the urban heat budget has since been significantly refined. In short, UHIs are caused by several factors. Urban morphology, because of wind and sky obstruction, reduces convective exchanges in addition to favouring radiative trapping. During the day, solar radiation tends to be absorbed by urban surfaces through multiple reflections, as does the infrared radiation emitted by mineral surfaces at night. The higher-inertia urban fabric also favours heat storage, while the lack of vegetation reduces latent exchanges and anthropogenic heat release further increases city-scale heat gains (Oke, 1982). Various studies have examined the link between some of these mechanisms and urban configurations, such as the relationship between the sky view factor (form

factor between a point at ground level and the sky, dependent on sky masks such as trees, buildings, etc.) and UHI intensity, or that between radiative trapping and the canyon aspect ratio (H/W) (Oke, 1981, 1988a).

The UHI intensity (or magnitude), measured as a simultaneous temperature difference between an urban area and its surroundings, spans on average between 1° and 3°C (Grimmond, 2007). For example, Paris' urban core is 3°C warmer on a year average than its rural surroundings (Cantat, 2004). However, UHI is both spatially and temporally dependent, in addition to being related to a city's intrinsic characteristics (e.g. size, shape, building density, land-use, population, etc.) and external influence (local climate, seasons, weather). Because of the different behaviour of the city and its surroundings, UHI intensity can be negative in the morning (so-called urban cool island) when rural areas with a lower thermal inertia warm up faster than the city as the latter achieves its heat release. On the contrary, its maximum intensity is reached before sunrise (Oke, 1982).

Under clear skies and in the absence of wind, this difference can reach up to 10°C (Grimmond, 2007). This is typically the case during heat-waves, which are worsened by UHI, which in turn contributes to worsen their health impacts, and has been observed in Paris (Cantat, 2004; Météo-France and CSTB, 2012) as for other cities around the world (Li and Bou-Zeid, 2013). Thus, in addition to altering the local atmosphere, heat islands affect human thermal comfort and public-health, by increasing the heat-related morbidity (Grimmond, 2007). For instance, the 2003 European heat-wave caused about 70,000 deaths (Robine et al., 2008). Unfortunately, climate change is expected to increase the frequency, duration and intensity of these events (Meehl and Tebaldi, 2004; Dousset et al., 2011; Lemonsu et al., 2013). For Paris, the number of heat-wave days per year on average should increase from one to twelve by the end of the century. Additionally, UHIs also cause a significant increase of cooling demand during summer (Mallick et al., 2009; Stone et al., 2010), and a degradation of air quality by favouring the formation of ozone air pollution and smog (Rosenfeld et al., 1998; Shimoda, 2003).

For these reasons, cities are strongly motivated to seek out urban cooling with growing interest from decision-makers. As a result, research efforts can be observed regarding urban cooling techniques. In France, the 2003 heat-wave raised awareness regarding the need to deploy adaptation measures for the population, included since 2007 and regularly updated in the Paris Climate Plan (Paris City Hall, 2017a). In the scientific literature, various countermeasures have been proposed with that aim, all tackling different mechanisms involved in the urban heat budget. As well, several urban canopy models have been developed and refined over the years, such as the Town Energy Balance (TEB) model (Masson, 2000). Simulations of larger scale implementations provide assistance for decision-makers trying to reduce the impact of UHIs in cities (Météo-France and CSTB, 2012) and target appropriate UHI-countermeasures based on the urban configuration.

2.2 Urban Heat Budget

The heat budget of an urban surface or volume helps identify the physical parameters driving urban heat flows and that need modification in order to limit the heating of the atmosphere. Figure 2.1 shows the energy balance of an urban surface.
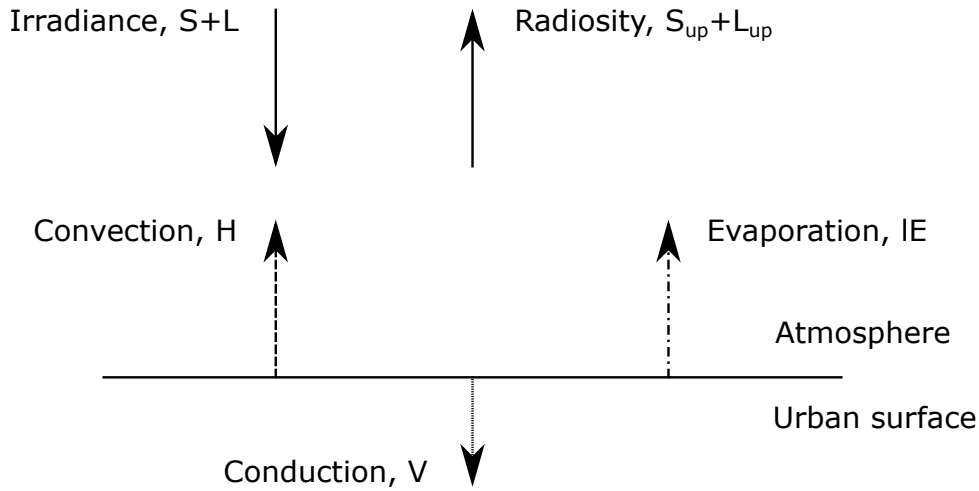
Figure 2.1: Urban surface heat budget.

H is the atmospheric convective exchange with the surface, V is the heat conduction flux, lE is the latent heat flux if the surface is wet or vegetated (evapotranspiration), with l the latent heat of vaporization of water and E the evaporation rate. S and S_{up} are respectively incident and reflected (upward) shortwave radiation (SW), while L and L_{up} are respectively incident and upward longwave radiation (LW). Radiosity designates the sum of radiation reflected and emitted by the ground (upward flows), while irradiance designates the incident (downward) flows. SW designates solar radiation, i.e. both the visible and near-infrared (NIR) bands (0.3 – 3 μm) while LW covers the mid-infrared band and part of the far-infrared (3 – 100 μm). The heat budget an urban surface can be summarized by equation 2.1:

$$S + L = S_{up} + L_{up} + H + V + lE \tag{2.1}$$

The radiative balance of incident radiation and radiosity can be condensed into the term R_n, net radiation, defined as follows:

$$R_n = S + L - (S_{up} + L_{up}) \tag{2.2}$$

For clear sky conditions in summer, net radiation is positive during the day (radiative absorption) with a predominant component of solar irradiance (S), and negative at night (radiative release) with no SW component neither incident nor upward (Oke, 1988b). SW and LW radiosity can respectively be developed into equations 2.3 and 2.4, with α the albedo of the surface, ϵ the emissivity, σ the Stefan-Boltzmann's constant (5.67×10^{-8} W.m^{-2}.K^{-4}) and

T_s the surface temperature. The albedo of a surface represents its solar (SW) reflectivity, while its emissivity quantifies the ability of a surface to emit thermal radiation in proportion to its surface temperature.

$$S_{up} = \alpha S \tag{2.3}$$

$$L_{up} = (1 - \epsilon)L + \epsilon\sigma T_s^4 \tag{2.4}$$

According to Jürges (1924) and to Fourier's law, respectively, atmospheric convection and heat conduction can be expressed as:

$$H = h(T_s - T_a) \tag{2.5}$$

$$V = -\lambda \frac{\partial T_z}{\partial z}\Big|_{z=0} \tag{2.6}$$

with h the convective heat transfer coefficient, T_a the air temperature, λ the thermal conductivity of the urban surface and z the depth considered. For its part, the evaporation rate is principally driven by the vapour pressure gradient in the near air, mainly proportional to the water film temperature, but also depending on other meteorological variables such as radiation, air pressure, wind speed, etc. Several methods exist to estimate the evaporation rate, either based on the energy or water budget or the mass convection transport problem (MCTP), each making certain assumptions. According to Xu and Singh (2001), the latter method offers a satisfying accuracy with limited input data. Derived from the MCTP (Pagliarini and Rainieri, 2011), for a continuous water film whose temperature is that of the surface, the latent flux is:

$$lE = 0.622 \frac{lh}{c_a p_0} T_s \left(\frac{p_s}{T_s} - \frac{p_v}{T_a} \right) \tag{2.7}$$

with p_s, p_v and p_0 respectively the saturation vapour pressure at temperature T_s, partial vapour pressure at temperature T_a and the total air pressure and c_a the specific heat of air (1.005 kJ.kg^{-1}.K^{-1}). Therefore, the terms of equation 2.1 can be developed into the following:

$$S + L = \alpha S + (1 - \epsilon)L + \epsilon\sigma T_s^4 + h(T_s - T_a) - \lambda \frac{\partial T_z}{\partial z}\Big|_{z=0} + 0.622 \frac{lh}{c_a p_0} T_s \left(\frac{p_s}{T_s} - \frac{p_v}{T_a} \right) \tag{2.8}$$

The left-hand side term of equation 2.8 represents the inbound flows, while outbound flows are on the right. Among equation 2.8's terms, only SW and LW reflections (i.e. $\alpha S + (1 - \epsilon)L$) and irradiance are independent from the surface temperature, which changes over time to balance irradiance with outbound flows.

Figure 2.2 illustrates the energy balance of an urban volume delimited between the upper border of the urban canopy layer and below a depth into the ground such that the conductive heat flux is negligible over the time scale considered, with Q_F the atmospheric anthropogenic
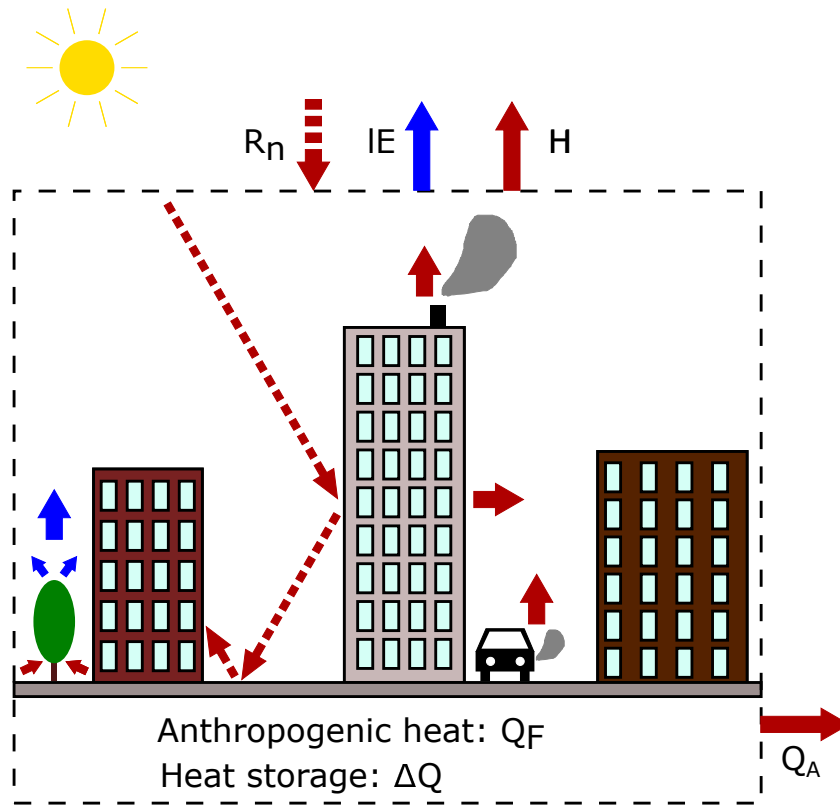
Figure 2.2: Urban volume heat budget (Hendel, 2020).

heat release, Q_A the heat advection outside of the volume and ΔQ the heat storage term in the urban materials. At this scale, heat conduction V is internalized in ΔQ. The energy budget thus becomes:

$$R_n + Q_F = H + \Delta Q + lE + Q_A \tag{2.9}$$

For clear skies and low wind speed, it is noteworthy the atmospheric component of the advective term Q_A is almost null (excluding natural heat advection, e.g. by rivers, or forced heat sink-transfer). Typically, urban areas experience stronger and positive values of atmospheric convection H both day and night compared to a rural area, stronger heat storage and anthropogenic heat release and less latent flows (Oke, 1988b). Regardless of the scale considered, H is the term causing atmospheric warming in cities (Asaeda et al., 1996; Christen and Vogt, 2004). Existing cooling strategies all aim to reduce this term. This requires the reduction of air and surface temperatures, either by reducing inbound flows or increasing outbound flows, using the following mechanisms:

Reducing inbound flows:

- Reducing irradiance via:
    - shading (decrease S)

  - lower LW radiation (decrease L)
- Reducing atmospheric anthropogenic heat release via:
  - energy efficiency (decrease Q_F)
  - heat sink transfer (from Q_F to Q_A)

Increasing outbound flows:

- Increasing radiosity via:
  - higher albedo (increase S_{up})
  - higher emissivity (increase L_{up})
- Increasing the in-depth proportion of conducted/stored heat via:
  - higher material thermal conductivity (increase V)
  - higher material thermal inertia
  - in-depth heat harvesting (increase V and from ΔQ to Q_A)
- Increasing latent flows (lE) via:
  - vegetation evapotranspiration
  - artificial watering

For a cooled surface, convective (H), emitted LW radiation ($\epsilon\sigma T_s{}^4$) and conductive flows (V, due to a smaller temperature gradient between the surface and depth) are reduced, resulting in a cooler atmosphere with reduced radiosity. In the literature, the reduction of LW irradiance is often associated with shading. However, shading devices can defeat this purpose if their temperature rises under solar exposition. It is also noteworthy that most cooling techniques act on several of those physical mechanisms simultaneously. Additional information is provided in Section 2.4.

2.3   Pedestrian Heat Stress

Mitigating urban warming mainly addresses the reduction of the air temperature, but also seeks to reduce the other parameters likely to worsen the thermal comfort of a person. Thermal comfort is defined by ASHRAE (2017) as a "*condition of mind that expresses satisfaction with the thermal environment and is assessed by subjective evaluation*". Heat stress on the other hand generally refers to a physiological state in which the human body's thermoregulation is challenged, resulting from an unfavourable heat balance of the human body. The difference between thermal comfort and stress is losely defined, and both terms are often used interchangeably. However, the word "stress" is meant as less subjective than "comfort", as thermal heat stress depends on the heat budget of the considered individual. The energy balance between the human body and the environment, illustrated in Figure 2.3, depends on several factors: metabolic rate, clothing insulation, air temperature, radiant temperature, air speed and humidity.
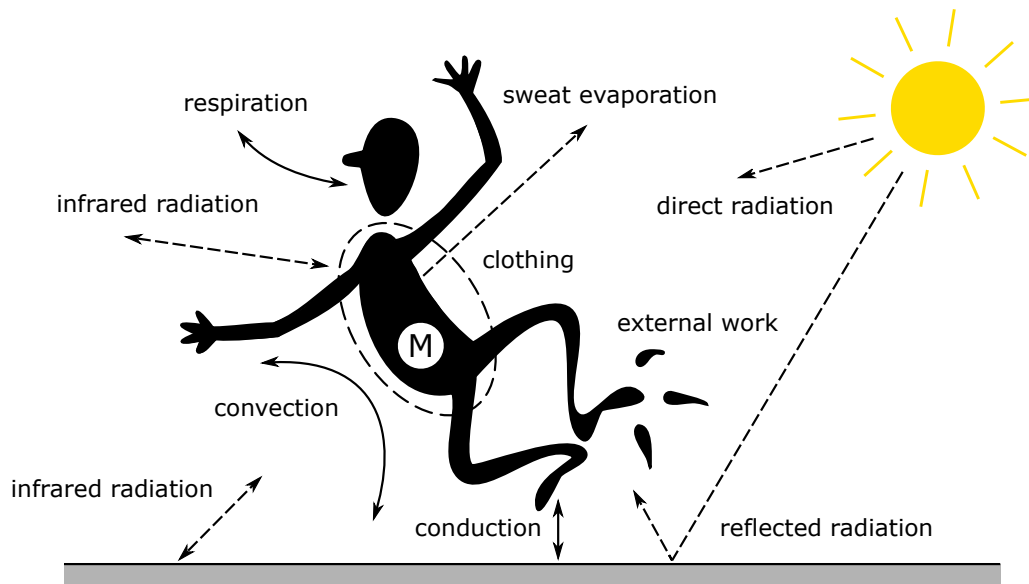
Figure 2.3: Human heat budget (adapted from Havenith, 1999). *M* is the metabolic heat production.

Several indices for heat stress have been developed over the years, each making certain assumptions on the human heat budget. Before presenting some of them, we start by describing the radiative environment, crucial to the pedestrian heat budget.

2.3.1 Radiative Environment and Mean Radiant Temperature

Proper characterization of the radiative environment is crucial to estimating the impact of a UHI-countermeasure on pedestrian heat stress. Mean radiant temperature (MRT or T_{mrt}) plays a decisive role in thermal comfort in the built environment. It is formally defined as "*the temperature of a uniform, black enclosure that exchanges the same amount of heat by radiation with the occupant as the actual surroundings*" (ASHRAE, 2017). In other words, MRT encapsulates incident radiation received in a particular point into one single metric.

A variety of methods exist to estimate MRT, reviewed by Guo et al. (2019). Based on its definition, calculating MRT to the fourth requires summing the radiative flows emitted by each surface at its average temperature, weighed by view factors between the person and the corresponding surface. However, determining all the appropriate view factors is complex, especially for elaborate spaces, even when modelling the human body as a sphere or point.

Experimentally, MRT can be estimated more easily using different instruments, the most common of which is the globe thermometer. In this case, the simplified geometry of the considered person is that of a sphere. Once the instrument reaches thermal equilibrium, according to Kirchhoff's law of thermal radiation, the energy balance between convective and radiative heat exchanges can be expressed as follows, with incident flows (ambient radiation) on the left, and outbound flows (black-body emission and convection) on the right:

$$\epsilon\sigma(T_{mrt} + 273.15)^4 = \epsilon\sigma(T_g + 273.15)^4 + h(T_g - T_a) \tag{2.10}$$

with T_g the globe temperature, σ the Stefan-Boltzman constant, ϵ the globe-thermometer's emissivity, T_a the air temperature and h the convective exchange coefficient, which depends on wind speed and globe diameter. The energy balance of the globe thermometer (equation 2.10) can be illustrated with Figure 2.4.
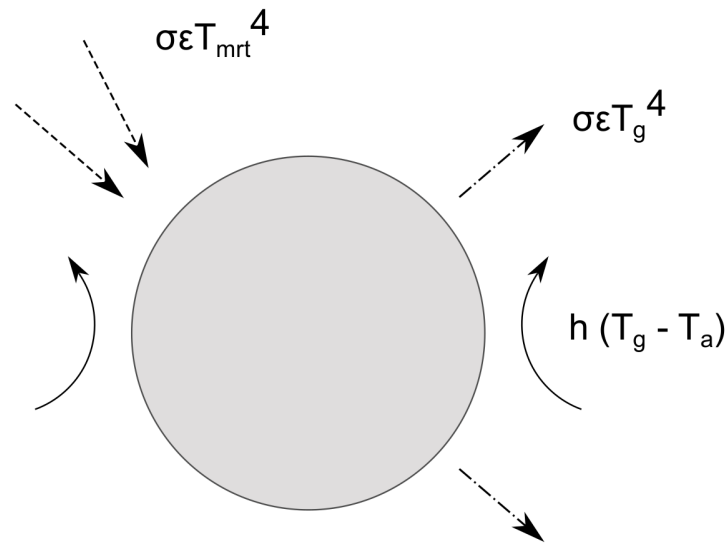
Figure 2.4: Energy balance of a globe thermometer. Heat gains and losses flows are isotropically received and lost by the globe. Temperatures are expressed in Kelvins.

According to ASHRAE (2001), the governing equation from empirical measurements with globe thermometers for estimating MRT is:

$$T_{mrt} = \left((T_g + 273.15)^4 + \frac{1.1 \times 10^8 v^{0.6}}{\epsilon D^{0.4}} (T_g - T_a) \right)^{0.25} - 273.15 \tag{2.11}$$

with D the globe's diameter and v the wind speed. The knowledge of equation 2.11's parameters at a given height thus gives MRT. In principle, this formula applies for any kind of globe thermometer, but the World Meteorological Organization (WMO) standard globe (ISO 7726, 1998) is a hollow matte-black copper globe (with emissivity of 0.95), 150 mm in diameter and 0.4 mm in thickness and equipped with a Pt100 resistance thermometer in its center, the measured temperature of which is assumed to be equal to that of the black-globe once thermal equilibrium is reached. This instrument has a typical stabilization time of 20-minutes.

Various globe sizes exist in the literature. Smaller acrylic globes (40 mm in diameter) were found to reach their thermal equilibrium within 5 minutes, and within 4 minutes for acrylic ping-pong balls (Guo et al., 2019; Thorsson et al., 2007; Nikolopoulou et al., 2001). Nonetheless, smaller globes tend to be more sensitive to wind speed which undermines their accuracy

(Graves, 1974). There is general consensus in the literature that there is a trade-off between accuracy of the instrument and its response time, the former and the latter respectively being proportional and inversely proportional to the globe's diameter (Guo et al., 2019). Furthermore, Wang and Li (2015) showed that low-conductivity-acrylic globes performed poorly compared to copper globes under asymmetrical radiation, compromising the hypothesis of isothermal conditions inside the globe.

Modelling tools as well as alternative instruments suited to the estimation of MRT also exist, each governed by a specific empirical equation. To cite but a few alternatives, MRT can be determined with integral radiation measurements (IRM), using a net radiometer simultaneously measuring short and longwave radiation into the four lateral directions as well as upward and downward (12 instruments in total) (Thorsson et al., 2007). This method is much more demanding than a simple globe thermometer, as it requires computing the mean radiant flux density with the appropriate view factors, but is the most accurate outdoors since it can be adapted to a standing or seated person, when the globe considers equal view factors in all directions instead (Kántor and Unger, 2011). Other than that, the constant-air-temperature sensor is maintained at the surrounding air temperature with a heat supply, to apply a correction on convective exchanges and deduct MRT. Similarly, a two-heating-spheres radiometer can be used to reach MRT. Each sphere has a different emissivity and are maintained at the same temperature with a heat supply in order to estimate the convective heat loss to deduct MRT (Guo et al., 2019).

Having presented the radiative environment and MRT, we now briefly present some of the most commonly found thermal stress indices in the scientific literature.

2.3.2   Thermal Stress Indices

Researchers have developed several thermal comfort indicators to assess the effects of the environment on thermophysiology, each making certain assumptions and taking into account more or less input parameters relevant for the human heat budget (Figure 2.3). We now present some of the most reported thermal indices in the scientific literature (Binarti et al., 2020).

Wet-Bulb Globe Temperature

One of the most widely used indices is the Wet-Bulb Globe Temperature (WBGT), originally developed to control heat strokes and applied to the United States army (Yaglou et al., 1957). This index is calculated from dry- and wet-bulb ($T_{wet-bulb}$) air temperatures as well as globe temperature. WBGT thus includes information on radiative environment and air temperature and indirectly on humidity and wind speed through $T_{wet-bulb}$, but not on metabolic state or clothing. Respectively, for outdoor (with direct shortwave radiation) and indoor environments WBGT is defined as (Lemke and Kjellstrom, 2012):

$$WBGT = 0.7\, T_{wet-bulb} + 0.2\, T_g + 0.1\, T_a \tag{2.12}$$

$$WBGT = 0.7\, T_{wet-bulb} + 0.3\, T_g \tag{2.13}$$

Humidex

The Humidex (HD) is a hot-weather index developed by Canadian meteorologists (Masterton and Richardson, 1979) that empirically scales thermal comfort into bands of thermal stress, accounting for heat and humidity:

$$HD = T_a + \frac{5}{9}\left(6.11 \times exp^{5417.7530\left(\frac{1}{273.16} - \frac{1}{273.15 + T_{dew}}\right)} - 10\right) \qquad (2.14)$$

with T_{dew} the dew point temperature. The exponential factor is a constant based on the latent heat of vaporization of water, the molar mass of water and Boltzmann's gas constant. Although the Humidex is homogeneous to a temperature, it does not express an HD-equivalent temperature. The correspondence between the index range and thermal stress is given on a scale of comfort. The Humidex equivalent for cold weather is the Wind Chill Index (WCI), calculated on the basis of air temperature and wind speed (Siple and Passel, 1945).

Physiological Equivalent Temperature

According to Binarti et al. (2020), the Physiological Equivalent Temperature (PET) is currently the most commonly used outdoor thermal comfort index. PET was developed to understand the impact of meteorological parameters on a "standard" person, thus making assumptions on the metabolic activity and clothing insulation. The index defines an equivalent temperature based on the human heat budget under reference conditions. It is the air temperature at which the indoor human heat budget is balanced with the same core and skin temperature as under the actual outdoor conditions (Höppe, 1999).

The calculation of PET is based on the Munich Energy Balance Model for Individuals (MEMI), a thermophysiological heat balance model for the human body (Höppe, 1993). The model takes into account meteorological parameters, i.e. air temperature, humidity, wind velocity and MRT, and thermophysiological parameters such as heat resistance of clothing (clo units, equivalent to 0.155 K.m².W^{-1}) and human activity (in Watts). The MEMI includes basic thermoregulatory processes, such as constriction/dilation of blood vessels and sweat rate. The standard person considered in the model is characterised by a work metabolism of 80 W (light activity) in addition to basic metabolism, and by a clothing heat resistance of 0.9 clo. For the reference indoor setting, MRT is taken equal to air temperature, wind speed is 0.1 m/s, and water vapour pressure is set to 12 hPa (roughly equivalent to a relative humidity (RH) of 50% at a dry air temperature of 20°C) (Matzarakis and Amelung, 2008).

The PET-equivalent temperature is then divided into 9 bands of thermal perception (from "very cold" to "very hot", respectively below -4°C and above 41°C) each corresponding to a level of physiological stress, valid for the standard person considered. Shortcomings of PET mainly concern its poor response to clothing insulation and humid conditions. Recently, the mPET (modified Physiological Equivalent Temperature) was proposed to address this problem and improve thermal comfort predictions (Lin et al., 2019).

Universal Thermal Climate Index

The Universal Thermal Climate Index (UTCI) is a relatively recent index, developed by experts of the International Society of Biometerology with expertise from various fields (thermophysiology, medicine, physics, biometeorology and environmental sciences). The index takes into account physical variables (air temperature (T_a), MRT (T_{mrt}), wind speed v and humidity in the form of the saturation vapour pressure, p_s) and makes assumptions on the metabolic rate and clothing of pedestrians. As for PET, UTCI is an equivalent temperature defined as the air temperature under reference conditions that would provoke the same thermophysiological response as in the actual environment (Błażejczyk et al., 2010).

According to Błażejczyk et al. (2013), hypotheses made on the seasonal clothing and on the metabolic rate are chosen to be representative of most people (average person of 73.5 kg with body fat content of 14% walking at 4 km/h, thus with a metabolic heat production of 135 W/m²). The reference environment is set to be relevant across the broad spectrum of climate zones, and is similar to conditions experienced in an indoor setting, all else being equal. It assumes a wind speed of 0.5 m/s (1.8 km/h) at 10 m height (about 0.3 m/s (1 km/h) at pedestrian height), a MRT equal to air temperature and a vapour pressure representing a relative humidity of 50% or constant vapor pressure of 20 hPa above 29°C. A clothing model based on seasonal clothing adaptation habits of Europeans is used, adjusted to air temperature and wind speed (Havenith et al., 2012).

The calculation of UTCI is based on the multinodal Fiala et al. (2012) model, abstracting the human body to twelve spherical and cylindrical body elements built as annular concentric tissue layers. Individual body parts or the whole body can be considered. The model accounts for the complete human heat budget and predicts thermoregulatory reactions such as vasoconstriction and vasodilation of the blood vessels, shivering thermogenesis, and sweat moisture excretion (Błażejczyk et al., 2013). The fast-calculation script for UTCI written by Bröde (2009) can be found online freely, for which UTCI is interpolated with a 6th order polynomial function of T_a, v (10 m), p_s and $T_{mrt} - T_a$. The model automatically adjusts 10-m-height wind speeds to 1.5 m above ground level. For wind speed measurements made at height z (different than ten meters), Bröde et al. (2012) provides the following equation based on Oke (1987) to feed the model:

$$v_{10m} = v_z \frac{log(10/0.01)}{log(z/0.01)} \tag{2.15}$$

Finally, the UTCI scale is divided into ten levels of thermal stress, for warm or cold conditions (from "extreme heat stress" to "extreme cold stress", with UTCI-equivalent temperature respectively ranging from above 46°C to below -40°C). The scale is defined based on the physiological response (sweat rate, latent heat loss, skin-core temperature difference, etc.) under the actual environmental conditions.

According to Błażejczyk et al. (2013), the comparison of UTCI to other thermal comfort indices made from various datasets highlighted that the index was found to better depict biothermal conditions for humans than other indices.

Other Indices

Many other heat stress indices exist (De Freitas and Grigorieva, 2015; Teodoreanu, 2016; Binarti et al., 2020). For example, the Predicted Mean Vote (PMV) empirically fits the human sensation of thermal comfort based on the prediction of the mean response of a large group of people on the ASHRAE seven-points thermal sensation scale (from -3 "cold" to +3 "hot"). PMV was later adapted to outdoor settings with the Klima-Michel-Model using weather data as input with assumptions on the activity and clothing (Jendritzky and Nübler, 1981). Also, the Standard Equivalent Temperature (SET*), based on the Gagge et al. (1986) two-node model, is defined as the equivalent temperature in an environment with a relative humidity of 50%, a wind speed of 0.1 m/s and a MRT equal to air temperature, where a person with standard clothing adapted to its metabolic activity experiences the same heat stress (skin temperature and wetness) as in the actual environment (Binarti et al., 2020).

2.3.3   Cooling Strategies and the Human Heat Budget

Having provided the basics mechanisms behind pedestrian heat stress and indices suited to its assessment, we now briefly discuss implications of urban cooling strategies on the human heat budget.

Cooling strategies most often target urban surfaces, and as such modify their energy balance, by the levers listed in Section 2.2, aiming at decreasing inbound and increasing outbound flows. Each term of the urban surface heat budget either has a direct or indirect effect on the parameters impacting the heat balance of a pedestrian. For instance, H will have an influence on air temperature, lE on relative humidity, S_{up}+L_{up} impacts the radiative heat budget of the pedestrian, while V has no significant impact on a standing pedestrian during the day. At night, the heat released by the pavements will tend to increase atmospheric convection H. This delays the impact of part of the heat absorbed during the day and explains the important magnitude of UHI at night.

Reducing atmospheric convection thus always has a positive effect both on pedestrians and on the surface. In contrast, other physical mechanisms can have a beneficial cooling effect on the surface, but a negative impact on the pedestrian. For example, evaporation of water on a surface slightly increases the humidity (detrimental to a pedestrian's heat stress) but significantly reduces its temperature (and thus H, S_{up}, L_{up} and V, all of which is beneficial for a pedestrian). Similarly, increasing the albedo of a surface reduces its temperature (and thus H, L_{up} and V), but by definition increases the SW radiosity S_{up}, unfavourable for the radiative budget of a person.

In such cases, care must be given to ensuring that the potential drawbacks of a countermeasure do not offset the benefits on the pedestrian's heat balance. In practice, such a condition is rarely achieved, except for very specific cases, depending for example on the urban configuration. This is further discussed in the following Section (2.4), describing urban heat mitigation strategies.

2.4 Urban Heat Mitigation Strategies

Having presented the physical mechanisms of the urban heat budget and the background to pedestrian heat stress, in this Section we now present a non-exhaustive list of typical urban heat mitigation strategies found in the literature. These designate a method that aims to mitigate or counteract the mechanisms responsible for urban warming, in some instances in order to reduce the inhabitants' thermal stress. Such measures have been studied for decades, either *in situ*, in the laboratory or numerically simulated, aiming to quantify the performance of each method (Spronken-Smith and Oke, 1999; Rosado et al., 2014).

Since urban cooling and UHI challenges are close notions, as they both depend on urban characteristics (land cover, morphology, anthropogenic heat, etc.), according to Martilli et al. (2020), this can sometimes lead to confusion in the literature or for decision-makers to attribute thermal discomfort in cities solely to UHI. However, the efficiency of heat mitigation strategies is studied as an absolute impact on thermal stress in urbanized areas, which can sometimes go hand in hand with UHI mitigation, but not systematically.

Indeed, it should be emphasized that counteracting UHI has little relevance for mitigating heat in urban areas. Contrary to the latter, mitigating UHI intensity requires considering both urban and rural characteristics. Thus, the intensity of the phenomenon is not necessarily related to thermal discomfort in the city, as well as its reduction does not necessarily lead to an improvement. For example, greening and irrigating the surroundings of un urbanized area would increase UHI intensity without modifying the urban area. Furthermore, the phenomenon's maximum intensity occurs at night, while thermal stress and building energy consumption peak during the day. Finally, a number of cities experience weak UHIs but would still benefit from heat mitigation studies due to their very high urban temperatures. This is for example the case for Phoenix which is surrounded by a desert (Balling Jr and Brazel, 1987).

Having said that, heat mitigation and countermeasures to UHIs are not necessarily conflicting terms. Yet, the term "UHI-countermeasure" can be abusive and as such misleading or inaccurate. Although implementation of UHI-countermeasures do marginally contribute to locally mitigate the UHI-intensity, it should not be confounded with the mitigation of negative aspects of urban heat.

2.4.1 Cool Materials

One of the most widely used heat mitigation strategies is the use of so-called "cool materials". The term refers to materials designed to reduce their surface temperature compared to "traditional" urban materials, in order to limit sensible heat exchanges with the atmosphere and its temperature. Cool materials can be used for façades, rooftops or pavements, and have been largely studied in the lab, the field or numerically. Several reviews can be found on the topic (Santamouris, 2013, 2015; Qin, 2015; Mohajerani et al., 2017; Hendel, 2020). Nonetheless, some research topics generally lack to this day in the cool pavements literature, as underlined by Qin (2015). For instance, although surface temperature reductions tend to be extensively reported,

the beneficial impact on air temperature and pedestrian thermal comfort is often overlooked and needs refinement. The same goes for the long term performance of cool pavements and their effect on adjacent buildings' heat load. Finally, the precise energy partition of a cool pavement surface is generally not reported and would merit investigation. We start by presenting reflective materials.

Reflective Materials

Reflective materials have higher reflectivity than their standard counterparts, as quantified by their albedo, in order to counterbalance the mechanisms of radiative trapping and thus reduce their surface temperature. The proportion of solar radiation reflected by a surface is quantified by its albedo. For the global irradiance AM 1.5 solar spectrum, respectively 49% and 46% of solar energy is partitioned in the visible ($0.38 - 0.74$ μm) and NIR ($0.74 - 3$ μm) bands (ASTM G173, 2003). Therefore, research effort focus on increasing the solar reflectivity of materials in the SW band.

While the utility of a high surface reflectivity is easy to understand, a material counteracting on radiative trapping must also present a relatively high thermal emittance in order to radiate LW away and maintain a cooler surface temperature. This is generally the case for commonly used urban materials (asphalt, concrete, granite etc.), the principal exceptions being metallic materials (e.g. Haussmanian buildings' zinc roofs in Paris, France), which would benefit from high emissivity coatings.

The most common materials of the urban fabric are usually asphalt and concrete. The albedo of asphaltic materials is very low, spanning between 0.05 and 0.20 depending on their aging and soiling, while that of concrete varies between 0.2 to 0.35, although the albedo of concrete surfaces tend to decrease with time contrary to asphalt (Santamouris, 2013; Mohajerani et al., 2017). The albedo of pavements can be increased either by modifying the reflectivity of the aggregates, that of the binder or both. It can be up to $0.80 - 0.90$ for white highly reflective paints (Synnefa et al., 2006), while some other coatings can have a lower typical range of albedo, e.g. between 0.25 and 0.62 for some NIR reflective paints (Synnefa et al., 2007), or between 0.20 and 0.58 for white-topped and slag-cement concretes (Boriboonsomsin and Reza, 2007; Sultana, 2010).

The work on cool materials began decades ago, with the testing of reflective white rooftop coatings (Akbari and Taha, 1992; Taha, 1997). Reflective rooftops are acknowledged in literature as an effective UHI-mitigation measure and help reduce building energy demand (Akbari et al., 1997). According to Kolokotsa et al. (2013), depending on the city, roofs with a reflectivity of 0.9 reduce summer sensible heat release by $25 - 35$ kWh/m² compared to a roof with a reflectivity of 0.3. Other studies have found that the use of reflective rooftops lead to air temperature reductions, typically between 0.5° and 2°C depending on the scenario (Synnefa et al., 2008).

In order to turn a surface reflective, specific coatings can also be used. For instance, thermochromic coatings become reflective passed a reversible colour temperature transition, which can be adjusted based on the thermochromic agents and their dosage (Ma and Zhu, 2009). This property allows such coatings to remain relatively cool during the summer while remaining

absorbent during winter, although Akbari and Hosseini (2014) indicate that the winter penalties of using reflective surfaces generally do not offset summer benefits even for cold climates. Additionally, coatings highly reflective in the NIR band provide cooling performance while allowing for various colours, while significantly reducing glare compared to reflective materials in the visible-band (Levinson et al., 2007; Xie et al., 2019).

The benefits of reflective pavements have also largely been studied. In all cases, reflective pavements were found to efficiently reduce surface temperatures. In the literature, a typical reduction ranging from 3° to 7°C per 0.1 increase in albedo is reported, depending on the experimental conditions and type of solutions tested (Qin and Hiller, 2014; Li et al., 2013c; Levinson et al., 2007; Synnefa et al., 2007; Pomerantz, 2000; Pomerantz et al., 2003). As well, reflective pavements also help reduce air temperatures, although few studies report this effect. Météo-France and CSTB (2012) simulated a scenario of reflective and emissive building materials for Paris that lead to a 2 m air temperature reduction in the order of 1°C, both day and night. For their part, Santamouris et al. (2012) showed that appropriate reflective pavements decreased the summer peak air temperature up to 2°C under specific climatic conditions. However, the main drawback of reflective pavements is their rapid and intense aging compared to roofs and façades because of traffic abrasion and soiling, which deteriorates their cooling effect (Alchapar et al., 2013; Rosado et al., 2014).

Nonetheless, as mentioned in Section 2.3, high-albedo pavements can occasionally be detrimental to pedestrian heat stress, as they increase SW reflections and can thus offset the gains of a reduced surface temperature and defeat their original purpose. According to Erell et al. (2014), this is the case for certain urban configurations and insolation conditions, typically for reflective building façades coupled with a grazing trajectory of the sun. This is also concerning in case the reflected SW is likely to be absorbed by adjacent buildings, leading to increased indoor temperatures (Yaghoobian and Kleissl, 2012). The implementation of reflective materials is also associated with other penalties. Typically, their production can be more energy demanding (e.g. for white cement due to the higher furnace temperature) and thus entail more carbon emissions that traditional pavements (Gilbert et al., 2017). For these reasons, reflective materials must therefore be implemented with care.

Modified Material Properties

In order to reduce a surface's temperature, materials can also rely on a higher-than-usual thermal inertia. One way to achieve this is by incorporating a phase-change material (PCM) into the mix. A PCM is a substance with one or several physical phase transitions, but used into urban materials they usually refer to a solid-liquid transition at a desired target temperature, because of their volumetric stability.

During the day, PCMs absorb heat when melting at constant pressure and temperature, and inversely release the same amount of heat at night during solidification. For that reason, high inertia pavements do not alter the pavement's energy balance (contrary to reflective or evaporative pavements), but increase the material's apparent specific heat. For this reason, the rate of the temperature rise and that of the sensible heat exchange with the atmosphere is smoothed out during the day, but temperature will reduce more slowly at night. High thermal inertia thus acts as a heat mitigation tool during the day, but tends to exacerbate the UHI effect

at night compared to a traditional structure, all else being equal.

PCMs can either be directly incorporated into the material or microencapsulated, the latter option usually being safer to avoid potential leakage at liquid state. They have been widely used for building applications (roofs, ceilings, walls etc.) (Koschenz and Lehmann, 2004; Tyagi and Buddhi, 2007; Pasupathy et al., 2008; Royon et al., 2014) but on lesser occasions for pavements. PCMs are often made of paraffin although other substances exist. Depending on the chemical agent and its dosage, the melting temperature, latent heat of fusion/solidification and thermal conductivity can be tuned. The melting temperature can be chosen to match that reached by the pavement during a given season. For example, it can be used during winter to prevent freeze-thaw on pavements (Mahedi et al., 2019). During the summer, Karlessi et al. (2009) found that PCM-coated tiles dampened peak temperature by $3° - 8°C$. Other studies report surface temperature reductions between $2°$ and $5°C$ depending on the characteristics of the PCMs used (Chen et al., 2011; Ryms et al., 2015; Athukorallage et al., 2018).

As with thermochromic coatings, one main disadvantage of PCM materials is the limited number cycles they can achieve before losing performance. In addition to that, high temperatures are found to be damaging to PCMs' properties, limiting their application in pavements depending on the manufacturing requirements.

Another possibility is to use highly conductive pavements (increasing V). High conductivity pavements exhibit lower surface temperature as in-depth heat absorption is facilitated compared to more insulating materials. This can be done by several approaches, e.g. by incorporating a fraction of graphite powder into the binder, or with less common designs using vertical steel rods in a traditional pavement's sub-layer, reducing surface temperatures up to $3.5°C$ (Yinfei et al., 2018). However, at night the heat stored during the day is discharged. As for PCMs, highly conductive pavements can therefore help mitigate heat daytime but might help maintain hotter temperatures at night.

To make up for this, heat-harvesting pavements can be used. These pavements harvest solar energy, most of the time via heat-exchanger pipes embedded into the pavement subcourse. Harvested heat can then be used productively, e.g. for domestic hot water supply of nearby buildings (Van Bijsterveld et al., 2001) or underground storage for snow melting during winter (Pan et al., 2015). Heat-harvesting pavements allow the reduction of surface temperature by artificially increasing the temperature gradient below the surface layer. This is achieved by adding an outbound flow to the urban heat budget in equation 2.8. Zhou et al. (2015) reported temperature reductions between $3°$ to $6°C$ during the summer, however the cooling efficiency and heat harvested highly depend on the pavement's characteristics (Bobes-Jesus et al., 2013).

Finally, other energy-harvesting pavements exist, such as photovoltaic pavements (harvesting solar radiation), thermoelectric and piezoelectric pavements (harvesting mechanical energy) (Efthymiou et al., 2016; Guo and Lu, 2017; Jiang et al., 2017). All of these pavements slightly help reduce surface temperature while harvesting energy, either based on the photoelectric effect, the Seebeck effect or piezoelectricity. The small amounts of power generated can typically be used to provide public lighting. Heat-harvesting pavements still pose several engineering challenges, mainly regarding their mechanical resistance and maintenance and the

improvement of their efficiency.

Evaporative Materials

Pavements can be designed in order to hold water to enable evaporative cooling and thus reduce their surface temperature via increased latent flows. The cooling effects provided by such materials being directly proportional to the amount of water evaporated, the latter needs to be available near the surface. Indeed, only the water stored near the top of the pavement rapidly evaporates (Nemirovsky et al., 2013). Different types of evaporative pavements exist. They are most often made of concrete, although other materials can be used. The internal structure of an evaporative pavement presents voids to allow the flow of water, making it pervious (sometimes called "porous" or "permeable" also). This is often achieved by increasing the proportion of large aggregates with regard to that of finer aggregates. For that reason, the typical reflectivity of such materials is slightly lower than that of a similar plain pavement. The typical porosity of pervious pavements is 15% to 30% (Qin, 2015). Pervious pavements are interesting to reduce stormwater runoff.

In case no impervious sublayer is present below the porous surface-course, infiltration in-depth might be too rapid to enable evaporative cooling efficiently. This led to the development of water-retaining (or water-holding) pavements, for which water-absorbing (slag, pervious mortar, etc.) fillers are incorporated into the mixture (Takahashi and Yabuta, 2009). According to Yamagata et al. (2008), depending on the composition, storing capacities can reach 15 kg of water per m². In addition, the pore structure of water-absorbing fillers can also induce a capillary action that drags water from the bottom to the top of the pavement as the surface dries out (Liu et al., 2018). In the literature, it has been demonstrated that wet evaporative pavements provide significant surface temperature reductions compared to traditional ones, with reductions up to $10° - 15°C$ (Kubo et al., 2006; Qin et al., 2018). However, when dry, pervious pavements were found to be as hot as normal pavements because of their lower thermal inertia and conductivity due to their void content, although this is positive in winter to avoid damage to the sub-layer caused by the freezing of water (Kevern et al., 2009; Haselbach et al., 2011). In addition to that, pervious pavements require regular cleaning to avoid clogging of the pores.

Evaporative pavements can also refer to so-called green pavements that present low-level vegetation, providing cooling with evapotranspiration during photosynthesis. Typically, green pavements can be implemented in pedestrian areas (i.e. without traffic). Several studies reported reductions of surface temperature between green pavements and standard pavements up to $20° - 25°C$, the higher reductions being obtained for an extensive grass lawn (Takebayashi and Moriyama, 2009, 2012; Asaeda and Ca, 2000). As for mineral or green evaporative pavements, their cooling performance is entirely dependent on their degree of wetness. Nonetheless, pervious sublayers are beneficial to soil biodiversity compared to impervious pavements.

Similar to the cooling mechanisms of evaporative pavements, pavement-watering, i.e. the intentional watering of ground surfaces (whether impervious or not) to mitigate heat, has been studied in a number of articles. The method is fully reviewed in the next Chapter (3).

2.4.2   Urban Greening and Shading

The many benefits of urban greening have been widely studied, either through the planting of trees, developing of lawns, green roofs or façades, or creation of parks (Bowler et al., 2010; De Munck et al., 2018; Chun and Guldmann, 2018). Urban greening increases latent flows thanks to evapotranspiration and can also provide shading if the vegetation is tall enough, reducing the incident irradiance received by a surface.

Météo-France and CSTB (2012) simulated a low-level vegetation greening scenario for Paris, France, and obtained a cooling effect up to 5°C (1°C on average) for 2 m air temperature with irrigation, but had a negligible impact without irrigation. Similarly, De Munck et al. (2018) evaluated the effect of several greening scenarios, with a maximum cooling of air temperature varying between 0.5° and 2°C. Armson et al. (2012) found that tree shade could reduce air temperatures by $1 - 2$°C, while grass reduced surface temperature up to 24°C compared to traditional pavements. In order to reduce building energy consumption all year, green roofs can be implemented, although they were found to have no significant impact on the street level air temperature (De Munck et al., 2018).

Yet, in order to provide a cooling effect, it has been demonstrated that irrigation was crucial, and greening scenarios often come with considerable water costs (Météo-France and CSTB, 2012; De Munck, 2013). Alternatively, shading alone is itself found to be greatly efficient compared to other cooling techniques, with UTCI-equivalent temperature reductions up to $8° - 11$°C compared to a sunny area (Watanabe and Ishii, 2016; Park et al., 2014). However, in addition to cooling, greening plays a key role for urban biodiversity, unlike other strategies.

2.4.3   Other Cooling Techniques

Many other techniques exist to mitigate heat or fight against UHIs. Deploying energy efficiency policies helps limit anthropogenic heat release, such as favoring the use of urban water networks for emergency cooling (Guo and Hendel, 2018). Actions can be undertaken to improve the insulation, sun exposure and ventilation of buildings (e.g. with green roofs and façades, the building enveloppe, etc.), which indirectly helps limit the release of anthropogenic heat associated with the use of air-conditioning during summer (Tremeac et al., 2012; De Munck, 2013). Cities under development can favour open urban designs (low canyon aspect ratios H/W, high sky view factor) in order to reduce radiative trapping. However, dense urban designs limit solar exposure in daytime and urban sprawl and reduce energy costs associated with transportation. In the summer, temporary devices can be deployed, such as potable water mist sprayers, very efficient as far as they directly target pedestrians.

Lastly, several authors have argued that the combination of various cooling techniques increased the overall cooling effect (Mohajerani et al., 2017; Daniel et al., 2018). Météo-France and CSTB (2012) showed that combining reflective buildings, irrigated vegetation and pavement-watering yielded by far the highest cooling effects compared to the isolated effects of each strategy, with maximum cooling up to 6°C with an average of 2.3°C. In addition, by combining strategies, several problems caused by UHIs can be addressed simultaneously, as challenges

and solutions interact (temperature, thermal stress, energy use, air pollution, carbon emissions, building insolation, stormwater management, etc.). As an example, Mullaney et al. (2015) highlighted that an appropriate pervious pavement design improved the draining capacity of soils and was thus beneficial to the growth and health of street trees. Such synergies are numerous in the literature and should be considered in urban planning.

2.5 Conclusion

In this Chapter, we have presented the background of the UHI effect, the physical mechanisms involved in the urban heat budget, the basics of pedestrian thermal stress and various heat mitigation strategies.

The UHI effect emerges from urban morphology and materials, low proportion of vegetation and pervious soils and human activity. These factors cause radiative trapping, lack of evapotranspiration, wind obstruction and anthropogenic heat release. The phenomenon has multiple consequences for urban areas compared to their rural surroundings, including higher average temperatures (exacerbated during heat-waves), increased cooling energy use, air pollution, increased health risks and deterioration of thermal comfort. To counteract UHIs and/or to mitigate heat, several strategies can be used, each operating on one or several physical mechanisms of the urban heat budget of a surface or volume. The impact of UHI-countermeasures on thermal stress can be assessed using various indices, each making certain assumptions on the pedestrian heat budget.

Most of the solutions presented can either be implemented on rooftops, pavements or even building façades. In particular, significant research efforts were made on the study of cool materials. Such materials can be reflective, evaporative, or present modified thermo-physical properties compared to traditional materials, in order to lower their surface temperature. However, their production can be associated with a higher environmental impact compared to traditional materials. Future research avenues for cool materials include refining the study of their air temperature and thermal comfort effects as well as the energy partition at the surface. While the study of the former topic usually requires field testing or simulation tools, the latter can also be assessed in the lab. Urban greening on the other hand seeks to reintroduce latent exchanges in the urban fabric with parks, lawns or trees, which can also provide shading.

Generally, for each heat mitigation strategy, especially for reflective pavements, care must be given to the area of implementation and on the effect on pedestrian comfort, such that potential drawbacks on the human heat budget do not to offset the gains, although according to the literature this is rarely the case except for certain urban configurations. Other mitigation strategies exist that can be preferentially implemented to target a specific mechanism in particular. Combining different strategies provides the highest cooling effects.

The following Chapter specifically reviews pavement-watering studies, a technique seeking to mitigate heat by creating additional latent flows leading to lower ground surface temperature. The review will help identify the research questions that need to be addressed.

Literature Review of Pavement-Watering

This Chapter reviews literature studies focusing on pavement-watering, i.e. the intentional watering of ground surfaces with the aim of cooling the urban area by increasing latent heat flows.

As the pavement is sprinkled with water, additional latent heat flows is created with evaporation. An additional non-atmospheric sensible heat flow is also created via heat absorption, which can be advective in case of runoff. As a consequence, the ground is cooled down, which results in reduced atmospheric convection (H), pavement heat flux (V), black-body emissions ($\epsilon \sigma T_s^4$) and also SW reflections, since the albedo of a wet surface is lower than that of a dry one (Lekner and Dorf, 1988). A schematic representation of the effect of watering on a surface heat budget is presented in Figure 3.1.
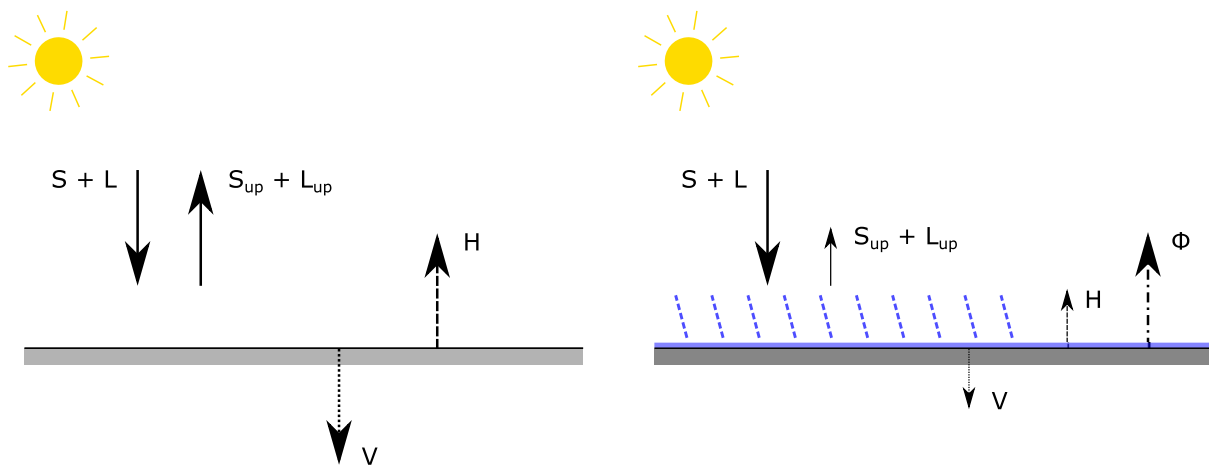
Figure 3.1: Illustration of the heat budget of a dry (left) and watered (right) surface. The cooling flux Φ includes a latent and sensible component and potential advection.

Apart from the slightly increased humidity, pavement-watering is thus beneficial for a pedestrian's heat stress, since in addition to reduced sensible atmospheric heating, the reduction of the surface's radiosity also decreases MRT.

The viability of pavement-watering is a trade-off between the consumption of the local water resource and the cooling needs and effects. Bearing this in mind, provided the increase in water consumption is marginal/negligible, the method is viewed as an interesting emergency heat mitigation tool for densely built environments, as it can easily be performed on existing pavements for areas where other countermeasures are either absent or difficult to implement.

This Chapter aims to identify aspects that may have already been studied in the literature in relation with our research question. Special focus is lent to the assessment method used to report thermal and microclimatic cooling effects, as well as potential attempts to optimize the parameters of the watering strategy. Close attention is also given to the target pavement material.

Studies were selected following a number of criteria. Articles may mention watering using various terms, such as "pavement-watering", "*uchimizu*", "evaporative cooling", or "irrigation". The topic was narrowed down to the study of pavements only, thus excluding buildings, façades and rooftops, unless they are part of a broader watering strategy including ground surfaces. Solutions involving mist sprayers or vegetation evapotranspiration are not considered either. In addition, papers were selected if their primary focus was the study of watering itself, as opposed to the study of the evaporative behaviour of the target material, if the latter is pervious. Out of simplicity, we thus choose to exclude laboratory studies on evaporative pervious pavements. These stand out in that they are often attached to identifying driving design parameters (porosity, aggregate size, slab thickness, etc.) influencing drainage, retention capacity and the evaporation rate depending on the amount of water or when saturated after complete immersion. Such studies were instead briefly presented in Section 2.4's paragraph about cool pavements. Among the remaining field studies selected, findings on pervious pavements are presented only if the cooling performance is compared to dry conditions. Finally, heat-related studies were privileged. If mentioned, cold-weather scenarios are thus excluded.

On the basis of these criteria, 26 articles were found, describing either numerical or experimental studies, published between 1997 and 2020 and describing studies conducted between 1993 and 2016, and including a 2100 projection. Among these articles, two are written in French and are published in a professional journal (Bouvier et al., 2013; Maillard et al., 2014), three are conference papers (Kinouchi and Kanda, 1998; Takahashi et al., 2010; Kubo et al., 2006), while one is a freely-available report by Météo-France and CSTB (2012). The rest of the selected articles were all published in international scientific journals. In addition, five of the articles published in scientific journals (Hendel et al., 2014, 2015a,b; Hendel and Royon, 2015; Hendel et al., 2016) are part of a PhD manuscript, focusing on a field study of pavement-watering. Instead of mentioning each corresponding article, the whole manuscript will be referenced hereafter (Hendel, 2015), unless an article's specific piece of data is needed.

We start with a general description of the selected studies, their methodology, the watering protocol adopted and optimization goals when relevant. We then turn to reporting the microclimatic and thermal cooling effects of pavement-watering. Data not available (NA) or not

relevant (NR) will be explicitly indicated in each table used for this review.

3.1 Methodology

3.1.1 Scale and Approach

Selected studies can be classified according to the typical scale of analysis (slab, street, district or city scale), or the chosen approach, i.e. experiment, numerical, or combined. Table 3.1 classifies the articles by scale (smallest to biggest) and approach, and specifies the location of the study.

Table 3.1: Experimental, numerical or combined articles among the literature studying pavement-watering at slab-, street-, district- or city-scale.

Scale	Author	Type	Location
Slab	Kinouchi and Kanda (1998)		Nagaoka City, Japan
	Pyun et al. (2010)		Goyang, Korea
	Takebayashi and Moriyama (2012)	exp.	Osaka, Japan
	Li et al. (2013a)		Davis, California, USA
	Li et al. (2013b)		Davis, California, USA
	Nayak et al. (2020)	com.	Fukuoka, Japan
Street	Kinouchi et al. (1997)		Nagaoka City, Japan
	Yamagata et al. (2008)		Tokyo, Japan
	Bouvier et al. (2013)	exp.	Paris, France
	Maillard et al. (2014)		Lyon, France
	Hendel (2015)		Paris, France
	Solcerova et al. (2018)		Delft, the Netherlands
	Kubo et al. (2006)		Tokyo, Japan
	Cohard et al. (2018)	com.	Nantes, France
	Azam et al. (2018)		Nantes, France
District	Takahashi et al. (2010)	exp.	Nagaoka City, Japan
	Wei and He (2013)	num.	Tokyo, Japan
	Broadbent et al. (2018)		Adelaide, South Australia
City	Nakayama et al. (2012)		Kawasaki City, Japan
	Météo-France and CSTB (2012)	num.	Paris, France
	Daniel et al. (2018)		Paris, France
	Nakayama and Fujita (2010)	com.	Kawasaki City, Japan

As can be seen, numerical and experimental studies operate on complementary scales. Most of the experimental studies tend to focus on rather small scale (slab- or street- scale) while numerical studies prefer greater scales (district- or city-scale), except for Takahashi et al.

(2010) who conducted parallel experimental campaigns at district-scale.

Articles combining the numerical and experimental approach mostly operate at the street-scale. All of them use pavement-watering simulations as a complementary tool to field tests, using small-scale measurements as input data for the models. Nayak et al. (2020) also proposed a numerical model complementary to measurements on an asphalt rooftop (typical street-scale), although we will only consider the experiments performed on an asphalt pavement slab that are also presented in the study. Similarly, Nakayama and Fujita (2010) simulated the city-scale cooling effects of water-retaining pavements during a heat-wave, using measurements on pavement slabs embedded in a building rooftop as input data. In light of this, future experimental work investigating the large-scale effects of pavement-watering, or numerical slab-scale work would be most welcome, to better appreciate the cumulative effects of the method and refine lab-scale findings with predictive simulation tools.

The reason for this likely comes from practical considerations. Indeed, small-scale experiments are easier and cheaper to implement, when numerical simulations can relatively easily be conducted at larger spatial scales. Finally, a vast majority of the studies were performed in Japan (10) or France (11), leaving only five of the studies performed in Korea, California (USA), Australia or the Netherlands. Since the number of locations is limited, mostly two different climate types were investigated, namely humid temperate with hot summers (Cfa) for Japan, and maritime temperate climate (Cfb) for France, according to the Köppen-Geiger classification (Peel et al., 2007). At the local scale (i.e. for street or district-scale studies), it is recommended that basic metadata regarding the site's surface cover and structure is provided following the local climate zone (LCZ) classification. Indeed, LCZs provide a standardized framework for comparing worldwide urban temperature observations (Stewart and Oke, 2012).

3.1.2   Watering Strategy and Target Area

We now turn to the watering protocols investigated in each one of the articles, as well as the target area. A watering strategy is fully defined based on four parameters: 1) the target area, 2) the period, 3) the frequency and 4) the watering rate.

1) The target area refers to the surface that is watered, defined by its location and size expressed in m² for the general case, or for any given street by simply the pavement, the sidewalk or both (in this manuscript, the terms "sidewalk" and "pavement" are used in American English, respectively "walkway" and "roadway" in British English). Additional information about the target area can also be provided with the paving material as well as other features: street orientation, curvature, roughness, perviousness, etc. 2) The period outlines the time span during which watering is conducted. 3) The frequency (in Hz) is that at which watering cycles are conducted in the case of discontinuous watering. 4) Finally, the rate sets the amount of water delivered per area and time units averaged over the watering period (expressed in L/m².h, equivalent to mm/h). Knowledge of the watering rate, the period and the surface of the target area is sufficient to determine water consumption. The different watering strategies used in the literature selection are summarized in Table 3.2 following the same classification as that of Table 3.1.

Table 3.2: Detailed pavement-watering methods used in the surveyed studies.

Author	Watering Protocol		
	Frequency	Period	Rate
Kinouchi and Kanda (1998)	once	morning	NA
Pyun et al. (2010)	once	NA	10 mm/d
Takebayashi and Moriyama (2012)	continuous	5 − 6 pm	10 mm/h
Li et al. (2013a)	once	afternoon	∼200 mm/h
Li et al. (2013b)	continuous	3 pm − 1 am	∼22 mm/h
Nayak et al. (2020)	rainfall		1 − 38 mm
Kinouchi et al. (1997)	continuous	10 am − 2 pm	11.9 mm/h
Yamagata et al. (2008)	continuous	8 − 8:20 am	27 m^3/d
	continuous	8 − 8:20 am 11 − 11:10 am 4 − 4:10 pm	52 m^3/d
	continuous	8 − 8:20 am 11 − 11:20 am 4 − 4:10 pm	53 m^3/d
Bouvier et al. (2013)	continuous	10 am	1 mm/d
Maillard et al. (2014)	every 15 min	2 − 6 pm	5 − 12 mm/h
	every 60 min	6 am − 6 pm	
	every 60 min	6 − 11 am	
	every 30 min	2 − 6 pm	
Hendel (2015)	every 60 min	6:30 − 11:30 am	1 mm/h
	every 30 min	2 − 6:30 pm	2 mm/h
	continuous	7 am − 7 pm	25 mm/h
Solcerova et al. (2018)	once	afternoon	1 − 5 mm
Kubo et al. (2006)	rainfall		NA
Cohard et al. (2018) Azam et al. (2018)	every 2 − 30 min	morning and afternoon	0.8 − 8.5 mm
Takahashi et al. (2010)	every 30 min	8:30 − 10:30 am 5 − 7 pm	2 mm/h
Wei and He (2013)	once	midnight	NA
Broadbent et al. (2018)	continuous	all day	0.2 − 1.25 mm/h
		11 pm − 5 am 11 am − 5 pm	0.2 − 4.17 mm/h
Nakayama et al. (2012) Nakayama and Fujita (2010)	rainfall or groundwater		NA
Météo-France and CSTB (2012)	every 60 min	5 am − 7 pm	0.2 mm/h
Daniel et al. (2018)	every 60min	8 am − 8 pm	2.77 mm/d

Some of the selected studies merit further comment. For instance, Cohard et al. (2018) and Azam et al. (2018) address the same experimental campaign of June 2004 for which artificial rain showers were performed for several days in a 2,500 m² semi-impervious asphalt parking lot in Nantes, France. Similarly, Bouvier et al. (2013) and Hendel (2015) shared the same location (rue du Louvre, Paris, France), although the watering campaigns were different. Bouvier et al. (2013) implemented nighttime watering during the summer 2012, while Hendel (2015) performed daytime watering during the summers of 2013 and 2014 and also studied anoter site. Daniel et al. (2018) simulates pavement-watering of the Paris metropolitan area, building on the framework laid by Météo-France and CSTB (2012). Three vegetation watering scenarios and one pavement-watering scenario are considered, although we will only consider the pavement-watering scenario in the Section 3.2 on reported cooling effects. As stated before, Nayak et al. (2020) performed experiments on both a rooftop and an asphalt pavement slab, although only the latter is mentioned in Table 3.2. Nakayama and Fujita (2010) and Nakayama et al. (2012) focus on the same district. Finally, Li et al. (2013a) and (2013b) both performed watering experiments at the same test facility in California (USA), although the watering strategy, target slab and orientation were different.

As seen in Table 3.2, a broad range of watering protocols are tested in the literature sample. When not performed by hand, implementation of watering can involve a sprinkler network (Azam et al., 2018; Cohard et al., 2018), cleaning trucks or pierced watering hoses (Hendel, 2015), snow-melting pipes (Takahashi et al., 2010) or even water sprinklers built into the street curb (Maillard et al., 2014).

Apart from city-scale studies for which the distinction between the materials being watered cannot be appreciated, a vast majority of the target areas are made of asphalt or concrete, some of which sometimes include a pervious or a water-retaining option. Exception is noted for Takebayashi and Moriyama (2012) who studied sixteen 2x2 m slabs including traditional and water retaining asphalt and concrete, but also bare soil and grass. Hendel (2015) studied two test sites among which one was made of sandstone cobblestones. However, this site did not yield statistically significant effects and is therefore not reported for the rest of this Chapter. Lastly, Solcerova et al. (2018) watered a red brick herringbone block pavement.

For street- or greater-scale studies (if relevant), most articles consider pavement-only watering, or pavement and sidewalk sometimes (for Bouvier et al., 2013; Hendel, 2015; Kubo et al., 2006; Météo-France and CSTB, 2012), but rarely sidewalk-only watering (except for Daniel et al., 2018 and Wei and He, 2013). Targeting both the pavement and the sidewalk should give the best results, as the effects of the watering can be expected to be commensurate to the area that is watered. Since sidewalks are often smaller that pavement surfaces in most streets, their watering should provide reduced cooling at the street-scale. However, since pedestrians are almost exclusively present on the sidewalk, it may still be preferable to water the sidewalk exclusively, provided that the benefit in the pedestrian's radiative budget is sufficient to offset the weaker microclimatic cooling compared to what would have been obtained when watering only the pavement. This would also save water, and would be of particular interest in E-W oriented streets for which one side receives much more solar radiation than the other. Comparing the effects of watering both pavement and sidewalk to the that of a restricted portion under the same experimental conditions would therefore be useful.

3.1.3 Protocol Optimization and Water Consumption

Among the papers selected, only a few describe attempts to optimize the watering protocol. The watering protocol is deemed optimal if increasing the rate only marginally increases cooling. Depending on the water-holding capacity of the target area, the frequency between cycles can also be adjusted to avoid runoff. Finally, the choice of watering period will also influence the amplitude of the cooling effects.

Takahashi et al. (2010) optimize the watering rate and frequency using surface and 90 cm air temperature observations over one hour after watering. They find that the optimal amount of water per cycle is 1 L/m², yielding the highest cooling effects with the least water. They also conclude that watering during the day between 11 am and 3 pm is not effective as no temperature difference could be observed, and that watering should be performed before and after this time window to yield the best results. The authors also compare two watering frequencies and conclude that the 30 min intervals (against 1 h) allow the effects to last longer, as it prevented the pavement from drying off. Finally, their analysis shows that watering sunny areas yielded more prominent air temperature effects compared to shaded areas.

Météo-France and CSTB (2012) use findings from Takahashi et al. (2010) for their optimization assuming a pavement water-holding capacity of 1 mm. On this basis, they optimize the watering rate using 2 m air temperature simulations with a one-hour time step.

Although not on a pavement surface, it is noteworthy Nayak et al. (2020) optimized the rate and frequency of watering on an asphalt rooftop using a numerical model. Optimal conditions are found by comparing both the thermal load of the building and the average drop in temperature versus various watering rates. The optimal amount of water is found to be 5 kg/m² applied once to minimize the building's thermal load and the watering rate while maximizing the temperature surface drop.

Only Hendel (2015) conducts a formal optimization process, explicitly mentioning optimization targets and goals: 1) the maximization of the cooling effects, 2) the minimization of the watering frequency, 3) the minimization of the watering rate, and 4) the minimization of the watering period. He then proceeds using heat flux measurements 5 cm deep in the pavement (Hendel et al., 2015a) and surface temperature measured with an infrared camera (Hendel et al., 2014). His analyses also showed that the cooling effects of watering were greatest for an insolated surface and occurred simultaneously with peak daily temperatures, and for a constantly wet pavement (drying undesirable) similarly to what Takahashi et al. (2010) found. Hendel (2015) showed that only enough water should be sprinkled for evaporation to be continuous while avoiding surface drying and runoff. Runoff represented 80% of sprinkled water but only 20% of total cooling. On the other hand, 80% of the cooling effects were provided by the evaporation of the remaining 20% of sprinkled water. He thus found that watering should be conducted every 30 minutes during pavement insolation at a rate of $0.31 - 0.40$ mm/h (that is $0.16 - 0.20$ mm/cycle).

The scalability of the water consumption of this optimized watering strategy were also assessed by Hendel (2015). In the case of watering all street surfaces in Paris (2,550 ha) would

represent about 25 L of water per inhabitant per day (56,100 m^3/d in total), i.e. about 30% of the production of Paris' non potable water network, and below the total installed capacity (500,000 m^3/d). This is approximately three times less than the water consumption of green spaces during the summer (about 8 mm/h), although vegetation has a far more powerful cooling effect in addition to providing shading. A similar finding is reported by Daniel et al. (2018), who constructed an efficiency coefficient weighing the cooling effects of watering by the water footprint of the watering scenario. Among the scenarios investigated by the authors (watering of vegetation with realistic or unrestricted water supply, pavement-watering only or combined scenario), pavement-watering yields the most efficient results due to its limited water consumption, although the cooling effects are low compared to other scenarios. Finally, Bouvier et al. (2013) emphasize that for the case of Paris, the daily production of the non-potable network was sufficient during the 2003, 2008 and 2010 heat-waves to cover the city's needs with no notable negative impact on the Seine's level or on the production of potable drinking water.

Azam et al. (2018) made the same observations as Hendel (2015) regarding the 80% water runoff and the proportion of cooling due to evaporation only. The cooling flux is thus limited by the water-holding capacity of the target pavement. Although they did not conduct any optimization procedure, they briefly mention that one valuable application of the numerical tool they developed could be to optimize watering scenarios depending on the surface characteristics. This would allow the impact assessment of different materials with a microclimate model and is of primary interest.

In a similar way, even though Broadbent et al. (2018) did not attempt to optimize the watering protocol, they tested a range of irrigation scenarios with different rates and periods of implementation. By doing so, they observed that the mean diurnal air temperature cooling benefit linked to increasing the irrigation rate was non-linear, with marginal additional cooling passed the threshold of 20 L/m² per day above which cooling began to plateau. A similar trend was used by (Hendel et al., 2015a) to achieve their optimization goals. For Broadbent et al. (2018), this happened to be correlated to the water saturation of soil. As a result, they mention it implies that irrigation volume and timing can be optimised to achieve maximum efficiency of cooling, but did not go any further.

It is recommended that future studies of pavement-watering attempt to formally optimize the method's water consumption, given the current concerns for future water resource availability.

3.1.4 Dry-Wet Difference Assessment Method

We now turn to the description of the analysis method to assess the impact of pavement-watering adopted by each article, which naturally falls into three groups based on the chosen approach (experimental, numerical or combined).

Experimental Studies

All of the slab-scale studies use the same approach, namely visualizing the change in behaviour over time of the studied area once it has been watered. In addition to that, except for

Kinouchi and Kanda (1998), studies also compared the watered area (case area) simultaneously with a conventional area composed of the same impervious material (control area).

For all street- or higher-scale experimental studies, field trials always include a simultaneous comparison of the measurements performed at the case area with a non-watered control area for several test days. All but one study Hendel (2015) then deduct the microclimatic effects of pavement-watering using a direct comparison between watered-case and dry-control sites, interpreting the observed difference as exclusively due to watering. Takahashi et al. (2010) (district-scale), also proceeds that way though using average observations from several watered and non-watered weather stations.

Hendel (2015) is the only study proposing a statistical analysis to isolate the microclimatic effects of pavement-watering, although thermal effects are deterlined directly. Instead of focusing on the difference between case and control areas on a watered day to obtain the microclimatic effects, Hendel (2015) compares the average interstation difference obtained on watered days to that obtained on reference days, which present similar weather conditions as watered days, but without watering. He then performs a two-sample t-test on the interstation differences on watered and reference days, thus assuming that the latter are both normally distributed and independent. This approach has several advantages. Indeed, it allows to fully isolate and quantify the effect of pavement-watering alone, by factoring pre-existing differences between case and control sites out. It also allows to determine the impact of watering throughout an entire average day, while giving a corresponding level of significance (for instance 95%) for each time sample.

The approach Hendel (2015) uses can be compared to the Lowry (1977) approach defined as a set of guidelines for investigating the differences between urban and rural climates. This framework comes in particularly handy to understand the potential pre-existing differences between case and control sites. A rigorous analysis should indeed always rule these out, as there is no theoretical basis for attributing case and control microclimatic differences solely to the effect of pavement-watering, as demonstrated by Hendel (2015).

Despite this important methodological flaw, when available, reported microclimatic cooling effects are listed in Section 3.2 for the street-scale experimental articles, although it should be emphasized that their findings could potentially be unreliable as a result.

Numerical Studies

All of the selected numerical studies, regardless of the scale, analysed the effect of watering by comparing an irrigation scenario to a reference non-irrigated scenario applied to the same study area subject to the same conditions, all else being equal. The observed differences between both scenarios are then attributed to pavement-watering. The method is deemed robust and reliable given that all models went through a proper calibration phase on actual data. Various urban canopy models are used in the considered articles.

Combined Studies

In all combined studies, lab- or street-scale experimental findings are used as real-data input to calibrate the simulations.

It is noteworthy that the primary purpose of a few combined studies is not to assess the cooling effects of pavement-watering, but to calibrate their model based on small-scale field measurements. As a result, Nayak et al. (2020), Cohard et al. (2018) and Azam et al. (2018) visualize the change in behaviours of various indicators (surface and pavement temperature, humidity, ground fluxes, etc.) over time once watering is implemented. They also use water or surface budgets to estimate sensible convective fluxes, latent flows or the evaporation rate.

Nayak et al. (2020) use outdoor slab measurements to estimate the latent flux and evaporation rate with the surface heat budget during rain showers. This finding is then integrated into a numerical model based on the water budget coupled with the unsteady heat transfer equation. The model is then used to find optimal watering conditions depending on the thermal load, average temperature drop and watering rate. For their part, Cohard et al. (2018) use the surface energy balance (SEB) model and an eddy covariance method to characterize the water and energy flows at an urban surface with field experiments performed on an asphalt concrete parking lot. Azam et al. (2018) develop a soil model for pavement-watering within the urban climate micro-scale model SOLENE-microclimat. Parameters of the model are calibrated using the same field measurements as that used by Cohard et al. (2018). This model aims to be used to assess the cooling effects of pavement watering at micro-scale, as well as the impact on local comfort.

As with other numerical studies, the two remaining combined-approach articles determine the effects of watering by comparing a given study site with and without watering.

Kubo et al. (2006) use experimental measurements of a slab's surface temperature reductions in their street-scale simulation. Their model only simulates a forced pavement and sidewalk surface temperature reduction of 10°C corresponding to their experiment. Since the model does not take into account heat and mass transfer from evaporation, the effect of watering on humidity and thus thermal comfort cannot be assessed. Finally, Nakayama and Fujita (2010) use a numerical model for solving the water budget of their study area, pre-calibrated with a slab-scale study of the water mass transfer in pervious materials.

3.2   Reported Cooling Effects of Pavement-Watering

In this Section, we present the cooling effects of pavement-watering reported in the literature. Effects are split into two distinct categories: microclimatic and thermal. Microclimatic effects describe the effects of pavement-watering on climatic indicators above ground level, which are relevant for pedestrians' thermal comfort: air temperature, humidity, wind speed and radiative environment. Thermal effects describe the impacts of pavement-watering on the ground or at the surface-atmosphere interface: surface and in-depth temperatures, pavement heat flux, latent flow, sensible convective exchanges, etc. Thermal effects are more prominent than microclimatic effects, as the former cause the mechanisms responsible for the latter.

For the following section, only dry-wet differences attributable to pavement-watering are reported. Many articles performed microclimatic measurements using weather stations (Takebayashi and Moriyama, 2012; Wei and He, 2013; Pyun et al., 2010; Cohard et al., 2018; Li et al.,

2013b; Nayak et al., 2020 etc.), or estimated the heat budget of the target area based on measured thermal indicators (Kinouchi et al., 1997; Takebayashi and Moriyama, 2012; Hendel, 2015; Cohard et al., 2018; Azam et al., 2018 etc.). However, these are not reported below if no comparison between dry and watered conditions for a given parameter is provided. Simulation results for the rooftop studied by Nayak et al. (2020) are not presented either.

The heat transfer analysis framework proposed by Solcerova et al. (2018) strongly differs of that of other articles. Indeed, although they propose an interesting Distributed Temperature Sensing set-up to measure temperature along a fiber-optic-cables cage, their analysis lacks several physical phenomena. The most concerning aspect, along with some debatable assumptions, is that no proper surface heat budget is presented. Instead, the authors consider energy exchanges within an undefined isolated thermodynamic system, assuming thermal equilibrium is reached. By doing so, instantaneous atmospheric convection, radiation, pavement conduction fluxes and heat and mass transport from evaporation are absent. The reliability of their findings is thus questionable, and for this reason they are not reported hereafter.

Only the maximum effects of pavement-watering are listed, unless mentioned otherwise, as very few studies provide average effects. Results of watering pervious surfaces are reported only if a dry-wet comparison is made in the corresponding study. When provided, the instrument and height used to perform the measurement is also given, although only a few of articles provided detailed information about the instrumentation used (Kinouchi et al., 1997; Takebayashi and Moriyama, 2012; Li et al., 2013b,a; Hendel, 2015; Cohard et al., 2018; Azam et al., 2018; Nayak et al., 2020).

3.2.1 Microclimatic Effects

Air Temperature

Table 3.3 presents the air temperature effects of pavement-watering, the most reported indicator in the literature. The instrument and its height, when available, is also specified. Values span between -0.4°C and -5°C. Yet, findings are difficult to compare, as heights and watering protocols are different between articles. The value reported by Broadbent et al. (2017) is that of the diurnal average cooling. Furthermore, Bouvier et al. (2013), Hendel (2015) and Li et al. (2013b) provide average effects in addition to maximum effects, while only the two former provide information regarding the duration of the effects (up to several hours). Lastly, Daniel et al. (2018) assessed the effects of pavement-watering for a theoretical future heat-wave scenario in 2100 based on current trends. The reported reduction up to -1°C is located in the city center due to its high fraction of roads compared to suburban areas. A slight cooling effect (less than 0.5°C) is reported at night due to the reduced energy absorbed by roads during the day.

Relative Humidity

Pavement-watering effects on humidity, rarely provided, are listed in Table 3.4. In each case, an increase of a few percent of relative humidity is observed, although heights are not the same. Although Broadbent et al. (2018) did not report information about humidity, they mentioned vapour pressure conditions.

Table 3.3: Reported maximum air temperature effects.

Author	Instrument	Height	Max. effect
Kinouchi et al. (1997)	Pt resistance	1 m	-1°C
Yamagata et al. (2008)	NA	0.5 m	-2.5°C
Bouvier et al. (2013)	NA	2 m	-0.4°C
Hendel et al. (2016)	Pt-100 resistance	1.5 m	-0.8°C
Hendel et al. (2016)	Pt-100 resistance	4 m	-0.7°C
Kubo et al. (2006)	numeric	0.5 m	-2.13°C
Kubo et al. (2006)	numeric	1.5 m	-0.73°C
Takahashi et al. (2010)	NA	0.9 m	-4.°C
Broadbent et al. (2018)	numeric	2 m	-2.31°C
Météo-France and CSTB (2012)	numeric	2 m	-2.°C
Daniel et al. (2018)	numeric	2 m	-1°C
Nakayama et al. (2012)	numeric	1.5 m	-5°C

Table 3.4: Reported maximum air humidity effects.

Author	Instrument	Height	Max. effect
Kinouchi et al. (1997)	Capacitive hydrometer	1 m	+4%
Bouvier et al. (2013)	NA	2 m	+4%
Hendel et al. (2016)	Capacitive hydrometer	1.5 m	+4.6%
Hendel et al. (2016)	Capacitive hydrometer	4 m	+3.4%
Météo-France and CSTB (2012)	numeric	2 m	A few%

Radiative Environment

Indicators representative of the radiative environment (MRT, globe temperature) are listed in Table 3.5.

Table 3.5: Reported maximum effects on the radiative environment.

Author	Instrument	Height	Max. effect
Kinouchi et al. (1997)	Globe temperature	1 m	-4°C
Hendel et al. (2016)	MRT	1.5 m	-3.7°C
Wei and He (2013)	MRT	1.5 m	-6°C

As seen, although such indicators are essential for estimating the impact of pavement-watering on thermal comfort, they are scarcely provided in the present literature selection. The standard WMO black-globe thermometer (see Section 2.3.1) with a typical 20-minutes stabilization time was used by Hendel (2015), while Kinouchi et al. (1997) did not specify the type of globe they used.

UHI-Mitigation

Some articles investigated UHI-mitigation-mitigation effects of pavement-watering. One such indicator is defined as the difference in the average air temperature between watered and reference states when the UHI intensity is the highest, i.e. between 3 am and 6 am (local daylight savings time UTC+2 for the case of Paris, France). This indicator is used by Météo-France and CSTB (2012) and Hendel (2015) who both obtain similar results given their respective study scale. Wei and He (2013) use the Heat Island Potential (HIP) with and without watering, defined as the difference between urban surfaces and the atmosphere (positive if the former are warmer than the latter). Values are reported in Table 3.6.

Table 3.6: Reported maximum UHI-mitigation effects.

Author	Indicator	Height	Max. effect
Hendel et al. (2016)	UHI-mitigation	1.5 m	-0.14°C
Hendel et al. (2016)	UHI-mitigation	4 m	-0.22°C
Wei and He (2013)	HIP	NR	-25°C
Météo-France and CSTB (2012)	UHI-mitigation	2 m	-0.5°C
Météo-France and CSTB (2012)	UHI-mitigation	30 m	NA

Thermal Stress

Among the selected articles, several studies present the effects of pavement-watering on thermal comfort indices, shown in Table 3.7.

Table 3.7: Reported maximum thermal comfort effects.

Author	Indicator	Height	Max. effect
Kinouchi and Kanda (1998)	Thermal sensation	NR	-3°C
Kinouchi et al. (1997)	Discomfort index	NR	Almost no difference
Kinouchi et al. (1997)	Thermal load	NR	-10 W/m^2
Yamagata et al. (2008)	WBGT	0.5 m	-2°C
Maillard et al. (2014)	WBGT	1.5 m	-0.5°C
Hendel et al. (2016)	UTCI	1.5 m	-1.5°C
Broadbent et al. (2018)	Humidex index	2 m	-2.3 (from 36.9 to 34.6)
Daniel et al. (2018)	UTCI	2 m	-2°C

Kinouchi et al. (1997) provide a discomfort index for indoor environments calculated with an empirical expression accounting for air temperature and relative humidity, while they describe thermal load as the net amount of heat a human receives from his surroundings, the latter being considered as an outdoor thermal index accounting for temperature, humidity, wind and radiation. Kinouchi and Kanda (1998) estimate thermal stress with a numerical analysis of the human heat budget accounting for physical parameters and find that the corresponding stress gives equivalent thermal sensation of a decrease of air temperature by 3°C. Further detail is difficult to obtain as supporting references are in Japanese.

Two papers provide the effects of watering on the WBGT (equation 2.12), which takes into account dry and wet-bulb air temperatures as well as globe temperature. Broadbent et al. (2018) use the humidex, solely accounting for heat and humidity (equation 2.14). The authors report a reduction of the humidex with pavement-watering, though it is likely to be underestimated as it does not account for the MRT reduction. Even though humidex decreases, its value remains within the 30 to 39 range corresponding to "some discomfort".

Finally, only Hendel et al. (2016) and Daniel et al. (2018) use the UTCI. Daniel et al. (2018) did not explicitly report the UTCI-reduction, although it can be assessed based on cooling efficiency coefficients they construct, expressing the averaged UTCI decrease in °C per total Mm^3 of water used to achieve it. In the end, Table 3.7 indicates that pavement-watering is beneficial to thermal stress in all studies, despite of the increase of relative humidity of a few percent.

3.2.2 Thermal Effects

Having listed the microclimatic effects of pavement-watering, we now present the thermal effects.

Surface Temperature

As for air temperature for the microclimatic effects, surface temperature is the most reported parameter for the thermal effects. Dry-wet differences, measured with an infrared (IR) camera or with a thermocouple, are summarized in Table 3.8.

Table 3.8: Reported maximum surface temperature effects.

Author	Instrument	Height	Max. effect
Kinouchi and Kanda (1998)	Net radiometer	65 cm	-14° to -18°C
Pyun et al. (2010)	Type-K thermocouple	0 cm	-8° to -11°C
Takebayashi and Moriyama (2012)	Infrared thermometer	15 cm	-10°C
Li et al. (2013a)	Type-T thermocouple	0 cm	-15° to -35°C
Kinouchi et al. (1997)	IR thermometer	1 m	-10° to -30°C
Yamagata et al. (2008)	IR camera	NA	-3° to -8°C
Bouvier et al. (2013)	IR camera	NA	-6°C
Maillard et al. (2014)	NA	-1 cm	-5°C
Hendel et al. (2014)	IR camera	20 m	-4° to -13°C
Cohard et al. (2018)	Thermocouple	0 cm	-5° to -15°C
Azam et al. (2018)	numeric	0 cm	-5° to -15°C
Kubo et al. (2006)	Thermocouple	0 cm	-16.4°C
Wei and He (2013)	numeric	NR	-5°C
Nakayama and Fujita (2010)	NA	0 cm	-5° to -20°C

Li et al. (2013a) report the highest reductions from -10° to -35°C, recorded in the early after-

noon during the summer and depending on the surface (asphalt, concrete or concrete pavers). The same goes for Nakayama and Fujita (2010) (concrete, grass etc.). In addition, Li et al. (2013b) also provide 7-day averaged surface temperature, and report a dry-wet difference of 2° to 7°C three days after watering. Kinouchi et al. (1997) also report a broad range from -10° to -30°C, measured on four points from the periphery to the middle of the road where watering was implemented with respect to the temperature range. Judging by their graph, Cohard et al. (2018) as well as Azam et al. (2018) observe a reduction ranging from -5° to -15°C depending on the day. Azam et al. (2018) also simulated surface temperature and find good agreement with observations (mean daily RMSE <1°C). Takebayashi and Moriyama (2012) present surface temperatures of slabs watered the day before and compare them to dry slabs. Some authors also report nighttime reductions ranging from -3° to -6°C (Bouvier et al., 2013; Hendel, 2015; Wei and He, 2013; Yamagata et al., 2008).

All in all, surface temperature reductions are generally around 10°C, although it is difficult compare findings as watering protocols and duration and intensity of insolation of the tested sites are very different.

Pavement Temperature

Table 3.9 presents pavement temperature reductions. Hendel (2015) and Kinouchi and Kanda (1998) report very similar results, while that of Cohard et al. (2018) and Li et al. (2013b) strongly differ. This could be due to different thermophysical properties of the watered materials, or to the watering strategy, insolation etc. Azam et al. (2018) also simulate in-depth temperatures and report good agreement with observed measurements, though they are not presented explicitly.

Table 3.9: Reported maximum pavement temperature effects.

Author	Instrument	Depth	Max. effect
Kinouchi and Kanda (1998)	Thermocouple	5 cm	-7°C
Li et al. (2013a)	Type-T thermocouple	1.3 cm	-7°C
Li et al. (2013a)	Type-T thermocouple	3.8 cm	-12°C
Li et al. (2013a)	Type-T thermocouple	6.4 cm	-14°C
Li et al. (2013a)	Type-T thermocouple	25.4 cm	-15°C
Hendel and Royon (2015)	Type-T thermocouple	5 cm	-8°C
Cohard et al. (2018)	Thermocouple	1 cm	-12°C
Cohard et al. (2018)	Thermocouple	6 cm	-6°C
Cohard et al. (2018)	Thermocouple	10 cm	-4°C
Cohard et al. (2018)	Thermocouple	15 cm	-1°C
Cohard et al. (2018)	Thermocouple	24 cm	dampened
Cohard et al. (2018)	Thermocouple	50 cm	dampened

Latent Heat Flux

Estimated latent heat flux density created by pavement-watering is listed in Table 3.10. Four articles estimate latent flows with the energy balance based on measurements, while four

others use numeric simulations. Kinouchi and Kanda (1998) estimated the latent flow using an example of energy balance. Kinouchi et al. (1997) provided results from the gradient method also ($200 - 300$ W/m² peaking at 400 W/m²), as they encountered difficulties with their pavement heat flux intervening into the energy balance (thus not reported here). For their part, Takebayashi and Moriyama (2012) report the latent fluxes for several material slabs, as low as 100 W/m² for concrete, 200 W/m² for asphalt and up to 400 /m² for grass. A cooling effect is still perceived two days after watering though it is significantly dampened. Cohard et al. (2018) estimated latent flows for six consecutive days with the surface energy balance model and two eddy covariance correlations. The latter method uses the covariance of the vertical wind speed component 1 and 2 meters high as well as temperature and humidity signals. Good agreement is found between the methods with latent flows mostly between 100 to 200 W/m², marginally peaking at 400 W/m². The same goes for Azam et al. (2018), though the latent flux they simulate reaches up to 700 W/m². Nakayama et al. (2012) also used a numerical and experimental approach to estimate latent heat flux, although no further detail is provided. For their part, it should be noted that Yamagata et al. (2008) provided the daytime-averaged value from daily latent energy transfer.

Table 3.10: Reported maximum latent heat flow densities.

Author	Instrument	Max. effect
Kinouchi and Kanda (1998)	Estimated	600 W/m^2
Takebayashi and Moriyama (2012)	Energy balance	100 to 400 W/m^2
Nayak et al. (2020)	Energy balance	200 W/m^2
Kinouchi et al. (1997)	Gradient method	400 W/m^2
Yamagata et al. (2008)	Evaporation gauge	365 W/m^2
Hendel et al. (2015a)	Energy balance	229 W/m^2
Cohard et al. (2018)	numeric	100 to 400 W/m^2
Azam et al. (2018)	numeric	100 to 400 W/m^2
Nakayama et al. (2012)	NA	337 W/m^2
Nakayama et al. (2012)	numeric	345 W/m^2
Météo-France and CSTB (2012)	numeric	180 W/m^2
Daniel et al. (2018)	numeric	50 W/m^2

Pavement Heat Flux

We end this Section with reported changes in pavement heat flux density, listed in Table 3.11. Only experimental studies investigate reductions in pavement heat flux, all measured with a heatflowmeter. The value provided by Hendel (2015) is an average reduction over several days. Kinouchi et al. (1997) attempted to measure the pavement heat flux at surface but encountered difficulties (value not reported here). Takebayashi and Moriyama (2012) report a reduction spanning from -50 to -100 W/m² respectively for water-retaining asphalt and concrete compared to dry impervious slabs composed of the same material. As with pavement temperature reductions, the range of values may be due to the varying thermal properties of pavements and site specifics, all else being equal.

Table 3.11: Reported maximum pavement heat flow densities.

Author	Instrument	Depth	Max. effect
Kinouchi and Kanda (1998)	Heatflowmeter	5 cm	-50 W/m^2
Takebayashi and Moriyama (2012)	Heatflowmeter	10 mm	-50 to -100 W/m^2
Hendel et al. (2015a)	Heatflowmeter	5 cm	-100 to -150 W/m^2
Cohard et al. (2018)	Heatflowmeter	5 cm	-100 to -150 W/m^2
Azam et al. (2018)	Heatflowmeter	3 cm	-100 to -150 W/m^2

3.3 Conclusion

The present Chapter reviewed 26 articles investigating the effects of pavement-watering. The number of papers addressing pavement-watering currently remains relatively limited, and a vast majority of the field tests were conducted either in Japan or France. A recap of the dry-wet variation reported by each article is provided in Table 3.12 for concerned parameters (microclimatic and thermal).

It is striking from Table 3.12 that small-scale studies focus on thermal effects, when street- or higher-scale studies tend to focus on microclimatic effects. In such studies, some thermal effects are reported as well. The reason for this is that slab-scale experiments are often too small to observe significant microclimatic effects, or to be adequately instrumented.

Globally, based on the selected studies, pavement-watering seems to reduce surface temperatures by approximately 10°C and increase humidity by a few percentage points, while air temperature is reduced in the order of 1°C. However, most of the indicators provided are not comparable, because of the diversity in the physical parameters measured, the instruments used and their varying heights, the analysis methods and the watering protocols deployed. For some articles, lack of detailed information regarding the experimental set-up is also a problem. Additionally, since articles' findings aren't comparable, the influence of the surface of the area watered on the efficiency of the method is currently unknown, although different portion sizes were studied in the literature (pavement, sidewalk or both). This aspect deserves further investigation, under identical experimental and weather conditions and with a given watering protocol. Indeed, this aspect is primordial for implementing a pavement-watering strategy in accordance with a site's characteristics and the portions that need to be watered for yielding significant cooling effect.

These shortfalls have been identified by Stewart (2011) and Johansson et al. (2014) for the broader field of urban climatology. In their literature review, Johansson et al. (2014) found a great variety of instruments (especially for MRT and wind speed), methods and thermal stress indices used in outdoor urban cooling studies, and called for a standardization of techniques. For his part, Stewart (2011) found that a large proportion of heat island studies are spoiled by poor scientific practice, principally because they lack instrumentation metadata, site characteristics, time of reported effects, as well as failure to control or account for the confounding effects of meteorological conditions.

In relation with the latter topic, the reliability of the microclimatic effects reported by experimental field studies is questionable. Apart from one study, the effects are indeed assessed with a direct comparison between the case (watered) site and control (non-watered) sites measured simultaneously. This assumes that both sites behave identically in the absence of watering. However, this is contradictory to established conceptual frameworks in urban climatology (Lowry, 1977, mentioned in Stewart, 2011) and has been proven incorrect in the general case (Hendel et al., 2016), especially given the complexity of the urban built environment.

As a response, Hendel et al. (2016) proposed a statistical approach based on a two-sample t-test to take into account the pre-existing differences between case and control sites. This explicitly assumes that the reference (non-watered) and watered interstation profiles (constructed with several acquisition data) are both normally distributed and independent. While the former assumption seems reasonable, the latter lacks justification. Therefore, adapted evaluation methods must be identified and tested.

Finally, some studies attempted to optimize the watering protocol, although they often omit defining clear optimization goals. In most cases, optimization concerns the minimization of the water consumption while maximising one cooling effect of pavement-watering (temperature, latent heat flux, etc.), sometimes with additional goals such as minimizing the frequency or period. When the water footprint was assessed, the method was deemed reasonable compared to the cooling effects provided, as its realistic deployment only marginally increases the city-wide water needs. The optimal watering rate should take the target area's characteristics into account (material, water retention, etc.). Yet, nearly all articles targeted traditional paving materials, i.e. mostly asphalt or Portland-cement concrete (impervious and pervious). As a result, the effects of watering alternative materials, such as cool pavements, have not been investigated at all in the scientific literature, both in terms of efficiency and water consumption. As for choosing an adapted watering strategy depending on the target material or for knowing the precise cooling effects of watering on those pavements, such information would be useful to decision-makers seeking to deploy pavement-watering as a cooling tool in urban areas.

Table 3.12: Literature review summary for maximum dry-wet differences on ground surfaces only.

Scale	Type	Author	Microclimatic effects					Thermal effects			
			T_a	RH	MRT/T_g	UHI	Th. comfort	T_s	T_z	lE	V_z
Slab	exp.	Kinouchi and Kanda (1998)						×	×	×	×
		Pyun et al. (2010)						×			
		Takebayashi and Moriyama (2012)						×		×	×
		Li et al. (2013a)							×		
		Li et al. (2013b)						×			
	com.	Nayak et al. (2020)								×	
Street	exp.	Kinouchi et al. (1997)	×	×	×		×		×	×	×
		Yamagata et al. (2008)	×				×	×		×	
		Bouvier et al. (2013)	×					×			
		Maillard et al. (2014)					×	×			
		Hendel (2015)	×	×	×	×	×	×	×	×	×
	com.	Kubo et al. (2006)	×								
		Cohard et al. (2018)						×	×	×	×
		Azam et al. (2018)						×		×	×
District	exp.	Takahashi et al. (2010)	×								
	num.	Wei and He (2013)			×	×		×			
		Broadbent et al. (2018)	×				×				
City	num.	Nakayama et al. (2012)	×							×	
		Météo-France and CSTB (2012)	×	×		×				×	
		Daniel et al. (2018)	×				×			×	
	com.	Nakayama and Fujita (2010)						×			

Research Questions Adressed

In order to counter the urban heat island effect and to decrease pedestrian thermal stress, several solutions exist, which were presented in Chapters 2 and 3.

The scientific background, as well as general countermeasures to UHI, were covered in Chapter 2, with emphasis on cool pavements. These were extensively studied in the literature, yet according to Qin (2015) some areas still need refinement, such as the comparison of cool pavements' heat budgets to that of traditional pavements.

Chapter 3 took a closer look at the pavement-watering literature. Although the thermal and microclimatic effects of pavement-watering have been studied in a number of scientific articles, several gaps were identified. In general, urban climatology studies would benefit from a more transparent approach along with standardized methods in order to properly assess urban cooling scenarios, while allowing for future comparisons, although this aspect can only be addressed through collective practices. More specifically, other identified limitations were identified, mostly concerning the following aspects:

(1) The assessment method of the cooling effects of pavement-watering or more broadly of UHI-countermeasures. Indeed, for field studies, accounting for pre-existing differences between case and control sites in the analysis procedure is a *sine qua none* condition to obtaining reliable results. Statistical procedures adapted to the field of UHI-countermeasures should therefore be identified and tested.

(2) The influence of the surface area that is watered. This should be assessed under specific experimental conditions given the fact that most studies aren't currently comparable.

(3) The optimization of pavement-watering on a variety of target areas. Currently, the method has only been tested and optimized on traditional pavements (asphalt, concrete). This calls for the study of the efficiency of watering on cool or innovative pavements, as well as identifying parameters driving the optimization of watering under given experimental conditions. Furthermore, complete pavement surface heat budgets, under dry and wet conditions, should be provided, as few comparisons with traditional pavements exist and those of watered cool pavements is absent.

As formulated in Chapter 1, our main research question addresses the adaptation of the watering strategy to the specific features of a site. With respect to this question, addressing the aspects listed above raises the following research questions:

- What statistical tools can be used to evaluate the field effects of UHI-countermeasures?

- How are the cooling effects of watering affected by the proportion of street that is watered?

- What is the efficiency of pavement-watering for a variety of traditional and cool pavements, and what do the corresponding optimal watering rates depend on?

- Based on their surface heat budgets, how is the energy partition of dry and optimally-watered traditional and cool pavements affected?

Answers to these questions will provide useful information for decision-makers seeking to implement pavement-watering, as well as for the scientific community. To answer them, Part II will propose a suited statistical procedure for assessing the effects of UHI-countermeasures in the built environment. The method is tested on a pavement-watering case-study located in Paris, France. Microclimatic effects are assessed for two watering scenarios: the watering of both the pavement and the sidewalk during the summers of 2013, 2014 and 2015, and a restricted scenario where only the pavement is watered during the summers of 2016, 2017 and 2018. Part III will present a laboratory experiment for optimizing the effects of pavement-watering on an asphalt road structure, using the field study of Part II to validate the lab results. Finally, building on this work, Part IV will focus on the generalization of the optimization procedure to a variety of traditional and cool pavements.

Part II is based on published work in *Urban Climate* (Parison et al., 2020d). Part III and IV are based on peer-reviewed work published in *Road Materials and Pavement Design* (Parison et al., 2019a), *Urban Climate* (Hendel et al., 2018; Parison et al., 2020b) as well as in *Energy and Buldings* (Parison et al., 2020c).

PART II

FIELD EFFECTS ASSESSMENT OF UHI-MITIGATION TECHNIQUES

Introduction to Part II

As discussed in the first Part of this manuscript, typical UHI-countermeasures have been studied in the lab or on small-scale demonstrators for decades (Spronken-Smith and Oke, 1999; Rosado et al., 2014). Such studies are of growing interest to decision makers and have provided a basis for the simulation of larger scale implementations (Météo-France and CSTB, 2012). In this regard, tools to validate the predicted effects of large scale field implementations are of prime importance to evaluate and follow-up on the effectiveness of UHI-mitigation policies put in place.

Current urban microclimate impact assessment tools mostly consist of direct comparisons between more-or-less-carefully selected case and control sites (Kinouchi et al., 1994; Yamagata et al., 2008; Takahashi et al., 2010; Wong and Yu, 2005; Hoelscher et al., 2016; Kyriakodis and Santamouris, 2018). However, this approach has been shown to be ill-founded, as pre-existing variations in microclimate must be taken into account when comparing case and control site measurements (Hendel et al., 2016; Tsin et al., 2016). Yet, appropriate methods for measuring the effects of UHI countermeasures are necessary, both for the scientific community as well as for decision-makers who need to assess the effectiveness of UHI mitigation techniques as a guide for the choice of relevant policies.

As a response to this, in this Part, we propose a statistical methodology suited for UHI countermeasure impact assessment in ever-changing field conditions. The methodology, presented in Chapter 6 is based on the BACI experimental design which requires performing measurements from case and control sites both before and after the countermeasure is implemented. This design is then combined with a proper statistical test, i.e. a linear mixed model (or fixed-effects model) used to isolate the impact of the countermeasure. The test accounts for the dependence between datasets, contrary to other commonly used statistical tests (t-test, Welch-test, ANOVA, etc.).

Finally, in Chapter 7, the developed methodology is applied as a case-study on data collected from pavement-watering campaigns conducted in Paris since 2013. Two watering strategies are compared in order to determine the influence of the surface area that is watered on the cooling effects, which are assessed in terms of heat stress reduction for pedestrians. The rele-

vance and limitations of the proposed approach are discussed as well as their applicability to other UHI-mitigation strategies.

This Part is based on the peer-reviewed work published in *Urban Climate* (Parison et al., 2020d).

Methodology

6.1 Mathematical Framework

To account for microscale variations in microclimate, case and control sites in urban areas require characterization before and after UHI-countermeasures, rendering direct comparisons between case and control sites for impact assessment ill-founded (Hendel et al., 2016). Thus, microclimatic measures on each site must be performed before any definitive countermeasure is implemented. In this respect, it has been shown that an appropriate sampling configuration for detecting environmental impacts is that of the BACI design (Before-After-Control-Impact). This configuration has been largely covered in the scientific literature (Hurlbert, 1984; Stewart-Oaten et al., 1986; Smith, 2014; Loughin et al., 2018; Conner et al., 2016). Although most widely used in the study of ecological and biological systems, it is theoretically suited to in-field impact assessment studies in general, including that of UHI-countermeasures in urban environments. Thus, using the BACI configuration, let us consider measurements conducted at control site x_1 and case site x_2, during the period t, i.e. either before (reference period, denoted *ref*) and after (countermeasure period, denoted *counter*) countermeasure implementation, as depicted in Figure 6.1.
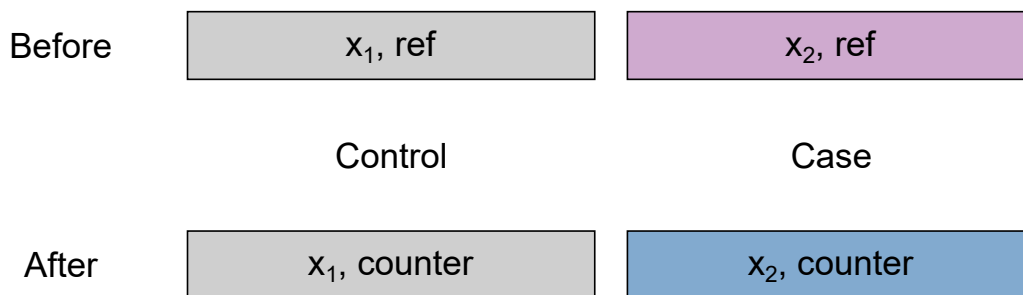
Figure 6.1: BACI design: control and case sites, before and after countermeasure implementation (Parison et al., 2020d).

With the approach described by Lowry (1977), the problem of empirical estimation of urban effects on climate can be formalized in an analytical manner. In his own words, *"the problem is*

one of devising a suitable 'control' in the series of experiments being conducted by Man and Nature." This is also true when attempting to evaluate the effects of UHI-countermeasures. The Lowry approach is summarized by a simple empirical expression:

$$M_{itx} = C_{itx} + A_{itx} + U_{itx} \tag{6.1}$$

where M, the measured meteorological parameter, is the result of the conceptual partitioning of the "background" climate C, the effect of local landscape A, and the effects of local urbanization U for a given weather type i, during time period t and at location x. Lowry discusses the implications of this equation more broadly, but it should be noted that the term U is a residual and includes the effects of local site characteristics such as urban canyon aspect ratio, material properties, anthropogenic heat release, etc. When a UHI countermeasure is implemented, it is U which is modified at the case site, while C is equal to the value M would take in the absence of landscape or urban effects (the "flat-plane" climatological background for the region), and A represents the departure from C attributable to landscape effects solely (local natural features in relation to the site's topography, shorelines, etc.). Building on Lowry's approach for the configuration illustrated in Figure 6.1, both sites are characterized by the next two equations under weather type i for the period t, i.e. the reference or countermeasure periods:

$$\begin{cases} M_{itx_1} = C_{itx_1} + A_{itx_1} + U_{itx_1} \\ M_{itx_2} = C_{itx_2} + A_{itx_2} + U_{itx_2} \end{cases} \tag{6.2}$$

Noting that UHI-countermeasure implementation has no effect on local climate or landscape, and assuming that no changes occur at x_1 between reference and countermeasure periods, i.e. that the UHI countermeasure implemented at case site x_2 does not affect control site x_1, we get the following equations:

$$\begin{cases} C_{i,ref,x_1/x_2} = C_{i,counter,x_1/x_2} \\ A_{i,ref,x_1/x_2} = A_{i,counter,x_1/x_2} \\ U_{i,counter,x_1} = U_{i,ref,x_1} \\ U_{i,counter,x_2} = I_{i,x_2} + U_{i,ref,x_2} \end{cases} \tag{6.3}$$

where I_{i,x_2} is the impact of the countermeasure on the case location x_2 under a given weather type i. By simply comparing case and control sites during the countermeasure period, based on the set of equations 6.2 and 6.3, we obtain the interstation profile for the countermeasure period under weather type i:

$$\begin{aligned} \Delta M_{i,counter} &:= M_{i,counter,x_2} - M_{i,counter,x_1} \\ &= C_{i,ref,x_2} - C_{i,ref,x_1} + A_{i,ref,x_2} - A_{i,ref,x_1} + I_{i,x_2} + U_{i,ref,x_2} - U_{i,ref,x_1} \end{aligned} \tag{6.4}$$

It is immediately clear from equation 6.4 that the effect of the UHI countermeasure cannot be determined from the direct comparison $\Delta M_{i,counter}$ alone. Indeed, preexisting differences in

terms C, A and U between x_1 and x_2, i.e. case and control locations, remain present and prevent I_{i,x_2} from being singled out. This demonstrates that direct case-control site comparisons are inherently flawed to determine the effects of UHI-countermeasures. This remains true even if it is assumed that x_1 and x_2 are close enough to have identical background climate and landscape effects, i.e. if terms C and A are assumed equal: $\Delta M_{i,counter} = U_{i,counter,x_2} - U_{i,counter,x_1} = I_{i,x_2} + U_{i,ref,x_2} - U_{i,ref,x_1}$. To eliminate these, we must first characterize the reference interstation profile $\Delta M_{i,ref}$:

$$\begin{aligned} \Delta M_{i,ref} &= M_{i,ref,x_2} - M_{i,ref,x_1} \\ &= C_{i,ref,x_2} - C_{i,ref,x_1} + A_{i,ref,x_2} - A_{i,ref,x_1} + U_{i,ref,x_2} - U_{i,ref,x_1} \end{aligned} \tag{6.5}$$

Equations 6.4 and 6.5 demonstrate that reference and countermeasure profiles are not independent, since $\Delta M_{i,counter} = \Delta M_{i,ref} + I_{i,x_2}$. For the reference and countermeasure interstation profiles to be considered as independent requires vector $I_{i,x_2} = V - \Delta M_{i,ref}$ with V a vector that is orthogonal to $\Delta M_{i,ref}$. This would imply significant changes associated with the countermeasure that seem unlikely *a priori*, affecting the entire area of influence of the meteorological parameters being studied at the case site sufficiently to counter the climatological, topographical and local urbanization factors. For the general case, this will be assumed not to be true. Regardless, to isolate the effects of the UHI countermeasure, we must subtract equation 6.5 from equation 6.4:

$$\Delta M_{i,counter} - \Delta M_{i,ref} = I_{i,x_2} \tag{6.6}$$

With this approach, one is interested in the change observed between the countermeasure and reference periods of the interstation profile described in equation 6.6. This is sometimes referred to as the "BACI contrast". That way, if sites are properly matched, background environmental changes will have the same effect at both sites, without affecting the interstation difference.

However, because the measurements required to obtain equation 6.6 cannot be conducted simultaneously, a statistical analysis must be conducted to determine the significance of the observed difference. Furthermore, the data necessary to construct the reference and countermeasure interstation profiles implies that monitoring at locations x_1 and x_2 must begin sufficiently ahead of UHI countermeasure implementation in the case of a permanent countermeasure (reflective pavements, vegetation, etc.) in order to capture sufficient observations of the weather types of interest, i.e. a minimum of $10 - 30$ reference and countermeasure observations. On this basis, we now present appropriate statistical tests, i.e. tests that account for the dependence between two datasets.

6.2 Suited Statistical Tests

From a practical standpoint, determining the impact of the UHI countermeasure consists of comparing two datasets: the reference $\Delta M_{i,ref}$ and countermeasure $\Delta M_{i,counter}$ interstation profiles. These two datasets are constructed from the same measurements: one for the reference

period and one for the countermeasure period. In addition, each dataset is composed of observations (measured meteorological data) made under the same weather type and at the same time of day. For example, under heat-wave conditions, all measurements made at 2:07 pm are grouped into a single dataset. The total number of datasets K depends on the measurement frequency used, e.g. $K = 1,440$ if measurements are made every minute, $K = 24$ if measurements are made every hour. The number of reference and countermeasure observations for the k-th dataset is noted N_{ref} and $N_{counter}$, respectively. A sample mean and variance can then be calculated for each of the k reference and countermeasure datasets. This is valid for a given dataset k measured under a given weather type i, however these indexes are dropped for the following equations out of simplicity.

Comparing the obtained mean interstation profiles will provide an estimate of the mean difference between datasets. However, given the statistical nature of meteorological observations, the difference between datasets means must be tested for statistical significance. As mentioned, the reference and case interstation profiles cannot be considered as independent. Thus, commonly used tests (t-test, Welch-test, ANOVA, etc.), which typically assume independence, cannot be used (Stewart-Oaten et al., 1986). Nonetheless, in many studies this assumption is often taken for granted and thus automatically overlooked (Bernstein and Zalinski, 1983; Stewart-Oaten et al., 1986; Conquest, 2000). A handful of papers, principally in the field of ecology, have sought and proposed suited statistical procedures to account for dependence between datasets, whether heavy or weak (Millar and Anderson, 2004; Chaves, 2010; Bolker et al., 2009). For example, a matched-pairs t-test or a mixed model can be conducted. It should be noted that the type of test, even an independent one, does not affect the amplitude of the observed reference-countermeasure difference, but simply how its significance is tested.

The natural alternative to the independent t-test, which is not suited to comparing dependent datasets, is the matched-pairs t-test, which requires pairing observations two-by-two. However, using this method is problematic when dealing with non-simultaneous different-sized datasets due to the multiple possible pairing schemes, resulting in dropping some of the data. Linear mixed models (LMMs) provide a more robust alternative which do not require identically-sized datasets.

LMMs assume a linear relationship between experimental observations and both fixed and random effects. For the general case, fixed effects are often those of the tested treatment (e.g. UHI countermeasure implementation), while random effects reflect the variability of the observations due to external factors (e.g. weather conditions, time-of-year, etc.). For instance, let us consider a set of interstation observations ΔM_t made during period t, i.e. during the reference or countermeasure period. A reasonable assumption is that this observation is systematically influenced by the countermeasure put in place. Thus, we expect a direct, predictable relationship between ΔM_t and this fixed effect I. Building on equation 6.6, considering only one given weather type (e.g. typical heat-wave conditions), the linear fixed-effects model (FEM) applied to our problem is expressed by equation 6.7:

$$\Delta M_t = \Delta M_{ref} + I.t + \epsilon_t \qquad (6.7)$$

with t the indicator function for the treatment ($t = 1$ for the countermeasure period, with the subscript t thus being "*counter*", and $t = 0$ for the reference period, with the subscript t thus being "*ref*"). The corresponding deviation from the linear model is noted ϵ_t. Here, the indicator function t represents the fixed effects, i.e. either considering the "countermeasure" or "reference" period. Thus, based on equation 6.7, the intercept is the countermeasure profile ΔM_{ref}, while the slope represents the quantity that is needed to go from ΔM_{ref} to $\Delta M_{counter}$, in other words the countermeasure impact I.

In addition to a fixed-effects model, a linear mixed model also accounts for "random effects". These refer to identifiable factors (e.g. different weather types, insolation, solar masks, etc.) which are expected to unpredictably influence the datasets ΔM_t. For our problem, the linear mixed model is:

$$\Delta M_t = (\Delta M_{ref} + R_{intercept}) + (I + R_{slope})t + \epsilon_t \tag{6.8}$$

with $R_{intercept}$ and R_{slope} the random intercept and slope respectively for the modelled random factor. Both are assumed Gaussian, centered on zero and with their own variance. A conceptual illustration of a LMM applied to our framework is depicted in Figure 6.2.
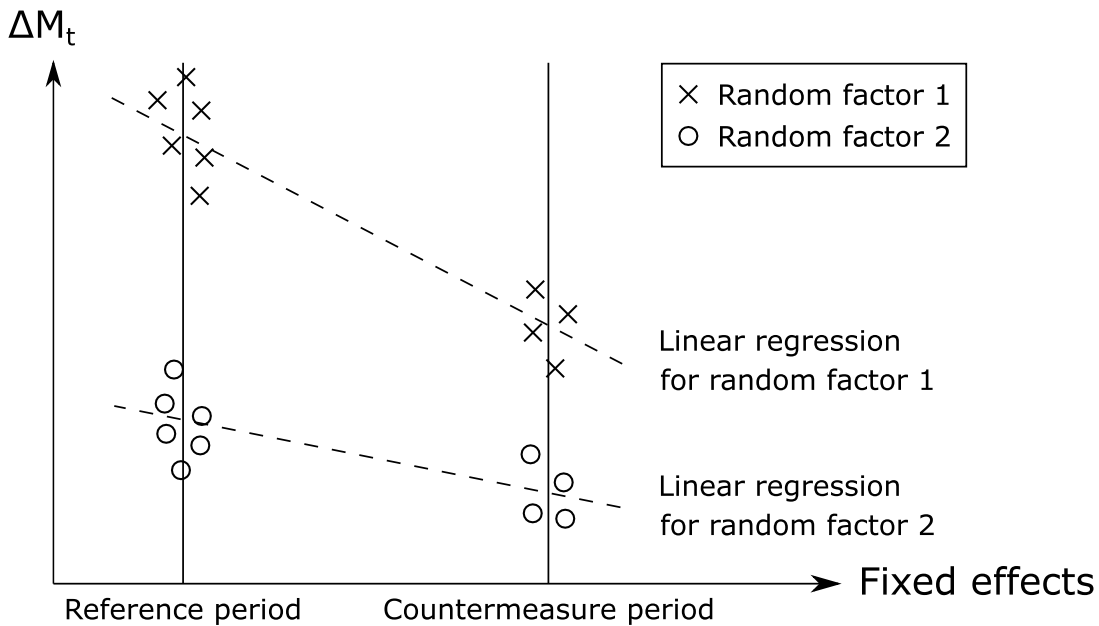
Figure 6.2: Conceptual representation of a LMM applied to our framework. ΔM_t is a function of the fixed-effects, while random effects manifest as different clusters, each with its own linear regression (dashed-lines) (Parison et al., 2020d).

LMMs are exhaustive and flexible tools, which can be used to account for any number of random factors which may uncontrollably affect observations besides the tested fixed effect. They can be used to test the influence of external factors not controlled for during the experiment. However, adding random factors splits the total number of observations into additional datasets. In doing so, the population size of each sample decreases. This is acceptable so long

as a minimum sample size of 10 to 30 observations is reached for each dataset. If there isn't enough data to reach this threshold while accounting for random factors, the LMM proposed in equation 6.8 cannot be applied. The random factors must be dropped and the analysis must be conducted only on the fixed-effects, as per equation 6.7. In the schematic illustration in Figure 6.2, this is equivalent to combining the two random factors into one, i.e. performing only one linear regression.

Applying the model to the dataset yields a best-estimate of the slope and intercept as well as their variance, p-value and confidence interval. The slope provides the estimate of the UHI countermeasure's effect.

6.3 Pavement-Watering

The proposed analysis method will be applied to pavement-watering observations conducted in Paris, France as a case study. Pavement-watering has been under study as an emergency cooling technique during heat-waves in Paris since 2013. The methodology is presented hereafter. Rue du Louvre is used as a test site, for which an optimal watering rate of 0.4 mm/h was estimated in previous work (Hendel et al., 2014, 2015a; Hendel and Royon, 2015; Hendel et al., 2016) as discussed in Section 3.1 in Chapter 3.

6.3.1 Watering Protocol

For the present case study, meteorological data was collected from two weather stations located at case and control sites under a BACI design on rue du Louvre (1st and 2nd Arrondissements) in Paris, over the summers of 2013 to 2018. Table 6.1 sums up the watering protocols carried out from 2013 to 2015 and from 2016 to 2018 between June and mid-September, if the criteria were met. As the pavement is shaded in the morning, the watering frequency is lower than in the afternoon while under direct insolation.

Table 6.1: Watering protocols carried out from 2013 to 2015 and from 2016 to 2018.

Watering protocol	Portion watered	Period	Frequency
From 2013 to 2015	Road and sidewalk (100% of the street width)	6:30 am to 12 pm	1 to 2 hours
		2 pm to 6:30 pm	30 minutes
From 2016 to 2018	Road only (66% of the street width)	7 am to 11:30 pm	1.5 hours
		2 pm to 6:30 pm	30 minutes

6.3.2 Sites Characteristics and Instrumentation

An illustration of the watered (case) and control portions as well as a photograph of a City services cleaning truck ensuring watering are provided in Figure 6.3. Unfortunately, from 2016 to 2018 construction work was undergoing in rue du Louvre preventing us from watering the

sidewalk. Each portion is about 200 m long and 20 m wide and is equipped with a weather station in its center placed near the edge of the sidewalk. The street has a canyon aspect ratio (H/W) of approximately one and is paved with impervious asphalt concrete laid on a cement-treated base.

Figure 6.3: Illustration of the case and control portions in rue du Louvre (left) and photograph of a cleaning truck performing watering (right) (Parison et al., 2020d).

Case and control weather stations measure a number of microclimatic parameters either at pedestrian height, 4 m above ground level or both, including air temperature, relative humidity, black globe temperature, wind speed and net radiation (in the spectral band $0.3 - 50 \mu$m). All measured parameters are listed in Table 6.2.

Table 6.2: Instrument type, measurement height and uncertainty.

Parameter	Instrument	Height	Uncertainty
Air temperature, T_a	Sheltered Pt 100	1.5/4 m	0.1°C
Relative humidity, RH	Sheltered capacitive hygrometer	1.5/4 m	1.5% RH
Black globe temperature, T_g	Black globe Pt 100 - ISO 7726	1.5 m	0.15°C
Wind speed, v	2D ultrasonic anemometer	4 m	2%
Net radiation, R_n	Net radiometer with thermopile	4 m	5% daily

Instruments were placed inside white-painted cylindrical cages to prevent them from being vandalized. The net radiometer placed 4-meter height was laterally deported with a 1.5 m-metallic arm to limit the station's cage potential impact on the measurement. Net radiation between case and control sites is well matched (Hendel et al., 2016). A photograph of each station is shown in Figure 6.4.
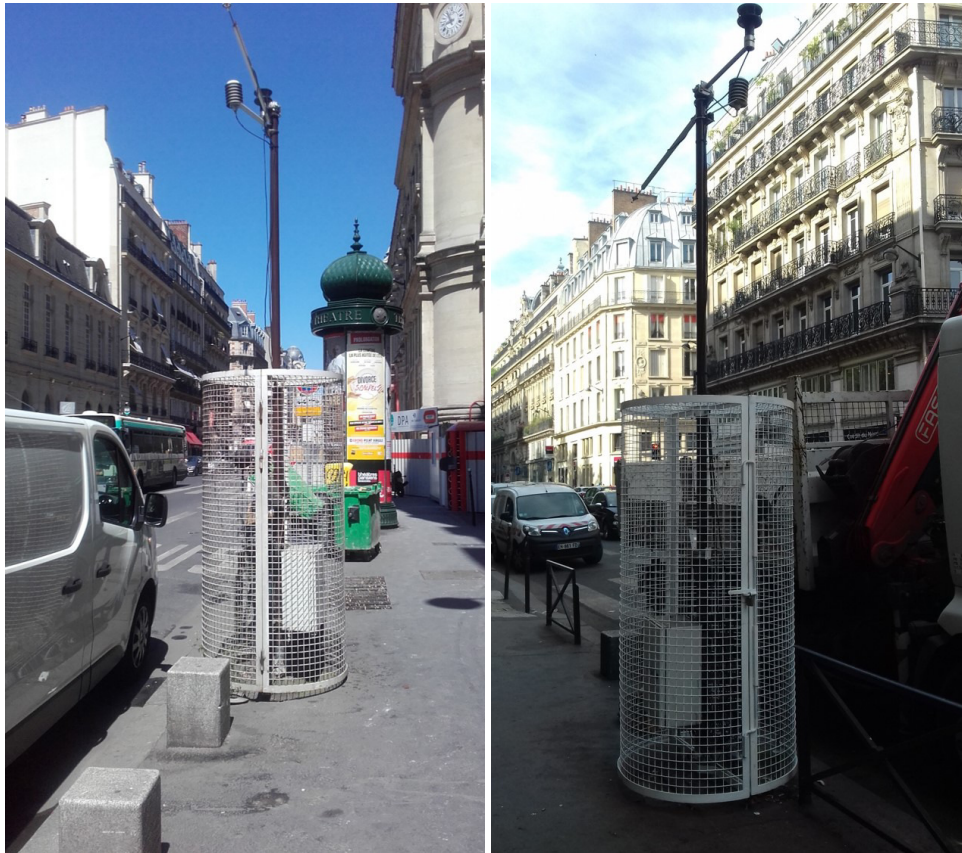
Figure 6.4: Photographs of the case (left) and control (right) weather stations in rue du Louvre (Parison et al., 2020d).

6.3.3   Watering Criteria

Pavement-watering is conducted with a cleaning truck and manual operator if certain meteorological conditions are met, corresponding to relaxed heat-wave conditions in order to increase the number of test days compared to strict heat-wave criteria given that the latter only occur during two days on an average Parisian summer (Lemonsu et al., 2013; Hendel et al., 2016). These conditions are based on Météo-France's 3-day forecast for the test day. Pavement-watering criteria, as well as the heat-wave warning criteria for Paris are shown in Table 6.3.

Table 6.3: Weather conditions required for pavement-watering and heat wave warnings (Hendel et al., 2016).

Parameter	Pavement-watering	Heat-wave warning level
Air temperature, T_a	T_{min}>16°C	>21°C for 3 consecutive days
Air temperature, T_a	T_{max}>25°C	>31°C for 3 consecutive days
Wind speed, v	<10 km/h	-
Sky conditions	Sunny (<3 oktas cloud cover)	

The sky and wind speed conditions automatically filter for days of Pasquill Stability Class A or A-B, i.e. strong to moderate solar radiation with wind speeds lower than 3 m/s (Pasquill, 1961). The three-day mean condition imposed on maximum and minimum air temperature entails that observations in the days leading up to or following pavement-watering are often also of Pasquill Stability Class A or A-B. Since these days are not watered, they are used as reference observations. Furthermore, since pavement-watering is a fully reversible UHI countermeasure, reference and watered observations continue to be obtained every summer that the weather stations continue recording and that pavement-watering is tested. Reference and countermeasure periods are thus intertwined, occurring throughout the summer.

Two families of datasets are constructed from the same measurement stations: one for the reference days and one for the watering days. Measures were performed every minute (i.e. the total number of datasets is K = 1,440). For all the upcoming analyses, one-minute data series are smoothed with a ten minute centered moving average, as per Van der Hoven (1957) to filter out outliers and spikes caused by meteorological turbulence.

The effects on pedestrian heat stress were assessed using the Universal Thermal Climate Index (UTCI) (Błażejczyk et al., 2010). The UTCI-equivalent temperature was calculated using the fast-calculation script available online (Bröde, 2009). The adjustment for wind speed measurement height is implemented before hand as per equation 2.15 (Bröde et al., 2012).

Results

We begin this Chapter by presenting the results of the 2013 to 2015 campaigns for which 100% of the street width was watered.

7.1 Effects of Street and Sidewalk Watering: 2013 to 2015

During the experimental campaigns from 2013 to 2015, a total of $N_{counter}$= 16 watering days and N_{ref}= 28 reference days were recorded based on the criteria presented in Table 6.3, the vast majority of which occurred in June and July. For the linear fixed-effects approach, the relationship between interstation profiles was studied considering the implementation of the countermeasure as the fixed effect, i.e. is the pavement watered (countermeasure period) or not (reference period). To avoid compromising the statistical robustness of the method, no random effects were considered due to the lack of observations.

On the results, we will only take interest in the value of the slope of the model, which is equivalent to the impact of watering (see equation 6.7). Both the intercept (ΔM_{ref}) and slope (I) are left free (not imposed) as far as they are expected to change throughout the day. The calculation of the statistical significance is independent from the measurement frequency: for each minute, a test is performed to compare the random variables from each population (namely ΔM_{ref} and $\Delta M_{counter}$) on the whole sample available (that is $N_{counter}$ and N_{ref} observations). That way, all 1,440 datasets are tested independently, each with all reference and watered observations recorded. Figure 7.1 shows the results for the 2013 to 2015 campaign using the FEM model for air temperature (T_a) and relative humidity (RH) at 1.5 m (left) and 4 m height (right), mean radiant temperature (MRT) and UTCI-equivalent temperature.

Average effects are plotted as solid blue lines. 95%-confidence intervals are plotted as dashed green lines while statistically significant (stat. sign.) observations (i.e. those outside of the 95% confidence interval) are emphasized in red. A close-up of the statistically significant results is provided in Table 7.1.
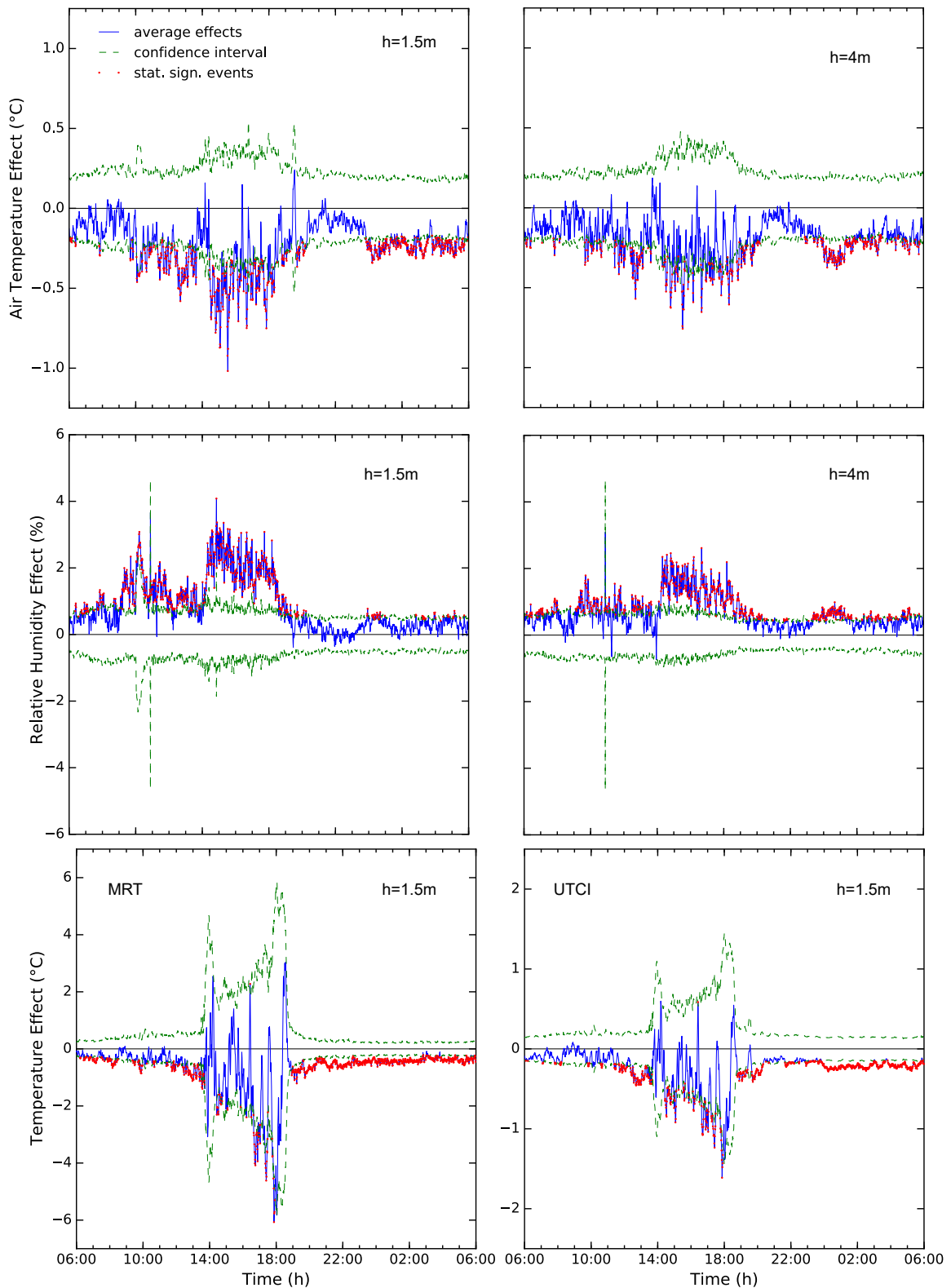
Figure 7.1: Average watering effects at Louvre from 2013 to 2015 ($N_{counter}$= 16, N_{ref} = 28) (top to bottom) for T_a and RH 1.5 m (left) and 4 m (right) height and MRT (bottom left) and UTCI (bottom right). Average effects are solid blue, confidence interval is dashed green and stat. sign. events are red (Parison et al., 2020d).

Table 7.1: Duration, average and maximum values and occurrence hour of maximum effect for statistically significant events of pavement-watering at Louvre between 2013 and 2015 using a linear fixed-effects model (Parison et al., 2020d).

Parameter	Height	Mean effect	Max. effect	Time of max. effect	Duration (hours/day)
T_a	1.5 m	-0.34°C	-1.02°C	15:32	15.4
	4 m	-0.31°C	-0.76°C	15:32	13.6
RH	1.5 m	+1.53%	+4.08%	14:51	14.3
	4 m	+1.00%	+2.61%	16:40	15.7
MRT	1.5 m	-0.70°C	-6.07°C	18:14	18.6
UTCI	1.5 m	-0.38°C	-1.93°C	17:53	15.8

Table 7.1 summarizes mean and maximum statistically significant effects. The total duration of stat. sign. events is used as a control parameter that quantifies the robustness of the watering effects. Although not presented here, the analysis could be further refined by averaging the effects in the morning only, or the afternoon or evening.

Compared to previous work by Hendel et al. (2016) on the assessment of the watering effects in 2013 and 2014 only, very similar results are found, especially for the mean effects and the duration of stat. sign. events. The total duration of the latter helps quantify their robustness. The only significant exception is noted for RH for which fewer stat. sign. events are identified, not because of a larger margin of error but because of a reduction of the average effects when adding 2015 data to the analysis, i.e. a smaller signal-to-noise ratio.

On the other hand, thanks to the additional days of the summer of 2015 and to the analysis method, maximum effects are roughly doubled for all microclimatic indicators with regard to previous analyses (Hendel et al., 2016). Globally, for T_a and RH, stat. sign. events occur soon after the beginning of watering (around 9 am) and remain so until 6 am the next day. Two main interruptions in the stat. sign. events are noted though: approximately between 1 pm and 2 pm, corresponding to the interruption of watering due to operational team turnover, and the another one between 8 pm and 10 pm. Although the reason for the latter is unclear, even if effects are not stat. sign., average profiles are always positively affected by watering. For MRT and UTCI, most of the stat. sign. events occur in the morning and the evening with fewer stat. sign. effects in the afternoon because of the stronger data variability, while some stat. sign. effects can even be observed at night up until the next morning.

Possibly, the latter events could be influenced by the data treatment, in case watering were to affect the suitability of the previous/following day to be used as a reference day. However, this is only true if a reference day directly precedes (leading to a cumulative watering effect) or follows (leading to an underestimation of the impact in the following morning) a watering day. Here this seems unlikely as only one reference day directly follows watering, while remaining watering and reference observations are decorrelated. The same goes for the 2016-to-2018 period with two reference days following watering. Thus, possible lagged-correlation in time should be smoothed out in the complete set of observations used in the FEM. Furthermore,

night-time and next-morning effects have a particularly small amplitude (close to zero for all indicators), and as such are the only effects eliminated when setting the statistical significance to 99% instead of 95%. Their microclimatic impact therefore remains limited, although not unlikely: slight thermal effects were observed at night after watered on 5 cm deep pavement heat flux signal (Hendel et al., 2015a).

In all cases, maximum effects occur during the afternoon, i.e. under direct insolation of the street. An improvement of UTCI-equivalent temperature up to -1.93°C is detected.

7.2   Effects of Street-Only Watering: 2016 to 2018

For the $2016 - 2018$ campaign where only the pavement was watered, 9 watering days and 20 reference days were recorded. Results using the fixed-effects model are plotted in Figure 7.2 and associated results are summarized in Table 7.2.

Table 7.2: Duration, average and maximum values and occurrence hour of maximum effect for statistically significant events of pavement-watering at Louvre between 2016 and 2018 using a linear fixed-effects model (Parison et al., 2020d).

Parameter	Height	Mean effect	Max. effect	Time of max. effect	Duration (hours/day)
T_a	1.5 m	-0.36°C	-0.97°C	13:50	7.5
	4 m	-0.37°C	-0.81°C	13:31	10.8
RH	1.5 m	+1.34%	+3.03%	16:27	13.7
	4 m	+1.13%	+2.33%	15:57	14.8
MRT	1.5 m	-0.82°C	-10.01°C	17:49	12.6
UTCI	1.5 m	-0.46°C	-3.42°C	17:49	6.0

In this configuration, similar mean and maximum effects are obtained compared to watering both road and sidewalk (Table 7.1), with the exception of MRT and UTCI, discussed below. The duration of stat. sign. effects however is globally halved compared to the $2013 - 2015$ campaign. For T_a, most of the stat. sign. effects are observed either in the morning or in the evening, but vanish in the afternoon, that is during the direct insolation period. This holds true for MRT as well. On the other hand, RH is only weakly affected by the change of watering strategy both in terms of duration and mean value of stat. sign. effects, although maximum effects are reduced by one percentage point compared to Table 7.1, which is, all else being equal, beneficial for thermal comfort.

For both T_a and RH, the mean effect and duration of stat. sign. effects are higher 4 m above ground level than at pedestrian height. This can be interpreted as being the result of the microclimatic spatial contrast between the sidewalk (dry) and the road (wet). This contrast between the wet road and dry sidewalk is stronger 1.5 m above ground level than at a height of 4 m where the air is better mixed.
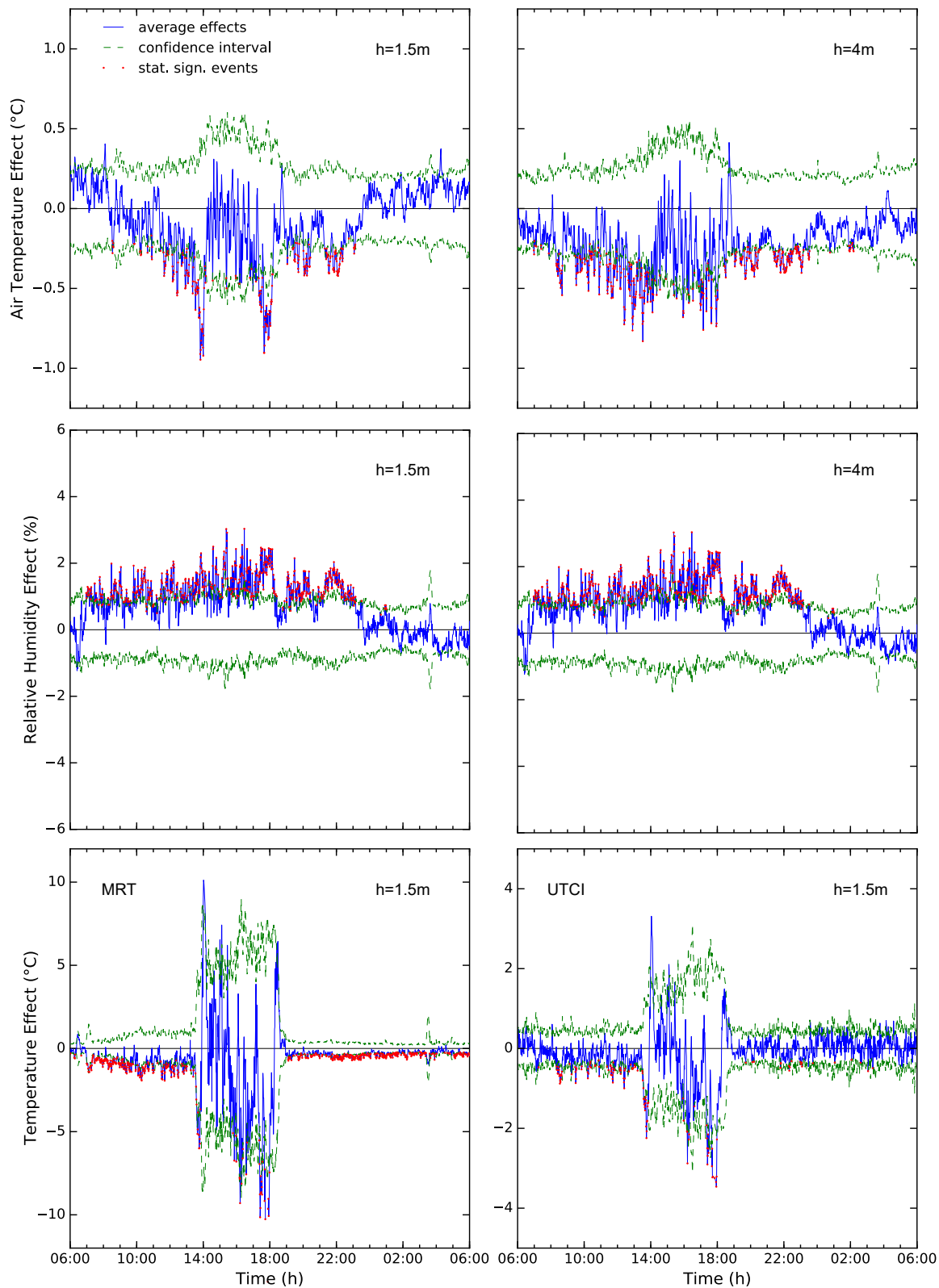
Figure 7.2: Average watering effects at Louvre from 2016 to 2018 ($N_{counter}$ = 9, N_{ref} = 20) (top to bottom)for T_a and RH 1.5 m (left) and 4 m (right) height and MRT (bottom left) and UTCI (bottom right). Average effects are solid blue, confidence interval is dashed green and stat. sign. events are red (Parison et al., 2020d).

Concerning MRT, a strong variability of the profile is observed in the afternoon with an important margin of error. As a result, only sporadic stat. sign. effects are observed during this period. This is also true for UTCI, although stat. sign. effects are only observed in the morning for the latter while some are also observed in the evening for MRT. As a result, compared to $2013 - 2015$, three times fewer stat. sign. effects are observed in $2016 - 2018$ (with respective durations of the effects of 6h versus 15.8h). Also, under direct insolation, maximum effects reached for MRT seem to be unreasonably high with regard to results obtained from the $2013 -$ 2015 campaign (with maximum effects of -6.07°C versus -10.01°C here), given that results from $2016 - 2018$ are expected to be smaller since a smaller surface is watered. Consequently, UTCI is also affected. Possibly, this could be due to the sudden passage of a cloud thus shading the black globe, or to its unintended watering by the City services, for example.

From 2016 to 2018, data from only 9 watering days is available for this analysis. Combined with the strong variability in both ΔM_{ref} and $\Delta M_{counter}$ in the afternoon, especially for black globe temperature, we assume that the lower signal-to-noise ratio in 2016 to 2018 compared to that of 2013 to 2015 partly explains the results mentioned in the previous paragraph. The higher maximum effects for 2016 to 2018 could also be explained by summer 2018's harsher-than-usual meteorology which may have increased the efficiency of watering that year. It should be noted that, 12 reference days out of 20 and 7 watering days out of 9 occurred in 2018.

Discussion of Part II

In both watering strategies tested, stat. sign. effects were observed for each microclimatic indicator considered, resulting in a reduction of pedestrian heat stress with longer-lasting effects when watering both road and sidewalk. To push the investigation further, a FEM analysis can be performed on the 24-hour averaged watering effects to test for its statistical significance or not with a 95% confidence interval. Results are reported in Table 8.1 for each watering strategy. No average effect is presented if not stat. sign.

Table 8.1: p-value and associated 24-hour average stat. sign. effect at Louvre for the $2013 - 2015$ and $2016 - 2018$ campaigns (Parison et al., 2020d).

Parameter	Height	$2013 - 2015$ (100% surface watered)		$2016 - 2018$ (66% surface watered)	
		p-value	Average effect	p-value	Average effect
T_a	1.5 m	0.003087	-0.24°C	0.135768	not stat. sign.
	4 m	0.006012	-0.20°C	0.173297	not stat. sign.
RH	1.5 m	8.43E-6	+0.89%	0.003686	+0.76%
	4 m	2.22E-6	+0.72%	0.000216	+0.73%
MRT	1.5 m	0.000960	-0.63°C	0.005091	-0.71°C
UTCI	1.5 m	0.002882	-0.29°C	0.123531	not stat. sign.

For 2013 to 2015, for each parameter, we denote that the p-value is much lower than 0.05, meaning that the 24-hour average effect is highly stat. sign. This was already the case for $2013 - 2014$ (Hendel et al., 2016). Also, the p-values for $2013 - 2015$ are systematically lower than for $2016 - 2018$ for all parameters. For the latter campaign, the 24-hour average effect is nonetheless stat. sign. for RH at both heights and for MRT. On the other hand, no stat. sign. effect is observed for T_a nor for UTCI when considering a significance level of 0.05.

In terms of heat stress, this confirms that watering of the road and the sidewalk, i.e. 100% of the street width, is more efficient than watering only the road, i.e. about 66% of the street width for this site. Such results were already highlighted in previous work where only 33% of

the pavement at Belleville site were watered compared to 100% at Louvre (Hendel et al., 2016). This is unsurprising since the cooling effects are directly linked to the watered surface area, though other factors directly influencing evaporation must be taken into account such as the ground surface temperature, air temperature, convection exchanges, vapour pressure gradient in the near air, etc.

The first limitation when comparing both watering campaigns is that the weather stations used to perform the measurements were placed on the sidewalk where pedestrians are expected to be present. As such, the stations were not in the watered area (road) from 2016 to 2018 contrary to watering conducted from 2013 to 2015. Watering only the sidewalk instead of only the road for the same watered surface area might lead to greater cooling effects than those exhibited here. The second limitation of the comparison of both strategies is due to the fact that the number of days used to conduct the statistical analyses is much smaller for $2016 - 2018$ than for $2013 - 2015$ (respectively, 20 versus 28 for reference days and 9 vs 16 for watered days). For the general case, the main risk is that even though the average interstation profile is positively affected by watering, the higher variance of the measurements results in p-values greater than the significance level (thus not statistically significant). This may not necessarily be due to the less efficient strategy itself, but because of an increased standard deviation due to the smaller sample size. This compounds with the fact that the expected effects of a reduced watering strategy are particularly small and decrease the signal-to-noise ratio, requiring a larger number of measurements to compensate for this. In a nutshell, ideally, different strategies should be compared under the same conditions. Here, this means using the exact same number of days in the analysis for each campaign. This is necessary to obtain identical noise and thus properly isolate the exact impact of each strategy. However, this does not affect the average effects found here. Again, the best way to overcome this problem is to increase the sample size.

In the case of our experiment, acquiring more data can be complicated since it is quite time-consuming (several summers in Paris given the weather criteria that were set) and operationally-intense, combined with the fact that weather station failures reduce the number of observations further. The use of even looser filtering criteria for reference and watered days could artificially compensate for this. However, increasing the number of observations with looser criteria can result in increased variance, defeating the initial goal. Finally, the use of a greater number of days acquired on a large time span should be carefully performed in a BACI experiment and is only relevant provided that the difference between stations either remains constant or depends on known factors that can be accounted for in a LMM.

CHAPTER 9

Conclusion of Part II

A methodology for assessing the effects of UHI-countermeasure in the field was proposed by adapting the Lowry approach. The framework identified that the performance of UHI counter-measures cannot be evaluated in the field with direct comparisons between case and control observations as these do not eliminate pre-existing interstation differences. To evaluate their performance, the difference between reference (before) and countermeasure (after) measurements must be tested under the BACI design. Furthermore, it was also shown that countermeasure and reference observations cannot be considered independent and the statistical tools used to test their statistical significance must account for this. A statistical methodology was proposed to evaluate the cooling performance of pavement-watering conducted at rue du Louvre in Paris from 2013 to 2018. The methodology can be generalized to other UHI countermeasures, provided that microclimatic measurements start sufficiently ahead of the implementation of the countermeasure put in place.

For the linear fixed-effects model, the interstation difference for each parameter was expressed as a function of fixed effects, i.e. before or after implementation of the countermeasure. Unfortunately, the total number of observations was too small to account for random factors and conduct a linear mixed model analysis. A fixed-effect model was therefore used in place of a LMM. This approach does not require data pairing and can therefore be used with asymmetric sample datasets, making it much simpler to implement in the general case.

From 2013 to 2015, the whole street width was watered (pavement and sidewalk). Results showed that watered days were cooler and more humid than reference days and is effective for reducing pedestrian heat stress. In particular, watering effects reached up to -1.02°C and -0.76°C for 1.5 and 4 m air temperature respectively, +4.08% and +2.61% for 1.5 and 4 m relative humidity, and -6.07°C and -1.93°C for 1.5 m MRT and UTCI-equivalent temperature. These effects are slightly greater than those found for previous reports from 2013 to 2014. This is most likely thanks to the addition of observations from summer 2015 which was particularly hot. Indeed, the analysis of the watering effects of only 2015 at Louvre exhibited even greater cooling effects, with reductions up to -2.84°C and average reduction of -1.16°C for 1.5 m air temperature. From 2013 to 2015, daily average effects of -0.34°C and -0.31°C for 1.5 m and 4 m air temperature, +1.53% and +1.00% for 1.5 and 4 m relative humidity, -0.70°C and -0.38°C

71

for 1.5 m MRT and UTCI-equivalent temperature. Such effects were observed all day almost as soon as watering begins, with less robust marginal effects lasting until 6 am the next day. Fewer but stronger statistically significant effects are observed in the afternoon in general. While watering only represents a 9-hour intervention per day, its effects can be felt until the next morning.

From 2016 to 2018, only 66% of the street width was watered (pavement only). Unsurprisingly, this strategy was found to be less efficient than the previous though similar effects were observed. Of interest, a significant decrease of the duration of stat. sign. effects was found, i.e. two or three times shorter depending on the parameter. The duration of stat. sign. relative humidity effects is the least affected and UTCI-equivalent temperature the most. Stat. sign. effects mainly occurred in the morning, apart for relative humidity, when the area is shaded.

Finally, to test for the robustness of the effects, an analysis conducted on the 24-hour watering effects revealed that air, mean radiant and UTCI-equivalent temperature as well as relative humidity still yielded highly stat. sign. effects when 100% of the street was watered. On the contrary, no stat. sign. effects were found for air and UTCI-equivalent temperatures when only the road was watered. Therefore, analyses carried out per minute and over a 24-hours average both help determine the efficiency and robustness of different watering strategies in order to guide the operational choice for the implementation of watering.

Having studied the effects of pavement-watering on a traditional asphalt pavement in the field and applied suited statistical tools, we now turn our attention on the fine-tuning of the process in the lab in Part III.

PART III

LABORATORY OPTIMIZATION OF PAVEMENT-WATERING

Introduction to Part III

In Part II, the microclimatic effects of pavement-watering were studied in the field. A suitable statistical method for the field evaluation of pavement-watering (or other UHI-countermeasures) was proposed and applied to data collected from two watering protocols. The method was found to reduce the UTCI-equivalent temperature at pedestrian height up to 2°C during the day despite the increase in relative humidity up to a few percent. Reducing the watered surface area by one-third was found to roughly halve the duration of the stat. sign. effects, although similar amplitude for the latter was found for both strategies.

However, the optimization of the watering rate and efficiency of the method has not yet been addressed. Hendel et al. (2015a) proposed a formal optimization procedure for pavement-watering field campaigns, that lead to the chosen watering protocol used in Part II. In addition to evaluating the method's cooling effects, these studies underlined the important role played by the materials themselves on the performance of the process.

Indeed, because of their low albedo and great heat storage capacity, man-made pavement materials commonly used in the urban fabric play a major role in the UHI phenomenon (Mohajerani et al., 2017; Asaeda et al., 1996; Erell et al., 2014). Some of the countermeasures discussed in Chapter 2 tackle this aspect by promoting the use of cool materials (Santamouris, 2013; Qin, 2015). Yet, substituting one material with another is not always feasible, since the design goals of a pavement is decisive regarding the viability of a given mitigation strategy. For instance, road structures are determined by mechanical requirements rather than thermal behaviour. Bearing this in mind, pavement-watering constitutes an interesting emergency heat mitigation tool, as it can easily be performed on existing pavements for areas where other countermeasures are difficult to implement (Kinouchi et al., 1994; Bouvier et al., 2013; Li et al., 2013b; Daniel et al., 2018).

In this regard, pavement-watering needs to be optimized according to the diversity of urban paving structures. In order to avoid long-lasting and costly field trials, a laboratory approach is preferable. Thus, in this Part, we propose a lab experiment for the study of the thermal behaviour of various paving structures, with and without watering. We start by testing an asphalt concrete road structure, which is one of the most common paving materials found

in cities. This Part presents the methodology and applies it to a traditional paving structure. Results are then compared to the optimized field tests presented in Part II which are used as a validation tool for the lab protocol.

The road sample used was manufactured by the Paris City Hall Public Space Laboratory (Road and Traffic Division) and is thus compliant with its prescriptions and representative of realistic structures implemented in Parisian public spaces. Many studies have focused on the thermal behaviour of pavements (Asaeda et al., 1996; Doulos et al., 2004; Takebayashi and Moriyama, 2012; Li, 2015), but very few of them account for the influence of the underlying layers of the structure. These base layers have an impact on the global behaviour of the pavement structure as a whole (Hendel et al., 2018). Some laboratory-scale studies have also been conducted (Ueno and Tamaoki, 2009; Wu et al., 2018), but to date none of them include pavement-watering.

Part III presents analyses of experimental lab results to characterize the thermal behaviour of the watered asphalt road structure under heat-wave-like conditions. The set-up has been used in a previous stage under dry conditions only on five pavement structures including asphalt road and sidewalk, granite sidewalk, stabilized sand and grass. Results showed that grass was the coolest structure, followed by stabilized sand and granite, while asphalt road and sidewalk were the hottest (Hendel et al., 2018). Here, a wide range of watering rates are tested on the asphalt road with the aim of determining the optimal watering rate. Both temperature and heat flow are measured at several depths.

Chapter 11 first presents the methodology, while Chapter 12 presents the experimental results. The evaporative cooling flux, as well as the convective, radiative and conductive contributions were assessed for each rate, and the contribution on the urban climate in terms of heat storage and release was estimated and discussed. Finally, Chapter 13 confronts lab results to pavement-watering field tests conducted on a similar asphalt road structure by Hendel et al. (2015a), in order to evaluate the relevance of the present lab protocol and give insights on its potential transposition to the field. In the end, good agreement was found with field studies, thus validating the experimental approach.

The work described in this Part is based on peer-reviewed articles published in *Building and Environment* (Hendel et al., 2018), and in *Urban Climate* (Parison et al., 2020b).

CHAPTER 11

Methodology

11.1 Experimental Set-Up and Protocol

The experimental protocol aims to reproduce simplified heat-wave-like conditions typically observed in Paris. Cylindrical pavement samples undergo a 24-hour cycle inside a closed climate chamber including an 8-hour day phase with artificial insolation, and a 16-hour night phase without insolation. Air temperature and relative humidity are controlled inside the chamber and irradiance is ensured with a seven-bulb dichroic halogen lamp with a color temperature of 6500 K placed above the sample. Air circulation inside the chamber is auto-regulated by the chamber and deemed identical between tests. A diagram and photograph of the experimental set-up are shown in Figure 11.1.
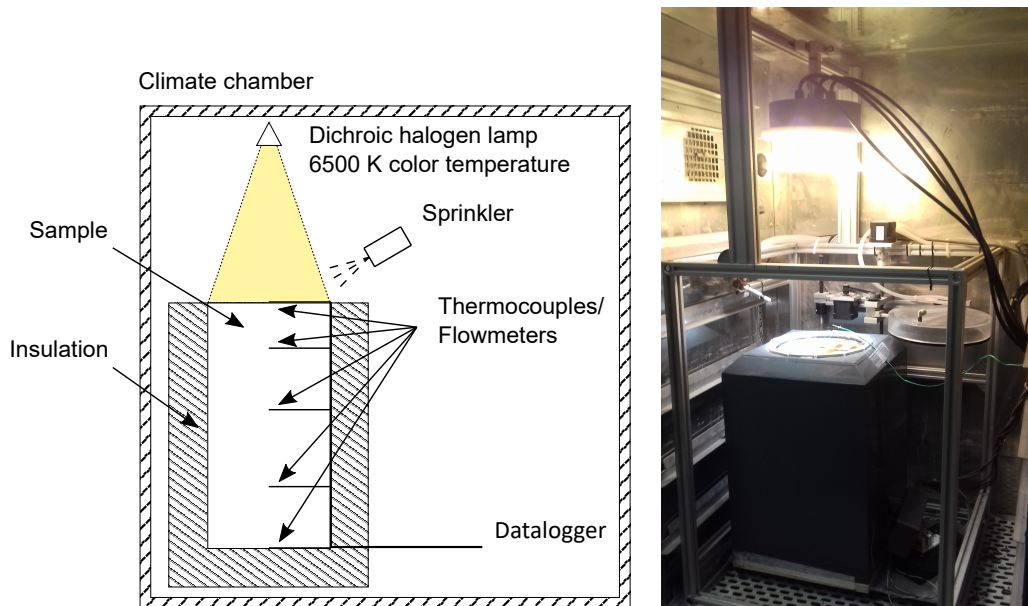
Figure 11.1: Diagram (left) and photograph (right) of the experimental set-up (Parison et al., 2020c).

During the day phase, the air temperature inside the chamber is set to 35°C with 35% relative humidity, while at night temperature is 25°C with 70% humidity. These setpoints correspond to conditions typically encountered during heat-waves in Paris as seen in the field with continuous measurements conducted since 2013 (Hendel et al., 2016). Before each trial, samples are stabilized under night phase conditions. The radiation intensity, measured at the sample surface, is specified for both short (SW) and long wavelength radiations (LW), respectively of $0.3 - 3$ μm and $3 - 100$ μm. The SW/LW proportion (resp. 70/30%) is measured using a pyrgeometer for the LW band and using a pyranometer with thermopile for the SW band. Irradiance measurements were conducted inside the closed chamber during the day and night phases, and thus take into account SW and LW reflexion within the chamber. Air temperature and relative humidity measured inside the chamber over a 24h-cycle are presented in Figure 11.2. Table 11.1 sums up the characteristics of each climate phase.
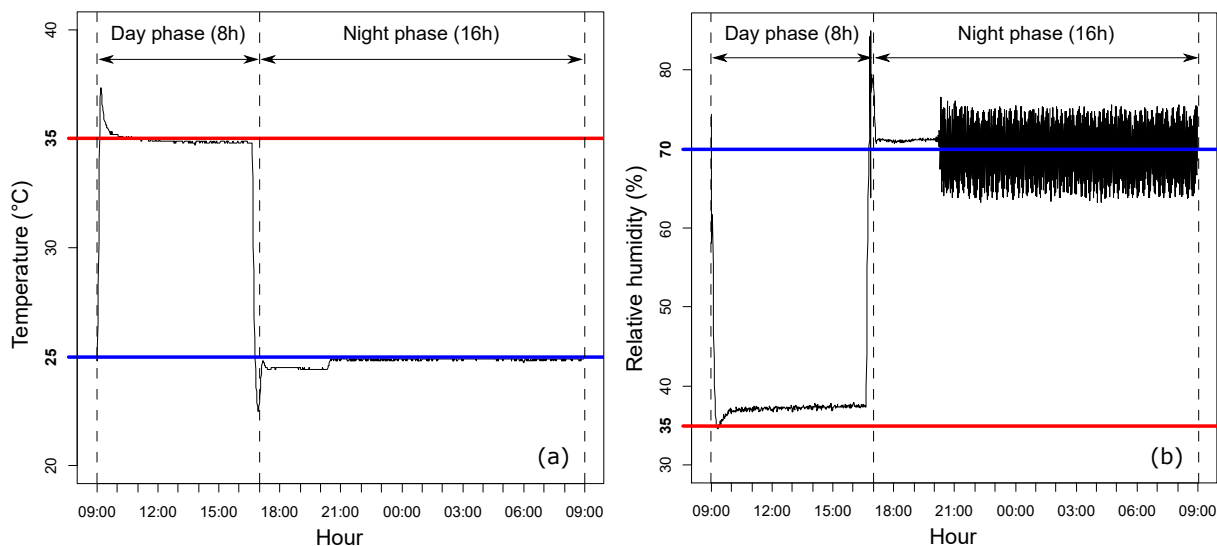
Figure 11.2: Temperature and relative humidity regulation over 24 h inside the climate chamber. Daytime and nighttime setpoints are indicated with horizontal red and blue lines, respectively (Hendel et al., 2018).

Table 11.1: Characteristics of the day and night phases (Parison et al., 2020c).

Characteristics	Day phase	Night phase
Duration	8 h	16 h
Air temperature, T_a	35°C	25°C
Relative humidity, RH	35%	70%
SW radiation ($0.3 - 3$ μm)	930 W/m²	0 W/m²
LW radiation ($3 - 100$ μm)	450 W/m²	450 W/m²

Besides, the presence of a pressurized-water sprinkler near the sample's surface allows surface watering at desired frequency during the day. Each spray delivers about 1 mL on average, i.e. a film of approximately 0.05 mm (0.05 L/m²) in water height given the surface area of the sample. Different watering rates (Q) are programmed by modifying the frequency between

two consecutive sprays. All in all, one dry trial and twelve watered trials were performed, listed in Table 11.2.

Table 11.2: Watering rates tested.

	Watering rates, Q (mm/h)
Day phase	$0 - 0.1 - 0.25 - 0.4 - 0.5 - 0.6 - 0.75 - 1.0 - 1.25 - 1.5 - 2.0 - 2.5 - 3.0$
Night phase	Not watered

To avoid water infiltration, the edges of the asphalt road sample were sealed. Thermal insulation of its bottom and periphery is ensured using a 5 cm thick polyurethane foam casing to create a zero heat-flux boundary condition (no thermal leakage). The sample is equipped with thermoflowmeters on its surface positioned using silicon thermal paste, and 6 and 14 cm deep, and only with a thermocouple 25 cm deep. Material layers were sawed to allow instrument placement and reconstructed with bitumen or cement for the cement-treated base. Pavement sample thermal behaviour is monitored at a frequency of 0.1 Hz using the surface and in-depth sensors, while air temperature is measured with a thermocouple placed above the sample's surface.

It is noteworthy the spectral irradiance of the halogen lamp is different from that of solar spectrum AM 1.5, although the irradiance flux density measured at the sample surface, both day and night, is of the same order as that of a mid-latitude city for clear summertime skies (Oke, 1988a, 1997), summarized in Table 11.3.

Figure 11.3 illustrates spectral irradiance for the halogen lamp in the $200 - 1700$ nm band as provided by the manufacturer as well as that of AM 1.5 solar spectral irradiance. The halogen lamp's spectrum is shifted in the infrared band and slightly lower in the UV or visible bands compared to AM 1.5.
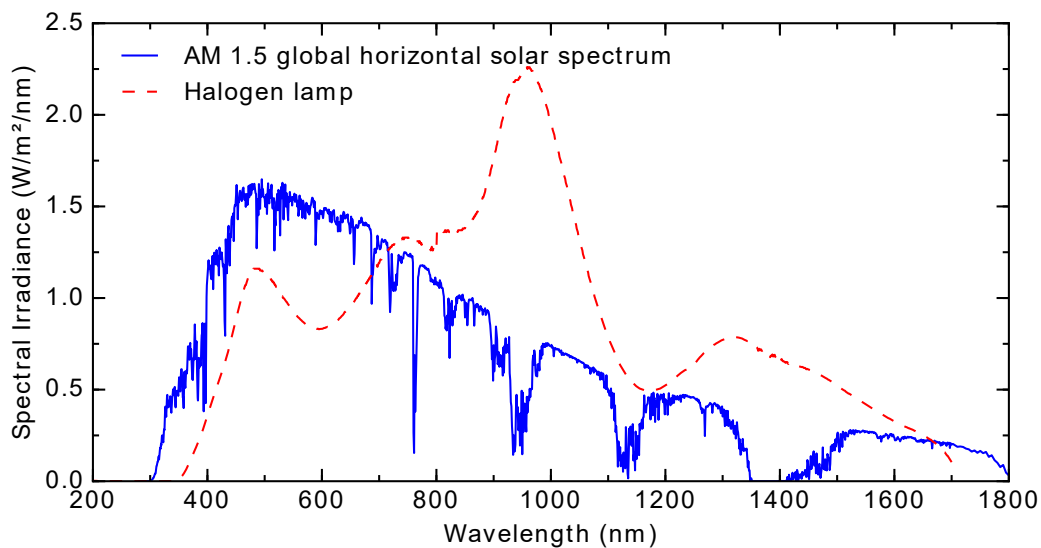
Figure 11.3: Spectral irradiance of the halogen lamps (red) and of the AM 1.5 global horizontal solar spectrum (blue) in the $200 - 1700$ nm band (Hendel et al., 2018).

Table 11.3: Typical radiative balance of a mid-latitude city of about one million inhabitants under clear summertime skies and low wind speeds (Oke, 1988b).

	S	L	S_{up}	L_{up}
Day (W/m²)	760	365	106	503
Night (W/m²)	0	335	0	415

Given the conditions imposed for the climate cycle, the set-up is not intended to faithfully reproduce outdoor conditions, but is rather used as a comparison tool of the thermal behaviour of various paving structures undergoing the same conditions, though they may differ from a real environment.

11.2   Case-Study Structure

For this part, a single asphalt road structure was tested with and without watering of its surface at the different watering rates of Table 11.2. The cylindrical sample is 32 cm tall and 16 cm in diameter. The structure was directly prepared in a cylindrical test tube following the quality control procedures of the Paris City Hall public space laboratory. Its structure is identical to that prescribed for Parisian roadways and is composed of three different layers: a 4 cm asphalt concrete surface course, a 12 cm asphalt concrete mid-course, and a 16 cm cement-treated base. A diagram and photograph of the asphalt road structure equipped with thermoflowmeters once the sample is embedded in the insulating casing and placed inside the climate chamber, are provided in Figure 11.4.
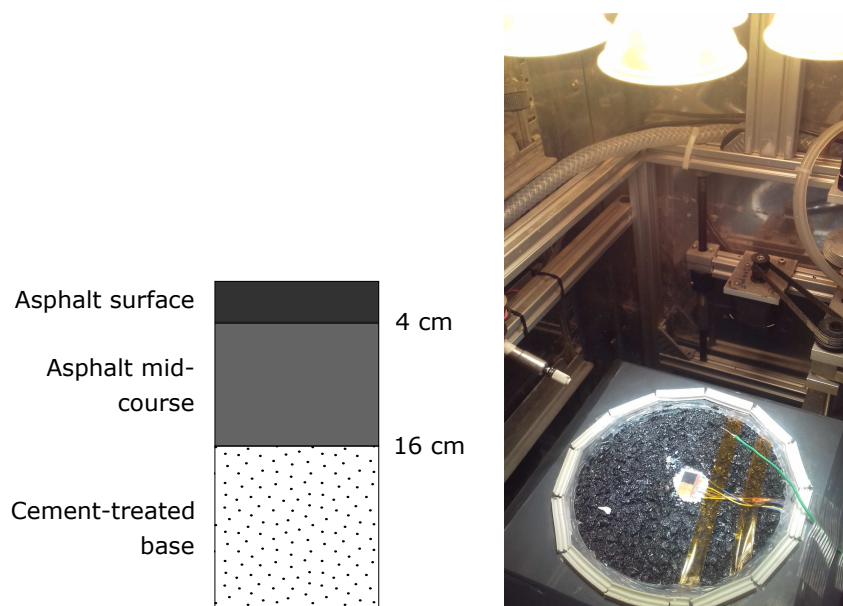
Figure 11.4: Asphalt-road-sample diagram (left) and photograph once placed inside the climate chamber (right) (Parison et al., 2020b).

In order to determine the change in albedo resulting from watering, comparative reflectivity measurements were conducted on the sample with a Cary 5 UV-Vis-NIR spectrophotometer and integrating sphere, for both a dry and a wet surface. Albedo was calculated using the set-up halogen lamp spectrum. Albedo of dry (α_{dry}) and wet (α_{wet}) surface calculated using the halogen lamp spectrum are respectively 0.076 and 0.057. Dry surface emissivity (ϵ_{dry}) was determined by infrared camera using the reference black body method.

11.3 Heat Transfer Analysis

We now present the heat transfer analysis for determining the latent heat flux created by pavement-watering. The surface heat budget is illustrated in Figure 11.5.
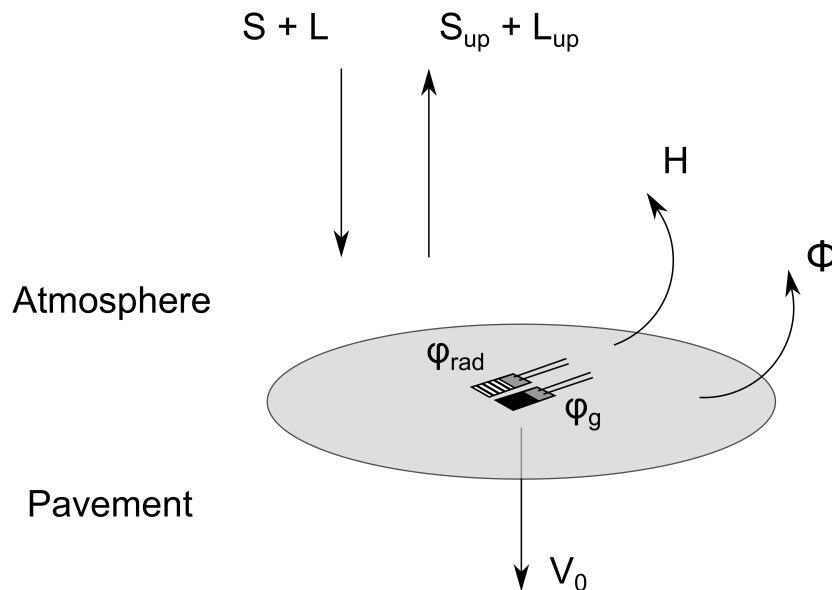
Figure 11.5: Schematic diagram of heat balance at the pavement surface. φ_{rad} is the radiative flux measured by a radiative heat flow sensor and φ_g the global heat flux measured by the fluxmeter (both sensors with $\epsilon = 0.95$ and $\alpha = 0.05$) (Parison et al., 2020c).

For a dry surface, the energy balance is completely described by equation 11.1:

$$R_n^{dry} = H^{dry} + V_0^{dry} \tag{11.1}$$

with R_n the net downward radiation received by the surface, H the upward atmospheric convective heat flux and V_0 the downward conduction heat flux at the surface. If the surface undergoes pavement-watering, the budget becomes:

$$R_n^{wet} = H^{wet} + V_0^{wet} + \Phi \tag{11.2}$$

with Φ the total cooling flux due to watering. Φ includes a sensible and a latent cooling component. The former is provided as the sprinkled water heats up, the latter as the sprayed water film evaporates:

$$\Phi = lE + c_w \rho_w Q(T_s^{wet} - T_w) \tag{11.3}$$

The latent heat of vaporization of water is noted l (2,260 kJ/kg), E is the evaporation rate of the water film, c_w is the specific heat of water (4.18 kJ.kg^{-1}.K^{-1}) and ρ_w the water density (1000 kg.m^{-3}). The watering rate is denoted Q, T_s^{wet} is the surface temperature when wet, and finally T_w is the water temperature, i.e. 35°C during the day phase (verified by measurement). Experimentally, Φ can be obtained by subtracting equation 11.2 from equation 11.1:

$$\Phi = (H^{dry} - H^{wet}) + (V_0^{dry} - V_0^{wet}) + (R_n^{wet} - R_n^{dry})$$
$$= \Delta H^{dry-wet} + \Delta V_0^{dry-wet} - \Delta R_n^{dry-wet} \tag{11.4}$$

Equation 11.4 shows that the total cooling flux is partitioned into changes of convective, conductive and radiative heat flows. We now unpack the terms of these equations. Based on its definition, net radiation can be developped into the following equation (see equations 2.3 and 2.4 of section 2.2 in Chapter 2):

$$R_n := S + L - (S_{up} + L_{up})$$
$$= (1 - \alpha)S + \epsilon(L - \sigma T_s^4) \tag{11.5}$$

S and S_{up} are respectively incident (downward) and reflected (upward) SW radiation, while L and L_{up} are respectively incident and upward LW radiation. α is the surface albedo, ϵ the emissivity and σ the Stefan-Boltzmann's constant. Hence, since irradiance $S+L$ do not vary between trials:

$$\Delta R_n^{dry-wet} = (L_{up}^{wet} - L_{up}^{dry}) + (S_{up}^{wet} - S_{up}^{dry})$$
$$= \sigma(\epsilon_{wet} T_s^{wet\,4} - \epsilon_{dry} T_s^{dry\,4}) + (\epsilon_{dry} - \epsilon_{wet})L + (\alpha_{wet} - \alpha_{dry})S \tag{11.6}$$

For the convective term, according to Jürges (1924), H can be written as:

$$H = h(T_s - T_a) \tag{11.7}$$

where h is the convective heat transfer coefficient and T_a is the air temperature. Since the air temperature inside the climate chamber is maintained at 35°C during the day phase, the dry-wet difference in convective flux can be expressed by the following:

$$\Delta H^{dry-wet} = h^{dry} T_s^{dry} - h^{wet} T_s^{wet} - (h^{dry} - h^{wet}) T_a \tag{11.8}$$

with h^{dry} and h^{wet} the respective convective heat transfer coefficient for a dry and wet surface. Assuming that the difference between the convective exchanges coefficients for dry and watered trials is negligible (i.e. $h^{dry}=h^{dry}\approx h^{wet}$), equation 11.8 can be simplified into:

$$\Delta H^{dry-wet} = h(T_s^{dry} - T_s^{wet}) \tag{11.9}$$

This hypothesis was verified when comparing the mean evaporation rate for each trial calculated using two methods: the surface heat budget on the one hand and the mass convection transport problem (based on the water vapour pressure gradient in near air) on the other hand (further detailed in Section 12.6). Results using these two methods converge for a difference less than 3 W/m²/K between h^{dry} and h^{wet}. For the rest of this dissertation, a single convective coefficient noted h (thus considered constant and independent of the chosen watering rate), is used for all trials.

Finally, an analytical expression exists for heat conduction using the Fourier's law (see equation 2.6), but $\Delta V_0^{dry-wet}$ can also easily be determined experimentally, as detailed in equation 11.10:

$$\begin{aligned}
\Delta V_0^{dry-wet} &= V_0^{dry} - V_0^{wet} \\
&= (V_{-6}^{dry} + \Delta Q^{dry}) - (V_{-6}^{wet} + \Delta Q^{wet})
\end{aligned} \tag{11.10}$$

with V_{-6} the pavement heat flux density measurement 6 cm deep and ΔQ the heat flux absorbed by this 6-cm top-layer. Assuming that watering does not influence the thermal properties of the material and thus the heat transfer process through the sample, ΔQ can be deemed constant. Hendel et al. (2015a) used this hypothesis that proved to be valid for field experiments. Relationship 11.10 then becomes:

$$\Delta V_0^{dry-wet} = V_{-6}^{dry} - V_{-6}^{wet} \tag{11.11}$$

Equation 11.10 is deemed valid close to the surface, and provided that thermal leakage at insulating walls cercling the sample remains negligible. Overall, this assumption proved to be true for previous observations on five non-watered paving structure based on heat flow measurements 6 and 14 cm deep (Hendel et al., 2018). To determine the quantities of interest for our experiment, the sample's surface was equipped with a black-painted global heatflowmeter measuring denoted φ_g, and a radiative heatflowmeter measuring φ_{rad}, both with $\epsilon = 0.95$ and $\alpha = 0.05$). Applying equation 11.5 to the sensors, quantities measured by each sensor are given below:

$$\varphi_g = R_n^{\epsilon=0.95,\,\alpha=0.05} - H = 0.95\,(S + L - \sigma T_s^4) - H \tag{11.12}$$

$$\varphi_{rad} = R_n^{\epsilon=0.95,\,\alpha=0.05} = 0.95\,(S + L - \sigma T_s^4) \tag{11.13}$$

Surface temperature is measured by the global heatflowmeter. Using equation 11.13, total incident irradiance $S+L$ received at the sample surface (specified in Table 11.1, i.e. 1380 W/m²

during the day and 450 W/m² at night) is constant and measured for the 24h-cycle following equation 11.14:

$$S + L = \frac{\varphi_{rad}}{0.95} + \sigma T_s^4 \tag{11.14}$$

Thus, R_n^{dry} is obtained directly from equation 11.5 knowing the surface albedo and emissivity, while H, not knowing h, is calculated using equation 11.7, derived from equation 11.12.

$$H^{dry} = 0.95 \left(S + L - \sigma T_s^4 \right) - \varphi_g \tag{11.15}$$

V_{0cm} is then calculated as the residual term from equation 11.1. The dry surface heat budget is therefore entirely resolved. However, this method cannot be used during watering when the radiation flowmeter is not useable and when φ_g also includes Φ (with $\varphi_g = R_n^{\ \epsilon=0.95,\ \alpha=0.05} - H^{wet} - \Phi$). Instead, since V_{-6}, T_s, ΔQ are measured, since irradiance is unaffected by surface watering, and since the albedo and emissivity of the surface is known, Φ can be determined on the basis of equations 11.6, 11.9 and 11.11 using equation 11.4. Knowing Φ and the sensible term of equation 11.3, we can therefore obtain the evaporation rate for each trial. On the basis of previous work (Hendel et al., 2015a), two cooling regimes are expected: latent and sensible. The former begins at the start of watering and ends once the maximum evaporation rate is reached, at which point additional watering only increases sensible cooling.

11.4   Watering Optimization Goals

The aim of this part is to optimize the watering process on the basis of a previously-developed framework (Hendel et al., 2015a). The goal of pavement-watering is to decrease the pavement surface temperature, which in turn limits atmospheric heating and helps improve pedestrian thermal stress. As only thermal measurements are performed inside the climate chamber, the following optimization goals are selected:

- Maximise pavement cooling Φ

- Minimize the watering rate Q

These goals can be combined into maximizing the ratio of pavement cooling to watering rate, Φ/Q. The cooling effect of pavement watering is assessed by performing a heat transfer analysis, following the steps exposed in section 11.3. By doing so, a preliminary analysis of V_0, H and R_n is required. Using the two cooling regimes expected from the above-mentioned framework, both goals can eventually be achieved. Finally, results on the asphalt road structure will be compared to field tests conducted on a similar structure (Hendel et al., 2015a) in order to evaluate the relevance of the present experimental set-up. We now present the response of the asphalt road in both dry and watered conditions, beginning with surface temperature observations.

Experimental Results

12.1 Surface Temperature

Figure 12.1 shows surface temperature as function of time for different watering rates. For clarity, only six out of thirteen different watering rates are presented.
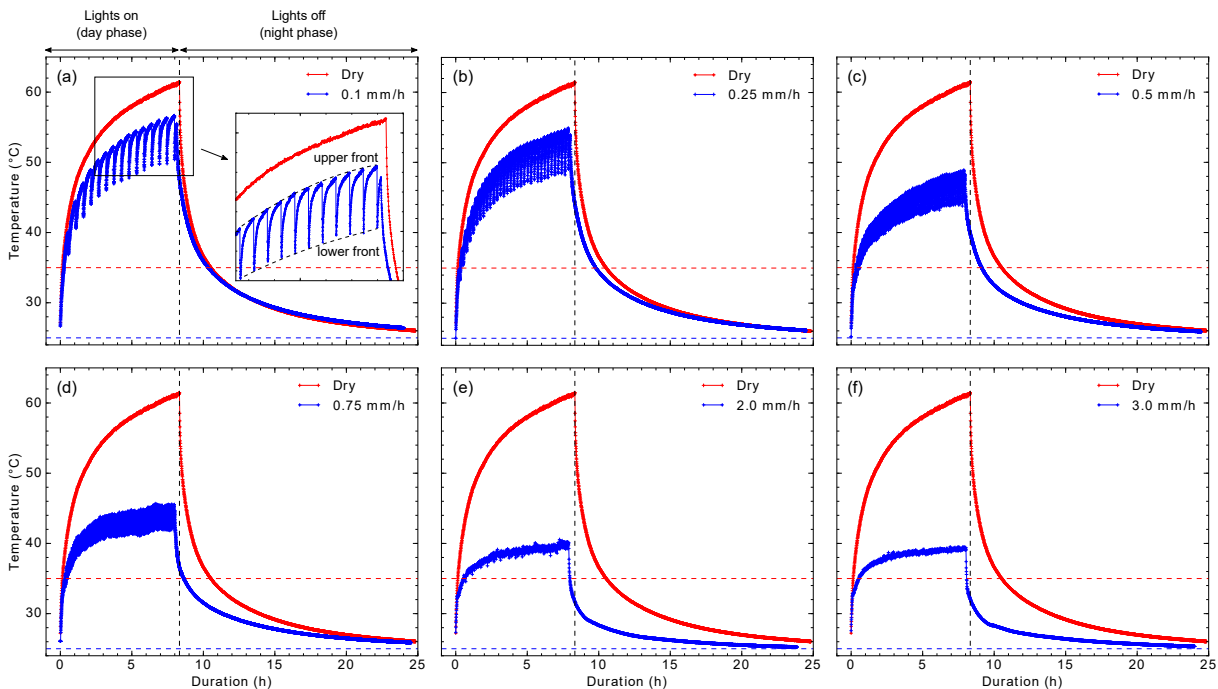
Figure 12.1: Asphalt road surface temperature with (blue) and without (red) watering for various watering rates (namely 0.1 (a), 0.25 (b), 0.5 (c), 0.75 (d), 2.0 (e) and 3.0 (f) mm/h). Horizontal dashed lines represent day (red) and night (blue) phases air temperature, while the black vertical dashed line marks the transition between day and night phases (Parison et al., 2020b).

As can be seen, at the end of day phase for the non-watered trial, surface temperature reaches a maximum of about 62°C, which is usual for an asphalt structure under such conditions (Doulos et al., 2004; Hendel et al., 2014). At the end of the day phase, an exponential decrease of temperature is immediately observed as the lights are being turned off and the setpoint temperature and humidity switch to their night values. For relatively small watering rates, the appearance of spikes throughout day phase is observed. These spikes are simultaneous with watering. These temperature spikes are caused by the rapid cooling and drying created by water sprinkling (Hendel et al., 2015a, 2018). As illustrated in Figure 12.1 (a), the limit formed by the spike maxima is referred to as the "upper front" while the spike minima limit is designated as "lower front" for the rest of this manuscript. The presence of spikes suggests that the watering rate should be increased to maximise cooling effects of the method (Hendel et al., 2014).

As the watering rate increases, spike frequency increases with the watering frequency while spike amplitude and maximum surface temperatures decrease. Finally, once a certain watering rate is reached, no additional variation in temperature is observed with increased watering, as can be seen for example between Figure 12.1 (e) and 12.1 (f). This means that the maximum evaporable quantity of water under these conditions has been sprinkled, and that additional water does not provide additional latent cooling. A close-up at the watering spikes is provided in Figure 12.2 for two rates: 0.1 and 0.75 mm/h.
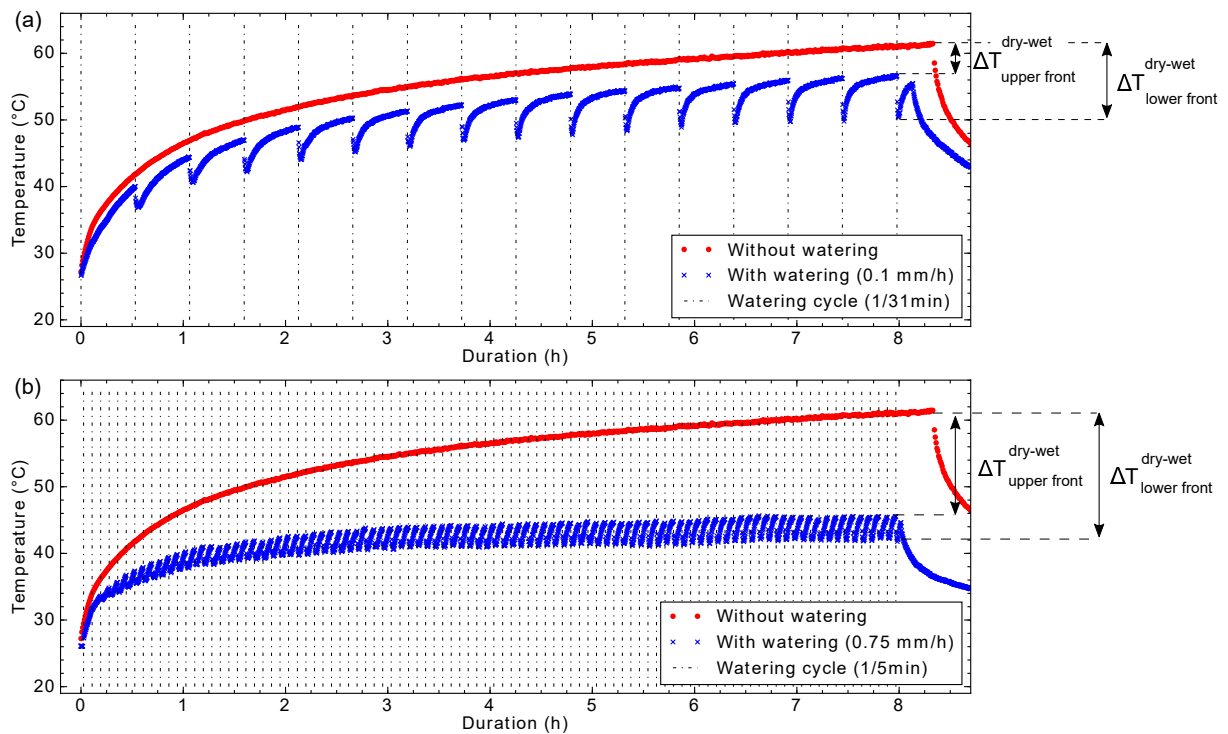
Figure 12.2: Asphalt road surface temperature during day phase with (blue) and without (red) watering, for 0.1 (a) and 0.75 mm/h (b) (Parison et al., 2020b).

Watering cycles are indicated with dot-dashed vertical lines. Observed dry-wet maximum temperature difference, $\Delta T_{max}^{dry-wet}$, is indicated for the upper and lower fronts. The watering

effect is plotted as a function of the watering rate Q in Figure 12.3. Corresponding error bars take into account the fluctuations observed for watered trials and for the initial temperature value of the current test. They are then propagated into the calculation of $\Delta T_{max}^{dry-wet}$.
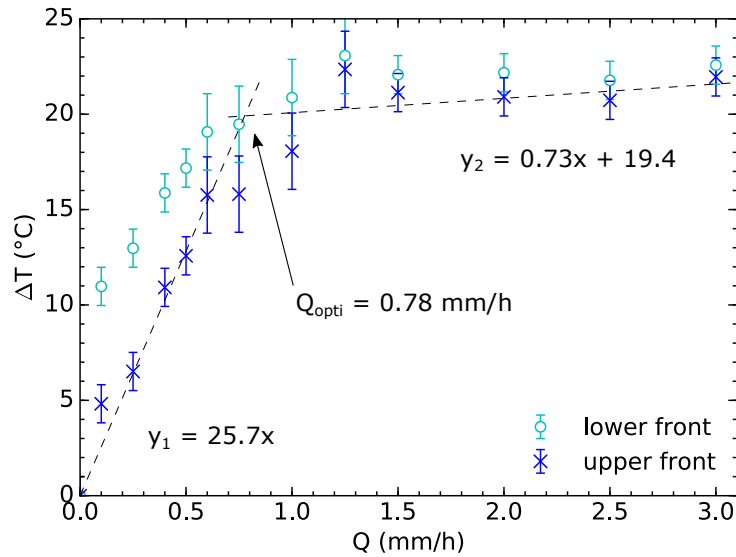
Figure 12.3: Dry-wet maximum surface temperature difference $\Delta T_{max}^{dry-wet}$ for lower and upper fronts as a function of the watering rate for the asphalt road. A double linear piecewise regression with zero-intercept is used (dashed lines) to distinguish the two regimes (Parison et al., 2020b).

As expected, two linear regimes are visible: latent and sensible. The former is characterized by a significant increase of surface cooling along with Q. For the latter, cooling only marginally increases with Q. A double piecewise linear regression with forced zero-intercept is performed and plotted beside the upper front observations as well as the equation of the obtained fit. The same applies for the rest of this article when relevant. All R^2-coefficients were found greater than 0.95. Roughly, 26°C is gained per additional millimetre sprinkled per hour while evaporation isn't maximized, whereas only a few tenths of a degree are gained once the surface remains wet. The intersection between these regimes, denoted Q_{opti}, is 0.78 mm/h and represents the optimal watering rate.

12.2 In-Depth Temperature

In-depth temperature variations are illustrated in Figure 12.4 for a dry trial and for the same watering rates as those shown in Figure 12.1. Overall, the thermal behaviour is similar to that at the surface, except for the magnitude of cooling which is reduced, and for a shift in maximum values relative to the end of the day phase due to thermal diffusivity. In addition, no temperature spikes are visible.

$\Delta T_{max}^{dry-wet}$ is plotted in Figure 12.5. Optimal reductions reach around 13°, 9° and 3°C respectively 6 cm, 14 cm and 25 cm deep. Similar values of the optimal watering rate are found,

although slightly greater, especially for 25 cm deep. These provide a good range of values for estimating Q_{opti}, i.e. between 0.8 and 1.0 mm/h.
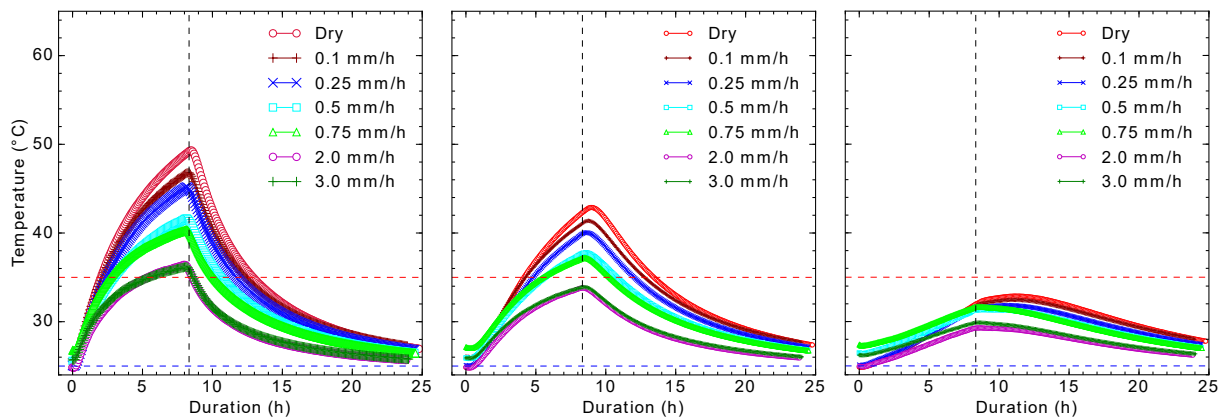
Figure 12.4: Asphalt road temperature 6 cm (left), 14 cm (center) and 25 cm (right) deep for non-watered and watered trials (i.e. 0.1, 0.25, 0.5, 0.75, 2.0 and 3.0 mm/h) (Parison et al., 2020b).
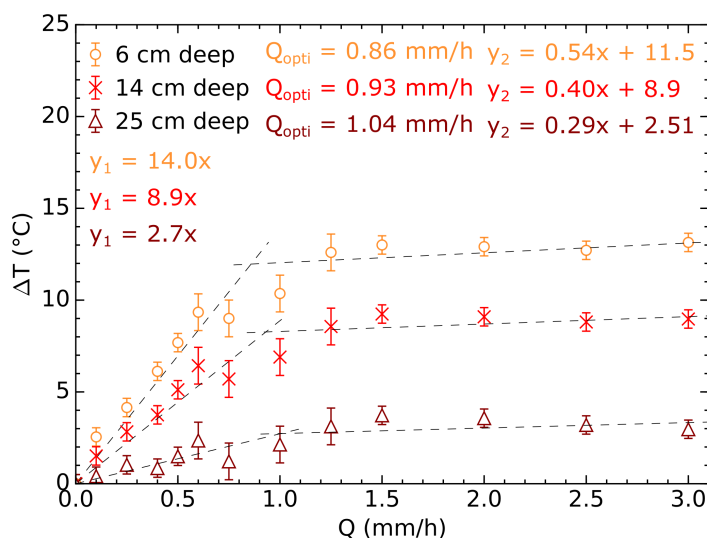
Figure 12.5: In-depth dry-wet maximum temperature difference $\Delta T_{max}^{dry-wet}$ 6 cm, 14 cm and 25 cm deep as a function of the watering rate for the asphalt road. Best double piecewise fits for both regimes and each depth are illustrated with dashed lines (Parison et al., 2020b).

12.3   In-Depth Conductive Heat Flux

Conduction heat-flows 6 cm and 14 cm deep are illustrated in Figure 12.6. At both depths, significant heat absorption (positive values) is exhibited during the day phase, while heat release (negative values) is observed at night. Unlike temperature signals 6 cm deep, watering heat flux spikes are still visible for the two lowest rates, i.e. 0.1 mm/h and 0.25 mm/h, with an ap-

proximate ten-minute delay with respect to water sprinkling. However, spikes are completely dampened for higher rates and for 14 cm deep temperature. Besides, as can be seen during the day phase, the heat flow signal slope is unchanged by watering, similarly to field observations of pavement-watering (Hendel et al., 2015a). This lends credibility to the hypothesis made that watering does not influence the heat transfer process, i.e. that ΔQ is unchanged 6 cm deep, as assumed in equation 11.10.
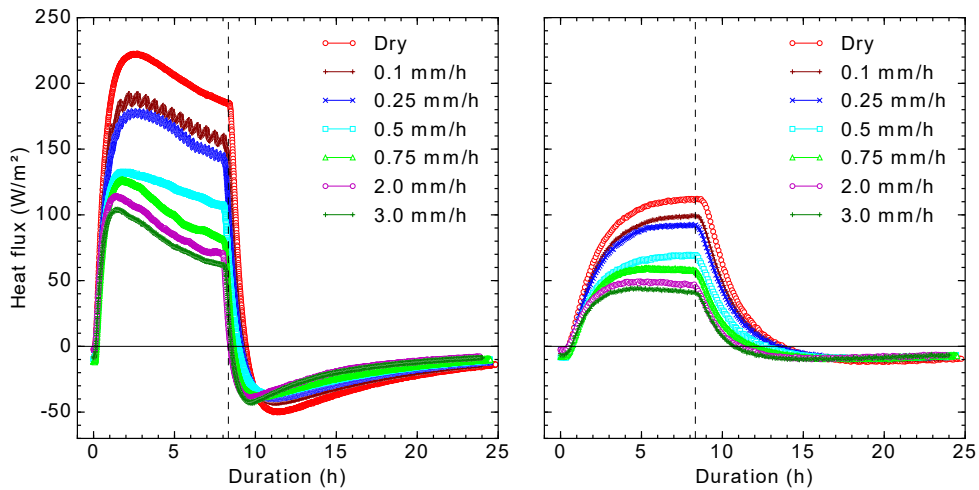
Figure 12.6: Asphalt road conduction heat flux 6 cm deep (left) and 14 cm deep (right) for dry and watered trials (i.e. 0.1, 0.25, 0.5, 0.75, 2.0 and 3.0 mm/h) (Parison et al., 2020b).
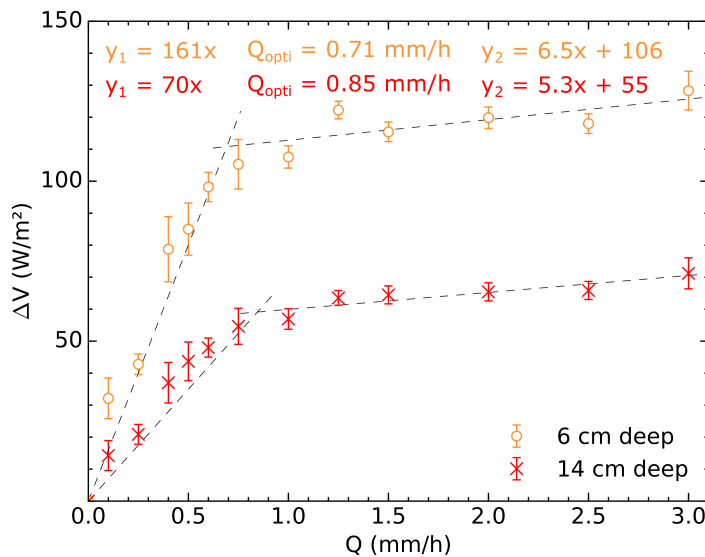
Figure 12.7: Average day-phase dry-wet difference in conduction heat flux to watering rate, for 6 and 14 cm deep asphalt road signals (Parison et al., 2020b).

Following the method of section 11.3, $\Delta V_0^{dry-wet}$ the conduction heat flux average difference between a non-watered and a watered trial at the surface, was characterized against the watering rate and is illustrated in Figure 12.7. Error bars are estimated by taking into account

the initial value of the conduction heat flow and the standard deviation of the difference between dry and watered signals on the 8h-time window used to compute the average. For 6 cm deep (close to the surface), this quantity is the same as for equation 11.11. Reductions of 120 and 65 W/m² are exhibited 6 cm and 14 cm deep respectively, for rates greater than Q_{opti}. This compares well with field observations by Hendel et al. (2015a) where reductions between 100 and 150 W/m² were observed 5 cm deep.

12.4   Atmospheric Convective Heat Flux

Following the method presented in section 11.3, we now address the assessment of the atmospheric heat flux H. It is determined for a non-watered trial using equation 11.15. It is illustrated in Figure 12.8 as a function of $T_s - T_a$, the difference between surface and air temperature.
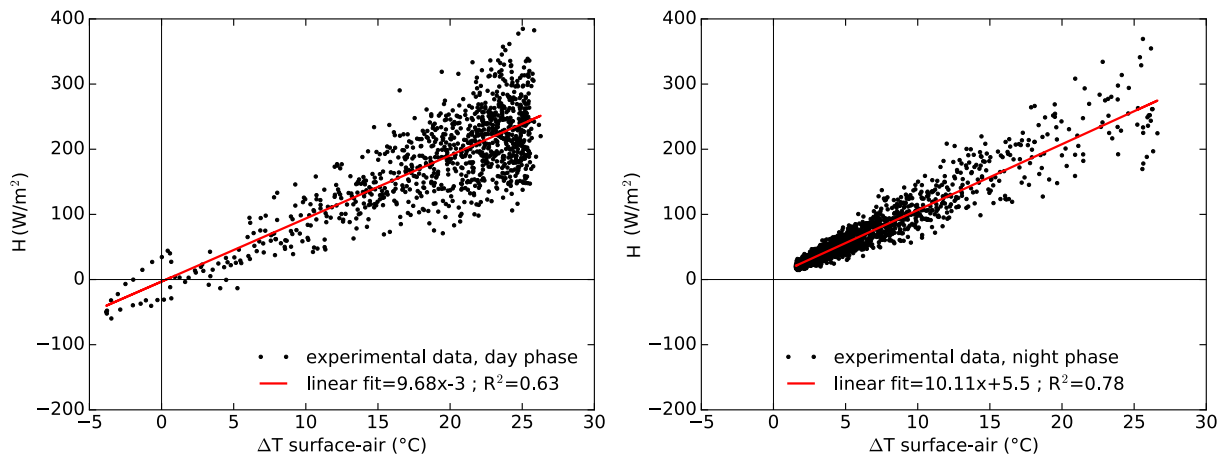
Figure 12.8: Asphalt road convective heat flux during the day phase (left) and the night phase (right) versus surface-air temperature difference, both fitted using a linear regression (Parison et al., 2020b).

A linear regression was performed on both datasets for day and night phases on the basis of equation 11.9, coefficient h being the slope of the regression. Very similar values were found for day and night phases, namely 9.7 and 10.1 W/(m².K), respectively. These values are coherent considering natural convection and are similar to what was observed in the field by Hendel et al. (2015a) for heat-wave like conditions (i.e. 3.5 vs 10 W/(m².K) here). It is noteworthy that any error in the estimated value of irradiance $S+L$ only creates an upwards or downwards shift in the data (intercept), but no change in slope. In other words, a non-zero intercept elegantly indicates inaccuracies in the measurement of incident radiation, without affecting the convective heat transfer coefficient.

12.5 Stored and Released Energy

We now look at heat storage and release in terms of energy, for both pavement conduction and convection. On the one hand, pavement surface conduction energy density, E_0, is obtained by integrating V_0, using relationship $V_0^{wet}=V_0^{dry}-\Delta V_{-6}^{dry-wet}$ for watered trials. Positive values of V_0 (day phase) indicate storage, while negative (i.e. night phase) indicate heat release. On the other hand, atmospheric convective energy density, $E_{H,atm}$, is equal to the integral of T_s-T_a times h (equation 11.7, assuming h is unchanged by watering). Since T_s-T_a is nearly always positive (except at the very beginning of the day phase when the lights are switched on and air temperature is set to 35°C), this energy is almost continually released to the atmosphere regardless of the considered phase, meaning that the material has a negative impact on thermal comfort. Both E_0 and $E_{H,atm}$ are illustrated in Figure 12.9.
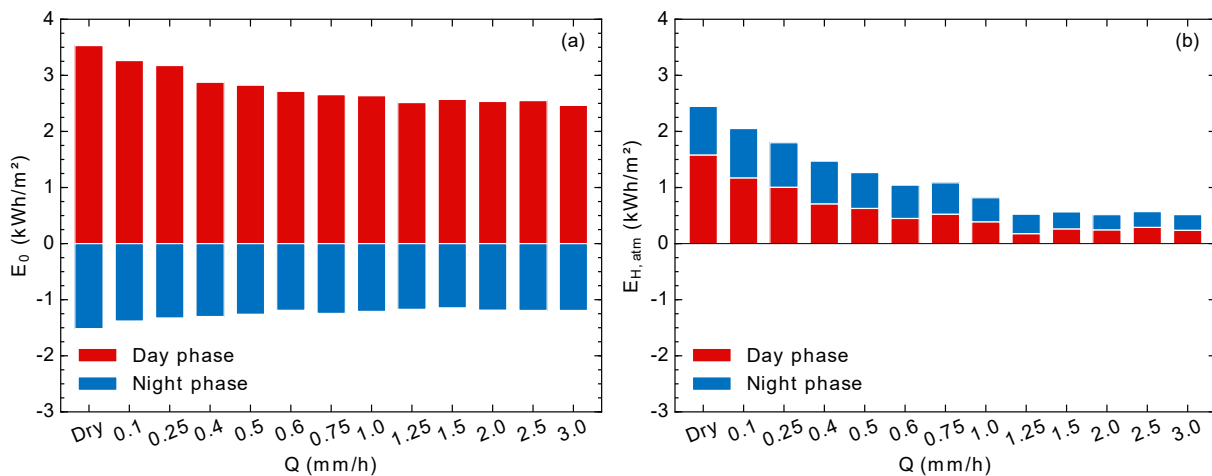
Figure 12.9: Stored (day phase) and released (night phase) pavement surface conduction energy density, E_0 (a), and released (day and night phases) atmospheric convective energy density, $E_{H,atm}$ (b), to watering rate (Parison et al., 2020b).

From Figure 12.9, it is clear that the asphalt structure stores much more conductive energy that it is able to release, even for watered trials, and even though the night phase is twice as long as the day phase. For high watering rates, a reduction of up to about 1 kWh/m² is exhibited during the day phase, and up to 0.3 kWh/m² during the night phase. Those values correspond to a 28% and 21% reduction of stored and released energy, respectively.

As seen in Figure 12.9 (b), both day and night contributions to convective heat release are significantly reduced by watering, although it is only conducted during the day phase. Also, we observe that released atmospheric convective energy is 3.2 to 23 times (dry test to highest watering rate, respectively) smaller than absorbed net radiation energy. Besides, with watering, convective exchanges are reduced up to $70-85\%$ during day phase and up to $40-68\%$ during night phase compared to a dry test. Thus, pavement-watering has a much stronger impact on the atmospheric convective exchanges that it has on conductive storage.

12.6   Evaporative Cooling Flux

We now consider total pavement cooling flux Φ, calculated from equation 11.4. Having determined h and assuming that it is constant during the day regardless of the watering rate, $\Delta H^{dry-wet}$ is obtained immediately using equation 11.9. $\Delta V_0^{dry-wet}$ has already been calculated using equation 11.11 and was plotted in Figure 12.7 for 6 cm deep signals. $\Delta R_n^{dry-wet}$ is obtained with equation 11.6. In wet conditions, the emissivity of the surface, ϵ_w, is that of water, equal to 0.98. Dry emissivity, ϵ_{dry}, and albedo difference $\Delta\alpha$ in both conditions were measured experimentally (section 11.2). All three contributions and Φ are illustrated in Figure 12.10 at the end of day phase. Error bars were estimated by propagating the sources of error on the calculation of Φ from equation 11.4. Results of the piecewise regression are also indicated in Figure 12.10 (b).
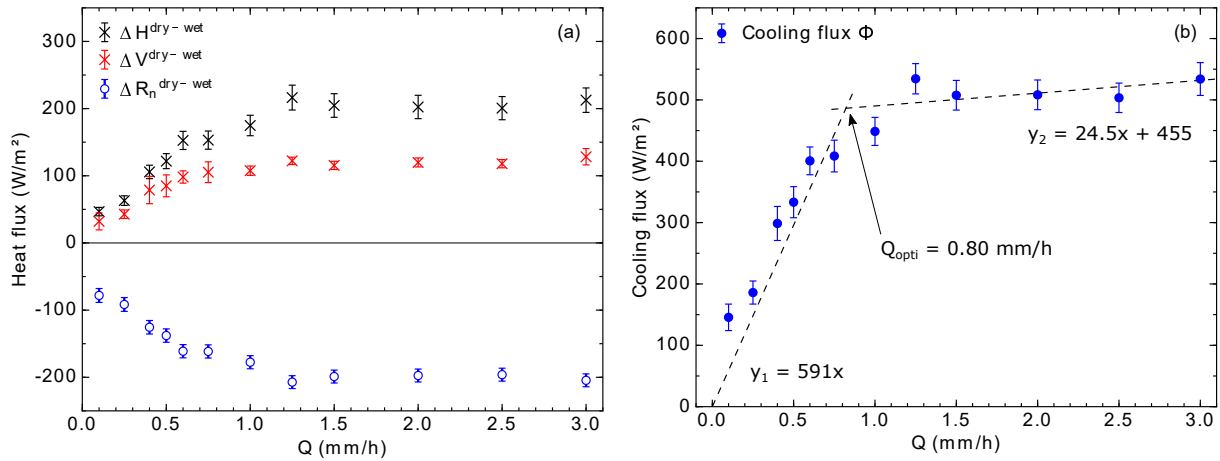
Figure 12.10: Dry-wet differences in net radiation $\Delta R_n^{dry-wet}$, in absorbed surface heat flux $\Delta V_0^{dry-wet}$ and in atmospheric convective heat flux $\Delta H^{dry-wet}$ (a), and total pavement cooling flux Φ (b) to watering rate Q at the end of day phase. A double linear piecewise regression with zero-intercept is used on Φ (b) (dashed lines) (Parison et al., 2020b).

In Figure 12.10 (a), $\Delta R_n^{dry-wet}$ strongly decreases with Q, i.e. net radiation increases as a result of watering. On the contrary, pavement conduction and convective exchanges are both reduced by watering, as seen by the increase of $\Delta V_0^{dry-wet}$ and $\Delta H^{dry-wet}$. Indeed, for a given watering rate, pavement cooling is partitioned into a reduction of atmospheric convective exchanges (40% of Φ) and of pavement conduction (20%) and an increase in net radiation (40%). Given the negative impact of pavement convective exchanges and upward radiation on pedestrians during the day, it is interesting to find that these terms are the most impacted by watering. The significant reduction of pavement conduction is also noteworthy since it mostly affects heat release during the night, thus limiting the night time heat release and therefore the pavement's contribution to UHI.

In Figure 12.10 (b), compared with Figure 12.3, the overall shape of Φ is comparable and a similar value for Q_{opti} is found. Pavement cooling ranges from 150 to 550 W/m² during these trials, reaching nearly 500 W/m² for Q_{opti}. It should be noted that for small rates, since the

surface does not remain wet throughout the experiment, Φ corresponds to an average value. In reality, it oscillates between a maximum and a zero value.

We finally take interest in determining the maximum evaporation rate under our experimental conditions. First, sensible and latent contributions of the cooling flux were assessed using equation 11.3. The sensible part is given by $\Phi_{sens} = c_w \rho_w Q \, (T_s^{wet}\text{-}T_w)$. Each term of the latter equation is known and the maximum surface temperature at the end of day phase is taken for T_s^{wet}. The latent flux, $\Phi_{lat} = lE$, is then obtained by subtracting the sensible flux Φ_{sens} from the total cooling flux Φ. Both Φ_{sens} and Φ_{lat} are presented in Figure 12.11.
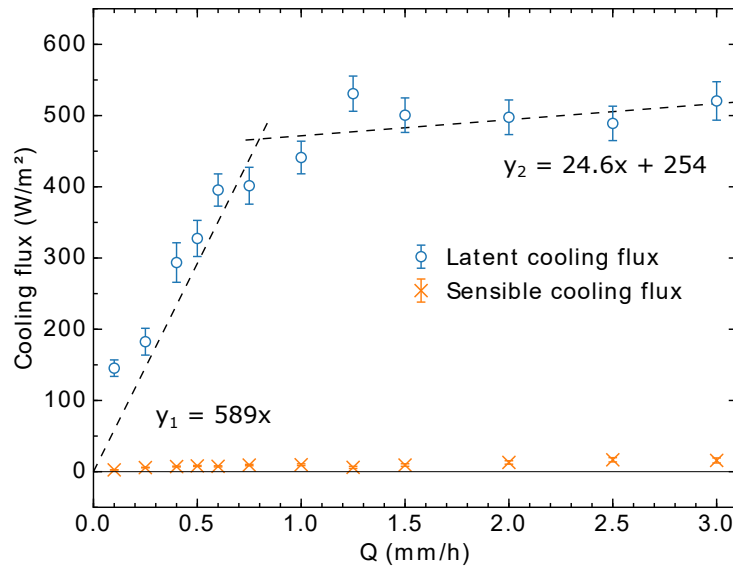
Figure 12.11: Latent and sensible cooling flux, lE and Φ_{sens} respectively, to watering rate (Parison et al., 2020b).

As expected, the sensible cooling flux only represents a few tens of W/m², whereas the latent flux reaches up to 500 W/m². In other words, more than 95% of total cooling is exclusively due to the evaporation of the water film. Finally, the evaporation rate E determined with this method is confronted with that obtained from the mass convection transport problem (MCTP) (see section 2.2 in chapter 2). Derived from Pagliarini and Rainieri (2011), the evaporation rate for a flat surface can be estimated from the latent cooling flux as follows:

$$lE = 0.622 \frac{lh}{c_a p_0} T_s \left(\frac{p_s}{T_s} - \frac{p_v}{T_a} \right) \tag{12.1}$$

with h the convective exchange coefficient calculated in section 12.4, c_a the specific heat of air (1.005 kJ.kg^{-1}.K^{-1}), p_0, p_s and p_v respectively total air pressure, saturation vapour pressure at temperature T_s and partial vapor pressure at T_a, equal to 35°C whether wet or dry in our case. Equation 12.1 assumes that the surface temperature is equal to that of water. Results are illustrated in Figure 12.12. It is noteworthy the mass convection transport problem of equation 12.1 is not valid for small watering rates during which evaporation is not continuous. For this reason, concerned data points were marked grey and labelled as "invalid" on Figure 12.12.
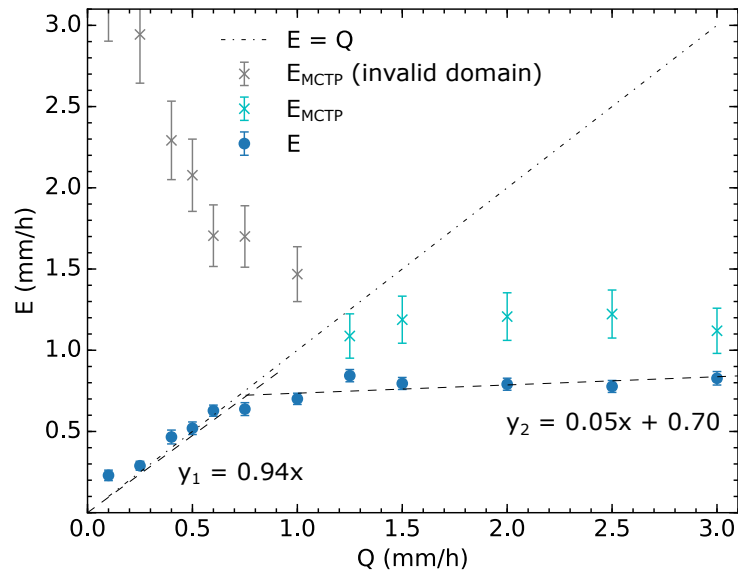
Figure 12.12: Evaporation rate of the water-film sprinkled during the day phase as a function of the watering rate (Parison et al., 2020b).

As can be seen, E is approximately equal to the watering rate, i.e. all sprinkled water is evaporated, until Q_{opti}. For higher watering rates, additional water does not evaporate, i.e. the maximum evaporation rate has been reached. This value is consistent with previous estimates of Q_{opti} obtained from surface temperatures and the total cooling flux Φ (around 0.8 mm/h). On the other hand, E_{MCTP} reaches a maximum value of 1.15 mm/h from about 0.75 mm/h i.e. once the surface remains wet, although E is not calculated from the watering rate values. This value is close to the one found with the other method, although slightly greater. It is however similar to the values found using in-depth temperature in section 12.2. No overlap is found between the error bars, which could indicate either an underestimation of the uncertainties, more likely for p_v which outweigh the other terms, and/or to a lesser extend h, p_s, or inaccuracies in the estimation of one of these term. Indeed, relative humidity strongly oscillates inside the chamber, which impacts the value of p_v significantly. Ultimately, the maximum evaporable quantity of water using this method was found, which is useful to know how much water should be sprinkled on the surface.

Discussion of Part III

We now compare results from this experimental set-up with field observations obtained in Paris since 2013 under similar weather conditions (Hendel et al., 2015a, 2014), summarized in Table 13.1 (values may not add up due to rounding errors). These field observations were gathered on the test site presented in Part II, and used to validate lab tests.

The structures studied in the field and in the lab are similar in composition though not identical. In the field, the sensor was placed after road construction, requiring excavation and filling. This required replacing the hot-mix asphalt surface course with cold-mix asphalt. In addition, upon excavation works, it was found that the mid-course at the location of the sensor was a 34-cm-thick concrete layer. This was later explained by the presence of a district-heating main. Other areas located nearby, not above the heat district main, had a normal, asphalt concrete mid-course. These differences were found to be responsible for an increase of surface temperature of up to 2°C at night with similar thermal behaviour (Hendel et al., 2014). Regarding the surface finish, it is expected that the field material should be "smoother" as a result of aging due to traffic, although this should only affect the water retention capacity of the surface, which doesn't impact lab results. All else being equal, these differences are likely to induce additional errors in the transposition of lab results to the field.

Compared to the field experiment, an approximate factor of two is observed for almost every parameter in the lab, except for the watering sensible cooling flux Φ_{sens} which is comparable. This is because only 5% of cooling is due to Φ_{sens} in our case vs 20% in the field. This can be at least partially explained because water sprinkled in our case is initially hotter (35°C against $20° - 25°C$) and the harsher conditions resulting in a higher maximum evaporation rate, all else being equal.

Table 13.1: Confrontation of lab and field observations for optimal watering rates found in both cases (Parison et al., 2020b).

Quantity of interest	Unit	Hendel et al. (2015a)	Lab experiment
Total daytime absorbed radiation (dry conditions), $\int^{day} R_n \, dt$	kWh/m²	$2.5 - 3.3$	5.1
Surface and air temperature difference (dry conditions), $T_s - T_a$	°C	$10 - 15$	25
Optimal evaporation rate	mm/h	$0.31 - 0.41$	$0.78 - 0.81$
Pavement-watering sensible cooling, Φ_{sens}	W/m²	$4 - 7$	$5 - 10$
Pavement-watering latent cooling, lE	W/m²	$198 - 256$	$470 - 500$
Proportion of cooling due to evaporation	%	$80 - 85$	95
Maximum surface temperature reduction, ΔT_{max}	°C	13 (average from 3 pm to 6:30 pm)	$20 - 21$
Sprinkled water temperature	°C	$20 - 25$	35
Convective heat transfer coefficient, h	W.m^{-2}.K^{-1}	3.5	10
Reduction in atmospheric convection, $\Delta H^{dry-wet}$	W/m²	40	$180 - 200$
Reduction in pavement conduction, $\Delta V_0^{dry-wet}$	W/m²	$70 - 130$ (-5 cm)	110 (-6 cm)
Black body emitted radiation increase, $\sigma \, (\epsilon_{wet} \, T_s^{wet \, 4} - \epsilon_{dry} \, T_s^{dry \, 4})$	W/m²	85	160
Reflected infrared radiation reduction, $(\epsilon_{dry} - \epsilon_{wet})L$	W/m²	assumed negligible	5
Reflected visible radiation increase, $(\alpha_{wet} - \alpha_{dry})S$	W/m²	assumed negligible	30
Increase in net radiation, $\Delta R_n^{dry-wet}$	W/m²	85	$180 - 190$

Surface temperature reductions are greater in the lab, which is consistent with the higher dry surface temperatures (respectively 62°C vs 50° − 55°C). This holds true for the latent cooling flux as well which is approximately twice as high as in the field. This can be understood when having a look at each term contributing to total cooling flux Φ detailed in equation 11.4, i.e. $\Delta H^{dry-wet}$, $\Delta V_0^{dry-wet}$ and $\Delta R_n^{dry-wet}$.

First, the reduction in convective exchange $\Delta H^{dry-wet}$ happens to be about 4 to 5 times greater than in the field. This is attributed to both a higher surface temperature reduction, i.e. approximately twice as much, and also to the higher convective heat transfer coefficient h, three times greater than in the field (3.5 vs 10 W.m^{-2}.K^{-1}), associated with the circulation conditions inside the climate chamber though satisfactory with heat-wave conditions (typically v <10 km/h). Indeed, h is strongly influenced by wind speed. Inside the chamber, air circulation creates a light breeze at the sample surface, *de facto* taken into account in the calculation of h (10 W.m^{-2}.K^{-1}). Similarly, h was calculated from field measurements (Hendel et al., 2015a).

On the other hand, the reduction in pavement conduction $\Delta V_0^{dry-wet}$ is similar despite the difference in measurement depth (5 cm deep in the field vs 6 cm deep here). In both cases, the pavement heat flux 6cm deep V_{-6} is halved by watering.

Also, the increase in black body radiation is also found to be two times greater than in the field, mostly because the surface temperature reduction is significantly greater in the lab than in the field. Finally, the changes in reflected SW and LW radiation were both neglected in Hendel et al. (2015a). This results in an additional 33 W/m² in the total net radiation increase, $\Delta R_n^{dry-wet}$, which is doubled in total.

These differences between lab and field observations can be explained by the stronger radiation inside the climate chamber. Although R_n is quite similar in terms of average value, i.e. approximately 650 W/m², artificial insolation in the lab is constant and lasts twice as long resulting in twice the amount of daily absorbed radiation. Also, air temperature is set to 35°C and relative humidity 35% during the day, while weather conditions for in-field campaigns are variable. Nonetheless, checking the difference between surface and air temperatures in dry conditions, also much greater in the lab than in the field (25° vs 10° − 15°C), confirms that the air temperature is not the main parameter influencing our results rather than the daily absorbed radiation, for instance. These conditions imply that the laboratory experiment approaches steady-state conditions at the surface at the end of the day phase, which is not the case in the field.

Surface cooling effects are partitioned into a reduction of convective exchanges (40% of surface cooling), of pavement conduction (20%) and an increase in net radiation (40%). All three of these components have positive implications for pedestrian thermal stress and the UHI phenomenon. Indeed, pavement energy storage (day) is reduced by 28% which in turn reduces heat release (night) by 21%, an important parameter in the formation of UHI. Furthermore, released atmospheric convection is reduced up to 70% during the day phase and up to 50% during the night phase compared to a non-watered test, even though watering was only performed during the day. This contributes to lower air temperatures in the immediate vicinity of the watered pavement. Finally, the increase in net radiation by 30% is also positive for pedes-

trians since it tends to alleviate their radiative budget by reducing the contribution from the pavement.

In the aim of transposing lab results to the field, it would seem that total daily absorbed radiation is an appropriate normalizing factor. Indeed, the comparison of lab and field results illustrates that all surface heat budget terms are more or less doubled, as per daily absorbed radiation. This parameter includes information on the past conditions underwent by the pavement in both the lab and the field, thus taking account of the non-steady state thermal conditions. This provides a first approach for transposing lab results to the field, whether for asphalt or other materials, in particular with respect to their implications in terms of an appropriate pavement-watering strategy. Further testing in the field and lab is necessary to confirm this.

Conclusion of Part III

A laboratory experiment was used to optimize the cooling effects and water consumption of pavement watering on a Parisian asphalt road structure that underwent a 24-hour climatic cycle of heat-wave-like conditions for several watering rates. Significant surface temperature reductions were exhibited, ranging from 5° to 22°C respectively for watering rates from 0.1 to 3.0 mm/h, while reductions of pavement conduction ranged from 30 to 120 W/m² and from 150 to 550 W/m² for total pavement cooling. These results suggest that this lab experiment faithfully reproduces the effects of pavement-watering when accounting for the difference in daytime net radiation.

Two distinct pavement-watering cooling regimes are observed: latent and sensible. In the latent phase, evaporation increases one-to-one with watering; in the sensible regime, only a limited increase in cooling is obtained from additional watering. The intersection of these two regimes corresponds to the point for which cooling effects are maximised while the water consumption is minimised and can thus be used to determine the optimal watering rate; this value is equal to the maximum evaporation rate under the prevailing conditions. With this approach, an optimal watering rate of approximately 0.8 mm/h was obtained from all indicators, thus building up a body of evidence converging towards this value. Accounting for the difference in daytime net radiation, good agreement was found with previous field results.

For a 0.8 mm/h watering rate, temperatures were significantly reduced (respectively by about 20°, 10°, 7° and 2°C for surface and 6, 14 and 25 cm deep). Pavement heat flux is reduced by about 110 W/m². Evaporative cooling flux was calculated and found to be up to 400 W/m² for the latent part and 20 W/m² for the sensible part, both for 0.8 mm/h. This cooling effect is partitioned into a reduction of atmospheric convective exchanges (40% of surface cooling), of pavement conduction (20%) and an increase in net downward radiation (40%), each of which contribute to improving the urban environment.

In case of the implementation of an outdoor watering campaign, the optimal watering rate could be estimated by normalizing lab results by net daytime radiation. However, field experimentation also poses other strong technical and operational constraints that draw the limits of this approach. For instance, because of road curvature and other factors not reproduced in the

lab including runoff, the retention capacity of the pavement should be considered in order to sprinkle no more than the amount of water a surface is able to hold, i.e. about its surface roughness. This will be further discussed in Chapter 20. In any case, the validity of these hypotheses will need to be confronted to future *in situ* watering campaigns.

Having fully investigated the effects of watering a traditional asphalt road structure in the lab, we now turn to the study of other Parisian paving structures sampled among the diversity of both traditional and innovative urban street materials.

PART IV

HEAT BUDGETS OF STANDARD, COOL AND
WATERED PAVEMENTS

Introduction to Part IV

In the literature, although a considerable number of studies address the study of traditional or cool pavements (Qin, 2015), with some of them providing detailed surface heat budgets (Qin and Hiller, 2014; Takebayashi and Moriyama, 2012; Anandakumar, 1999; Camuffo and Bernardi, 1982). As discussed in Part I, the scientific literature suggests this topic should be further examined, especially regarding cool pavements' energy partition and their comparison to traditional ones (Qin, 2015). Indeed, few studies present the partition of net radiation into convective, latent and conductive flux for traditional urban materials (Anandakumar, 1999; Asaeda et al., 1996; Qin and Hiller, 2014). Besides, the literature globally lacks comparisons under fixed weather conditions between pavement types and studies, namely due to the variability of outdoor conditions, study locations and test protocols. One way of tackling this limitation is to use a lab approach, such as the one proposed in Part III, or an *in situ* observation site with various paving structures exposed to the same weather conditions (Takebayashi and Moriyama, 2012; Li et al., 2013c; Asaeda et al., 1996).

As previously stated, several lab studies focusing on the behaviour of pavements with heat-up and cool-down phases can be found (Wu et al., 2018; Chen et al., 2009), some of which include pavement-watering or grass (Ueno and Tamaoki, 2009; Shin et al., 2019), but to the best of our knowledge these tend to focus on traditional asphalt or Portland-cement concrete pavements. Besides, studies rarely take into account the underlying layers composing realistic pavements and often use only a limited number of indicators (i.e. principally temperature), thus setting aside pavement heat budgets, with certain exceptions (Takebayashi and Moriyama, 2012; Qin and Hiller, 2014; Li et al., 2013a). Finally, we are unaware of any studies attempting to fine-tune pavement-watering for different pavement structures.

In Part III, these aspects were addressed by proposing a lab experiment reproducing heat-wave like conditions, including a day phase with artificial insolation and a night phase, with or without fine-tuning of surface watering. Based on a proper heat transfer analysis, the watering rate and efficiency of pavement-watering was optimized for an asphalt road structure. This Part exposed the methodology, applied it to a traditional paving structure and results were compared and validated against similar optimized field tests presented in Part II. In essence, relatively good agreement is found between the lab and the field taking into account that the

daily absorbed energy by the pavement is doubled.

Building on the previous experimental protocol, we now apply the methodology and specific indicators indicators to other traditional or cool pavements in Part IV. The thermo-climatic behaviour, with and without pavement-watering, will be presented for a range of Parisian pavement structures including both conventional (asphalt road and sidewalk, granite sidewalk, cobblestones etc.) and "innovative" structures, which fall under the category of cool pavements (permeable structures, slag concrete, reflective pavements etc.). The study of a wide range of road materials under identical weather conditions thus allows for direct comparisons between structures.

Similarly to Part III, study goals include the analysis and comparison of the behaviour of non-watered Parisian pavements and the optimization of their surface watering via the maximization of the cooling flux jointly with the minimization of the watering rate on the other hand. First, Chapter 16 presents the methodology for this Part. Chapter 17 focuses on the dry behaviour of the structures, while the relevant parameters (albedo, absorptivity, etc.) that condition the optimal watering rate and the efficiency of the method are identified for the paving structures in Chapter 18. Lastly, in Chapter 19, the surface heat budget and energy partition at the pavements' surface is determined and detailed. The partitioning of both net radiation and irradiance is considered in order to include the effects of modification of radiative properties (albedo and emissivity) on urban cooling. Through the calculation of the surface heat budget under steady-state conditions, energy partitioning into heat conduction, atmospheric convection and visible/infrared radiosity is thus characterized and detailed for each pavement as a function of a radiation absorptivity index, for dry as well as optimally-watered pavements.

This Part is based on work published in the peer-reviewed journal *Energy and Buldings* (Parison et al., 2020c).

Methodology

16.1 Studied Pavement Structures

The experimental set-up and the characteristics of the climate cycles were presented in Section 11.1, Chapter 11. For this Part, a wide range of tests were conducted in the lab on a total of twelve different pavement structures. Each sample is 32 cm tall and 16 cm in diameter. Half of them are standard pavement structures commonly found in the Parisian urban fabric: asphalt road, asphalt sidewalk, granite sidewalk, stabilized sand, cobblestones and grass. The other half are alternative "innovative" solutions to existing structures: two different reflective paints applied on the traditional asphalt sidewalk, two formulations of pervious Portland-cement concretes (PPCC) sidewalks, a slag concrete sidewalk and a pervious asphalt surface course. An illustration of the different structures' detailed composition is provided in Figure 16.1.
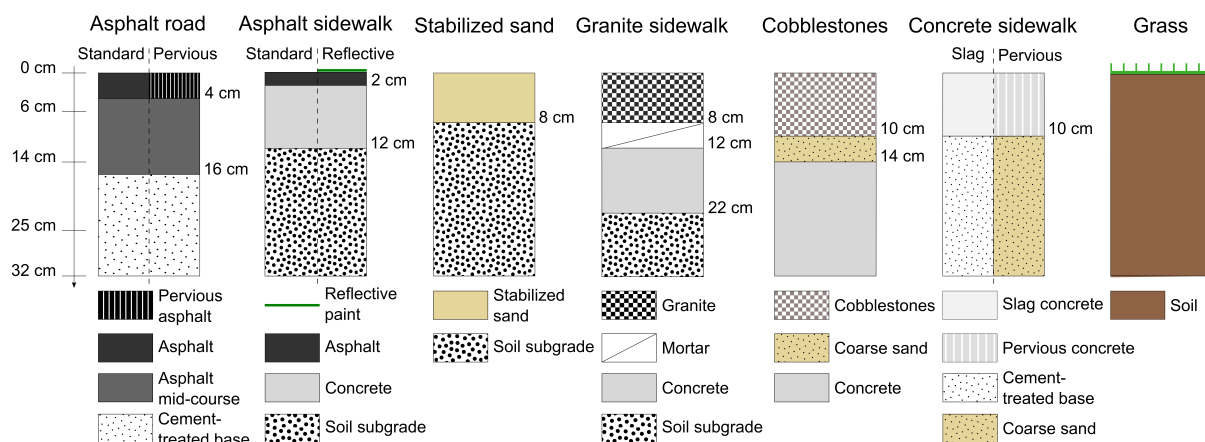
Figure 16.1: Pavement structures studied in the lab (Parison et al., 2020c).

Each structure is designed to the specifications of the Paris City Hall except for the two 10 cm-thick PPCC sidewalks which were laid on top of loose sand. All the pervious samples studied, i.e. PPCC 1 and 2 as well as the pervious asphalt, have a porosity of about 15%. In addition, the second PPCC sample incorporates about 20% of expanded clay pebbles in order to

improve its water retention ability. Slag concrete incorporates a large proportion of slag cement substituting about 80% of Portland cement, making it more reflective and thermally insulating than traditional Portland-cement concrete. The first reflective paint applied on the asphalt sidewalk is a thermochromic paint which is dark-green at ambient temperature and becomes more reflective in the visible band as it whitens above its transition temperature of 29°C. The second is a near-infrared (NIR) reflective paint, a "cool black". Unlike other structures, paints are a relatively cheap and easy-to-implement option, provided their durability is known (Xie et al., 2019). Both paints were mixed with an acrylic binder. A photograph of some samples surfaces is provided in Figure 16.2.
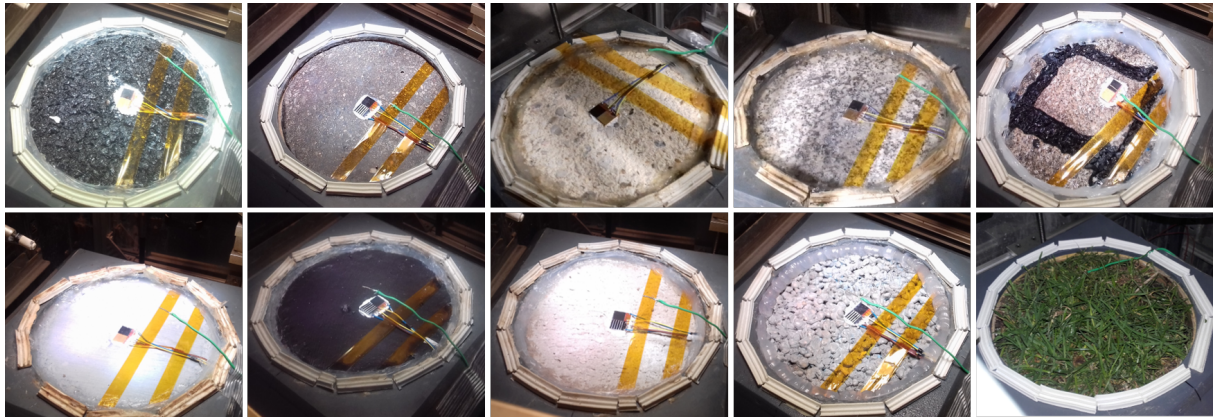
Figure 16.2: Photograph of some of the tested samples. From left to right and top to bottom: asphalt road, asphalt sidewalk, stabilized sand, granite sidewalk, cobblestones, thermochromic paint (>29°C), NIR reflective paint, slag concrete, PPCC sidewalk 1 and grass (Parison et al., 2020c).

Table 16.1: In-depth position of the thermal sensors for each structure (Parison et al., 2020c).

Pavement structure	Instrumentation	
	Thermoflowmeter	Type-T thermocouple
Asphalt road	6/14 cm	25 cm
Pervious asphalt road	6/14 cm	25 cm
Asphalt sidewalk	6 cm	14/25 cm
Stabilized sand	6 cm	14/25 cm
Granite sidewalk	6/14 cm	25 cm
Cobblestones	11 cm	14/25 cm
Slag concrete sidewalk	6/14 cm	25 cm
PPCC sidewalks	10/14 cm	25 cm

At the surface, all structures were equipped with a radiative and a black-painted thermoflowmeter, measuring both heat-flux as well as temperature. Other sensors were placed 6 cm, 14 cm and 25 cm deep, their nature depending on the samples' composition. Specific subsurface instrumentation is listed in Table 16.1. The grass sample was only equipped with thermocouples. Typical uncertainty of the type-T thermocouples is 0.5°C.

16.2 Albedo and Emissivity

The spectral reflectance of each sample surface was measured following the ASTM E903 (2012) standard with a UV-Vis-NIR Cary 5000 spectrophotometer and 150 mm integrating sphere. To obtain a result representative of the entire surface for heterogeneous structures, a minimum of five measurements were made at different positions. In each case, the relative measurement uncertainty is between 1% and 5% depending on the sample. Figure 16.3 illustrates the resulting averaged spectral reflectivity of the dry pavement structures. In addition to dry surfaces, the spectral reflectance of the moist samples was also measured following ASTM E903. For this procedure, the samples were completely soaked with water prior to conducting the standard measurement. For the thermochromic asphalt, two sets of measurements were performed independently: one at ambient temperature (<29°C), and another preheating the sample inside a climate chamber set to 50°C in order for the paint to turn reflective (>29°C).
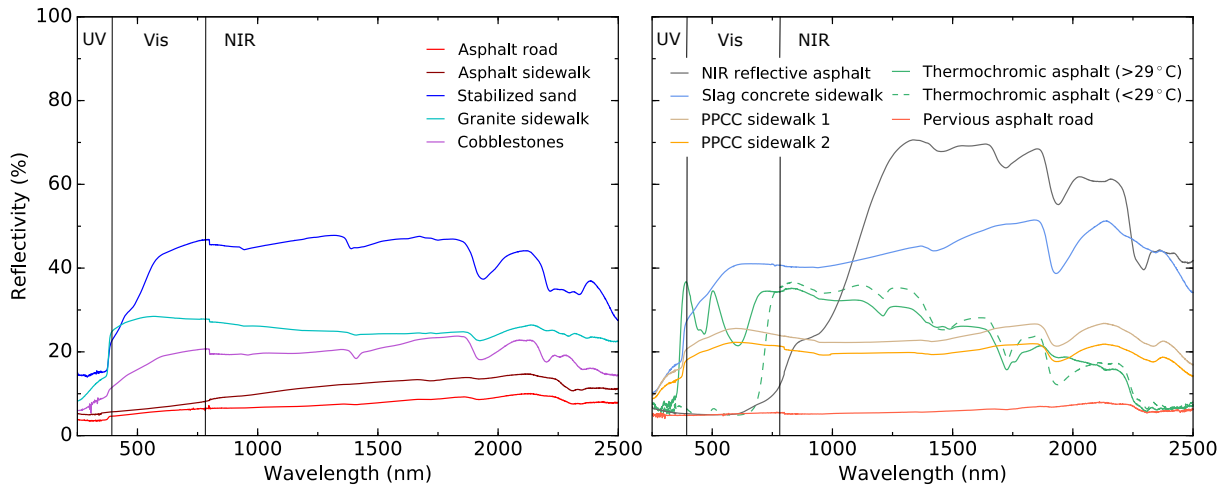
Figure 16.3: Spectral reflectance averaged over several trials for each dry pavement structure (Parison et al., 2020c).

Spectral reflectance was weighted using the irradiance spectrum of the halogen lamps to determine the effective albedo of the samples under the experimental conditions (see Figure 11.3 in Section 11.1). Surface emissivity was also measured using the reference black body method with a FLIR B400 infrared (IR) camera with a spectral band of $7.5 - 13$ μm using black tape with a known emissivity of 0.95. The albedo of each structure, both dry and wet, as well as emissivity values, are summarized in Table 16.2. For comparison, solar AM 1.5 albedo is also provided. Albedo with both spectra differ for surfaces for which a significant difference of reflectivity is observed between the visible and near-infrared bands. Of interest, the albedo of the NIR reflective paint marginally increases when wet.

Table 16.2: Albedo and emissivity of the studied paving structures (Parison et al., 2020c).

Structure surface	Albedo Halogen spectrum		Albedo AM 1.5 spectrum		Emissivity
	dry	wet	dry	wet	dry
Asphalt road	0.076	0.057	0.070	0.055	0.99
Asphalt sidewalk	0.094	0.058	0.081	0.050	0.98
Stabilized sand	0.438	0.387	0.396	0.323	0.92
Granite sidewalk	0.264	0.221	0.260	0.222	0.99
Cobblestones	0.192	0.144	0.178	0.132	0.99
Thermochromic asphalt (>29°C)	0.308	0.266	0.292	0.258	0.97
NIR reflective asphalt	0.303	0.310	0.193	0.201	0.95
Slag concrete sidewalk	0.409	0.308	0.380	0.281	0.98
PPCC sidewalk 1 (w/o clay)	0.233	0.130	0.232	0.124	0.97
PPCC sidewalk 2 (w/ clay)	0.203	0.111	0.202	0.104	0.97
Pervious asphalt road	0.063	0.048	0.054	0.040	0.98

16.3   Thermal Conductivity

The apparent thermal conductivity of the upper layers was determined using Fourier's law under semi steady-state conditions reached at the end of the day phase. Obtained values are summarized in Table 16.3. The conductivity λ_i of the layer i between depths z_i and z_{i-1} is thus obtained using corresponding depths temperature T_z and heat-flux measurements as follows, as described by Hendel et al. (2018):

$$V_{z_i} = V_{z_{i-1}} = \frac{\lambda_i}{z_{i-1} - z_i}(T_{z_{i-1}} - T_{z_i})\qquad(16.1)$$

Table 16.3: Apparent thermal conductivity λ of pavement structures' upper layers (Parison et al., 2020c).

Pavement structure	Layer's apparent conductivity (W.m^{-1}.K^{-1})	
	0 - 6 cm	0 - 14 cm
Asphalt road	0.88	2.03
Asphalt sidewalk	0.69	1.52
Stabilized sand	0.35	0.64
Granite sidewalk	1.16	1.49
Cobblestones	0.85 (0 - 11 cm)	0.35 (0 - 14 cm)
Slag concrete sidewalk	0.28	0.45
PPCC sidewalks	0.73 (0 - 10 cm)	0.35 (10 - 14 cm)
Pervious asphalt road	0.86	2.03

Of interest, thermal conductivity, density and specific heat of each material was properly characterized using a radiation-based technique suited to urban construction materials, available in Appendix A (Parison et al., 2019a). However, the samples used for this step were sourced from a different batch, as the technique required sawing at a thin slab thickness. Therefore, these values cannot be used for the sample structures employed here.

16.4 Watering Optimization Goals

As for Part III, goals chosen for this Part are to maximize the cooling flux Φ while minimizing the watering rate Q, i.e. maximizing the ratio of pavement cooling to watering rate, Φ/Q. Additionally, in the following analyses, we propose to compare the optimization performed on the basis of double piecewise linear regressions of experimental results, as done in Chapter 12, with a more theoretical approach for the optimization. In order to do so, we consider the two components of the total cooling flux, latent and sensible, as expressed in equation 11.3 and reminded below:

$$
\begin{aligned}
\Phi &= \Phi_{lat} + \Phi_{sens} \\
&= lE + c_w \rho_w Q(T_s^{wet} - T_w)
\end{aligned}
\tag{16.2}
$$

According to equation 16.2, the total cooling flux Φ versus Q is expected to be linear with two regimes, so-called "latent" and "sensible". During the latent regime, all the sprinkled water evaporates, with watering cycles separated by periods when the surface is dry. In the sensible regime, evaporation is maximized for a given structure and the only gain from additional watering comes from the sensible cooling. The latent and sensible regimes, respectively $\Phi_{reg,lat}$ and $\Phi_{reg,sens}$, are expressed by the two following equations:

$$
\begin{cases}
\Phi_{reg,lat} = lQ + c_w \rho_w Q(T_s^{wet} - T_w) & \text{while } Q \leq E^{max} \\
\Phi_{reg,sens} = lE^{max} + c_w \rho_w Q(T_s^{wet} - T_w) & \text{once } Q \geq E^{max}
\end{cases}
\tag{16.3}
$$

The intersection of these regimes renders the maximum ratio for Φ/Q. In principle, regardless of the material, in the first regime all the water evaporates (i.e. $E=Q$). Thus, plotting Φ versus Q, the expected slope for this regime is the latent heat of vaporization of water l (2,260 kJ/kg), i.e. the cooling flux created by evaporating 1 mm of water per hour (630 W/m² per mm/h). Therefore, the optimal watering rate can theoretically be obtained by intersecting the latent regime's 630 W/m²/(mm/h) slope with a zero-slope segment whose intercept is the maximum cooling flux reached during the sensible regime for a high watering rate ($Q>>E^{max}$). This approximation, however, requires neglecting sensible cooling in both regimes, (hence $\Phi_{reg,lat} = lQ$ and $\Phi_{reg,sens} = lE^{max}$), as illustrated in Figure 16.4. In practice, this can be achieved by performing only one highly watered 24-h test to estimate the cooling flux of the sensible regime.

We now present the experimental results. Chapter 17 presents the dry behaviour of the pavements during the entire 24-h trial.
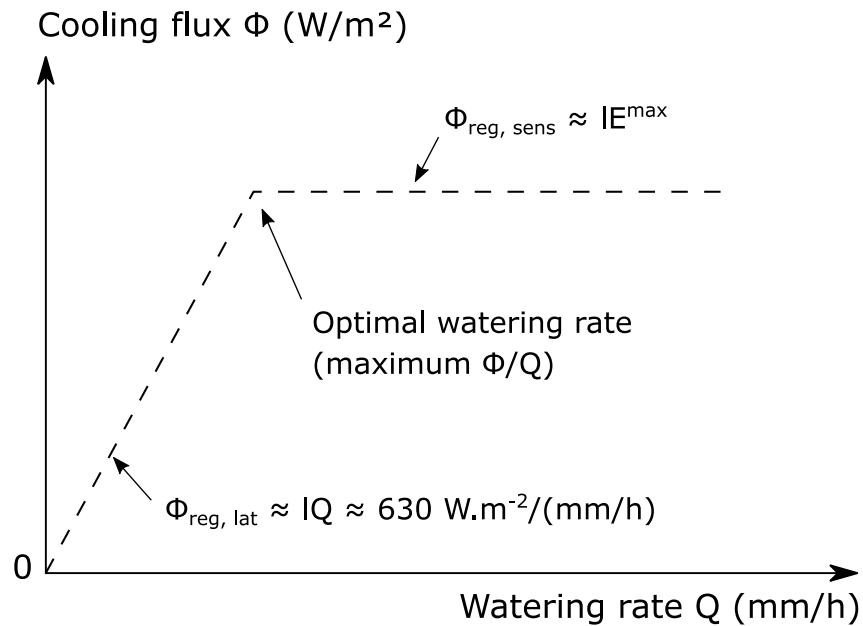
Figure 16.4: Schematic representation of the so-called latent and sensible cooling regimes when neglecting sensible cooling for each regime (Parison et al., 2020c).

Chapter 18 focuses on the maximization of Φ/Q in steady-state, i.e. determining the corresponding optimal watering rates and cooling flux for all the pavements, following the methodology described in Section 11.3. A wide range of watering rates were implemented to visualize both cooling regimes. Results from this optimization are then compared with the theoretical approach described in the above paragraph (Figure 16.4).

Lastly, having completed this optimization, Chapter 19 presents the steady-state thermal analysis and comparison of the dry and optimally-watered pavements. Energy partitioning, detailed heat-budgets and in-depth heat transmission are examined. In the end, the set-up is used to identify key parameters influencing the optimization of watering.

Pavement Dry Behaviour

17.1 Surface Temperature

We start by briefly presenting the non-watered temperatures of the structures. Surface behaviour of the sample is illustrated in Figure 17.1. Typical uncertainty on all presented temperature signals is about 0.5°C.
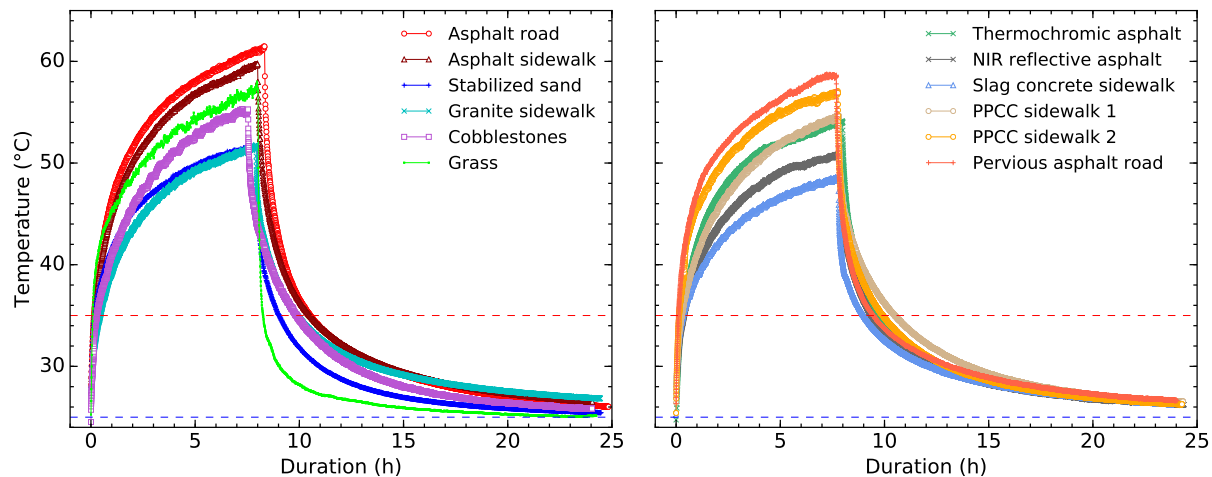
Figure 17.1: Surface temperatures of standard (left) and innovative (right) pavement structures over a 24-h non-watered trial. Dashed red and blue lines respectively represent day phase (35°C) and night phase (25°C) air temperature setpoints (Parison et al., 2020c).

As discussed in Chapter 10, the non-watered behaviour of the standard structures (except for cobblestones) and of a grass sample amply watered prior to the experiment has been described in Hendel et al. (2018). During the day, an exponential rise of surface temperature is exhibited for all samples, followed by a sudden drop as soon as the lamps are switched off and the air temperature setpoint is changed. With regard to initial work, irradiance of the halogen lamps has been slightly reduced to better match that of *in situ* conditions given the set-up, which only caused a small reduction of end-of-day-phase temperatures (2° to 3.5°C) for the

previously tested pavements. During the night, temperatures decrease towards their setpoint temperature, i.e. 25°C. This appears to be more rapidly achieved for the stabilized sand and the slag concrete sidewalks. At the end of the day phase, the structure with the lowest temperature is the slag concrete sidewalk with 48.4°C.

Contrary to previous work, the grass sample was not watered before the trial. As a result, the grass dried very quickly and turned yellow at the end of the trial. Unable to evapotranspirate, its surface temperature increased almost as high as that of the asphalt sidewalk (∼58°C). In contrast, previously amply watered grass maintained a temperature of about 40°C under similar conditions. Similar results are found in the literature, confirming that the cooling efficiency of vegetation and its positive impact on air temperature and pedestrian heat stress strongly relies on its irrigation (Daniel et al., 2018).

For the asphalt sidewalk structure, the application of reflective paint leads to a reduction of 5.7° and 8.9°C respectively for the thermochromic and the NIR reflective paints, making it as cool as the most reflective standard pavement tested (stabilized sand). Similar reductions can be found in the literature for green thermochromic and black NIR reflective paints (resp. 8° and 13°C) with comparable albedo (Karlessi et al., 2009; Levinson et al., 2007).

Surface temperatures seem to be principally driven by albedo, as darker pavements tend to be hotter and brighter ones cooler. Figure 17.2 illustrates the maximum increase of surface temperature compared to air temperature with a linear regression versus albedo and versus a dimensionless absorptivity index defined in equation 17.1. The index takes into account SW and LW absorptivities, resp. $(1-\alpha)$ and ϵ, and weights each by the corresponding proportion of SW and LW irradiance, i.e. 70% and 30% respectively. Error bars are up to 0.5°C for surface temperature signals.

$$a = \frac{S(1-\alpha) + L\epsilon}{S+L} \tag{17.1}$$
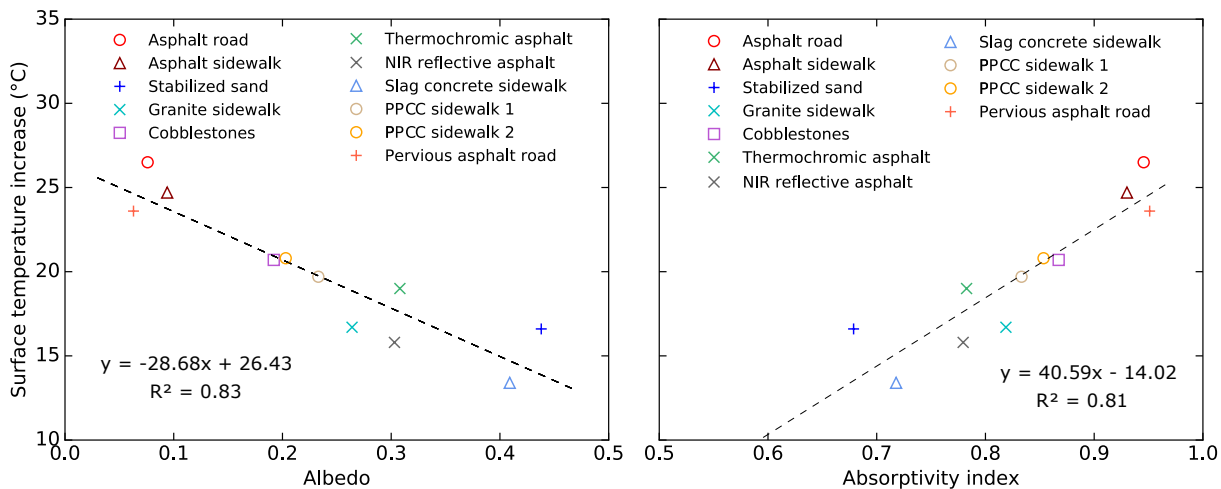
Figure 17.2: Daily surface temperature increase during a dry test versus albedo (a) and versus the absorptivity index (b) (Parison et al., 2020c).

As a can be seen, a reduction of nearly 3°C is obtained per 0.1 increase in albedo. This falls within the lower boundary of the typical range of 3° to 7°C found in the literature for different slabs, pavement and roof tiles (Qin and Hiller, 2014; Li et al., 2013c; Levinson et al., 2007; Synnefa et al., 2007; Pomerantz, 2000; Pomerantz et al., 2003). Although both paints have a very similar albedo (0.308 vs 0.303) and were applied on the same sample, thermochromic asphalt ends up 3.2°C hotter than the NIR reflective asphalt. Beyond the reasonable measurement accuracy (± 0.5°C), this can be attributed to differences between fresh paint prior to albedo measurement and its ageing inside the chamber, despite our precautions.

Finally, Figure 17.2 predicts negative values of the surface increase temperature, i.e. the existence of materials that would provide radiative cooling even in daytime. In principle, such materials should become colder than the air provided convection is low. Based on the regressions, it would require an albedo of at least 0.91 under the conditions of the lab. This aspect needs more investigation and is briefly discussed further in this manuscript.

17.2 In-depth Temperature

In-depth temperatures for a dry trial are provided in Figure 17.3. Thermochromic and NIR reflective asphalts remain cooler in-depth compared to the traditional asphalt sidewalk thanks to their higher albedo. Also, although the stabilized sand and the granite sidewalk exhibit similar "cool" behaviours at the surface, the latter stands out in depth by being progressively hotter than stabilized sand, ending up as hot as asphalt road and sidewalk 25 cm deep. This was explained by Hendel et al. (2018) as caused by the high effusivity $(\lambda \rho c)^{1/2}$ and diffusivity $(\lambda/\rho c)$ of the granite structure (granite, mortar and concrete), causing it to both rapidly absorb heat while limiting surface temperature increase, and quickly transmit the temperature signal to lower depths. As an example, the contrary is observed for the PPCC sidewalks, relatively hot at the surface and as far as 14 cm deep, but remaining cool 25 cm deep due to the low diffusivity of the sand base layer. Although the exact diffusivity of the layers and materials was not measured, information regarding the diffusive capacities of the structures is given looking at the time lag between each in-depth temperature peak with regard to the surface peak.

The grass sample, although relatively hot at the surface, stands out in-depth as it remains significantly cooler than other pavements. Although not measured, we presume this is due to the low thermal conductivity of loose dry soil relatively to the other materials. Since only temperature measurements were performed for the grass, this sample is not discussed further hereafter.
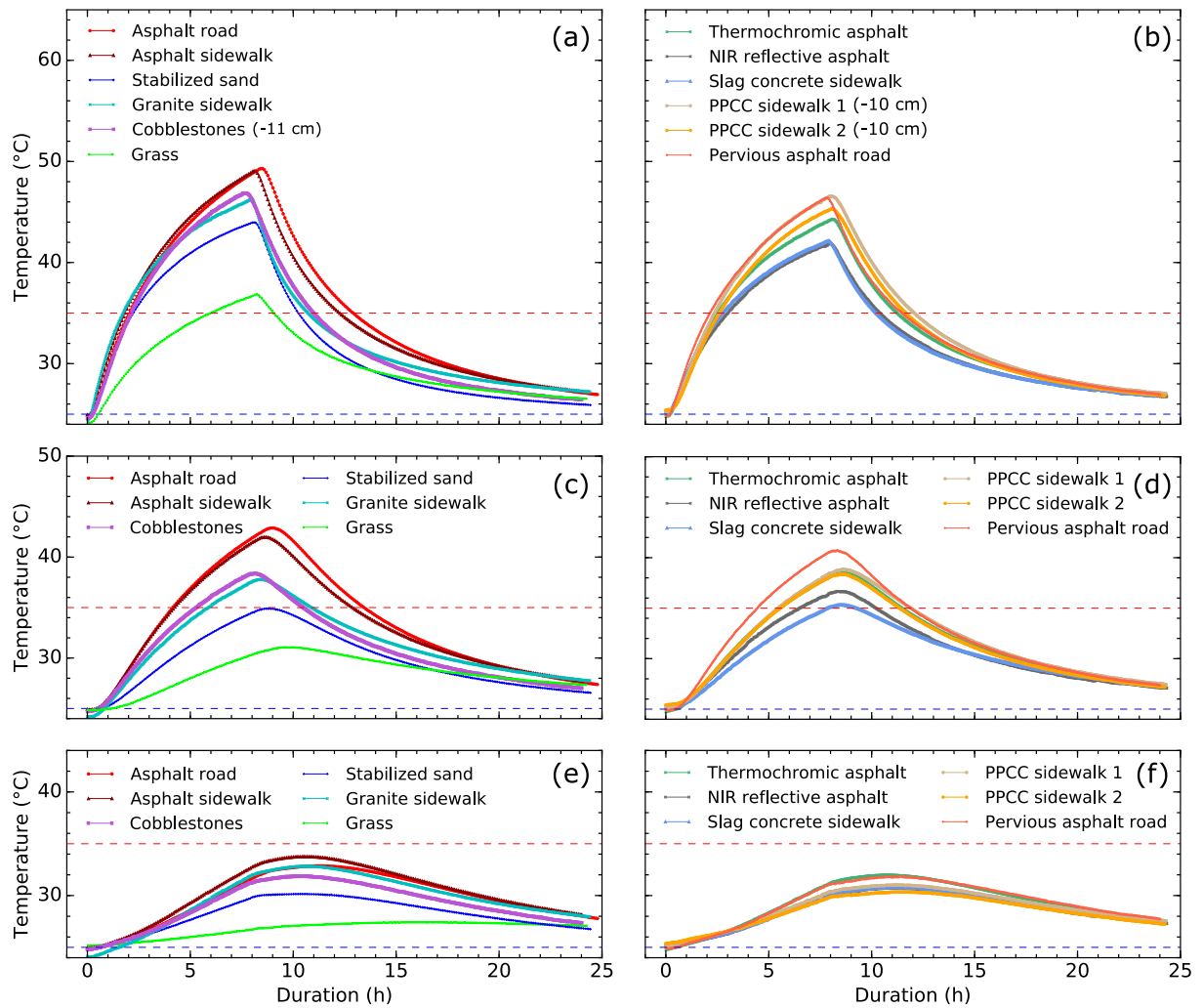
Figure 17.3: In-depth temperatures of standard (left-hand side) and innovative (right-hand side) dry pavement structures 6 (a and b), 14 (c and d) and 25 (e and f) cm deep. Dashed red and blue lines respectively represent day phase (35°C) and night phase (25°C) air temperature setpoints (Parison et al., 2020c).

Optimization of Watering

18.1 Temperature Reductions With Watering

We now turn to the analysis of the temperature reductions caused by watering of the pavements. For the asphalt road and sidewalk, the granite sidewalk, the stabilized sand, the thermochromic and NIR reflective asphalt and the slag concrete sidewalk, a total of twelve different watering rates were applied ranging from 0.1 to 3.0 mm/h (equivalent to L/(m².h)). These were summarized in Table 11.2. Typical uncertainty on the watering rate is estimated to be about 0.05 mm/h. Having fine-tuned the watering rate for these samples, fewer watering rates (six in total) were applied for the remaining structures, tested afterwards. Figure 18.1 shows the difference in maximum surface temperatures as a function of the watering rate Q. For all the upcoming analyses, steady-state (or quasi steady-state) results are shown, corresponding to the end of the 8-h day phase.
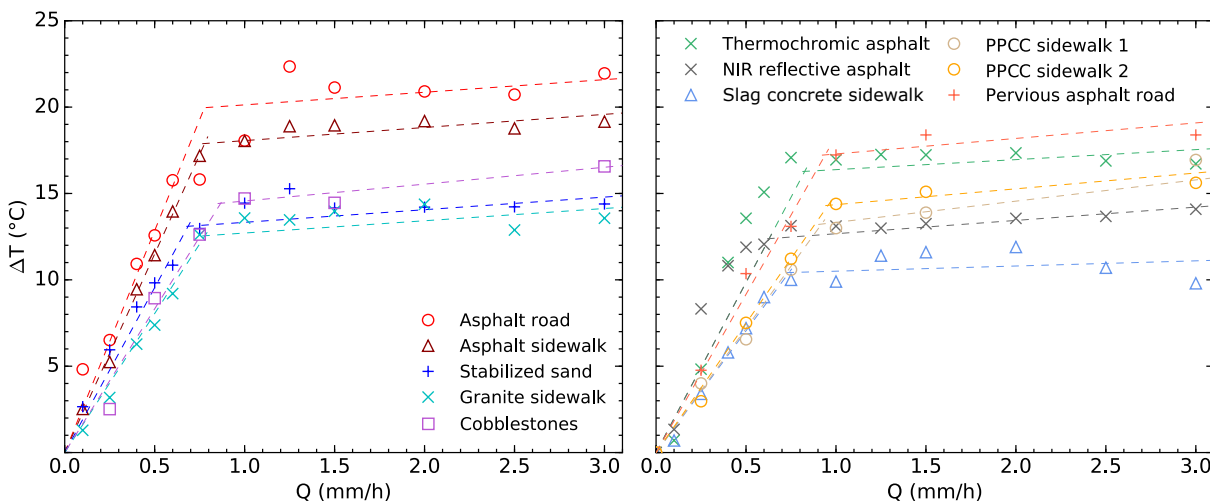
Figure 18.1: Maximum surface temperature dry-wet difference versus watering rate Q for traditional (left) and innovative pavements (right). The double piecewise linear regression is represented with dashed lines (see Table 18.1) (Parison et al., 2020c).

For all pavements, strong surface temperature reductions are exhibited with watering, ranging from 10° to 22°C. Higher decreases are observed for dark structures (asphalt road and sidewalk), as their final dry temperature is greater. With a watering rate of 3 mm/h, the steady-state temperature of each sample converges towards 40°C. As in Chapter 12, the two linear cooling regimes of equation 16.2 are observed for all pavements. These respectively correspond to the increase in evaporation due to watering, then to the marginal increase of cooling once the maximum evaporation rate is reached. For the latter "sensible" regime, the optimal watering rate Q_{opti} has been reached. This happens once the time span between two consecutive sprays is equal to the surface drying period, i.e. the surface no longer dries between two consecutive water sprays. Watered temperature signals (such as in Figure 12.1), are not presented here.

A double piecewise linear regression with a forced zero-intercept is used to model these regimes and is represented with dashed lines. In each case, an R^2 coefficient greater than 0.80 is found for both regimes. The optimal watering rate Q_{opti} is the intersection of the two segments and maximizes the cooling effects while minimizing the water consumption. Results of the regressions are summarized in Table 18.1.

Table 18.1: Best fitting equations for both cooling regimes and corresponding optimal watering rate Q_{opti} for each pavement (Parison et al., 2020c).

Pavement structure	Segment 1	Segment 2	Q_{opti} (mm/h)
Asphalt road	$y_1 = 25.7\,Q$	$y_2 = 0.73\,Q + 19.4$	0.80
Asphalt sidewalk	$y_1 = 23.0\,Q$	$y_2 = 0.76\,Q + 17.3$	0.78
Stabilized sand	$y_1 = 19.1\,Q$	$y_2 = 0.73\,Q + 12.6$	0.69
Granite sidewalk	$y_1 = 16.1\,Q$	$y_2 = 0.71\,Q + 12.0$	0.78
Cobblestones	$y_1 = 16.6\,Q$	$y_2 = 0.98\,Q + 13.6$	0.86
Thermochromic paint	$y_1 = 19.7\,Q$	$y_2 = 0.58\,Q + 15.8$	0.83
NIR reflective asphalt	$y_1 = 19.7\,Q$	$y_2 = 0.77\,Q + 11.9$	0.63
Slag concrete sidewalk	$y_1 = 14.1\,Q$	$y_2 = 0.30\,Q + 10.2$	0.74
Pervious sidewalk 1 (w/o clay)	$y_1 = 14.4\,Q$	$y_2 = 1.23\,Q + 12.1$	0.92
Pervious sidewalk 2 (w/ clay)	$y_1 = 15.0\,Q$	$y_2 = 0.92\,Q + 13.4$	0.96
Pervious asphalt road	$y_1 = 18.3\,Q$	$y_2 = 0.90\,Q + 16.4$	0.94

Globally, reflective (thus cooler) structures tend to have a lower optimal watering rate. This is however untrue for the pervious asphalt road and PPCC sidewalks, for which the highest Q_{opti} values are exhibited, most likely because of infiltration of sprinkled water. Very similar observations are made in-depth, although they are not presented here. The amplitude of the temperature reductions in-depth is smaller (with reductions of 7° to 12°C at 6 cm, 3° to 9°C at 14 cm and 0.5° to 3.5°C 25 cm deep), but the ranking of the "most cooled" pavement structures exhibited in Figure 18.1 is preserved.

18.2 Conductive, Convective and Radiative Dry-Wet Variations

Following the heat transfer analysis of Section 11.3, we now analyze the surface heat budget to determine $\Delta V_0^{dry-wet}$, $\Delta H^{dry-wet}$ and $\Delta R_n^{dry-wet}$ (equation 11.4), illustrated in Figure 18.2.
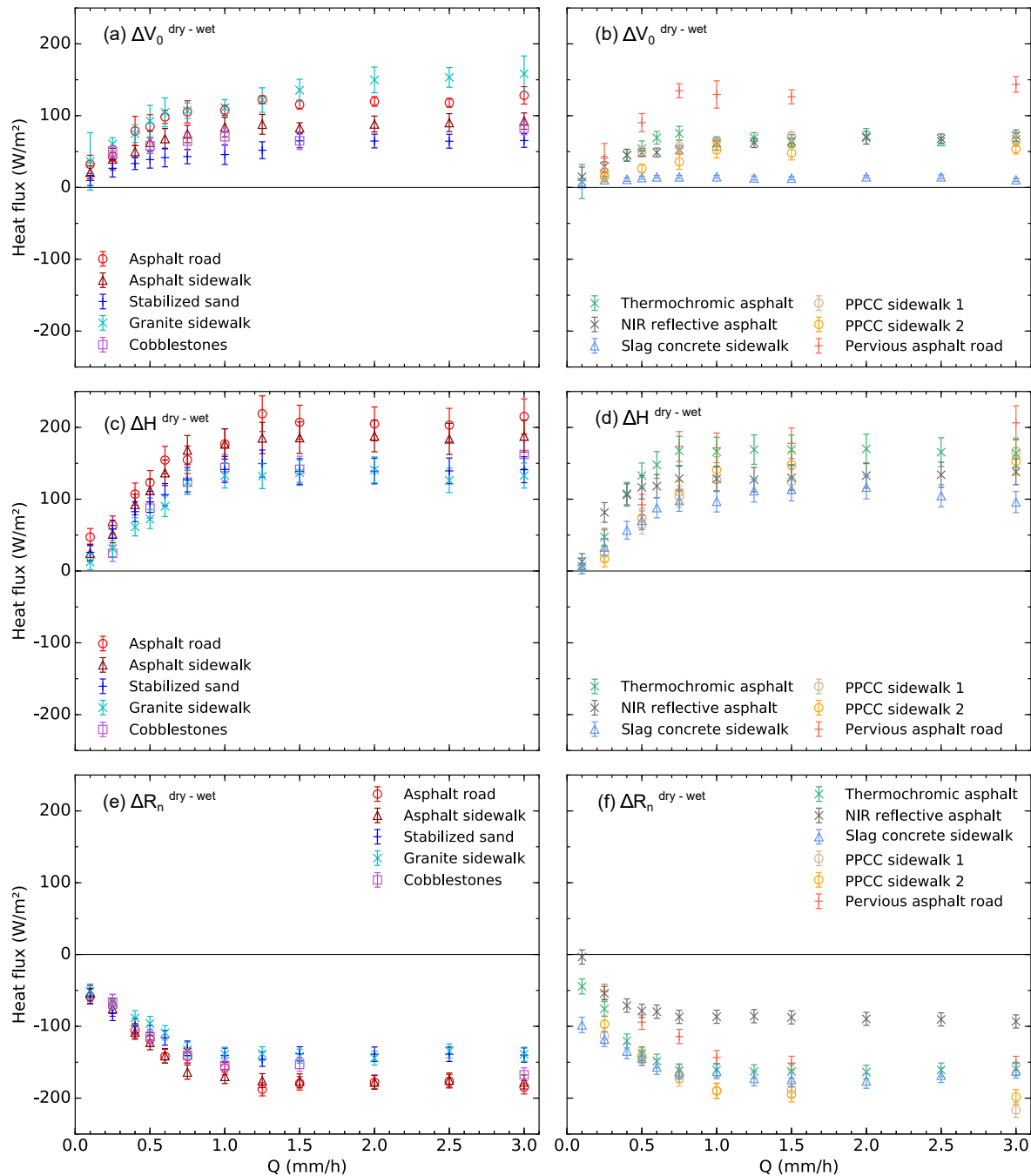
Figure 18.2: From top to bottom, dry-wet differences of conductive heat flux $\Delta V_0^{dry-wet}$, net radiation $\Delta R_n^{dry-wet}$ and convective flux $\Delta H^{dry-wet}$, versus watering rate Q, for standard (left column) and innovative pavements (right column) (Parison et al., 2020c).

These terms respectively represent the reductions in conductive and convective heat flows and the increase in net radiation due to watering. For dry trials, a convective exchange coefficient h of about 10 W/(m².K) was found (see Section 12.4). Having determined h for all structures, equation 11.7 was then directly applied to calculate H. For watered tests, the emissivity of the water (i.e. 0.98) is systematically assumed. Error bars were obtained by propagating the uncertainties of terms involved in equations 11.6 and 11.9 or using the standard deviation of the dry-wet difference between 6 cm deep signals during daytime for $\Delta V_0^{dry-wet}$.

In Figure 18.2 (a) and (b), heat storage is found to be greatly reduced by watering, i.e. $\Delta V_0^{dry-wet}$ increases with Q. The structure most impacted by watering is the granite sidewalk, although the latter remains relatively "cool" at its surface due to its high albedo. This is most likely due to its high conductivity. The contrary prevails for stabilized sand, poorly conductive. The same tendency is observed in Figure 18.2 (b): slag concrete exhibits the lowest reduction due to its very low conductivity.

In Figure 18.2 (c) and (d), convective exchanges between the surface and the ambient air decrease with Q, thus $\Delta H^{dry-wet}$ gradually increases with watering. This is directly proportional to the surface temperature difference between dry and wet trials, as shows equation 11.9. Since the convective exchange coefficient h is similar for each structure, tendencies follow that of such surface temperature differences shown in Figure 18.1. Hottest structures are therefore more impacted by watering than cooler ones.

Finally, in Figure 18.2 (e) and (f), $\Delta R_n^{dry-wet}$ decreases significantly with Q, i.e. net radiation increases with watering. Regarding its value, competing effects are at work. Indeed, following equation 11.6, $\Delta R_n^{dry-wet}$ can be decomposed into three components: dry-wet reductions of black-body emission (proportional to the surface temperature decrease, i.e. mainly to the albedo), of reflected infrared radiation (negligible here) and of reflected visible radiation (proportional to the dry-wet albedo reduction). This is further discussed in Section 19.2 of this manuscript.

18.3   Total Pavement Cooling Flux

Knowing $\Delta V_0^{dry-wet}$, $\Delta H^{dry-wet}$ and $\Delta R_n^{dry-wet}$, it is possible to calculate the total cooling flux Φ with equation 11.4 for each watering rate and pavement under steady-state conditions. This is shown in Figure 18.3. As predicted by equation 16.2, again, a double piecewise linear regression with forced zero intercept is performed and represented with dashed lines. Uncertainties are propagated for Φ through equation 11.4. Results are summarized in Table 18.2.

As a reminder, cooling in the lab is about twice as much as field observations, most likely because of the amount of daily absorbed net radiation which is also doubled in the lab, as previously discussed in Chapter 13. The amplitude of total cooling versus Q reflects observations of the previous Section: main factors generating an important cooling flux are: low albedo (both high $\Delta H^{dry-wet}$ and $-\Delta R_n^{dry-wet}$), high dry-wet albedo variation (high $-\Delta R_n^{dry-wet}$ dry-wet) and high thermal conductivity λ of the surface course (thus high $\Delta V_0^{dry-wet}$). As a result,
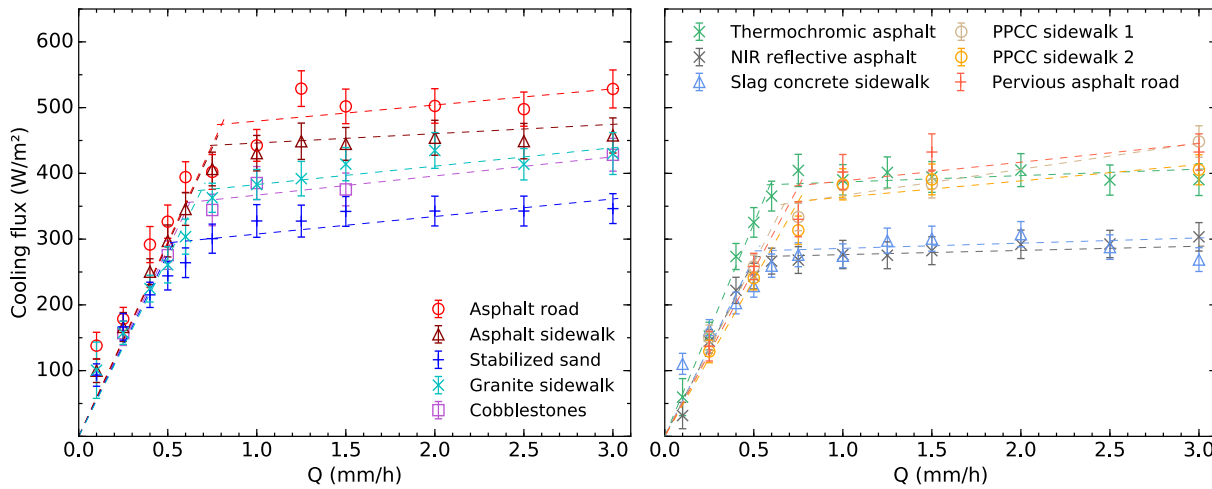
Figure 18.3: Total cooling flux Φ as a function of the watering rate Q for traditional (left) and alternative pavements (right). The double piecewise linear regression is represented with dashed lines. (see Table 18.2) (Parison et al., 2020c).

dark structures tend to be cooled more since they combine at least two out of three of the principal contributing factors to Φ, i.e. $\Delta H^{dry-wet}$ and $-\Delta R_n^{dry-wet}$. Potential limiting effects to Φ thus tend to be of less importance, such as the thermal conductivity or albedo variation, which is typically low if albedo is as well.

As mentioned in the study goals Section (16.4), theoretically, the 1st segment's slope (latent regime) should be close to 630 W/m² per mm/h (corresponding to l the latent heat of vaporization of water), given that sensible cooling is marginal. The corresponding slopes listed in Table 18.2 are globally lower than this, because of certain assumptions made for the calculation of Φ, impacting the latent regime's slope. In particular, both the albedo and the emissivity are considered to be that of a wet sample as soon as watering is implemented, when strictly, they should be weighted by the time span during which the surface is completely dried out during the day phase. Also, the maximum surface temperature is used for the calculations when it would be preferable to consider an average temperature instead. Both these aspects should slightly affect the first regime. No difference would be observed for the largest watering rates, since the surface has no time to dry out (surface peaks disappear).

In addition, the latent regime's slope is also influenced by the specific surface of the sample (shape, flatness, porosity, etc.). Pervious structures are expected to have a lower slope for the first regime, as they infiltrate water at depth. Thus, qualitatively, the ratio of the latent regime's slope to the theoretical slope (i.e. l) allows to estimate the perviousness of the sample, while it gives us the relative accuracy of this estimation with impervious samples. For PPCC sidewalks and pervious asphalt, this ratio ranges from a porosity of 15 to 25%. This ratio ranges between 5 to 10% for highly impervious structures (asphalt road sidewalk, granite), giving us the typical accuracy of the estimation.

In Table 18.2, as mentioned in section 18.1, brighter and thus cooler structures exhibit lower optimal watering rates Q_{opti}. Overall, this is better verified than for Table 18.1. The most sig-

Table 18.2: From left to right: optimal value of Φ, best fitting equations for both regimes, optimal watering rate Q_{opti} determined with the piecewise regression, and expected optimal rate neglecting sensible cooling, for all pavements.

Pavement structure	Φ_{opti} (W/m²)	Segment 1	Segment 2	Q_{opti} (mm/h)	$\Phi_{reg,lat}/630$ (mm/h)
Asphalt road	470	$y_1 = 591\,Q$	$y_2 = 24.5\,Q + 455$	0.80	0.80
Asphalt sidewalk	445	$y_1 = 585\,Q$	$y_2 = 14.2\,Q + 432$	0.76	0.72
Stabilized sand	290	$y_1 = 555\,Q$	$y_2 = 26.7\,Q + 281$	0.53	0.54
Granite sidewalk	375	$y_1 = 543\,Q$	$y_2 = 28.0\,Q + 355$	0.69	0.66
Cobblestones	345	$y_1 = 528\,Q$	$y_2 = 27.5\,Q + 327$	0.65	0.61
Thermochromic paint	380	$y_1 = 647\,Q$	$y_2 = 9.80\,Q + 377$	0.59	0.63
NIR reflective asphalt	270	$y_1 = 534\,Q$	$y_2 = 6.41\,Q + 270$	0.51	0.46
Slag concrete sidewalk	280	$y_1 = 542\,Q$	$y_2 = 7.94\,Q + 278$	0.52	0.47
PPCC 1 (w/o clay)	350	$y_1 = 527\,Q$	$y_2 = 39.9\,Q + 326$	0.67	0.66
PPCC 2 (w/ clay)	355	$y_1 = 479\,Q$	$y_2 = 25.2\,Q + 338$	0.74	0.63
Pervious asphalt road	380	$y_1 = 506\,Q$	$y_2 = 28.5\,Q + 360$	0.75	0.69

nificant difference concerns the PPCC sidewalks, for which much lower optimal watering rates are obtained using Φ instead of surface temperature variation (0.7 mm/h against 0.9 mm/h respectively). We assume this is because the calculation of Φ relies on in-depth signals (via $\Delta V_0^{dry-wet}$) which dampens surface signal fluctuations (caused by convection, insolation, water sprinkling, etc.) and thus mitigates the effects of water infiltration that caused Q_{opti} to increase with regard to impervious pavements. Furthermore, no significant difference in behaviour other than water infiltration is observed between PPCC 1 and 2, or between the pervious asphalt and the asphalt road, as runoff is inhibited in the chamber. As a result, impervious structures retain all of the sprinkled water at the surface, contrary to what would be observed in the field. This is more broadly discussed further in this manuscript.

Table 18.2's last column lists the expected optimal watering rates neglecting sensible cooling (see Section 16.4). The latter are estimated by intersecting the theoretical latent regime's slope, i.e. the cooling flux created by evaporating 1 mm of water per hour (630 W/m² per mm/h) ($y_1 = 630\,Q$), with the 2nd regime (sensible regime) zero-slope segment whose intercept is the maximum cooling flux reached on average for the last greatest rates ($y_2 = lE^{max} = <\Phi_{reg,lat}>$). The optimal rate is thus given by the average ratio $\Phi_{reg,lat}/630$, in mm/h. This method is found to be in good agreement with the values from the double piecewise regression, despite the first slope being underestimated, with residues less than 0.05 mm/h (apart from PPCC 2) which is within the typical accuracy of the watering rate calibration. This result indicates that a satisfying estimation of Q_{opti} can be obtained in the lab with only one highly-watered test instead of a complete range of tests, provided that enough information is known to fully estimate the corresponding pavement cooling flux and that sensible flux remains negligible.

Optimal watering rates versus albedo and absorptivity are plotted in Figure 18.4. Good linear agreement is found between Q_{opti} and the x-axis. Under the lab conditions, this Figure
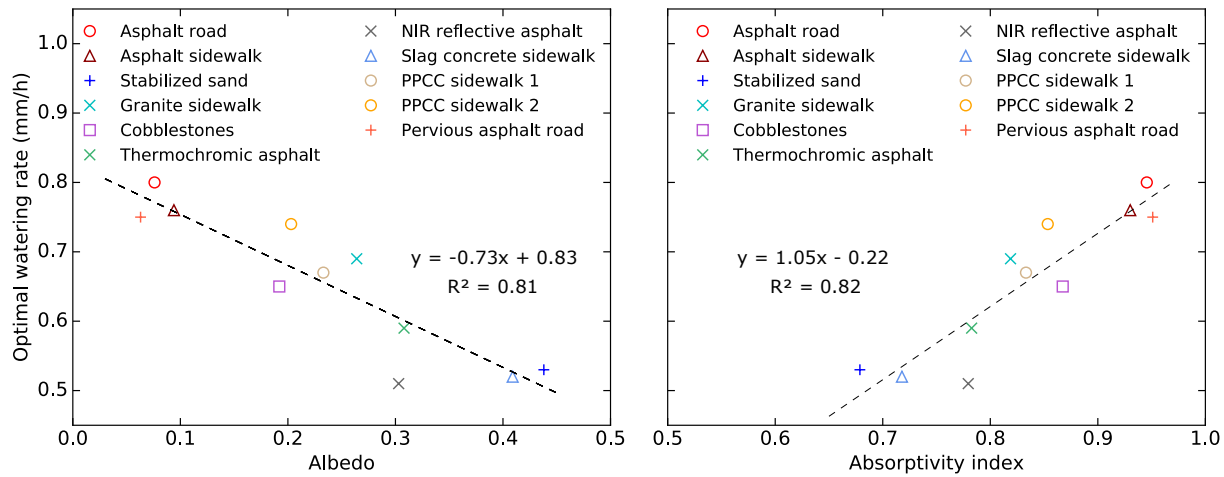
Figure 18.4: Optimal watering rate for each pavement structure as a function of their albedo (left) and their absorptivity (right) (Parison et al., 2020c).

infers that the theoretical maximum optimal watering rate would be around 0.83 mm/h for a conceptual surface with a null albedo, while the minimum would be 0.10 mm/h for a surface with an albedo of 1. Under known experimental conditions, such graph is useful to predict the amount of water a material would need to maximise the effects of pavement-watering only knowing its albedo and absorptivity. Good linear agreement is also found between Q_{opti} (in mm/h) and dry daily absorbed radiation (in kWh/m²), with $y = 0.13x + 0.11$ and $R^2 = 0.79$. Such cumulative daytime absorbed radiation for dry trials are summarized in the next section, in Table 19.1. This is unsurprising insofar as net radiation can be expressed as a function of the absorptivity index, and since surface temperature strongly depends on the albedo, a predominant term in the expression of the absorptivity index a. This should be taken into account in the field and is discussed further in this manuscript.

Steady-State Thermal Analysis

19.1 Surface Partitioning of Irradiance

We now compare how dry and optimally-watered pavements partition incident irradiance between convection, conduction, upward radiation and cooling flux. The heat budget of a pavement is expressed as:

$$S + L = S_{up} + L_{up} + H + V_0 + \Phi \tag{19.1}$$

Hence:

$$a(S + L) - \sigma \epsilon T_s^4 = R_n = H + V_0 + \Phi \tag{19.2}$$

Energy partitioning helps understand the potential impact of pavements on pedestrian's heat budget. For instance, while radiosity $S_{up}+L_{up}$ helps to limit surface heating, it is detrimental to a pedestrian's radiative budget. Heat conduction on the other hand has no significant impact on pedestrians, while convective exchanges, in the absence of wind (low h) or advection, typical of heat-wave conditions, should be minimized in order to reduce atmospheric heating and heat stress as much as possible. Indeed, sensible heat release from a pavement, whether during day or night time, is identified as a major contributing factor to the warming of the near-surface air (Asaeda et al., 1996).

Figure 19.1 illustrates the heat flux to irradiance ratio for convective exchanges S_{up}, upward radiosity $S_{up}+L_{up}$, heat conduction V_0 and total cooling flux Φ as a function of the absorptivity index a (eq. 17.1) in steady-state. Dry trials and trials closest to the optimal watering rates Q_{opti} (Table 18.2) are represented. Note that for optimally-watered trials, the wet albedo and wet emissivity values are used for the calculation of a. For each dataset, the best linear regression is plotted with its equation and coefficient of determination R^2. Typical propagated uncertainties for H, V_0, and $S_{up}+L_{up}$ are about $10-20$ W/m², i.e. a few percent of $S+L$, and about $20-30$ W/m² for Φ.
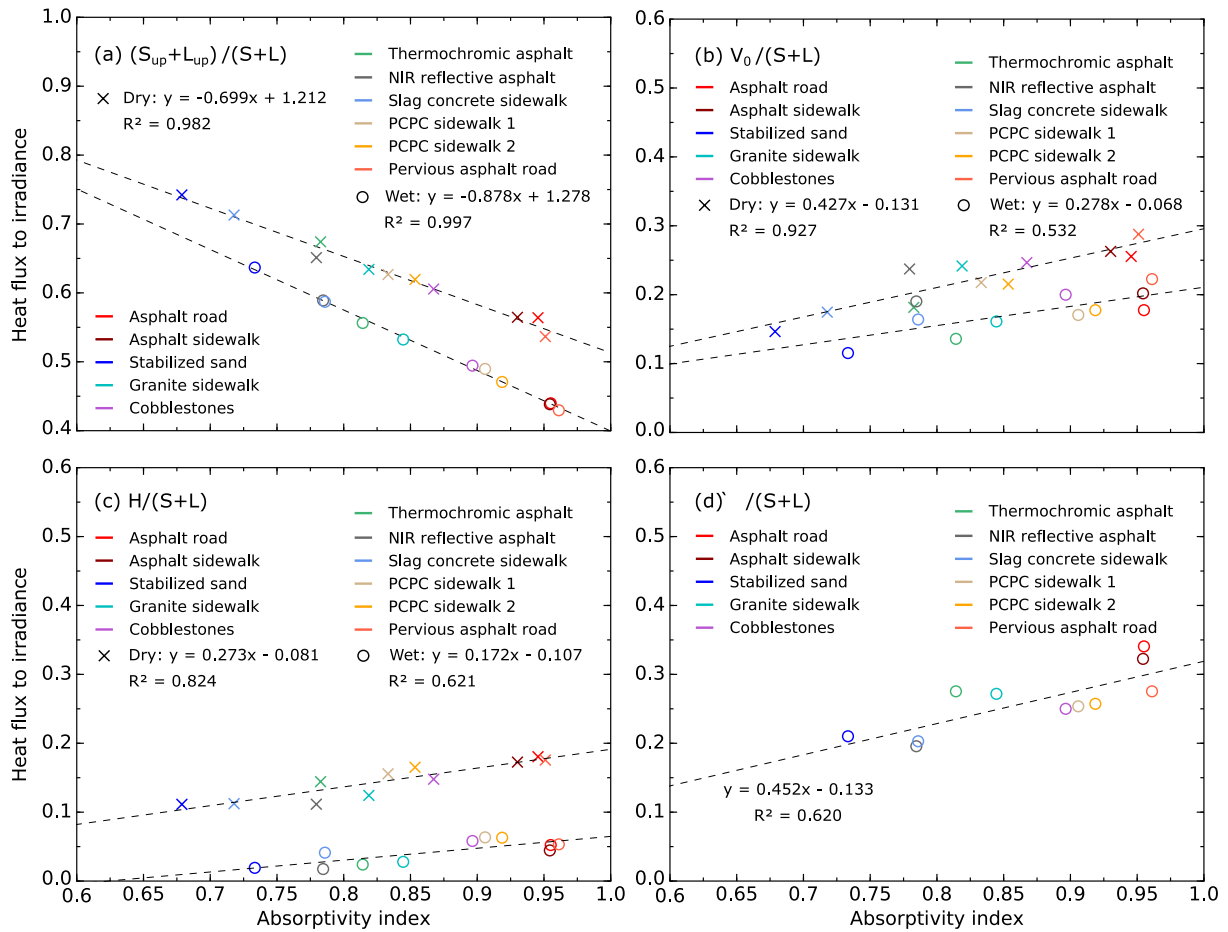
Figure 19.1: Steady-state surface partitioning of irradiance: (a): radiosity $S_{up}+L_{up}$, (b): conduction heat flux V_0, (c): atmospheric convective heat flux H and (d): cooling flux Φ, all divided by irradiance $S+L$ and plotted as a function of the absorptivity index a for all pavements. Non-watered trials are represented with cross markers while optimally-watered trials with circle markers (Parison et al., 2020c).

Figure 19.1 confirms previous observations and analyses. For all subfigures (a), (b), (c) and (d), the data plotted as a function of absorptivity exhibits a linear trend. This is directly inherited from equation 19.2 above, which in essence states that highly absorbing pavements will have high net radiation, and thus high H and V_0 as a consequence, all else being equal. Qin and Hiller (2014) found a similar result for the daily cumulative energy flux, which decreased linearly with reflectivity. We start by describing the dry behaviour of the pavements.

In Figure 19.1 (a), materials with high absorptivity (low albedo and high emissivity) are found to absorb a large quantity of energy (lower radiosity $S_{up}+L_{up}$). Radiosity is as low as 56% of incident irradiance for the darkest structures while the dry pavement with the highest radiosity is the stabilized sand, closely followed by slag concrete, with resp. ratios of 74% and 71%. For the darkest pavements, black-body emission is predominant in radiosity, as S_{up} is low due to their small albedo. The contrary applies to the brightest pavements. As an example, the black-body emission of the asphalt road represents 51% of $S+L$ for a total

radiosity of 56%, while it is 42% for the stabilized sand, which has a total radiosity of 74% of $S+L$. For comparison, daily absorbed radiation is listed in Table 19.1. Finally, the reflected LW is negligible for all structures (since $(1-\epsilon)$ is close to zero, and LW only account for 30% of the irradiance).

Among the remaining absorbed energy (R_n), a portion is transmitted in-depth by conduction V_0 and the other is released via H, convection to the atmosphere (equation 11.1).

In Figure 19.1 (b), partitioning of incident irradiance to conduction V_0 ranges from 15% to 26% for pavements with the lowest to the highest absorptivity, that is respectively stabilized sand to asphalt pavements. The same tendencies are obtained for convection H (Figure 19.1 (c)), although smaller fractions of irradiance are involved. The latter ranges from 11% (stabilized sand) to 18% of $S+L$ at most (asphalt road). Discrepancies in the convective behaviour between pavements are thus significantly smoothed out. Finally, other pavements have an intermediate behaviour, while reflective paints significantly reduce each term compared to unpainted asphalt sidewalk.

We now continue the analysis of Figure 19.1 with the data from the optimally-watered trials (depicted with circle markers).

In all cases, solar absorptivity increases with watering compared to a dry test, especially since albedo decreases with surface moistening. When the surface of a pavement is watered, the resulting cooling flux causes a reduction of convection and conduction, as well as a reduction of reflected and re-emitted radiation, resulting in an increase in net radiation. In other words, Φ is partitioned into reductions of H, V_0 and increase of R_n (equation 11.4).

As can be seen in Figure 19.1 (d), a large proportion of irradiance is used to generate the cooling flux Φ. This ranges from 22% to 35% of $S+L$, pavement-watering being more efficient on materials with a higher absorptivity index. As a consequence, each term involved in the surface heat budget is strongly reduced by watering: radiosity drops between 42% and 64% of incident irradiance, conduction between 12% and 18% and convection between 2% and 5% of irradiance. Good agreement between Φ and a also indicates the lower importance of the materials' thermo-physical properties in the efficiency of watering, the latter remaining relatively similar between samples.

Similar observations, regarding the proportions of convective exchanges and heat conduction as well as the strong impact of watering on H were made by Takebayashi and Moriyama (2012) on asphalt and concrete pavements, whereas Qin and Hiller (2014) found a greater portion of sensible heat H with regard to heat conduction.

19.2 Total Cooling Flux Constitution

As seen in the previous Section, the value of total cooling flux Φ depends on the considered pavement. As a reminder, Φ is calculated using equation 11.4, provided as a reminder below:

$$\Phi = \Delta H^{dry-wet} + \Delta V_0^{dry-wet} - \Delta R_n^{dry-wet} \tag{19.3}$$

By energy conservation, variations of convective ($\Delta H^{dry-wet}$), conductive ($\Delta V_0^{dry-wet}$) and radiative ($\Delta R_n^{dry-wet}$) fluxes between a dry and a watered trial appear in the value of Φ. In other words, the cooling flux is constituted by the variations of the surface heat budget terms. We now take interest in how Φ draws from the different components of the surface heat budget for each pavement. In order to do so, similarly to Figure 19.1 (d), Figure 19.2 represents total cooling flux normalised by irradiance for optimal watering rates only, and shows each share of the fluxes variations in total cooling. Note that unlike $\Delta V_0^{dry-wet}$ and $\Delta H^{dry-wet}$ and $\Delta R_n^{dry-wet}$, the opposite of the dry-wet net radiation variation is represented (i.e. $-\Delta R_n^{dry-wet}$).
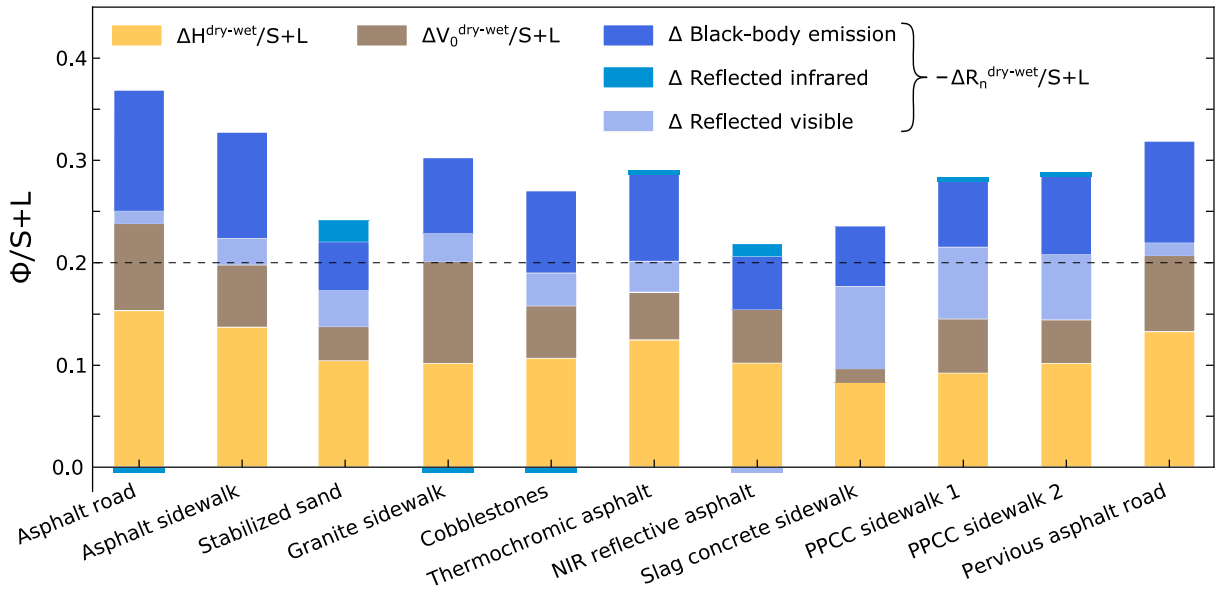
Figure 19.2: Detailed constitution of steady-state cooling flux normalized by irradiance for optimally watered trials.

Conduction reduction ($\Delta V_0^{dry-wet}$) over irradiance is represented in brown. Overall, this term constitutes a small portion of total cooling flux for pavements with a low thermal conductivity (in increasing order of the surface-layer apparent conductivity: slag concrete sidewalk, stabilized sand, asphalt sidewalk, PPCC sidewalk, cobblestones, pervious and standard asphalt roads and granite sidewalk (see Table 16.3)). This is particularly striking for the slag concrete sidewalk. As opposed to that, granite sidewalk optimal cooling flux includes a significant share of $\Delta V_0^{dry-wet}$.

For its part, the dry-wet convection reduction ($\Delta H^{dry-wet}$) over irradiance is represented in yellow. As seen in Section 18.2, for a given pavement, convective exchanges are further reduced with watering than conductive exchanges. Furthermore, $\Delta H^{dry-wet}$ appears to be higher for hotter structures. However, in proportion to Φ, little difference is exhibited between pavements, unlike $\Delta V_0^{dry-wet}$.

Finally, the variation in net radiation between a watered and dry trial ($-\Delta R_n^{dry-wet}$) over irradiance is shown in shades of blue in order to depict each component of equation 11.6. First, the dry-wet variation of black-body emission corresponds to $-\sigma(\epsilon_{wet} T_s^{wet4} - \epsilon_{dry} T_s^{dry4})$. This term is positive, i.e. black body emissions decrease with watering. As previously mentioned, structures with an important black-body emission reduction are those with important temperature reductions with watering (i.e. low-albedo structures). However, as for convection, proportionally to Φ, this term is roughly similar for all samples.

The variation of reflected infrared radiation corresponds to the term $(\epsilon_{wet} - \epsilon_{dry})L$. As seen, this term is either null or negligible with regard to total pavement cooling, since pavement emissivities are close to that of water and since LW only represents 30% of the incident irradiance. This term is only negative for the asphalt road, granite sidewalk and cobblestones whose emissivity is higher than that of water.

Lastly, the variation of reflected visible radiation illustrates the term $(\alpha_{dry} - \alpha_{wet})S$. Pavements with important variations in albedo when watered (about -10%), i.e. PPCC and slag concrete sidewalks, exhibit a reduction of reflected visible radiation even greater than that of their black-body emission, thus offsetting the contribution of the temperature reduction obtained with watering. For such pavements, the variation of reflected visible radiation constitutes a significant portion of Φ. In contrast, pavements with a negligible dry-wet albedo variation (typically dark structures) present a very low proportion of this term in the pavement cooling flux constitution.

A recap of all steady-state heat-fluxes as well as the cumulative absorbed daytime radiation for dry pavements is provided in Table 19.1. Summing errors may occur due to rounding, while Φ may slightly differ from Table 18.2 for which values are obtained directly from the piecewise regression, whereas values here are calculated as residuals of the heat budget.

Table 19.1: Cumulative absorbed daytime radiation of dry pavements ($\int^{day} R_n\, dt$, in kWh/m²), and detailed steady-state heat budgets for dry and optimally-watered pavements (in W/m²) (Parison et al., 2020c).

Pavement structure	Dry pavement					Optimally-watered pavement					
	$\int^{day} R_n\, dt$	R_n	V_0	H	S_{up}	L_{up}	R_n	V_0	H	S_{up}	L_{up}	Φ
Asphalt road	5.4	601	351	250	71	708	773	245	72	53	554	456
Asphalt sidewalk	5.2	598	360	238	87	695	775	279	61	54	551	435
Stabilized sand	3.1	357	203	154	407	616	501	159	26	359	520	316
Granite sidewalk	4.3	505	333	172	246	629	645	222	38	206	529	385
Cobblestones	4.5	543	340	204	179	658	698	276	80	134	548	342
Thermochromic asphalt	3.9	450	250	200	286	644	612	188	33	247	521	391
NIR reflective asphalt	4.1	482	328	154	282	616	567	275	25	288	525	267
Slag concrete sidewalk	3.3	397	241	155	380	603	570	226	57	286	524	287
Pervious sidewalk 1 (w/o clay)	4.4	513	300	215	217	650	704	235	88	121	555	381
Pervious sidewalk 2 (w/ clay)	4.4	534	306	228	189	657	730	245	87	103	547	398
Pervious asphalt road	5.2	639	397	242	59	682	787	307	74	45	548	406

19.3   In-Depth Heat Transmission

Having considered surface cooling efficiency, we now end the results section with heat transmission in-depth. We propose a dimensionless solar transmission index derived from Hendel et al. (2018), denoted τ, that takes into account the composite structure of the pavements to better understand their behaviour in-depth. The index τ depends on depth z through the thickness of the i-th composite layer e_i and its corresponding apparent conductivity λ_i, and also on the solar absorptivity index a define formerly. The transmission index is the following:

$$\tau(z < 0) = a \frac{e_0/\lambda_0}{\sum_i e_i/\lambda_i} \tag{19.4}$$

The term $1/(\sum_i e_i/\lambda_i)$ is the composite apparent thermal conductance of the overlaying material layers (in W/(m².K)). The numerator term e_0/λ_0 is taken as a reference thermal resistance equal to 1 K.m²/W to render τ dimensionless. Figure 19.3 illustrates the ratio of in-depth heat flux to irradiance $S+L$ as a function of the transmission index τ. Although heat conduction in-depth has no major impact on a pedestrian's heat budget during the day, it contributes to air temperature increase at night during pavement heat release.
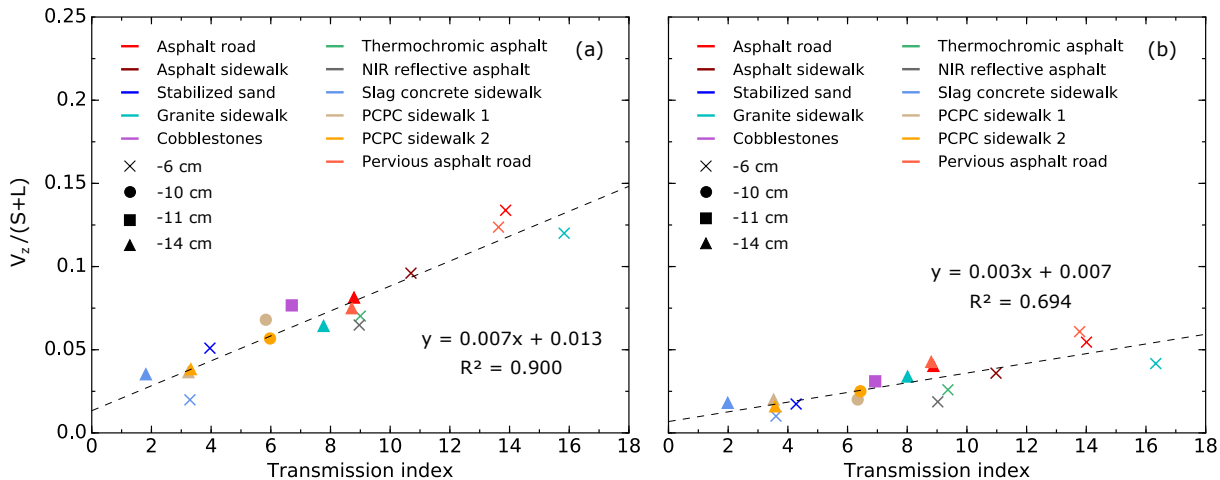
Figure 19.3: Steady-state heat fluxes in-depth (at 6, 10, 11 and 14 cm deep) to irradiance as a function of the transmission index for all pavements during a dry trial (a) and an optimally-watered trial (b) (Parison et al., 2020c).

As can be seen, good correlation is found with the proposed index. In Figure 19.3 (a), the granite sidewalk, although much more reflective than bituminous pavements, transmits as much heat 6 cm deep due to its high thermal conductivity. Similarly, cobblestones transmit as much 11 cm deep as the asphalt road 14 cm. In-depth, cobblestones are expected to exhibit a behaviour close to that of granite. However, cobblestones' apparent thermal conductivity is lower that granite's due to the composite nature of the sample. Conclusions are rendered even more difficult because of the different instrumentation of the samples (6 or 14 cm deep for granite against -11 cm for cobblestones).

The use of reflective paints on the asphalt sidewalk significantly reduces heat transmitted in-depth. Reflective asphalt thus transmits as little heat 6 cm deep as traditional asphalt does 14 cm deep. As expected, slag concrete is the structure transmitting the least heat both 6 cm and 14 cm deep, due to the combination of its low thermal conductivity and low absorptivity.

Figure 19.3 (b) shows that optimal watering does not modify the previous trends, but significantly reduces the amount of transmitted heat.

Although high-inertia pavements may dampen the temperature increase during the day, this reduction is only limited to a few degrees (Qin and Hiller, 2014), and accumulated heat remains a disadvantage at night and contributes to extend heat-waves. In such a case, heat-harvesting pavements (with heat exchangers for domestic hot water supply for example) can help limit heat release at night without prejudicing people during the day by decreasing surface temperature as well (Yinfei et al., 2018; Shaopeng et al., 2011; Chen et al., 2009). Depending on the purpose, in order to limit heat release at night, the use of relatively low heat-conducting pavements can be preferable. Nevertheless, such pavements tend to increase surface temperature increase during the day, detrimental for pedestrians when they are most exposed (Yinfei et al., 2014). Thus, they must be correlated with low surface temperature during the day (high albedo, shading, etc.).

Discussion: Transferability to the Field

Although the lab results presented in this manuscript do not accurately reproduce field conditions, we now discuss how lab findings can be transferred to field applications. It should be noted that this transposition is not straightforward, and is highly dependent on field parameters, particularly convection (e.g. the convective heat transfer coefficient h), conduction and net radiation, which are likely to increase or decrease optimal watering rates.

As previously discussed in Chapter 13, comparison of the lab results for the asphalt road to field experiment for a similar structure showed that the surface heat budget is roughly doubled (for conduction, convection and evaporative flux). Indeed, the structure's net radiation is about doubled in the lab compared to the field (Hendel et al., 2015a; Parison et al., 2020b). In addition, in the lab, good correlation is found between the optimal watering rate and the absorptivity index, as well as with daily absorbed net radiation (see section 18.3). This is used as a naïve approach for transposing results to the field for other pavements. Conditions inside the climate chamber approximately double the optimal watering rate for a given structure with regard to what would *a priori* be observed in the field, all else being equal (Parison et al., 2020b).

Yet, field experimentation poses strong technical and operational constraints, setting the limits of this approach. For instance, several factors are not reproduced in the laboratory, such as the curvature of the Haussmannian roads that causes water to run off into the sewer system. Therefore, under real conditions, it is essential to take into account the surface water retention capacity of the pavement to modulate the frequency between two consecutive waterings in order to sprinkle the structure with the optimal rate, adapted to the quantity of water it is able to retain (which is roughly equal to its surface roughness). For example, an optimal rate of 0.4 mm/h for the asphalt road (0.8 mm/h in the chamber) applied to a surface with a retention capacity of 0.2 mm requires watering every half hour. Thus, by adjusting the frequency between each cycle, the optimal watering rate can be achieved. However, more freedom on the watering frequency is permitted for pervious materials. Indeed, the optimal quantity of water to sprinkle at once per hour is *a priori* lower than the water retention capacity of the structure, unlike impervious structures. Thus, a pervious structure can be saturated with water, only to

sprinkle it again once the water has evaporated entirely, which as a result strongly decreases the frequency between consecutive sprinklings.

In this respect, the question of the infrastructure dedicated to pavement-watering is crucial. Field experiments presented in Part II were carried out in Paris using cleaning trucks and the city's non-potable water network, which brought up many constraints (noise and visual nuisances, discomfort for the workers, traffic, etc.), the strongest of which is the lack of flexibility in defining the time span between two consecutive watering cycles and the lack of fine control over the quantity of water sprinkled, due to the fixed volume of the water tank and the operating pressure of the cleaning truck. Important re-filling times spans at the devoted non-potable water outlets also proved to be a problem. These aspects limit the technical feasibility of the method.

In the future, if pavement-watering were to be deployed on a long term basis as an emergency cooling tool applied to specific pre-identified relevant areas, an automated sprinkling device should be considered, as it has already been done it other cities (Yamagata et al., 2008; Takahashi et al., 2010). The device could be connected to the non-potable water network or re-use collected rainwater.

Conclusion of Part IV

The lab experiment presented in Part III was used to study the thermal behaviour of six standard pavements commonly found in the Parisian urban fabric (asphalt road, asphalt sidewalk, granite sidewalk, stabilized sand, cobblestones and grass), as well as six innovative pavements (thermochromic and near-infrared reflective asphalt, slag concrete, two formulations of pervious concretes and a pervious asphalt road). Structures were constructed with the same composition as in the field. The experiment creates steady-state weather conditions representative of a heat-wave in Paris, with an 8h heat-up phase with artificial insolation followed by a 16h night phase, thus allowing the comparison of each pavement under given conditions without having to implement long-lasting and costly fields tests. Surface and in-depth measurements are used to study the dry or watered behaviour of the samples, with more than ten different watering rates carried out in order to fine-tune the process before deployment in the field.

The lowest surface temperature was observed for the slag concrete structure, while dry grass was quite hot in the absence of evapotranspiration. The application of reflective paints allowed the asphalt sidewalk surface temperature to be reduced up to $6° − 9°$C. Such solutions are of particular interest for urban planners as they remain relatively cheap and easy to implement.

The surface heat budget was evaluated under steady-state conditions to determine the cooling flux as well as the reductions in heat conduction and convective exchanges and the increase in net radiation due to watering. The optimal watering rate (i.e. the maximum evaporation rate) was determined for each structure on the basis of two linear cooling regimes, as for Part III. It was found that a first order estimate of the optimal watering rate could be obtained with a single high-watering-rate trial. This requires assessing the corresponding cooling flux and neglecting the sensible flux. The obtained value can be used to schedule additional testing at points around the predicted optimum. Optimal watering rates show good correlation with the surface absorptivity index. This indicates that this index can be used to predict the optimal amount of water to spray on a given surface.

From a practical standpoint, obtaining the optimal watering rate requires a proper instrumentation of the surface with a thermoflowmeter as well as a heatflowmeter installed in-depth,

even when performing two trials only. However, if such instrumentation cannot be used, parameters involved in the calculation of the total cooling flux still need to be properly estimated. In the lab, this is relatively low cost and easy to implement. On the other hand, in the field, it is invasive and requires the intervention of the relevant city services. For this reason, it is preferable to use the present lab approach and to then transpose it to the field. If not possible, Hendel (2015) has shown that a simple viable alternative for the field was to use surface temperature measurements (with an IR camera for example) to determine the optimal watering frequency and period, and to combine it with an independent measure of the pavement's water holding capacity.

Finally, the partitioning of irradiance and net radiation into atmospheric, ground, upwards and evaporative heat fluxes was studied versus the absorptivity, for dry and optimally-watered pavements. Results show that bituminous structures, i.e. those with the highest absorptivity, are the most detrimental in all regards, while stabilized sand and slag concrete, both fairly insulating and reflective, are the most favourable. From the most to the least favourable pavements respectively, the 1380 W/m² of incident irradiance are partitioned into $1,020 - 770$ W/m² of radiosity, $210 - 360$ W/m² of conduction and $150 - 250$ W/m² of convection. Watering significantly reduces each term, respectively dropping to $580 - 880$ W/m² for radiosity, $165 - 250$ W/m² for conduction and as low as $30 - 70$ W/m² for convection.

In the end, sensible atmospheric convection is significantly reduced, limiting the heating up of air negatively impacting pedestrians. Total optimal cooling ranges from $300 - 480$ W/m², with a greater efficiency for materials with a higher absorptivity index.

In-depth, the transmitted heat flux correlates linearly with a transmission index taking into account the absorptivity and apparent conductivity of the material layers. The most conductive structures (such as granite) tend to conduct as much heat in-depth as the darkest structures, even if they are less absorbent.

More generally, for increased efficiency, cooling techniques should be combined. As well, solutions adapted to the type of location (square, sidewalk, etc.), its characteristics (daily insolation, street orientation, pedestrian traffic, vulnerability of local inhabitants, existing pavement materials, etc.), the people targeted (pedestrians or others), etc., must be deployed in order to properly cool the population. To tackle this aspect, a GIS tool can be used to identify priority areas in terms of population exposure and vulnerability, foreseeing their redesigning into cooler areas. For the case of Paris, such a decision support tool has been developed during the thesis for city services, although not presented in this manuscript. It is based on both physical and socioeconomic criteria to identify sites that would most benefit from pavement-watering based on their cooling potential as well as other operational criteria (Hendel et al., 2020). The tool could also be generalized to propose other cooling solutions adapted to the high cooling potential sites identified. On this basis, simple cooling solutions may be proposed, such as sun-shading or vegetation.

Finally, solutions targeting buildings (solar exposition, ventilation and insulation) should also be considered. Additionally, other aspects could be used as selection criteria: pavement manufacturing CO_2 emissions, impact on biodiversity, water restriction measures, etc. Also, the frequent deployment of pavement-watering for emergency cooling merits implementing

an automated sprinkling system connected to the non-potable water network or re-using collected rainwater. In this respect, synergies with other urban planning projects are also interesting, such as the use of pervious materials for the collection and reuse of rainwater, whether for pavement-watering or not. In addition to reducing the watering frequency for a given rate, pervious materials are also useful for stormwater management and would help store water already used today for street cleaning, thus providing much welcome evaporation in the summer at the same time. For Paris, city services are already pursuing such measures to reduce discharge to the Seine river and other local waterways.

PART V

GENERAL CONCLUSION

CHAPTER 22

Conclusion

The analysis of field and lab pavement-watering tests is now completed. Over the summers of 2013 to 2018, two watering protocols were implemented at rue du Louvre. In the lab, an experiment reproducing heat-wave like conditions was developed and a variety of watering rates were applied on various paving structures, either traditional for the Parisian urban fabric, or innovative, i.e. so-called "cool" pavements. In order to guide decision-makers through the operational adaptation of pavement-watering to different sites, and based on identified limitations in the scientific literature, research questions were defined in Chapter 4. We now look back at these questions which, as a reminder, were the following:

- What statistical tools can be used to evaluate the field effects of UHI-countermeasures?

- How are the cooling effects of watering affected by the proportion of street that is watered?

- What is the efficiency of pavement-watering for a variety of traditional and cool pavements, and what do the corresponding optimal watering rates depend on?

- Based on their surface heat budgets, how is the energy partition of dry and optimally-watered traditional and cool pavements affected?

The research proposed in this manuscript has provided answers to these questions.

22.1 Field Testing

In Part II, a suitable analysis method for the field evaluation of pavement-watering (or other UHI-countermeasures) was proposed to our case study field tests to determine the microclimatic cooling effects associated with two watering protocols. This tool is crucial for evaluating the efficiency of public policies aiming to mitigate urban heat.

22.1.1   Analysis Method

Chapter 6 demonstrated that direct case-control site comparisons are inherently ill-suited to determine the effects of UHI-countermeasures, as they cannot eliminate pre-existing differences between case and control sites prior to the implementation of the countermeasure. To eliminate these, a BACI (Before-After-Control-Impact) experimental design must be adopted. This implies sampling meteorological data simultaneously at case (impact) and control sites, both before countermeasure implementation (reference period), and after the latter (countermeasure period). Additionally, the methodology showed that countermeasure and reference observations are not independent, as they can be expressed in relation to each other, i.e. countermeasure observations depend on the conditions under which the reference measurements were carried out. To account for this, a linear mixed model was proposed. Such model expresses the interstation difference of a meteorological parameter as a function of fixed effects, namely whether the countermeasure is implemented or not. Asymmetric datasets can be treated and clustered into known random factors influencing the observations.

22.1.2   Microclimatic Effects and Proportion of Street Watered

The analysis test identified in Chapter 6 was then applied to a case-study from a pavement-watering experiment conducted in Paris, France since 2013 in Chapter 7. In place of a linear mixed model, a fixed-effects model was used due to the limited number of reference and countermeasure observations. Therefore, no random effects were considered, which could have compromised the statistical robustness of the results. This assessment method is not specific to pavement-watering and can be used with other UHI-countermeasures.

From 2013 to 2015, the pavement and sidewalk were watered. The analysis revealed that the microclimatic effects of pavement-watering reached maximum statistically significant values up to -1.02°C for air temperature, +4.08% for relative humidity, -6.07°C for mean radiant temperature and -1.93°C for UTCI-equivalent temperature, all at pedestrian height. Overall, maximum effects are reached in the end of the afternoon.

From 2016 to 2018, only the pavement was watered (about 66% of total street width). Despite the reduced proportion, statistically significant effects were found, up to -0.97°C for air temperature, +3.03% for relative humidity, -10.01°C for mean radiant temperature and -3.42°C for UTCI-equivalent temperature, all at pedestrian height. However, the duration of the statistically significant effects was roughly divided by two for all parameters, thus unsurprisingly reducing the overall efficiency of the method. The lower statistical significance is most likely due to a less efficient strategy compounded by a reduced signal-to-noise ratio due to the fewer observations for this period. Analyses conducted with the 24-hour averaged watering effects further confirmed that this strategy was far less efficient than watering the whole street, as it yielded weak or no statistically significant effects in comparison.

22.2 Laboratory Testing

Parts III and IV focused on the fine-tuning of pavement-watering in the laboratory on realistic traditional and cool paving structures, forseeing their deployment in the field. Field measurements conducted for the purposes of Part II were used to validate the lab approach.

As previously mentioned in Chapter 3, although pavement-watering provides limited cooling effects compared to green spaces, its cooling efficiency is higher when considering its much lower water footprint (about three times less in the summer), thus making it interesting in densely built urban areas for which greening may not easily be implemented. This is for instance the case for a dense city such as Paris where pavement-watering can be considered as a potential emergency adaptation cooling tool, especially given the availability of its non-potable water network.

As a reminder, the optimal watering rate of the field trials carried out in rue du Louvre was 0.4 mm/h. As per Hendel (2015), for all Parisian street surfaces (2,550 ha) this would represent 56,100 m^3 per day, i.e. about 30% of the non-potable water network production, for a total installed capacity of 500,000 m^3 per day at the production facilities of Auteuil, Austerlitz and la Villette. With regard to its water consumption, the method is therefore considered viable, although the latter scenario is neither desirable nor technically feasible.

Future projections about the growing pressure on water resources confirm the relevance of the proposed optimization of the method's water consumption to limit its negative impact (Habets et al., 2013).

22.2.1 Optimization of Watering

In order to optimize the method, Chapter 11 presented a heat transfer analysis to determine total pavement cooling flux due to watering based on the measurements performed in the lab. In Chapter 12, this protocol was applied to an asphalt road structure similar to that implemented in the field, in order to compare the results of both approaches. In essence, results are consistent with pavement-watering field campaigns when factoring in the stronger (doubled) daily absorbed incident irradiance in the lab, as discussed in Chapter 13. Additional field data with alternative pavements is required to reinforce this comparison. That being said, the lab protocol is suited for comparing the thermal behaviour of different pavements under the fixed conditions of the chamber, even though these may differ from realistic outdoor conditions.

The procedure was thus generalized in Chapter 18 to twelve paving structures, including traditional and cool pavements. Total cooling flux is partitioned into reductions of convection and conduction and an increase in net radiation, the exact value for each component depending on the paving structure's characteristics (albedo, emissivity, conductivity, etc.). A formal optimization of the process was performed by maximizing the pavement cooling flux to watering rate ratio. To do so, a "latent" and a "sensible" cooling regimes were used, the former corresponding to the increase in evaporation of water along with the watering rate, and the latter to the marginal sensible cooling increase having passed the maximum evaporation rate.

The optimal watering rate is thus obtained at the intersection of two watering linear regimes.

The optimal watering rate is well correlated with the surface absorptivity of the pavements. Indeed, as seen in Chapter 17, the absorptivity is the principal driver of the steady-state surface temperature of the pavements, which is also a key parameter for the evaporation rate, all else being equal. In the absence of watering, those surface temperatures reached maximum values of 48° to 62°C depending on the pavement, while the use of thermochromic and near-infrared reflective paints helped reduce the asphalt sidewalk maximum temperature respectively by 6° and 9°C. A good correlation between the optimal watering rate and the albedo is also found.

Finally, results showed that a satisfactory estimate of the optimal watering rate could be obtained by performing one dry test coupled with only one highly watered test for which the cooling flux is assessed, using the theroretical value of the first latent regime's slope and neglecting the sensible regime's sensible cooling flux. Good agreement is found between both methods. Under steady-state conditions in the lab, depending on the pavement, corresponding optimal cooling flows range between 270 and 470 W/m² for optimal surface temperature reductions of 10° to 20°C and for optimal watering rates between 0.51 and 0.80 mm/h (roughly doubled with regard to what would be expected in the field). This information can be used to predict the optimal amount of water to spray on a given surface.

However, from an operational standpoint, complying with a fine-tuned watering rate remains very challenging, given that pavement-watering is currently implemented using cleaning trucks, as discussed in Chapter 20. In this respect, a dedicated watering infrastructure needs to be planned in collaboration with the relevant city services to gain control over the fine tuning of the watering protocol.

22.2.2   Energy Partitioning of Dry and Optimally Watered Pavements

Using the heat transfer analysis of Chapter 11 and the optimal watering rates obtained in Chapter 18, the surface heat budgets of the dry and optimally-watered pavements were fully determined in Chapter 19.

The partitioning of irradiance into radiosity, convective, conductive and cooling flows was analysed. From the less (stabilized sand and slag concrete) to the most (bituminous structures) absorbent pavements respectively, irradiance surface partitioning is split into 1,020 – 770 W/m² of radiosity, 210 – 360 W/m² of conduction and 150 – 250 W/m² of convection. For optimally-watered surfaces, for its part, total optimal cooling ranges from 300 – 480 W/m². Watering significantly reduces each term, respectively dropping to 580 – 880 W/m² for radiosity, 165 – 250 W/m² for conduction and as low as 30 – 70 W/m² for convection. All of those parameters showed good linear agreement with the absorptivity of the surface, including total cooling flux, meaning that the technique is more effective with highly absorptive materials.

Furthermore, an analysis of the cooling flux composition showed that the latter draws differently from the surface heat budget components, depending on the thermo-physical properties of the pavements considered.

Finally, it was found that the transmitted heat flux correlates linearly with a transmission index which accounts for both the surface absorptivity and apparent conductivity of the material layers. Thus, the most conductive structures (such as granite) tend to conduct as much heat in-depth as the darkest structures, even if they are less absorbing.

Discussion and Future Research

The adopted lab experimental protocol of Parts III and IV comes with several limitations and avenues for improvement. In particular, the following questions arose from the analyses of the experimental data:

- How should the protocol be modified to account for the material's perviousness and water retention capacity?

- How can the overall experimental protocol be improved to better describe *in situ* conditions?

- Can materials providing radiative cooling be studied in the lab?

First, as discussed in Chapter 20, the protocol proved to be ill-suited to study the benefits of a pervious structure with regard to an impervious material due to the lack of runoff in the lab. On the contrary, in the field, pervious sub-layers permit lowering the frequency while runoff makes it necessary to water an impervious pavement more frequently, all else being equal. Future improvements shall tackle this aspect by enabling runoff on the edges of the samples. Alternatively, pervious samples could also be watered once and then studied over several consecutive days to study their evaporative performance, provided that their pervious surface course is thin enough to allow water to evaporate.

Lab tests also highlighted that care should be lent to the manufacturing process of construction materials, given their diversity in composition and surface finish. Indeed, in the future the thermo-physical properties of the materials tested should be assessed on samples sourced from the same batch, and then compared to independent measurements performed inside the climate chamber. Such a comparison would permit the evaluation of the thermal resistance and losses inside the insulating casing of the set-up, although these are deemed low.

Additionally, as pointed out by the second question, although the setpoint values imposed for the day and night phases were selected to be representative of a Parisian heat-wave, they remain relatively far from realistic conditions. This leaves room for improvement, for example

by imposing dynamic ramps of temperature, relative humidity and artificial insolation rather than fixed values. This would also allow the study of the samples in transient state, which would be much more realistic and include the impact of a pavements' thermal inertia. The use of lamps better matching the AM 1.5 solar spectrum needs to be considered, as halogen lamps are shifted in the infrared band. This shift will mostly play a role on the value of the pavements' albedos. For instance, the near-infrared reflective paint's albedo is reduced by 11% considering the solar spectrum, and is thus expected to be less favourable under real outdoor conditions. Measuring the averaged irradiance at the sample surface using a disk-shaped sensor of 16 cm in diameter instead of the current 1 cm² sensor placed at the centre will also be considered. Regardless of how many improvements are implemented, a lab experiment will never capture the full reality of field conditions and can only provide simplified pavement behaviours. On the other hand, more flexibility is available for instrumentation of the samples than in the field.

Generally speaking, further comparison of the lab results with field tests would also be useful. These would assess the durability over time and soiling of paint coatings, and should be completed with microclimatic measurements to estimate the effective gain on pedestrian heat stress. Other surfaces could be tested with the set-up, such as façades, or rooftops in order to evaluate the energy savings of a building (Chaumont et al., 2019).

Finally, the last question of this discussion addresses radiative cooling as a heat mitigation strategy. While it is a well-known phenomenon which is frequently observed at night and is responsible for the formation of dew on urban surfaces (Trosseille et al., 2019), recently developed metamaterials can help materials remain cooler than the air even during the day (Hossain and Gu, 2016; Family and Mengüç, 2017; Ko et al., 2019). This is achieved thanks to selective optical properties, combining high reflectivity with high emissivity in the $8 - 13 \ \mu m$ range.

To begin investigating such materials, preliminary tests were conducted with the lab experiment on a white-painted concrete sample ($\alpha = 0.65$, $\epsilon = 0.95$). Figure 23.1 illustrates the radiative behaviour of the samples. The dashed line represents the behaviour predicted by using the linear regression obtained for the surface temperature increase as a function of absorptivity (a) from Figure 17.2 (Section 17.1), and injecting it into the expression of $R_n/S+L$.

As can be seen, the absorptivity of the sample remains too high to exhibit radiative cooling. Finding an appropriate material is very challenging as an albedo of at least 0.91 (see Section 17.1) is required, assuming an emissivity 0.95. Such materials may also modify the radiative environment of the experiment due to additional reflection within the climate chamber.
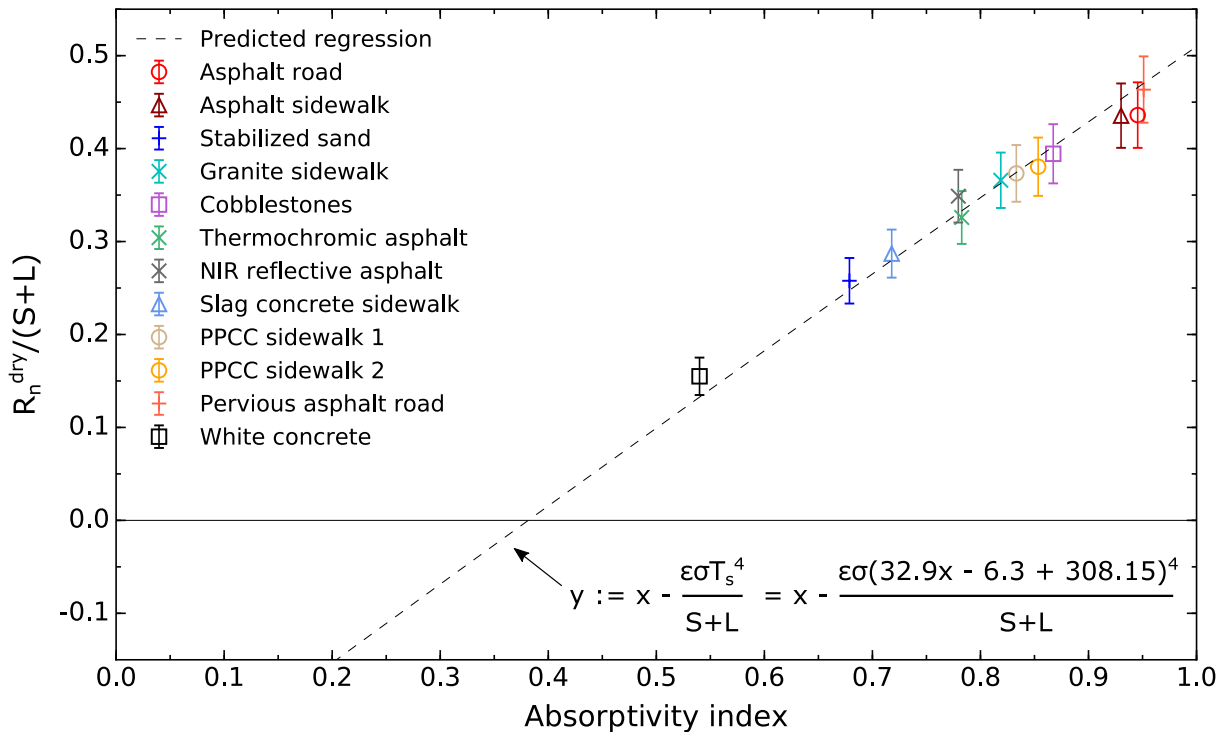
Figure 23.1: Steady-state net radiation to irradiance as a function of the absorptivity for non-watered pavements. The predictive behaviour (dashed) is obtained by injecting the linear regression of the surface temperature increase versus the absorptivity (Figure 17.2) into the analytical expression of $R_n/S{+}L$, as detailed on the Figure.

With regard to the *in situ* analysis method of the microclimatic effects, although our research questions were successfully answered, light still needs to be shed on several aspects presented in Part II that could be explored in future work:

- Which random effects can be identified and included in the analysis?

- What would the microclimatic cooling effects of pavement-watering be on other pavement materials, for another street orientation or canyon aspect ratio?

- Overall, how can the analysis method be improved?

Regarding the first question, future avenues for improvement of the analysis mainly concern taking into account relevant random factors to apply a proper LMM, as only a fixed-effects model was used in Part II. However, this requires a larger statistical sample to be relevant. In its current state, the FEM assesses a global impact of the countermeasure on the whole set of observations, regardless of potential intra-correlations between datasets caused by random factors (weather or insolation conditions, summer period, etc.). These must be investigated to incorporate their influence on the gathered data.

In particular, BACI requires paying attention to external factors influencing the measurements (weather typing, solar mask, wind conditions, etc.), especially given the complexity of

the urban microclimate.

In the general case, most of these factors cannot be controlled for and are additional nuisances to the analyses. This can be traffic conditions, instrument soiling, etc. However, some factors could be looked into. For example, meteorological conditions are likely to influence microclimatic measurements. Given the timeframe of the study, significant variations in solar irradiance occur. Even though weather conditions were filtered, they do not account for changes in insolation between June and mid-September. To illustrate this, Figure 23.2 shows the 24h net radiation for each summer at the case site from 2014 to 2018. Reference, watered and ordinary days are respectively represented in red, blue and light-grey.
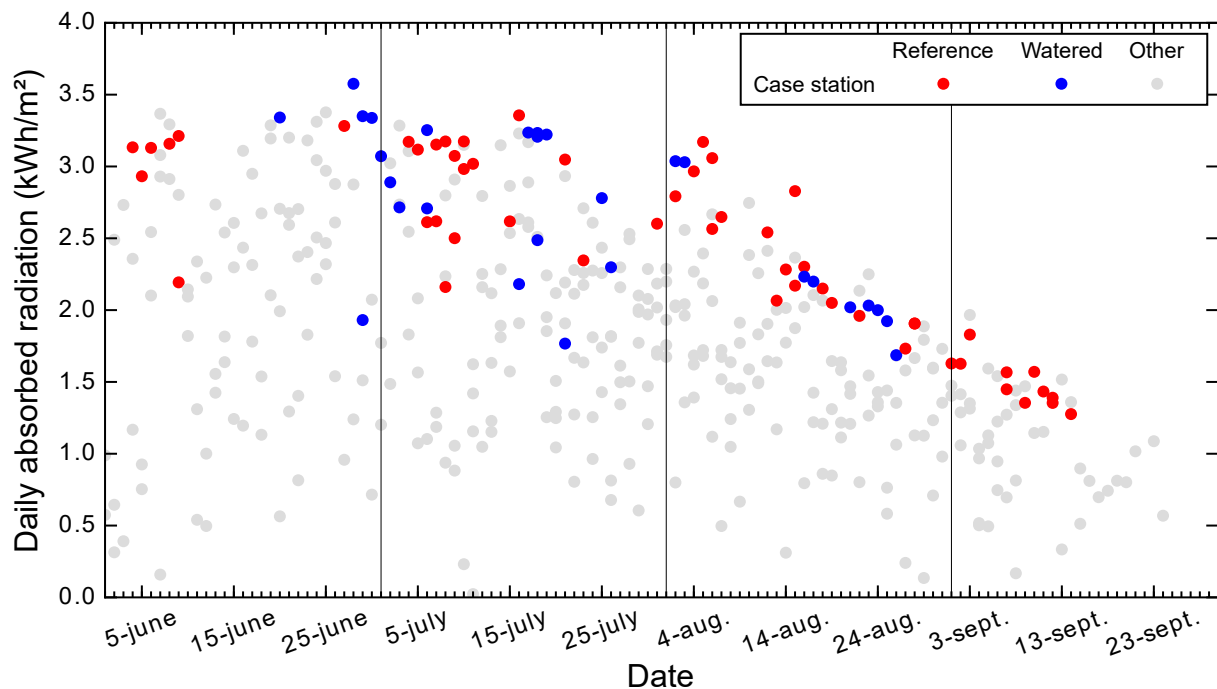
Figure 23.2: Daily net radiation at Louvre for the case site from summers 2014 to 2018. Reference, watered and ordinary days are represented by red, blue and grey markers, respectively (Parison et al., 2020d).

Another example would be to examine if the data analysis induces lagged-correlation in time when reference days either follow or precede watering days. Given the complete set of observations used with the FEM, if any, such effects were undoubtedly smoothed out. However, the exact influence could be studied using LMM.

Therefore, future analyses would merit investigation of random effects (e.g. influence of the summer period, potential time-lagged correlations, etc.) to identify and eliminate potential intra-correlations between our observations. However, such analyses require proper monitoring both before and after countermeasure implementation for the method to be robust, with at least $10 - 30$ reference and countermeasure observations for each random cluster.

The second question deals with the microclimatic effects of pavement-watering on alternative pavements and sites. In this manuscript, the impact of the proportion of street watered

on the microclimatic effects of pavement-watering was assessed. However, currently, these were only determined for a single site, i.e. for a given paving structure, street orientation and canyon aspect ratio. The thermal effects of watering were closely studied in the lab on a variety of traditional and cool structures, however their microclimatic cooling effects and of their watering still needs assessment. Indeed, according to Qin (2015), although low pavement surface temperatures should help reduce air temperature in urban areas, their precise effect on the urban canopy layer as well as pedestrians' thermal stress, surrounding buildings, etc., remains poorly known. Knowledge in this area will thus need to be refined in future research.

In this regard, the microclimatic cooling effects of alternative pavements and their watering should be assessed on other sites. This is one the goals of the Paris City Hall's project *Life Cool & Low Noise Asphalt* (2017), launched in July 2017, which in addition to the microclimatic effects aims to assess the acoustic performance of innovative pavements implemented on three experimental sites in Paris. Preliminary results were presented at three conferences (Parison et al., 2019b,c; Chanial et al., 2020). One of these is available in the Appendix B for more details.

The last question which arose in this discussion addresses the overall improvement of the analysis method, which is based on a BACI design and therefore inherits its limitations. For instance, in ever changing urban environments, a study lasting several years may be subject to data drifting due to long term or periodic effects, potentially making the earliest and latest observation periods incomparable. The design assesses the difference between countermeasure and reference interstation profiles, and attributes it to the countermeasure implementation exclusively. Also, in the case where control and case sites are close enough to both be affected by the UHI-countermeasure, the BACI contrast will likely be reduced, thus leading to an underestimation of the countermeasure effects. In the literature, those issues are pinpointed as the main limitations of the simple BACI design (Smith, 2014). Possibilities for improvement mainly concern the implementation of a multiple BACI design (MBACI), involving a network of control stations spread across the direct vicinity of the case station (Downes et al., 2002). This limits the problem of poorly-matched sites and improves the reliability of the analysis.

For the general case, provided that enough data is available, the impact of the expected causes of long-term or periodic data drifting can be isolated by adding a corresponding random effect in a LMM. In the case of strong dependence to these effects, it is expected that the margin of error of the test would be narrowed. In either case, correlation of the datasets to random effects will be even smaller provided that case and control stations are carefully paired and that analysis days are filtered using given criteria, for example such that shading patterns change in a similar fashion. Otherwise, the effects of the countermeasure may not be properly isolated. The criteria that is chosen will most likely help filter large, local and long-lasting random effects. Finally, Bayesian or machine learning approaches as alternative statistical tools could also be useful for further improvements of the method.

In the future, it will be possible to look into these aspects in greater detail thanks to the recent installation of numerous weather stations for the needs of various heat mitigation projects, such as the *Life Cool & Low Noise Asphalt* project, or the ERDF UIA *OASIS* project, part of the City of Paris' Resilience Strategy (Paris City Hall, 2017b), that aims to transform Parisian schoolyards into so-called "urban cool islands" that would benefit both pupils and local inhabi-

tants ([Karam et al.](), [2019a,b]()). As well, the project *Lisière d'une Tierce Forêt* in the Paris metropolitan area, consists in the conversion of a parking-lot from an asphalt-concrete paved area to an open green space with a pervious concrete pavement ([Parison et al.](), [2018](), [2020a](), see Appendix C).

The weather stations installed for the aforementioned projects constitute the *LUTECE* network, which offers extensive microclimatic coverage of Paris. The position of each weather station is depicted in Figure [23.3]() below.
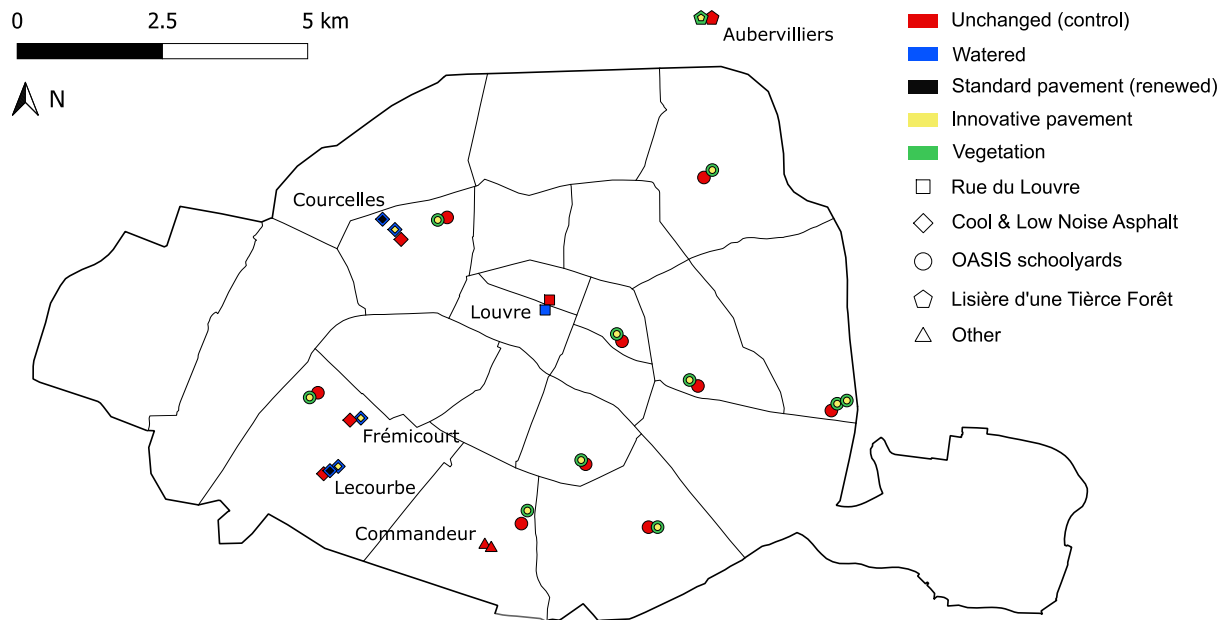
Figure 23.3: Position of the weather stations of the *LUTECE* network in Paris, France. The color and shape of each marker respectively describe the type of countermeasure implemented and the project to which stations are related. Control stations are depicted in red.

The *LUTECE* network creates opportunities for further improvement of the analysis method. For instance, the [MBACI]() design could be applied and tested to reinforce the degree of certainty about the estimated countermeasure impact. As well, for a given countermeasure type (pavement-watering, vegetation, etc.), all observation sites can be treated simultaneously with a fixed-effects approach, while the site position could be chosen as a random effect, in order to determine the influence of a site's characteristics on the countermeasure impact. The same goes for other parameters, such as the period of summer previously mentioned. Applying such an approach to the random effects could give valuable insights on the impact of a countermeasure and also help discard parameters identified as irrelevant *a posteriori*.

Although briefly discussed, the transfer of scientific results and knowledge to decision-makers and urban operators has not been formally addressed in this manuscript. In effect, the question of the actual implementation of studied urban cooling solutions remains unresolved, as well as that of decision-makers' arbitration between different cooling solutions. The use of a [GIS]() tool, briefly mentioned in Chapter [21](), can help address this question by integrating relevant data and methodologies within a tool urban stakeholders are often already familiar

with. Further investigation is required to determine the limits of this approach which may not be suited to all forms of scientific knowledge or results.

On a more general note, our research has mainly focused on the microclimatic and thermal effects of watering on the basis of physical measurements. However, other important dimensions were omitted, such as air pollution, energy and financial costs, the mechanical resistance and skidding properties of pavements, or the social perception of proposed solutions. The latter could be explored via surveys to determine user-perceived cooling on the one hand, and user perception of a specific cooling technique on the other, for example. Given the efforts made to promote water-saving measures in France and Europe, the social perception of cooling methods requiring the use of water is just as crucial as optimizing the methods' water consumption in the eyes of decision-makers and elected officials.

Bibliography

Akbari, H., Bretz, S., Kurn, D. M., and Hanford, J. (1997). Peak power and cooling energy savings of high-albedo roofs. *Energy and Buildings*, 25(2):117–126. 20

Akbari, H. and Hosseini, M. (2014). Cool roofs in cold climates: Savings or penalties? In *Proceedings of the Third International Conference on Countermeasures to Urban Heat Island*, pages 13–15. 21

Akbari, H. and Taha, H. (1992). The impact of trees and white surfaces on residential heating and cooling energy use in four canadian cities. *Energy*, 17(2):141–149. 20

Alchapar, N. L., Correa Cantaloube, E. N., and Canton, M. A. (2013). Solar reflectance index of pedestrian pavements and their response to aging. 21

Anandakumar, K. (1999). A study on the partition of net radiation into heat fluxes on a dry asphalt surface. *Atmospheric Environment*, 33(24-25):3911–3918. 103

Armson, D., Stringer, P., and Ennos, A. (2012). The effect of tree shade and grass on surface and globe temperatures in an urban area. *Urban Forestry & Urban Greening*, 11(3):245–255. 24

Asaeda, T. and Ca, V. T. (2000). Characteristics of permeable pavement during hot summer weather and impact on the thermal environment. *Building and Environment*, 4(35):363–375. 23

Asaeda, T., Ca, V. T., and Wake, A. (1996). Heat storage of pavement and its effect on the lower atmosphere. *Atmospheric environment*, 30(3):413–427. 11, 75, 76, 103, 123

ASHRAE (2001). Ashrae fundamentals handbook 2001 (SI edition). *American Society of Heating, Refrigerating, and Air-Conditioning Engineers*, 31. 14

ASHRAE (2017). *Thermal Environmental Conditions for Human Occupancy: ANSI/ASHRAE Standard 55-2017*. American Society of Heating, Refrigerating and Air-Conditioning Engineers. 12, 13

ASTM E903 (2012). Standard test method for solar absorptance, reflectance, and transmittance of materials using integrating spheres. 107

ASTM G173 (2003). Standard tables for reference solar spectral irradiances: direct normal and hemispherical on 37° tilted surface. 20

Athukorallage, B., Dissanayaka, T., Senadheera, S., and James, D. (2018). Performance analysis of incorporating phase change materials in asphalt concrete pavements. *Construction and building materials*, 164:419–432. 22

Azam, M.-H., Bernard, J., Morille, B., Musy, M., and Andrieu, H. (2018). A pavement-watering thermal model for SOLENE-microclimat: development and evaluation. *Urban Climate*, 25:22–36. 29, 31, 32, 34, 36, 37, 40, 41, 42, 43, 45

Balling Jr, R. C. and Brazel, S. W. (1987). Time and space characteristics of the Phoenix urban heat island. *Journal of the Arizona-Nevada Academy of Science*, pages 75–81. 19

Bernstein, B. B. and Zalinski, J. (1983). An optimum sampling design and power tests for environmental biologists. *Journal of Environmental Management*, 16(1):35–43. 56

Binarti, F., Koerniawan, M. D., Triyadi, S., Utami, S. S., and Matzarakis, A. (2020). A review of outdoor thermal comfort indices and neutral ranges for hot-humid regions. *Urban Climate*, 31:100531. 15, 16, 18

Błażejczyk, K., Broede, P., Fiala, D., Havenith, G., Holmér, I., Jendritzky, G., Kampmann, B., and Kunert, A. (2010). Principles of the new Universal Thermal Climate Index (UTCI) and its application to bioclimatic research in European scale. *Miscellanea Geographica*, 14(1):91–102. 17, 61

Błażejczyk, K., Jendritzky, G., Bröde, P., Fiala, D., Havenith, G., Epstein, Y., Psikuta, A., and Kampmann, B. (2013). An introduction to the Universal Thermal Climate Index (UTCI). *Geographia Polonica*, 86(1):5–10. 17

Bobes-Jesus, V., Pascual-Muñoz, P., Castro-Fresno, D., and Rodriguez-Hernandez, J. (2013). Asphalt solar collectors: a literature review. *Applied Energy*, 102:962–970. 22

Bolker, B. M., Brooks, M. E., Clark, C. J., Geange, S. W., Poulsen, J. R., Stevens, M. H. H., and White, J.-S. S. (2009). Generalized linear mixed models: a practical guide for ecology and evolution. *Trends in ecology & evolution*, 24(3):127–135. 56

Boriboonsomsin, K. and Reza, F. (2007). Mix design and benefit evaluation of high solar reflectance concrete for pavements. *Transportation research record*, 2011(1):11–20. 20

Bouvier, M., Brunner, A., and Aimé, F. (2013). Nighttime watering streets and induced effects on the surrounding refreshment in case of hot weather. the city of paris experimentations. *Tech. Sci. Méthodes*, 12:43–55. *(in French)*. 28, 29, 31, 32, 34, 37, 38, 40, 41, 45, 75

Bowler, D. E., Buyung-Ali, L., Knight, T. M., and Pullin, A. S. (2010). Urban greening to cool towns and cities: A systematic review of the empirical evidence. *Landscape and urban planning*, 97(3):147–155. 24

Broadbent, A. M., Coutts, A. M., Tapper, N. J., and Demuzere, M. (2018). The cooling effect of irrigation on urban microclimate during heatwave conditions. *Urban climate*, 23:309–329. 29, 31, 34, 37, 38, 39, 40, 45

Bröde, P. (2009). UTCI fast-calculation script. Documents available online: http://www.utci.org/utci_doku.php (accessed: February 2020). 17, 61

Bröde, P., Fiala, D., Błażejczyk, K., Holmér, I., Jendritzky, G., Kampmann, B., Tinz, B., and Havenith, G. (2012). Deriving the operational procedure for the universal thermal climate index (utci). *International journal of biometeorology*, 56(3):481–494. 17, 61

Camuffo, D. and Bernardi, A. (1982). An observational study of heat fluxes and their relationships with net radiation. *Boundary-Layer Meteorology*, 23(3):359–368. 103

Cantat, O. (2004). L'îlot de chaleur urbain parisien selon les types de temps. *(in French)*. 8

Chanial, M., Parison, S., Hendel, M., and Royon, L. (2020). Etude du comportement thermique et microclimatique de revêtements innovants pour le projet *Life Cool & Low Noise Asphalt*. 33*eme* colloque annuel de l'Association Internationale de Climatologie. *(in French)*. 149

Chaumont, M., Parison, S., Hendel, M., and Royon, L. (2019). Study of the thermal behaviour of unplanted extensive green roof sample according to the nature of the substrate. *5th International Conference on Countermeasures to Urban Heat Islands*. 146

Chaves, L. F. (2010). An entomologist guide to demystify pseudoreplication: data analysis of field studies with design constraints. *Journal of medical entomology*, 47(3):291–298. 56

Chen, B.-L., Bhowmick, S., and Mallick, R. B. (2009). A laboratory study on reduction of the heat island effect of asphalt pavements. *Journal of the Association of Asphalt Paving Technologists*, 78:209–248. 103, 130

Chen, M. Z., Hong, J., Wu, S. P., Lu, W., and Xu, G. J. (2011). Optimization of phase change materials used in asphalt pavement to prevent rutting. In *Advanced materials research*, volume 219, pages 1375–1378. Trans Tech Publ. 22

Christen, A. and Vogt, R. (2004). Energy and radiation balance of a central european city. *International Journal of Climatology: A Journal of the Royal Meteorological Society*, 24(11):1395–1421. 11

Chun, B. and Guldmann, J.-M. (2018). Impact of greening on the urban heat island: Seasonal variations and mitigation strategies. *Computers, Environment and Urban Systems*, 71:165–176. 24

Cohard, J.-M., Rosant, J.-M., Rodriguez, F., Andrieu, H., Mestayer, P. G., and Guillevic, P. (2018). Energy and water budgets of asphalt concrete pavement under simulated rain events. *Urban climate*, 24:675–691. 29, 31, 32, 36, 37, 40, 41, 42, 43, 45

Conner, M. M., Saunders, W. C., Bouwes, N., and Jordan, C. (2016). Evaluating impacts using a BACI design, ratios, and a Bayesian approach with a focus on restoration. *Environmental monitoring and assessment*, 188(10):555. 53

Conquest, L. L. (2000). Analysis and interpretation of ecological field data using BACI designs: discussion. *Journal of Agricultural, Biological, and Environmental Statistics*, pages 293–296. 56

Daniel, M., Lemonsu, A., and Viguie, V. (2018). Role of watering practices in large-scale urban planning strategies to face the heat-wave risk in future climate. *Urban Climate*, 23:287–308. 24, 29, 31, 32, 34, 37, 38, 39, 40, 42, 45, 75, 112

De Freitas, C. R. and Grigorieva, E. A. (2015). A comprehensive catalogue and classification of human thermal climate indices. *International journal of biometeorology*, 59(1):109–120. 18

De Munck, C. (2013). *Modélisation de la végétation urbaine et stratégies d'adaptation pour l'amélioration du confort climatique et de la demande énergétique en ville*. PhD thesis, École Doctorale Sciences de l'Univers, de l'Environnement et de l'Espace. 24

De Munck, C., Lemonsu, A., Masson, V., Le Bras, J., and Bonhomme, M. (2018). Evaluating the impacts of greening scenarios on thermal comfort and energy and water consumptions for adapting paris city to climate change. *Urban Climate*, 23:260–286. 24

Doulos, L., Santamouris, M., and Livada, I. (2004). Passive cooling of outdoor urban spaces. the role of materials. *Solar energy*, 77(2):231–249. 76, 86

Dousset, B., Gourmelon, F., Laaidi, K., Zeghnoun, A., Giraudet, E., Bretin, P., Mauri, E., and Vandentorren, S. (2011). Satellite monitoring of summer heat waves in the Paris metropolitan area. *International Journal of Climatology*, 31(2):313–323. 8

Downes, B. J., Barmuta, L. A., Fairweather, P. G., Faith, D. P., Keough, M. J., Lake, P. S., Mapstone, B. D., Quinn, G. P., et al. (2002). *Monitoring ecological impacts: concepts and practice in flowing waters.* Cambridge University Press. 149

Efthymiou, C., Santamouris, M., Kolokotsa, D., and Koras, A. (2016). Development and testing of photovoltaic pavement for heat island mitigation. *Solar Energy*, 130:148–160. 22

English, P. W. (1998). Qanats and lifeworlds in Iranian plateau villages. *Yale F&ES Bulletin*, 103:187–205. 3

Erell, E., Pearlmutter, D., Boneh, D., and Kutiel, P. B. (2014). Effect of high-albedo materials on pedestrian heat stress in urban street canyons. *Urban Climate*, 10:367–386. 21, 75

Family, R. and Mengüç, M. P. (2017). Materials for radiative cooling: a review. *Procedia environmental sciences*, 38:752–759. 146

Fiala, D., Havenith, G., Bröde, P., Kampmann, B., and Jendritzky, G. (2012). UTCI-Fiala multi-node model of human heat transfer and temperature regulation. *International journal of biometeorology*, 56(3):429–441. 17

Gagge, A. P., Fobelets, A., Berglund, L., et al. (1986). A standard predictive index of human response to the thermal environment. *ASHRAE trans*, 92(2):709–731. 18

Gilbert, H. E., Rosado, P. J., Ban-Weiss, G., Harvey, J. T., Li, H., Mandel, B. H., Millstein, D., Mohegh, A., Saboori, A., and Levinson, R. M. (2017). Energy and environmental consequences of a cool pavement campaign. *Energy and Buildings*, 157:53–77. 21

Girard, L. (1923). Lutte contre la poussière. In *Le nettoiement de Paris*, Chapter 13, 109–120. Paris, France, Léon Eyrolles. *(in French)*. 3

Graves, K. (1974). Globe thermometer evaluation. *American Industrial Hygiene Association Journal*, 35(1):30–40. 15

Grimmond, S. U. E. (2007). Urbanization and global environmental change: local effects of urban warming. *Geographical Journal*, 173(1):83–88. 8

Guo, H., Aviv, D., Loyola, M., Teitelbaum, E., Houchois, N., and Meggers, F. (2019). On the understanding of the mean radiant temperature within both the indoor and outdoor environment, a critical review. *Renewable and Sustainable Energy Reviews*, page 109207. 13, 14, 15

Guo, L. and Lu, Q. (2017). Potentials of piezoelectric and thermoelectric technologies for harvesting energy from pavements. *Renewable and Sustainable Energy Reviews*, 72:761–773. 22

Guo, X. and Hendel, M. (2018). Urban water networks as an alternative source for district heating and emergency heat-wave cooling. *Energy*, 145:79–87. 24

Habets, F., Boé, J., Déqué, M., Ducharne, A., Gascoin, S., Hachour, A., Martin, E., Pagé, C., Sauquet, E., Terray, L., et al. (2013). Impact of climate change on the hydrogeology of two basins in northern France. *Climatic change*, 121(4):771–785. 141

Haselbach, L., Boyer, M., Kevern, J. T., and Schaefer, V. R. (2011). Cyclic heat island impacts on traditional versus pervious concrete pavement systems. *Transportation research record*, 2240(1):107–115. 23

Havenith, G. (1999). Heat balance when wearing protective clothing. *Annals of occupational Hygiene*, 43(5):289–296. 13

Havenith, G., Fiala, D., Błazejczyk, K., Richards, M., Bröde, P., Holmér, I., Rintamaki, H., Benshabat, Y., and Jendritzky, G. (2012). The UTCI-clothing model. *International journal of biometeorology*, 56(3):461–470. 17

Hendel, M. (2015). *Pavement-Watering in Cities for Urban Heat Island Mitigation and Climate Change Adaptation: A Study of Its Cooling Effects and Water Consumption in Paris*. PhD thesis, Sorbonne Paris Cité. 4, 28, 29, 31, 32, 33, 34, 35, 37, 38, 39, 41, 42, 45, 134, 141

Hendel, M. (2020). Cool pavements. In Pacheco-Torgal, F., Amirkhanian, S., Wang, H., and Schlangen, E. (Eds.). *Eco-Efficient Pavement Construction Materials* (1st edition), Book Chapter 6, 96–125. Woodhead Publishing. 11, 19

Hendel, M., Bobée, C., Karam, G., Parison, S., Berthe, A., Bordin, P., and Royon, L. (2020). Developing a GIS tool for emergency urban cooling in case of heat-waves. *Urban Climate*. 134

Hendel, M., Colombert, M., Diab, Y., and Royon, L. (2014). Improving a pavement-watering method on the basis of pavement surface temperature measurements. *Urban Climate*, 10:189–200. 28, 33, 40, 58, 86, 95

Hendel, M., Colombert, M., Diab, Y., and Royon, L. (2015a). An analysis of pavement heat flux to optimize the water efficiency of a pavement-watering method. *Applied thermal engineering*, 78:658–669. 28, 33, 34, 42, 43, 58, 66, 75, 76, 83, 84, 86, 89, 90, 95, 96, 97, 131

Hendel, M., Gutierrez, P., Colombert, M., Diab, Y., and Royon, L. (2016). Measuring the effects of urban heat island mitigation techniques in the field: Application to the case of pavement-watering in Paris. *Urban Climate*, 16:43–58. 28, 38, 39, 40, 44, 51, 53, 58, 59, 60, 65, 69, 70, 78

Hendel, M., Parison, S., Grados, A., and Royon, L. (2018). Which pavement structures are best suited to limiting the UHI effect? A laboratory-scale study of Parisian pavement structures. *Building and Environment*, 144:216–229. 48, 76, 78, 79, 83, 86, 108, 111, 113, 129

Hendel, M. and Royon, L. (2015). The effect of pavement-watering on subsurface pavement temperatures. *Urban Climate*, 14:650–654. 28, 41, 58

Hendel, M. A., Colombert, M., Diab, Y., and Royon, L. (2015b). Measurement of the cooling efficiency of pavement-watering as an urban heat island mitigation technique. *Journal of Sustainable Development of Energy, Water and Environment Systems*, 3(1):1–11. 28

Hoelscher, M.-T., Nehls, T., Jänicke, B., and Wessolek, G. (2016). Quantifying cooling effects of facade greening: Shading, transpiration and insulation. *Energy and Buildings*, 114:283–290. 51

Höppe, P. (1999). The physiological equivalent temperature–a universal index for the biometeorological assessment of the thermal environment. *International journal of Biometeorology*, 43(2):71–75. 16

Höppe, P. R. (1993). Heat balance modelling. *Experientia*, 49(9):741–746. 16

Hossain, M. M. and Gu, M. (2016). Radiative cooling: principles, progress, and potentials. *Advanced Science*, 3(7):1500360. 146

Howard, L. (1833). The climate of London, vol. 1. *London: Harvey and Darton*. 7

Hurlbert, S. H. (1984). Pseudoreplication and the design of ecological field experiments. *Ecological monographs*, 54(2):187–211. 53

Husson, G. P. (1996). Historique de l'alimentation en eau potable de la ville de Paris. 4

ISO 7726 (1998). Ergonomics of the thermal environment — instruments for measuring physical quantities. 14, 59

Jendritzky, G. and Nübler, W. (1981). A model analysing the urban thermal environment in physiologically significant terms. *Archives for meteorology, geophysics, and bioclimatology, Series B*, 29(4):313–326. 18

Jiang, W., Yuan, D., Xu, S., Hu, H., Xiao, J., Sha, A., and Huang, Y. (2017). Energy harvesting from asphalt pavement using thermoelectric technology. *Applied Energy*, 205:941–950. 22

Johansson, E., Thorsson, S., Emmanuel, R., and Krüger, E. (2014). Instruments and methods in outdoor thermal comfort studies–the need for standardization. *Urban climate*, 10:346–366. 43

Jürges, W. (1924). Heat transfer on a flat wall. *Beihefte zum Gesundheits-Ingenieur*, 19(1):1227–1249. (*in German*). 10, 82

Kántor, N. and Unger, J. (2011). The most problematic variable in the course of human-biometeorological comfort assessment—the mean radiant temperature. *Open Geosciences*, 3(1):90–100. 15

Karam, G., Hendel, M., Bobée, C., Berthe, A., Bordin, P., and Royon, L. (2019a). The OASIS Project: UHI mitigation strategies applied to Parisian schoolyards. *5th International Conference on Countermeasures to Urban Heat Islands*. 150

Karam, G., Parison, S., Bobée, C., Berthe, A., Bordin, P., Hendel, M., and Royon, L. (2019b). Projet Cours OASIS: atténuation des îlots de chaleur urbains dans les cours d'école. *XIVeme Colloque International Franco-Québécois en Energie. (in French)*. 150

Karlessi, T., Santamouris, M., Apostolakis, K., Synnefa, A., and Livada, I. (2009). Development and testing of thermochromic coatings for buildings and urban structures. *Solar Energy*, 83(4):538–551. 22, 112

Kevern, J. T., Schaefer, V. R., and Wang, K. (2009). Temperature behavior of pervious concrete systems. *Transportation Research Record*, 2098(1):94–101. 23

Kinouchi, T. and Kanda, M. (1998). Cooling effect of watering on paved road and retention in porous pavement. In *Second Symposium on Urban Environment*, pages 255–258. 28, 29, 31, 35, 39, 40, 41, 42, 43, 45

Kinouchi, T., Kanda, M., Kuriki, M., and Kobayashi, H. (1994). An observation of the climatic effect of watering on paved roads. *Proceedings of Hydraulic Engineering*, 38:381–386. 51, 75

Kinouchi, T., Kanda, M., Kuriki, M., and Koboyashi, H. (1997). An observation of the climatic effect of watering on paved roads. *Journal of hydroscience and hydraulic engineering*, 15(1):55–64. 29, 31, 37, 38, 39, 40, 41, 42, 45

Ko, B., Lee, D., Badloe, T., and Rho, J. (2019). Metamaterial-based radiative cooling: Towards energy-free all-day cooling. *Energies*, 12(1):89. 146

Kolokotsa, D., Santamouris, M., and Zerefos, S. (2013). Green and cool roofs' urban heat island mitigation potential in European climates for office buildings under free floating conditions. *Solar Energy*, 95:118–130. 20

Koschenz, M. and Lehmann, B. (2004). Development of a thermally activated ceiling panel with PCM for application in lightweight and retrofitted buildings. *Energy and buildings*, 36(6):567–578. 22

Kubo, K., Kido, H., and Ito, M. (2006). Study on pavement technologies to mitigate the heat island effect and their effectiveness. *10th International Conference on Asphalt Pavements, Quebec City, Canada*, pages 223–232. 23, 28, 29, 31, 32, 36, 38, 40, 45

Kyriakodis, G. and Santamouris, M. (2018). Using reflective pavements to mitigate urban heat island in warm climates-results from a large scale urban mitigation project. *Urban Climate*, 24:326–339. 51

Lekner, J. and Dorf, M. C. (1988). Why some things are darker when wet. *Applied Optics*, 27(7):1278–1280. 27

Lemke, B. and Kjellstrom, T. (2012). Calculating workplace WBGT from meteorological data: a tool for climate change assessment. *Industrial Health*, 50(4):267–278. 15

Lemonsu, A., Kounkou-Arnaud, R., Desplat, J., Salagnac, J.-L., and Masson, V. (2013). Evolution of the Parisian urban climate under a global changing climate. *Climatic change*, 116(3-4):679–692. 4, 8, 60

Levinson, R., Akbari, H., and Reilly, J. C. (2007). Cooler tile-roofed buildings with near-infrared-reflective non-white coatings. *Building and Environment*, 42(7):2591–2605. 21, 112, 113

Li, D. and Bou-Zeid, E. (2013). Synergistic interactions between urban heat islands and heat waves: The impact in cities is larger than the sum of its parts. *Journal of Applied Meteorology and Climatology*, 52(9):2051–2064. 8

Li, H. (2015). A comparison of thermal performance of different pavement materials. In *Eco-Efficient Materials for Mitigating Building Cooling Needs*, pages 63–124. Elsevier. 76

Li, H., Harvey, J., Holland, T., and Kayhanian, M. (2013a). Corrigendum: The use of reflective and permeable pavements as a potential practice for heat island mitigation and stormwater management. *Environ. Res. Lett*, 8(4):049501. 29, 31, 32, 37, 40, 41, 45, 103

Li, H., Harvey, J., and Jones, D. (2013b). Cooling effect of permeable asphalt pavement under dry and wet conditions. *Transportation Research Record*, 2372(1):97–107. 29, 31, 32, 36, 37, 41, 45, 75

Li, H., Harvey, J., and Kendall, A. (2013c). Field measurement of albedo for different land cover materials and effects on thermal performance. *Building and environment*, 59:536–546. 21, 103, 113

Lin, T.-P., Yang, S.-R., Chen, Y.-C., and Matzarakis, A. (2019). The potential of a modified physiologically equivalent temperature (mPET) based on local thermal comfort perception in hot and humid regions. *Theoretical and Applied Climatology*, 135(3-4):873–876. 16

Liu, Y., Li, T., and Peng, H. (2018). A new structure of permeable pavement for mitigating urban heat island. *Science of the Total Environment*, 634:1119–1125. 23

Loughin, T. M., Bennett, S. N., and Bouwes, N. W. (2018). A comparison of asymmetric Before-After Control Impact (aBACI) and staircase experimental designs for testing the effectiveness of stream restoration. *BioRxiv*, page 359406. 53

Lowry, W. P. (1977). Empirical estimation of urban effects on climate: a problem analysis. *Journal of applied meteorology*, 16(2):129–135. 7, 35, 44, 53, 207

Ma, Y. and Zhu, B. (2009). Research on the preparation of reversibly thermochromic cement based materials at normal temperature. *Cement and Concrete Research*, 39(2):90–94. 20

Mahedi, M., Cetin, B., and Cetin, K. S. (2019). Freeze-thaw performance of phase change material (PCM) incorporated pavement subgrade soil. *Construction and Building Materials*, 202:449–464. 22

Maillard, P., David, F., Dechesne, M., Bailly, J.-B., and Lesueur, E. (2014). Characterization of the urban heat island and evaluation of a road humidification mitigation solution in the district of La Part-Dieu, Lyon (France). *Tech. Sci. Méthodes*, 6(6):23–35. *(in French)*. 28, 29, 31, 32, 39, 40, 45

Mallick, R. B., Chen, B.-L., and Bhowmick, S. (2009). Harvesting energy from asphalt pavements and reducing the heat island effect. *International Journal of Sustainable Engineering*, 2(3):214–228. 8

Martilli, A., Krayenhoff, E. S., and Nazarian, N. (2020). Is the urban heat island intensity relevant for heat mitigation studies? *Urban Climate*, 31:100541. 19

Masson, V. (2000). A physically-based scheme for the urban energy budget in atmospheric models. *Boundary-layer meteorology*, 94(3):357–397. 8

Masterton, J. M. and Richardson, F. (1979). *Humidex: a method of quantifying human discomfort due to excessive heat and humidity*. Environment Canada, Atmospheric Environment. 16

Matzarakis, A. and Amelung, B. (2008). Physiological equivalent temperature as indicator for impacts of climate change on thermal comfort of humans. In *Seasonal forecasts, climatic change and human health*, pages 161–172. Springer. 16

Meehl, G. A. and Tebaldi, C. (2004). More intense, more frequent, and longer lasting heat waves in the 21st century. *Science*, 305(5686):994–997. 8

Météo-France (2020). France : 2019 au 3e rang des années les plus chaudes. *Bulletin Météo-France*. 4

Météo-France and CSTB (2012). EPICEA project. *Final Report, Paris, France. (in French)*. 4, 8, 21, 24, 28, 29, 31, 32, 33, 38, 39, 42, 45, 51

Millar, R. B. and Anderson, M. J. (2004). Remedies for pseudoreplication. *Fisheries Research*, 70(2-3):397–407. 56

Mohajerani, A., Bakaric, J., and Jeffrey-Bailey, T. (2017). The urban heat island effect, its causes, and mitigation, with reference to the thermal properties of asphalt concrete. *Journal of environmental management*, 197:522–538. 19, 20, 24, 75

Mohamed, J. (2015). *The traditional arts and crafts of turnery or mashrabiya*. PhD thesis, Rutgers University-Camden Graduate School. 3

Mullaney, J., Lucke, T., and Trueman, S. J. (2015). The effect of permeable pavements with an underlying base layer on the growth and nutrient status of urban trees. *Urban Forestry & Urban Greening*, 14(1):19–29. 25

Nakayama, T. and Fujita, T. (2010). Cooling effect of water-holding pavements made of new materials on water and heat budgets in urban areas. *Landscape and urban planning*, 96(2):57–67. 29, 30, 31, 32, 36, 40, 41, 45

Nakayama, T., Hashimoto, S., and Hamano, H. (2012). Multiscaled analysis of hydrothermal dynamics in Japanese megalopolis by using integrated approach. *Hydrological Processes*, 26(16):2431–2444. 29, 31, 32, 38, 42, 45

Nayak, A. k., Hagishima, A., and Tanimoto, J. (2020). A simplified numerical model for evaporative cooling by water spray over roof surfaces. *Applied Thermal Engineering*, 165:114514. 29, 30, 31, 32, 33, 36, 37, 42, 45

Nemirovsky, E. M., Welker, A. L., and Lee, R. (2013). Quantifying evaporation from pervious concrete systems: methodology and hydrologic perspective. *Journal of irrigation and drainage engineering*, 139(4):271–277. 23

Nikolopoulou, M., Baker, N., and Steemers, K. (2001). Thermal comfort in outdoor urban spaces: understanding the human parameter. *Solar energy*, 70(3):227–235. 14

Oke, T. R. (1981). Canyon geometry and the nocturnal urban heat island: comparison of scale model and field observations. *Journal of climatology*, 1(3):237–254. 8

Oke, T. R. (1982). The energetic basis of the urban heat island. *Quarterly Journal of the Royal Meteorological Society*, 108(455):1–24. 7, 8

Oke, T. R. (1987). *Boundary layer climates*. Routledge. 17

Oke, T. R. (1988a). Street design and urban canopy layer climate. *Energy and buildings*, 11(1-3):103–113. 8, 79

Oke, T. R. (1988b). The urban energy balance. *Progress in Physical geography*, 12(4):471–508. 9, 11, 80

Oke, T. R. (1997). Urban environments. *The surface climates of Canada*, pages 303–327. 79

Pagliarini, G. and Rainieri, S. (2011). Dynamic thermal simulation of a glass-covered semi-outdoor space with roof evaporative cooling. *Energy and Buildings*, 43(2-3):592–598. 10, 93

Pan, P., Wu, S., Xiao, Y., and Liu, G. (2015). A review on hydronic asphalt pavement for energy harvesting and snow melting. *Renewable and Sustainable Energy Reviews*, 48:624–634. 22

Paris City Council (2012). Blue Paper. *Paris City Council, Technical report, France*. (*in French*). 4

Paris City Hall (2015). Paris Adaptation Strategy. *Paris City Council, France*. 4

Paris City Hall (2017a). Paris Climate Action Plan. *Paris City Council, France*. 4, 8

Paris City Hall (2017b). Paris Resilience Strategy. *Paris City Council, France*. 4, 149

Parison, S., Chaumont, M., Kounkou-Arnaud, R., Bernik, A., Da Silva, M., and Hendel, M. (2018). "Tierce Forêt": Measuring the cooling effects from greening a parking lot. *ICUC10 & 14th Symposium on Urban Environment*. 150

Parison, S., Chaumont, M., Kounkou-Arnaud, R., Long, F., Bernik, A., Da Silva, M., and Hendel, M. (2020a). "Tierce Forêt": Greening a parking lot. *33eme colloque annuel de l'Association Internationale de Climatologie*. 150

Parison, S., Hendel, M., Grados, A., Jurski, K., and Royon, L. (2019a). A radiative technique for measuring the thermal properties of road and urban materials. *Road Materials and Pavement Design*, pages 1–15. 48, 109

Parison, S., Hendel, M., Grados, A., Jurski, K., and Royon, L. (2020b). A lab experiment for optimizing the cooling efficiency and the watering rate of pavement-watering. *Urban Climate*, 31:100543. 48, 76, 80, 85, 86, 87, 88, 89, 90, 91, 92, 93, 94, 96, 131

Parison, S., Hendel, M., Grados, A., and Royon, L. (2020c). Analysis of the heat budget of standard, cool and watered pavements under lab heat-wave conditions. *Energy and Buildings*, page 110455. 48, 77, 78, 81, 104, 105, 106, 107, 108, 110, 111, 112, 114, 115, 116, 117, 119, 121, 124, 128, 129

Parison, S., Hendel, M., and Royon, L. (2019b). Comportement thermique de revêtements innovants à paris pour le projet Cool & Low Noise Asphalt. *XIVeme Colloque International Franco-Québécois en Energie*. (*in French*). 149

Parison, S., Hendel, M., and Royon, L. (2019c). In situ assessment of the cooling effects of pavement-watering: Application to Cool & Low Noise Asphalt roads. *5th International Conference on Countermeasures to Urban Heat Islands*. 149

Parison, S., Hendel, M., and Royon, L. (2020d). A statistical method for quantifying the field effects of urban heat island mitigation techniques. *Urban Climate*. *(under review)*. 48, 52, 53, 57, 59, 60, 64, 65, 66, 67, 69, 148

Park, S., Tuller, S. E., and Jo, M. (2014). Application of Universal Thermal Climate Index (UTCI) for microclimatic analysis in urban thermal environments. *Landscape and Urban Planning*, 125:146–155. 24

Pasquill, F. (1961). The estimation of the dispersion of windborne material. *Met. Mag.*, 90:33. 61

Pasupathy, A., Athanasius, L., Velraj, R., and Seeniraj, R. (2008). Experimental investigation and numerical simulation analysis on the thermal performance of a building roof incorporating phase change material (PCM) for thermal management. *Applied Thermal Engineering*, 28(5-6):556–565. 22

Peel, M. C., Finlayson, B. L., and McMahon, T. A. (2007). Updated world map of the Köppen-Geiger climate classification. 30

Pomerantz, M. (2000). The effect of pavements' temperatures on air temperatures in large cities. 21, 113

Pomerantz, M., Akbari, H., Chang, S.-C., Levinson, R., and Pon, B. (2003). Examples of cooler reflective streets for urban heat-island mitigation: Portland cement concrete and chip seals. Technical report, Lawrence Berkeley National Lab.(LBNL), Berkeley, CA (United States). 21, 113

Pyun, H. B., Kim, R. H., Lee, S. H., and Park, J. B. (2010). Study on thermal environmental characteristics of water-retentive asphalt pavement. In *Materials Science Forum*, volume 658, pages 264–267. Trans Tech Publ. 29, 31, 36, 40, 45

Qin, Y. (2015). A review on the development of cool pavements to mitigate urban heat island effect. *Renewable and sustainable energy reviews*, 52:445–459. 19, 23, 47, 75, 103, 149

Qin, Y., He, Y., Hiller, J. E., and Mei, G. (2018). A new water-retaining paver block for reducing runoff and cooling pavement. *Journal of Cleaner Production*, 199:948–956. 23

Qin, Y. and Hiller, J. E. (2014). Understanding pavement-surface energy balance and its implications on cool pavement development. *Energy and Buildings*, 85:389–399. 21, 103, 113, 124, 125, 130

Renou, E. J. (1855). *Instructions météorologiques*. 7

Robine, J.-M., Cheung, S. L. K., Le Roy, S., Van Oyen, H., Griffiths, C., Michel, J.-P., and Herrmann, F. R. (2008). Death toll exceeded 70,000 in Europe during the summer of 2003. *Comptes rendus biologies*, 331(2):171–178. 8

Rosado, P., Gilbert, H., Pomerantz, M., Mandel, B., and Levinson, R. (2014). Cool pavement demonstration and study. In *Third International Conference on Countermeasures to Urban Heat Island*, pages 815–826. 19, 21, 51

Rosenfeld, A. H., Akbari, H., Romm, J. J., Pomerantz, M., et al. (1998). Cool communities: strategies for heat island mitigation and smog reduction. *Energ. Build. 1998, 28, 51*, 62. 8

Royon, L., Karim, L., and Bontemps, A. (2014). Optimization of PCM embedded in a floor panel developed for thermal management of the lightweight envelope of buildings. *Energy and buildings*, 82:385–390. 22

Ryms, M., Lewandowski, W. M., Klugmann-Radziemska, E., Denda, H., and Wcisło, P. (2015). The use of lightweight aggregate saturated with PCM as a temperature stabilizing material for road surfaces. *Applied Thermal Engineering*, 81:313–324. 22

Santamouris, M. (2013). Using cool pavements as a mitigation strategy to fight urban heat island—a review of the actual developments. *Renewable and Sustainable Energy Reviews*, 26:224–240. 19, 20, 75

Santamouris, M. (2015). Regulating the damaged thermostat of the cities—status, impacts and mitigation challenges. *Energy and Buildings*, 91:43–56. 19

Santamouris, M., Xirafi, F., Gaitani, N., Spanou, A., Saliari, M., and Vassilakopoulou, K. (2012). Improving the microclimate in a dense urban area using experimental and theoretical techniques-the case of Marousi, Athens. *International Journal of Ventilation*, 11(1):1–16. 21

Shaopeng, W., Mingyu, C., and Jizhe, Z. (2011). Laboratory investigation into thermal response of asphalt pavements as solar collector by application of small-scale slabs. *Applied Thermal Engineering*, 31(10):1582–1587. 130

Shimoda, Y. (2003). Adaptation measures for climate change and the urban heat island in Japan's built environment. *Building Research & Information*, 31(3-4):222–230. 8

Shin, D. U., Bae, W. B., Park, Y. M., Kim, S. R., and Kim, Y. G. (2019). Method for evaluating the heat-island mitigation effect of porous/water-retentive blocks using a climatic chamber. *Water Science and Technology*, 80(5):855–863. 103

Siple, P. A. and Passel, C. F. (1945). Measurements of dry atmospheric cooling in subfreezing temperatures. *Proceedings of the American Philosophical Society*, 89(1):177–199. 16

Smith, E. P. (2014). BACI design. *Wiley StatsRef: Statistics Reference Online*. 53, 149

Solcerova, A., Van Emmerik, T., Hilgersom, K., Van de Ven, F., and Van de Giesen, N. (2018). Uchimizu: A cool (ing) tradition to locally decrease air temperature. *Water*, 10(6):741. 29, 31, 32, 37

Spronken-Smith, R. and Oke, T. (1999). Scale modelling of nocturnal cooling in urban parks. *Boundary-Layer Meteorology*, 93(2):287–312. 19, 51

Stewart, I. D. (2011). A systematic review and scientific critique of methodology in modern urban heat island literature. *International Journal of Climatology*, 31(2):200–217. 43, 44

Stewart, I. D. and Oke, T. R. (2012). Local climate zones for urban temperature studies. *Bulletin of the American Meteorological Society*, 93(12):1879–1900. 30

Stewart-Oaten, A., Murdoch, W. W., and Parker, K. R. (1986). Environmental impact assessment:" pseudoreplication" in time? *Ecology*, 67(4):929–940. 53, 56

Stone, B., Hess, J. J., and Frumkin, H. (2010). Urban form and extreme heat events: are sprawling cities more vulnerable to climate change than compact cities? *Environmental health perspectives*, 118(10):1425–1428. 8

Stull, R. B. (2012). *An introduction to boundary layer meteorology*, volume 13. Springer Science & Business Media. 7

Sultana, S. (2010). *Extending asphalt pavement life with thin whitetopping*. PhD thesis, Kansas State University. 20

Synnefa, A., Dandou, A., Santamouris, M., Tombrou, M., and Soulakellis, N. (2008). On the use of cool materials as a heat island mitigation strategy. *Journal of Applied Meteorology and Climatology*, 47(11):2846–2856. 20

Synnefa, A., Santamouris, M., and Apostolakis, K. (2007). On the development, optical properties and thermal performance of cool colored coatings for the urban environment. *Solar energy*, 81(4):488–497. 20, 21, 113

Synnefa, A., Santamouris, M., and Livada, I. (2006). A study of the thermal performance of reflective coatings for the urban environment. *Solar Energy*, 80(8):968–981. 20

Taha, H. (1997). Urban climates and heat islands; albedo, evapotranspiration, and anthropogenic heat. *Energy and buildings*, 25(2). 20

Takahashi, K. and Yabuta, K. (2009). Road temperature mitigation effect of "road cool", a water-retentive material using blast furnace slag. *JFE Tech Rep*, 13:58–62. 23

Takahashi, R., Asakura, A., Koike, K., Himeno, S., and Fujita, S. (2010). Using snow melting pipes to verify the water sprinkling effect over a wide area. *NOVATECH 2010*, page 10. 28, 29, 31, 32, 33, 35, 38, 45, 51, 132

Takebayashi, H. and Moriyama, M. (2009). Study on the urban heat island mitigation effect achieved by converting to grass-covered parking. *Solar energy*, 83(8):1211–1223. 23

Takebayashi, H. and Moriyama, M. (2012). Study on surface heat budget of various pavements for urban heat island mitigation. *Advances in Materials Science and Engineering*, 2012. 23, 29, 31, 32, 36, 37, 40, 41, 42, 43, 45, 76, 103, 125

Teodoreanu, E. (2016). Thermal comfort index. *Present Environment and Sustainable Development*, 10(2):105–118. 18

Life Cool & Low Noise Asphalt (2017). Project official website. https://www.life-asphalt.eu/. 149

Thorsson, S., Lindberg, F., Eliasson, I., and Holmer, B. (2007). Different methods for estimating the mean radiant temperature in an outdoor urban setting. *International Journal of Climatology: A Journal of the Royal Meteorological Society*, 27(14):1983–1993. 14, 15

Tremeac, B., Bousquet, P., de Munck, C., Pigeon, G., Masson, V., Marchadier, C., Merchat, M., Poeuf, P., and Meunier, F. (2012). Influence of air conditioning management on heat island in Paris air street temperatures. *Applied Energy*, 95:102–110. 24

Trosseille, J., Mongruel, A., Royon, L., Medici, M.-G., and Beysens, D. (2019). Roughness-enhanced collection of condensed droplets. *The European Physical Journal E*, 42(11):144. 146

Tsin, P. K., Knudby, A., Krayenhoff, E. S., Ho, H. C., Brauer, M., and Henderson, S. B. (2016). Microscale mobile monitoring of urban air temperature. *Urban Climate*, 18:58–72. 51

Tyagi, V. V. and Buddhi, D. (2007). PCM thermal storage in buildings: a state of art. *Renewable and Sustainable Energy Reviews*, 11(6):1146–1166. 22

Ueno, T. and Tamaoki, K. (2009). Thermal characteristics of urban land cover by indoor lamp-irradiation experiment. In *The Seventh International Conference on Urban Climate*, pages 1–4. 76, 103

Van Bijsterveld, W., Houben, L., Scarpas, A., and Molenaar, A. (2001). Using pavement as solar collector: effect on pavement temperature and structural response. *Transportation research record*, 1778(1):140–148. 22

Van der Hoven, I. (1957). Power spectrum of horizontal wind speed in the frequency range from 0.0007 to 900 cycles per hour. *Journal of meteorology*, 14(2):160–164. 61

Wang, S. and Li, Y. (2015). Suitability of acrylic and copper globe thermometers for diurnal outdoor settings. *Building and Environment*, 89:279–294. 15

Watanabe, S. and Ishii, J. (2016). Effect of outdoor thermal environment on pedestrians' behavior selecting a shaded area in a humid subtropical region. *Building and Environment*, 95:32–41. 24

Wei, J. and He, J. (2013). Numerical simulation for analyzing the thermal improving effect of evaporative cooling urban surfaces on the urban built environment. *Applied thermal engineering*, 51(1-2):144–154. 29, 31, 32, 36, 38, 39, 40, 41, 45

Wong, N. H. and Yu, C. (2005). Study of green areas and urban heat island in a tropical city. *Habitat international*, 29(3):547–558. 51

Wu, H., Sun, B., Li, Z., and Yu, J. (2018). Characterizing thermal behaviors of various pavement materials and their thermal impacts on ambient environment. *Journal of cleaner production*, 172:1358–1367. 76, 103

Xie, N., Li, H., Zhao, W., Zhang, C., Yang, B., Zhang, H., and Zhang, Y. (2019). Optical and durability performance of near-infrared reflective coatings for cool pavement: Laboratorial investigation. *Building and Environment*, 163:106334. 21, 106

Xu, C.-Y. and Singh, V. P. (2001). Evaluation and generalization of temperature-based methods for calculating evaporation. *Hydrological processes*, 15(2):305–319. 10

Yaghoobian, N. and Kleissl, J. (2012). An indoor–outdoor building energy simulator to study urban modification effects on building energy use–model description and validation. *Energy and Buildings*, 54:407–417. 21

Yaglou, C., Minaed, D., et al. (1957). Control of heat casualties at military training centers. *Arch. Indust. Health*, 16(4):302–16. 15

Yamagata, H., Nasu, M., Yoshizawa, M., Miyamoto, A., and Minamiyama, M. (2008). Heat island mitigation using water retentive pavement sprinkled with reclaimed wastewater. *Water science and technology*, 57(5):763–771. 23, 29, 31, 38, 39, 40, 41, 42, 45, 51, 132

Yinfei, D., Qin, S., and Shengyue, W. (2014). Highly oriented heat-induced structure of asphalt pavement for reducing pavement temperature. *Energy and buildings*, 85:23–31. 130

Yinfei, D., Zheng, H., Jiaqi, C., and Weizheng, L. (2018). A novel strategy of inducing solar absorption and accelerating heat release for cooling asphalt pavement. *Solar Energy*, 159:125–133. 22, 130

Zhou, Z., Wang, X., Zhang, X., Chen, G., Zuo, J., and Pullen, S. (2015). Effectiveness of pavement-solar energy system–an experimental study. *Applied Energy*, 138:1–10. 22

Appendices

A Radiative Technique for Measuring the Thermal Properties of Road and Urban Materials

A radiative technique for measuring the thermal properties of road and urban materials

Sophie Parison, Martin Hendel, Arnaud Grados, Kristine Jurski & Laurent Royon

Published online: 04 Sep 2019.

Submit your article to this journal ⤢

Article views: 66

View related articles ⤢

View Crossmark data ⤢

Taylor & Francis
Taylor & Francis Group

Check for updates

A radiative technique for measuring the thermal properties of road and urban materials

Sophie Parison[a,b*], Martin Hendel[a,c], Arnaud Grados[d], Kristine Jurski[d] and Laurent Royon[a]

[a]*Sorbonne Paris Cité, LIED, UMR 8236, CNRS, Univ Paris Diderot, Paris, France;* [b]*Water and Sanitation & Road and Transportation Departments, Paris City Hall, Paris, France;* [c]*Département SEN, Université Paris-Est, ESIEE Paris, Noisy-le-Grand, France;* [d]*Sorbonne Paris Cité, MSC, UMR 7057, CNRS, Univ Paris Diderot, Paris, France*

The impact of urban construction materials, including pavement structures, on the urban climate depends on their thermal properties. However, their determination with standard methods is made difficult by the presence of large heterogeneities and their surface roughness. We propose a radiation-based method to overcome these difficulties and characterise their apparent thermal properties (conductivity, specific heat, etc.). The approach is compared with results obtained by using the hot-disk and the hot-plate methods and shows good agreement for smooth and homogenous material samples. The method is found to be useful for characterising the thermal properties of materials with varying heterogeneity and surface roughness.

Keywords: apparent thermal property; heterogeneous materials; rough materials; urban material

Nomenclature

Symbols:

a	thermal diffusivity, $m^2.s^{-1}$
c_p	specific heat capacity, $J.kg^{-1}.K^{-1}$
D	sample diameter
e	element thickness, m
E	thermal effusivity, $J.m^{-2}.K^{-1}.s^{-1/2}$
FAA	fine-aggregate asphalt
k	thermal conductivity, $W.m^{-1}.K^{-1}$
PCC	Portland cement concrete
s	slope, $°C.s^{-1}$
t	time, s
T	temperature, $°C$

Greek letters:

δT	temperature interval, $°C$
ϕ	absorbed heat flux density, $W.m^{-2}$
ρ	density, $kg.m^{-3}$

---

*Corresponding author. Email: sophie.parison@univ-paris-diderot.fr

Indexes / Exponents:

0	initial
i	insulating
*	reduced

1. Introduction

Pavements and roads, which cover large areas in cities, contribute to the Urban Heat Island (UHI) effect. During the day, pavements absorb and store significant amounts of solar radiation and then release it back during the night to the surrounding environment. This phenomenon generates serious problems in terms of air quality (Shimoda, 2003), high urban energy consumption (Mallick, Chen, & Bhowmick, 2009), and public health problems (Knowlton et al., 2007), which explain why recent research efforts have been devoted to developing adaptation/mitigation strategies.

In order to understand the UHI effect with respect to pavements, many studies have focused on their thermal properties: albedo, thermal conductivity, heat capacity, dry density and emissivity (Gui, Phelan, Kaloush, & Golden, 2007; Mohajerani, Bakaric, & Jeffrey-Bailey, 2017; ShengYue, QiYang, YingNa, & PeiDong, 2013). Many of them show that surfaces with high albedo exhibit lower maximum daily surface temperature whereas materials with high emissivity have lower surface temperature during the night time (Harlan et al., 2014). Nevertheless, these studies still present inaccuracies due essentially to a lack of knowledge of the other thermal properties of a pavement system. This is mainly related to the complex structure of public roads which are composed of several different material layers such as Portland cement concrete (PCC), asphalt, mortar, granite, gravel, etc. These materials often include aggregates of various sizes reaching up to several centimetres. Such heterogeneities and surface roughness render standard thermal characterisation methods impractical for these materials. Nevertheless, a detailed knowledge of the thermo-physical properties of the urban fabric materials would allow a better understanding of their thermal behaviour (heating processes, heat storage and release etc.) and their contribution to the UHI phenomenon. This information would be useful to decision makers for urban planning in order to reduce pedestrians thermal stress during heat waves.

Among the different methods existing in the lab, contact transient methods using plane or linear heating elements (hot-wire (Andersson & Bäckström, 1976; Prelovsek & Uran, 1984), hot-plate (Huang, 2006; Jannot, Felix, & Degiovanni, 2010), hot-disk (Gustafsson, 1991; Log & Gustafsson, 1995), divided-bar (Danis, Gobbé, & Royer, 1996) or three-layer (Bahrani, Jannot, & Degiovanni, 2014) methods) allow direct identification of the thermal conductivity and diffusivity for a material assumed to be homogeneous and isotropic (Gobbé, Iserna, & Ladevie, 2004) but their implementation remains constraining for the case of a heterogeneous material (Olives, 2017; Yan, Chen, You, & Fu, 2019). Indeed, the sensor/heating element must be large enough in regard to the typical size of the heterogeneities for them to be taken into account. In addition, ensuring good thermal contact between the heating element and sample remains difficult for rough surfaces.

A radiative heating source can be used to overcome the issue of poor heating element contact with the sample surface. One such approach is the flash method, which provides an estimate of sample thermal diffusivity (Degiovanni, Batsale, & Maillet, 1996; Krapez, Spagnolo, Frieß, Maier, & Neuer, 2004; Parker, Jenkins, Butler, & Abbott, 1961). To obtain a good estimation of diffusivity, convective exchanges with the sample must be characterised, and additional corrections may be applied to take into account the duration of the flash-impulse (Degiovanni, 1987).

The present research proposes to apply a semi-steady-state laboratory method based on a radiative heat source (Crabol, 1989), similar to the flash method, which provides a direct assessment of apparent thermal conductivity (k) and of apparent volumetric heat capacity ($\rho.c_p$). The main strength of the method is the simplicity in the calculation of the thermal properties based on two temperature measurements. The method also proceeds during a short period of experiment and presents the advantage of doing without the need for contact between the heating element (radiative source) and the sample.

We apply this method to a set of six heterogeneous urban materials: fine-aggregate asphalt (FAA), granite, mortar, stabilised sand, asphalt concrete and PCC. Those materials were selected among the most commonly used in the parisian road fabric: FAA is traditionally used for sidewalk, granite for sidewalk borders or slabs, stabilised sand is commonly found in parks or green-spaces walking paths, asphalt concrete is used on traffic road while PCC and mortar are used as structural sub-layers.

Results are compared with those obtained with two other techniques for smooth and homogeneous samples: the hot-disk and the hot-plate methods (Jannot, 2011).

2. Methodology

2.1. *Radiation-based characterisation method*

A diagram of the experimental set-up is illustrated in Figure 1. To ensure a unidirectional thermal transfer, a cylindrical sample ten times wider than it is thick is placed in a polyurethane insulation ring with a bottom insulation layer, leaving only the top of the sample exposed. An infrared lamp is used to heat the top of the sample with a constant radiative heat flux. To normalise the radiative properties of different materials, the top of each sample is coated with matte black paint (absorptivity of 0.95). The sample is initially at thermal equilibrium.

A few minutes before $t = 0$, the lamp is switched on to allow it to heat up with the sample shielded from its radiation. At $t = 0$, the sample is exposed to the radiation source, thus submitting the sample to a step of uniform constant heat flux density.

Over the duration of the experiment, temperature and heat flux are measured on the top face with a combined T-type thermocouple and fluxmeter sensor (Captec, France). On the bottom face of the sample, a second T-type thermocouple is placed at the interface between the sample and the insulating material. The typical sensitivity of the heat flux sensor given by the manufacturer is
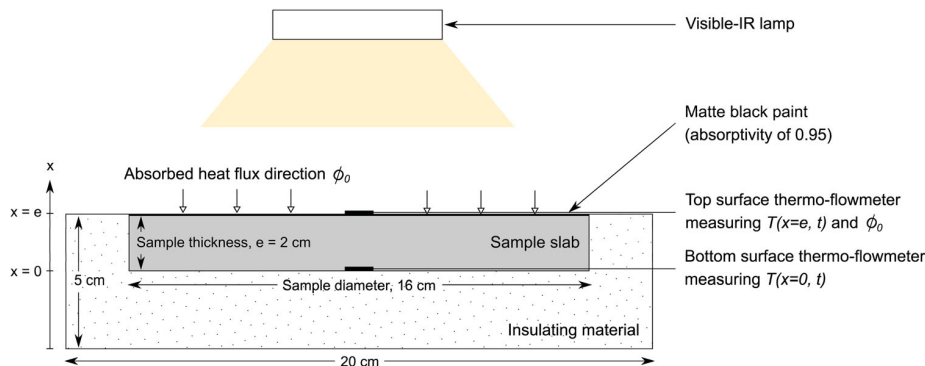
Figure 1.   Diagram of the experimental set up.

equal to 1.25 µV/(W.m^{-2}) and the accuracy of the copper–constantin thermocouple is $\pm$ 0.3°C. Data was acquired every second.

To ensure identical radiative conditions, the top sensor is also painted with the same matte black paint as the sample surface. This sensor measures absorbed radiation net of convective transfers with the ambient air, i.e. the net heat flux density ϕ_0 absorbed by the sample.

2.2. *Mathematical model of heat transfer*

The transient heat transfer problem is considered geometrically and thermally symmetric along the vertical direction (*x*-axis). Heat transfer equation along the *x*-axis inside the sample and on its surface is expressed by the following equation:

$$\rho c_p \frac{\partial T}{\partial t} = k \left(\frac{\partial^2 T}{\partial x^2} \right) \tag{1}$$

where k, c_p and ρ are the thermal conductivity, the specific heat capacity and the density of the sample, respectively.

Consider ϕ_0 the radiation heat density absorbed by the pavement sample and T_0 the initial temperature of the system. Initial and boundary conditions are explicitly given in equations (2), (3) and (4), respectively.

$$T(x, t = 0) = T_0 \tag{2}$$

$$\frac{\partial T}{\partial x}\Big|_{x=0} = 0 \tag{3}$$

$$-k \frac{\partial T}{\partial x}\Big|_{x=e} = \phi_0 \tag{4}$$

Considering that the sample thickness is approximately one tenth of its diameter ($e << D$) and that its periphery is thermally insulated, heat diffusion along the longitudinal axis can be neglected. The heat transfer is thus rendered unidirectional along the x-axis over the duration of the experiment. Also considering that the thermal properties of the sample are constant, the resolution of the heat equation thus gives the following analytical expression:

$$T(x, t) = T_0 + \frac{\phi_0 t}{\rho c_p e} + \frac{\phi_0 e}{k} \left[\frac{3x^2 - e^2}{6e^2} - \frac{2}{\pi^2} \sum_{n=1}^{\infty} \frac{(-1)^n}{n^2} \exp\left(-\frac{kn^2\pi^2 t}{e^2} \right) \cos\left(\frac{n\pi x}{e} \right) \right] \tag{5}$$

An example of temperature profiles on the upper ($x = e$) and lower ($x = 0$) surfaces of the sample as a function of time are reported in Figure 2. It can be observed that the temperature profiles increase strongly at first and then show a linear progression when a local quasi-steady state condition is reached.

After times t_{up} and t_{down}, which depend on the characteristic diffusion time over the sample thickness, the exponential term is simplified and thus temperature profiles at $x = 0$ and $x = e$ become linear, in agreement with the analytical solution of the heat transfer equation as follows (Jannot, 2012):

$$T(x = e, t > t_{up}) = T_0 + \frac{\phi_0 t}{\rho c_p e} + \frac{\phi_0 e}{3k} \tag{6}$$

$$T(x = 0, t > t_{down}) = T_0 + \frac{\phi_0 t}{\rho c_p e} - \frac{\phi_0 e}{6k} \tag{7}$$
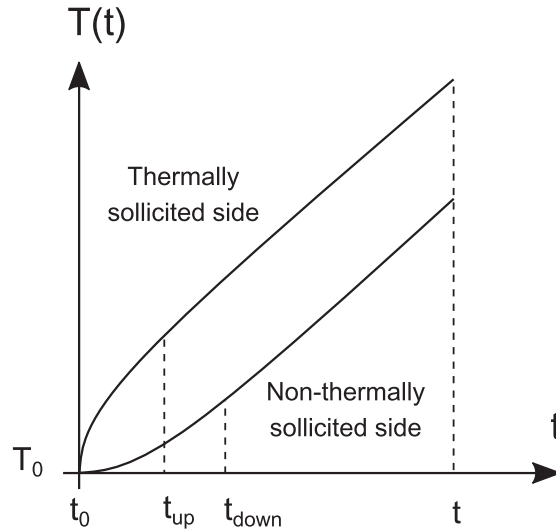
Figure 2.   Theoretical temperature profile for the top and bottom surfaces of a sample (Crabol, 1989).

Equations (6) and (7) allow us to establish the following expressions:

$$\rho c_p = \frac{\phi_0}{se}; k = \frac{\phi_0 e}{2\delta T} \tag{8}$$

where s is the slope of the temperature curve for $t > t_{down}$, and δT is the temperature difference between the top and the bottom faces of the sample for $t > t_{down}$. In the proposed method, we wait for the difference between both slopes to be stabilised. The estimation of the parameters k and c_p is obtained using the least squares method between the expressions of equation (8) and the experimental data.

The specific heat capacity c_p represents the quantity of heat a material is able to absorb with regard to its mass. The thermal conductivity k of a material quantifies its ability to conduct heat, while thermal diffusivity characterises the rate at which heat is transferred through a given material. Finally, thermal effusivity $E,$ also referred to as thermal admittance, represents the rate at which heat is absorbed by a material. The higher the effusivity, the higher the material will absorb energy without notably increasing its temperature. These four physical quantities allow the characterisation of thermal inertia, that is to say the ability for a material of storing heat and returning it through time.

The experiment is conducted five times for each sample to ensure that results are reproducible. To ensure that data from different tests is comparable despite slight variations in initial temperature and heat flux, a reduced temperature is used, noted T^* (in K.m².W^{-1}), defined as:

$$T^*(x, t) = \frac{T(x, t) - T_0}{\phi_0} \tag{9}$$

For each test and each method, the temperature and fluxmeter sensor positions were deliberately changed between two consecutive trials in order to ensure that this position did not influence the results, and different trials were then combined using T^*. The thermal properties estimated with this method are then compared with those obtained with the hot-disk and the hot-plate methods with the same samples.

2.3.   *Validation methods procedures*

The Hot Disk method is a transient thermo-physical technique allowing the determination the thermal conductivity, diffusivity and heat capacity of samples. The thermal solicitation is ensured using a Hot Disk sensor, acting as both a heat source and a temperature sensor (here, of radius 3.189 mm), placed in between two samples to test (Gustafsson, 1991). The solicitation time is short (about ten seconds) so that the edges of the sample do not influence the diffusion of heat process. The heat flux delivered by the sensor, of the order of a hundred of mW, is chosen so that the increase of the sample's temperature is included between 1° and 3°C. The variation of the sensor's electric resistance resulting from the increase of the material's temperature during the test is recorded, allowing us to deduce the values of k, a and c_p straightforwardly, following the method described by Gustafsson (1991).

The second validation method used is the hot plate method, which is a transient technique solely allowing the measurement of the thermal effusivity of a material. A heating element as well as a thermo-flowmeter are sandwiched between a semi-infinite sample of material and an insulating material which effusivity is known. By applying a pulse of constant flux, the resolution of the heat equation on the sample – heating element interface leads to the Laplace transform of the temperature (Jannot, 2011). In order to obtain the theoretical evolution of the temperature within the system, the corresponding expression is then numerically inverted using the Stehfest method (Stehfest, 1970). The conductance of the sample – heating element set is firstly calculated by using a symmetrical hot plate device with an insulating material of known effusivity. Contact resistances on each side of the heating element and the effusivity of the studied sample are then determined more precisely using the least squares method.

2.4.   *Case study materials*

Six materials commonly used in road construction are characterised: fine-aggregate asphalt (FAA), granite, mortar, stabilised sand, asphalt concrete and Portland cement concrete (PCC). A photograph of each sample is shown in Figure 3.

Figure 3.   Urban material samples

Table 1.   Formulation of the samples and characteristic size of their aggregates.

Material	Volumic formulation	Aggregates typical diameter	
		Minimal size	Maximal size
FAA	Bitumen (30%)	—	
	Sand (40%)	< 4 mm	
	Small Gravel (30%)	2 mm	4 mm
Granite	Core-sampled.	—	—
Mortar	Portland Cement (25%)	—	
	Fine sand (75%)	< 2 mm	
Stabilised sand	Portland Cement (25%)	—	
	Fine sand (30%)	< 2 mm	
	Coarse sand (25%)	< 5 mm	
	Gravel (20%)	2 mm	6 mm
Asphalt concrete	Bitumen (30%)	—	
	Fine sand (20%)	< 2 mm	
	Coarse gravel (50%)	6 mm	10 mm
PCC	Portland Cement (25%)	—	
	Sand (35%)	< 4 mm	
	Coarse gravel (40%)	4 mm	20 mm

Each sample was manufactured following the quality control procedure by the Paris City Hall public space laboratory. Mortar and stabilised sand were directly prepared in a 2 cm-deep cylindrical mould, while FAA, asphalt concrete and PCC were prepared in a cylindrical test tube, and then sawed to the smallest technically feasible thickness, that is 2 cm slices. Finally, granite was directly core-sampled from a larger sidewalk slab and then sawed. The formulation of the samples as well as the typical size of their aggregates are listed in Table 1.

From the formulations listed in Table 1, qualitative information on the homogenous/heterogeneous nature of the samples can be obtained. This strongly depends on the scale of analysis, which depends on the size of the instrument. In brief, a material is considered to be heterogeneous if its characteristic aggregates or minerals are similar or larger than the instrument's measurement area, homogeneous otherwise.

Thus, for the 1 cm² sensors used here, granite and mortar can be considered as homogeneous, since the characteristic size of their constituents, resp. their minerals and sand particles, is at least an order of magnitude smaller than the sensor. FAA, which incorporates a mix of small aggregates (sand and gravel) and bituminous binder, as well as stabilised sand can be considered mildly heterogeneous due to the significant presence of coarse sand and small gravel. Finally, asphalt concrete and PCC are both strongly heterogeneous since they include a significant portion of centimetric aggregates.

The manufacturing procedures employed to produce the samples imposed the sawing of asphalt concrete, FAA, PCC and granite, leaving them with and a smooth finish. The surface roughness of these is thus low, i.e. less than 0.1 mm. This holds true for mortar, which is smooth as well. On the contrary, stabilised sand is a porous material with a very rough finish, with a roughness estimated to be in the order of 3 mm.

For the radiative characterisation, cylindrical samples of 16 cm in diameter and 2 cm thick are considered in this study (see Figure 3), i.e. larger than the characteristic size of the heterogeneities. For the two validation methods (hot-disk and hot-plate), smaller samples were used (4.5 cm in diameter and 2 cm thick) to match the size of the hot-plate heating element. The density of the samples was measured at ambient temperature and are listed in Table 2. Uncertainties given in this Table are the standard deviation of the measurements.

Table 2.   Sample densities (at 20°C).

Material	Density (kg.m^{-3})
FAA	2325 ± 34
Granite	2608 ± 18
Mortar	2157 ± 14
Stabilised sand	2090 ± 42
Asphalt concrete	2360 ± 34
PCC	2301 ± 50

Thermal properties and density of various types of asphalts, concretes, mortars and granites found in the literature are listed in Table 3. As seen, these values vary noticeably, as the properties strongly depend on the composition of the sample and on its manufacturing procedure. They should therefore be used for comparison carefully since a vast diversity of civil engineering materials exist. No values were found for the stabilised sand.

3. Experimental results

The proposed radiation-based method is applied for each sample, as well as the hot-disk and hot-plate methods. The results obtained from the radiative method are then compared to those from the other two characterisation techniques for homogeneous and smooth materials. An example of the temperature variation of the top and bottom faces of the granite sample is provided on Figure 4. From those results, the reduced temperature T^* is calculated following equation (9). Several trials are combined to improve the representativeness of the measurement noise. Then, the slope s and difference between top and bottom averaged reduced temperatures δT are estimated using the least squares method. Specific heat capacity and thermal conductivity are deduced from equations (8) divided by ϕ_0. Knowing k, c_p and ρ, thermal diffusivity a is calculated using relation $a = k/\rho.c_p$ while thermal effusivity E is obtained using relationship $E = \sqrt{k.\rho.c_p}$.

3.1. *Comparison of the methods*

For the radiative method, the estimated parameter uncertainties provided hereafter are obtained by propagating the measurement uncertainties into relation (6). Diffusivity and effusivity are then calculated from k, c_p and ρ and the uncertainties are propagated likewise. For the hot-disk method, the parameter uncertainties are obtained using the standard deviation between each trial. Finally, for the hot-plate device, the uncertainties were obtained based on the probability distribution of the estimated effusivity using a 90% confidence interval in the numerical model (Stehfest, 1970).

3.2. *Validation: smooth and homogenous materials*

Table 4 presents the results obtained for smooth and homogeneous materials, i.e. the FAA, mortar and granite samples and are also illustrated on Figure 5.

As can be seen, results are in a good agreement for all three characterisation methods, with slightly greater uncertainties for diffusivity and specific heat than for conductivity. The greatest difference is observed for the thermal conductivity of FAA with both methods. This might be caused by the mildly heterogeneity of the FAA, causing this slight discrepancy observed here unlike other samples.

Table 3. Literature values for the thermal properties of various types of asphalt, concrete, mortar and granite. k: thermal conductivity (W.m^{-1}.K^{-1}), a: thermal diffusivity (mm².s^{-1}), c$_p$: specific heat capacity (J.kg^{-1}.K^{-1}), ρ: density (kg.m^{-3}), -: not provided.

Material	Reference	Specifications	k	a	c_p	ρ
Asphalt	Luca and Mrawira (2005)	Hot mixed asphalt	1.45–1.81	0.44–0.64	1120–1370	2297–2450
	Li (2015)	Dense-graded asphalt	1.73	0.85	852	2400
	Takebayashi and Moriyama (2012)	Asphalt	0.74	–	2100	–
	Kavianipour and Beck (1977)	Asphaltic pavement	2.28–2.88	1.15–1.44	$\rho.c_p = 1.97$–2.00 MJ.m^{-3}.K^{-1}	
	Highter (1984)	Asphaltic concrete	0.65–2.32	0.6–1.0	800–1600	–
	Carlson, Bhardwaj, Phelan, Kaloush, and Golden (2010)	Hot mix asphalt	0.90	–	–	2281
Concrete	Howlader et al. (2012)	Coarse aggregates PCC	1.41–2.35	0.57–1.01	1018–1260	1920–2340
	Li (2015)	Dense-graded concrete	1.83	0.81	1001	2257
	Carlson et al. (2010)	PCC	1.72	–	–	2857
	Khan (2002)	Different concretes	1.60–2.77	–	–	–
	Kodur and Sultan (2003)	Aggregate concretes	1.97–1.98	0.81–1.10	$\rho.c_p = 1.8$–2.45 MJ.m^{-3}.K^{-1}	
	Lee, Hawes, Banu, and Feldman (2000)	Concrete block	–	–	880	–
Mortar	Khan (2002)	Mortar	1.37–1.90	–	–	–
	Bentz et al. (2011)	Silica sand mortars	1.7–3.2	–	830–1025	2080–2380
	Demirboǧa (2003)	Portland Cement paste with silica sand	0.72–1.19	–	–	1790–2106
Granite	Cho et al. (2009)	Granite	2.12–3.12	–	–	2610–2690
	Heuze (1983)	Several granites	2.5–3.3	1.1–1.8	750–950	2600
	Petrov et al. (2005)	Krasnoyarsk granites	3.1–3.4	1.46–1.57	800–840	2610–2750
	Dwivedi et al. (2008)	Several granites	–	1.26–1.51	801–836	2590–2600
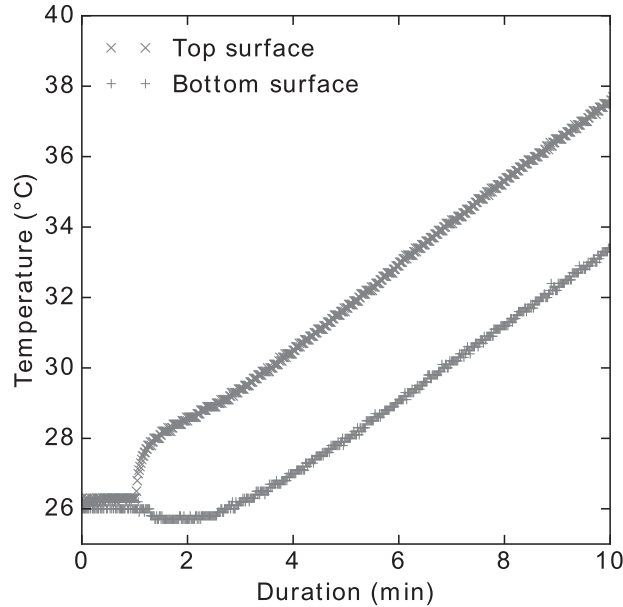
Figure 4.   Example of experimental temperature variation of top and bottom surfaces for the granite sample

In addition, for each parameter, results obtained in this paper seem to compare favourably with properties found in the literature given the wide range of existing construction materials (see Table 3). FAA matches literature values of an asphaltic concrete/pavement (Highter, 1984; Kavianipour & Beck, 1977). Granite is in very good agreement with most references (Cho, Kwon, & Choi, 2009; Dwivedi, Goel, Prasad, & Sinha, 2008; Heuze, 1983; Petrov et al., 2005) as is the mortar sample which matches literature properties of a silica sand mortar (Bentz, Peltz, Duran-Herrera, Valdez, & Juarez, 2011). These observations confirm that the proposed method is able to measure the properties of interest for smooth-surfaced and homogeneous materials.

3.3.   *Heterogeneous and rough materials*

Table 5 summarises results obtained for the three other case study materials, namely the stabilised sand, which surface is rough, as well as for the asphalt concrete and the concrete sample, highly heterogeneous and plotted in Figure 6. Unlike for homogeneous samples, good agreement is found between the hot-disk and the radiation method for thermal conductivity only.

With the hot-disk method, since thermal conductivity is determined at long time periods (Danis et al., 1996), it is reassuring to note small variability even with heterogeneous materials, since contact quality mostly influences the reproducibility of the transient portion of the temperature increase, which is mostly sensitive to diffusivity (Krapez, 2007).

However, for this reason, the diffusivity and the specific heat results obtained with the hot-disk are highly dispersed, as can be clearly seen in Figure 6. This is particularly the case for diffusivity, but holds true for specific heat as well, the values of which are completely unrealistic.

Indeed, the transient part of the temperature increase has a very strong influence on the evaluation of these properties, and is particularly sensitive to the experimental conditions. For the hot-disk method, rough materials cause a poor contact between the heating element and the

Table 4. Validation results obtained for homogenous and smooth materials.

	k (W.m^{-1}.K^{-1})		a (mm^2.s^{-1})		c_p (J.kg^{-1}.K^{-1})		E (J.m^{-2}.K^{-1}.s$^{-1/2}$)		
	Radiation	Hot-disk	Radiation	Hot-disk	Radiation	Hot-disk	Radiation	Hot-disk	Hot-plate
FAA	2.01 ± 0.05	2.42 ± 0.09	0.96 ± 0.07	1.23 ± 0.15	900 ± 56	856 ± 110	2051 ± 69.7	2192 ± 147	2130 ± 70.3
Granite	2.31 ± 0.15	2.60 ± 0.13	1.17 ± 0.12	1.34 ± 0.13	759 ± 63	750 ± 62	2138 ± 113	2256 ± 108	2419 ± 94.3
Mortar	2.90 ± 0.20	2.91 ± 0.04	1.42 ± 0.16	1.74 ± 0.25	946 ± 79	787 ± 120	2431 ± 129	2222 ± 169	2196 ± 108

Table 5. Results obtained for heterogeneous and/or rough materials

	k (W.m^{-1}.K^{-1})		a (mm^2.s^{-1})		c_p (J.kg^{-1}.K^{-1})		E (J.m^{-2}.K^{-1}.s$^{-1/2}$)		
	Radiation	Hot-disk	Radiation	Hot-disk	Radiation	Hot-disk	Radiation	Hot-disk	Hot-plate
Stabilized Sand	1.23 ± 0.03	1.25 ± 0.06	0.74 ± 0.06	2.65 ± 2.20	722 ± 21.7	369 ± 259	1351 ± 51.3	982 ± 346	1775 ± 28.4
Asphalt concrete	1.63 ± 0.03	1.87 ± 0.10	0.86 ± 0.13	2.61 ± 1.00	806 ± 118	334 ± 104	1759 ± 137	1214 ± 192	1876 ± 101
PCC	1.95 ± 0.05	2.10 ± 0.03	1.10 ± 0.04	1.54 ± 0.27	777 ± 10.1	140 ± 51.0	1872 ± 33.7	823 ± 150.6	1927 ± 67.4
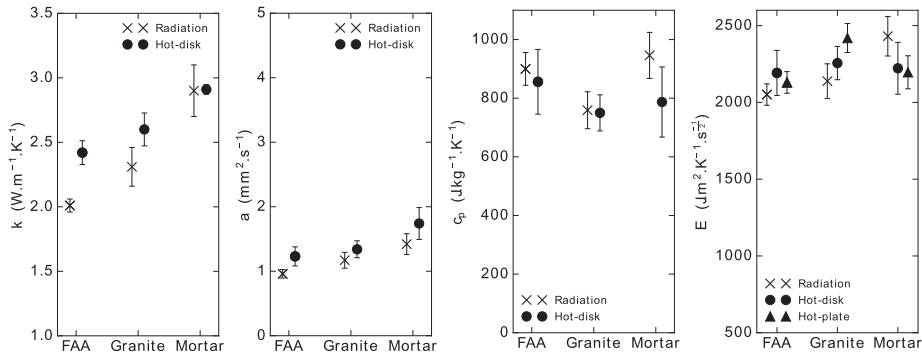
Figure 5.   Comparison of the results for homogeneous/smooth samples (fine-aggregate asphalt (FAA), granite and mortar) for all three methods.
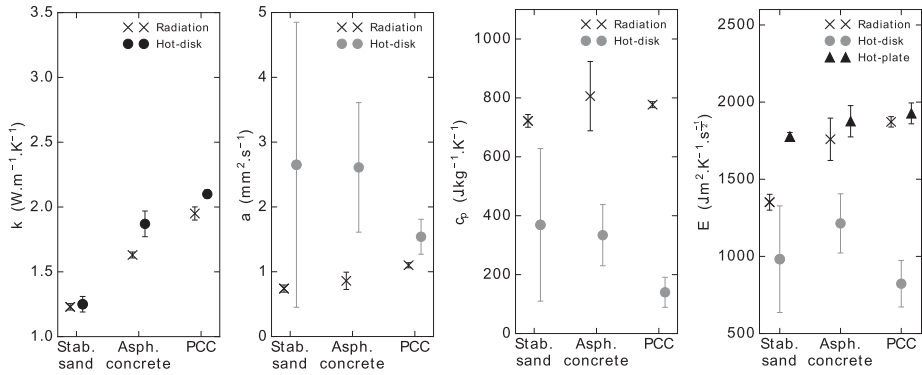
Figure 6.   Comparison of the results for heterogeneous/rough samples (stabilised sand (Stab. sand), asphalt concrete (Asph. concrete) and PCC) for all three methods.

sample. High thermal contact resistance therefore appears at this interface, explaining the variability between two successive measurements for which the sensor was deliberately displaced. Moreover, for highly heterogeneous materials (large aggregates), different aggregates are tested between trials. This is due to the inadequate size (too small) of the sensor with regard to the aggregates present in these samples and is a root cause of the observed variability.

Observations in Figure 6 thus confirm the strong impact of poor thermal contact between the sample and the hot-disk sensor for rough samples (stabilised sand) and of large heterogeneities, i.e. the large various-sized aggregates incorporated into the asphalt concrete and the concrete. Corresponding results are therefore greyed in Table 5 and Figure 6 to insist on the fact that they are not reliable and shouldn't be taken into consideration.

For such values, a relative error above 15% is systematically observed. In the worst case (diffusivity of stabilised-sand with the hot-disk method), this error is even up to 83%. Among the greyed values, the variability of the PCC sample with the hot-disk method seems to be lower compared to the other two materials when looking at the absolute error. Nevertheless, compared to the measured value, the relative error remains above 15%. Moreover, values obtained with the hot-disk technique for each material of Figure 6 are very far from the typical ones found in the literature. Thus, either in terms of variability or values themselves, the hot-disk method does

not seem suitable for measuring the thermal properties of our heterogeneous samples apart from conductivity, unlike other methods.

Indeed, effusivity values obtained for the asphalt concrete and PCC samples with the hot-plate and the radiative characterisation methods are in good agreement. Values obtained are quite stable (relative error $< 15\%$) and consistent with the literature. This confirms that these two methods have appropriately-sized heating elements for these materials, whereas only the conductivity could be reliably assessed using the hot-disk method.

For reliable results (blackened in Table 5), each measured parameter compares well with the literature (see Table 3). The asphalt concrete sample matches the values of a dense-graded asphalt (Li, 2015). Our PCC sample agrees very well with values obtained by Howlader, Rashid, Mallick, and Haque (2012) and Kodur and Sultan (2003). No value was found in the literature for stabilised sand.

All else being equal, the radiation technique gives more stable results compared to the hot-disk method for coarse-aggregate samples, meaning that it is likely to better take into account for the heterogeneities of these structures.

4. Conclusion

In order to thermally characterise construction materials with rough surfaces and/or including large aggregates (typically centimetric), a thermo-physical characterisation method based on a radiative heat source has been proposed and tested with six different construction materials. This approach was compared with the hot-disk and the hot plate methods for homogenous and smooth-surfaced materials.

For the tests run on smooth materials and with small aggregates, our radiation method showed good agreement with the other two characterisation techniques. Indeed, for the estimated parameters, each method exhibited very close results with only slight variability between each trial. Also, for rough and heterogeneous materials, the radiation technique was able to provide apparent thermal properties that were highly reproducible between trials, i.e. for the stabilised sand, asphalt concrete and PCC samples.

Generally-speaking, the proposed radiation-based characterisation technique provides satisfactory results for construction materials and agrees well with the hot-plate method. Overall, results are consistent with what can be found in the literature given the wide range of construction materials and the uncertainty of the method is globally acceptable given the heterogeneous nature of the samples and the fact that apparent parameters are measured.

To summarise, the proposed radiative characterisation method seems well suited for determining the apparent thermal properties of heterogeneous and rough-surfaces construction materials. In this respect, this method can be used to characterise other heterogeneous materials currently being considered for urban heat island mitigation.

References

Andersson, P., & Bäckström, G. (1976). Thermal conductivity of solids under pressure by the transient hot wire method. *Review of Scientific Instruments*, *47*(2), 205–209.

Bahrani, S. A., Jannot, Y., & Degiovanni, A. (2014). Extension and optimization of a three-layer method for the estimation of thermal conductivity of super-insulating materials. *Journal of Applied Physics*, *116*(14), 143509.

Bentz, D. P., Peltz, M. A., Duran-Herrera, A., Valdez, P., & Juarez, C. A. (2011). Thermal properties of high-volume fly ash mortars and concretes. *Journal of Building Physics*, *34*(3), 263–275.

Carlson, J. D., Bhardwaj, R., Phelan, P. E., Kaloush, K. E., & Golden, J. S. (2010). Determining thermal conductivity of paving materials using cylindrical sample geometry. *Journal of Materials in Civil Engineering*, *22*(2), 186–195.

Cho, W. J., Kwon, S., & Choi, J. W. (2009). The thermal conductivity for granite with various water contents. *Engineering Geology*, *107*(3–4), 167–171.

Crabol, J. (1989). *Transfert de chaleur, Tome 1*. Ed. Masson. pp. 88 *(In french)*.

Danis, M., Gobbé, C., & Royer, J. J. (1996). Procédures d'utilisation d'un conductivimètre à barre divisée pour des échantillons grenus: Application au cas des granites. *International Journal of Heat and Mass Transfer*, *39*(10), 2183–2187.

Degiovanni, A. (1987). Correction de longueur d'impulsion pour la mesure de la diffusivité thermique par méthode flash. *International Journal of Heat and Mass Transfer*, *30*(10), 2199–2200.

Degiovanni, A., Batsale, J. C., & Maillet, D. (1996). Mesure de la diffusivité longitudinale de matériaux anisotropes. *Revue Générale de Thermique*, *35*(410), 141–147. *(In french)*.

Demirboǧa, R. (2003). Influence of mineral admixtures on thermal conductivity and compressive strength of mortar. *Energy and Buildings*, *35*(2), 189–192.

Dwivedi, R. D., Goel, R. K., Prasad, V. V. R., & Sinha, A. (2008). Thermo-mechanical properties of Indian and other granites. *International Journal of Rock Mechanics and Mining Sciences*, *45*(3), 303–315.

Gobbé, C., Iserna, S., & Ladevie, B. (2004). Hot strip method: Application to thermal characterisation of orthotropic media. *International Journal of Thermal Sciences*, *43*(10), 951–958.

Gui, J., Phelan, P. E., Kaloush, K. E., & Golden, J. S. (2007). Impact of pavement thermophysical properties on surface temperatures. *Journal of Materials in Civil Engineering*, *19*(8), 683–690.

Gustafsson, S. E. (1991). Transient plane source techniques for thermal conductivity and thermal diffusivity measurements of solid materials. *Review of Scientific Instruments*, *62*(3), 797–804.

Harlan, S., Chowell, G., Yang, S., Petitti, D., Morales Butler, E., Ruddell, B., & Ruddell, D. (2014). Heat-related deaths in hot cities: Estimates of human tolerance to high temperature thresholds. *International Journal of Environmental Research and Public Health*, *11*(3), 3304–3326.

Heuze, F. E. (1983, February). High-temperature mechanical, physical and thermal properties of granitic rocks—a review. *International Journal of Rock Mechanics and Mining Sciences & Geomechanics Abstracts*, *20*(1), 3–10. Pergamon.

Highter, W. (1984). Thermal properties of some asphaltic concrete mixes. In *International Air Transportation Conference* (p. 1598).

Howlader, M. K., Rashid, M. H., Mallick, D., & Haque, T. (2012). Effects of aggregate types on thermal properties of concrete. *ARPN Journal of Engineering and Applied Sciences*, *7*(7), 900–906.

Huang, J. (2006). Sweating guarded hot plate test method. *Polymer Testing*, *25*(5), 709–716.

Jannot, Y. (2011). Théorie et pratique de la métrologie thermique. LEMTA, pp.97. *(In french)*.

Jannot, Y. (2012). Transferts thermiques. Ecole des Mines Nancy, pp.43. *(In french)*.

Jannot, Y., Felix, V., & Degiovanni, A. (2010). A centered hot plate method for measurement of thermal properties of thin insulating materials. *Measurement Science and Technology*, *21*(3), 035106.

Kavianipour, A., & Beck, J. V. (1977). Thermal property estimation utilizing the Laplace transform with application to asphaltic pavement. *International Journal of Heat and Mass Transfer*, *20*(3), 259–267.

Khan, M. I. (2002). Factors affecting the thermal properties of concrete and applicability of its prediction models. *Building and Environment*, *37*(6), 607–614.

Knowlton, K., Lynn, B., Goldberg, R. A., Rosenzweig, C., Hogrefe, C., Rosenthal, J. K., & Kinney, P. L. (2007). Projecting heat-related mortality impacts under a changing climate in the New York City region. *American Journal of Public Health*, *97*(11), 2028–2034.

Kodur, V. K. R., & Sultan, M. A. (2003). Effect of temperature on thermal properties of high-strength concrete. *Journal of Materials in Civil Engineering*, *15*(2), 101–107.

Krapez, J. C. (2007). *Mesure de l'effusivité thermique*. Ed. Techniques Ingénieur. *(In french)*.

Krapez, J. C., Spagnolo, L., Frieß, M., Maier, H. P., & Neuer, G. (2004). Measurement of in-plane diffusivity in non-homogeneous slabs by applying flash thermography. *International Journal of Thermal Sciences*, *43*(10), 967–977.

Lee, T., Hawes, D. W., Banu, D., & Feldman, D. (2000). Control aspects of latent heat storage and recovery in concrete. *Solar Energy Materials and Solar Cells*, *62*(3), 217–237.

Li, H. (2015). A comparison of thermal performance of different pavement materials. In *Eco-Efficient materials for Mitigating Building Cooling Needs* (pp. 63–124). Woodhead Publishing.

Log, T., & Gustafsson, S. E. (1995). Transient plane source (TPS) technique for measuring thermal transport properties of building materials. *Fire and Materials*, *19*(1), 43–49.

Luca, J., & Mrawira, D. (2005). New measurement of thermal properties of superpave asphalt concrete. *Journal of Materials in Civil Engineering*, *17*(1), 72–79.

Mallick, R. B., Chen, B. L., & Bhowmick, S. (2009). Harvesting energy from asphalt pavements and reducing the heat island effect. *International Journal of Sustainable Engineering*, *2*(3), 214–228.

Mohajerani, A., Bakaric, J., & Jeffrey-Bailey, T. (2017). The urban heat island effect, its causes, and mitigation, with reference to the thermal properties of asphalt concrete. *Journal of Environmental Management*, *197*, 522–538.

Olives, R. (2017). Intensification des transferts et efficacité énergétique du stockage thermique. Habilitation à Diriger des Recherches, Université de Perpignan Via Domitia, pp. 42–51. *(In french)*.

Parker, W. J., Jenkins, R. J., Butler, C. P., & Abbott, G. L. (1961). Flash method of determining thermal diffusivity, heat capacity, and thermal conductivity. *Journal of Applied Physics*, *32*(9), 1679–1684.

Petrov, V. A., Poluektov, V. V., Zharikov, A. V., Nasimov, R. M., Diaur, N. I., Terentiev, V. A., ... Lind, E. N. (2005). Microstructure, filtration, elastic and thermal properties of granite rock samples: Implications for HLW disposal. *Geological Society, London, Special Publications*, *240*(1), 237–253.

Prelovsek, P., & Uran, B. (1984). Generalised hot wire method for thermal conductivity measurements. *Journal of Physics E: Scientific Instruments*, *17*(8), 674.

ShengYue, W., QiYang, Z., YingNa, D., & PeiDong, S. (2013). Unidirectional heat-transfer asphalt pavement for mitigating the urban heat island effect. *Journal of Materials in Civil Engineering*, *26*(5), 812–821.

Shimoda, Y. (2003). Adaptation measures for climate change and the urban heat island in Japan's built environment. *Building Research & Information*, *31*(3–4), 222–230.

Stehfest, H. (1970). Algorithm 368: Numerical inversion of Laplace transforms [D5]. *Communications of the ACM*, *13*(1), 47–49.

Takebayashi, H., & Moriyama, M. (2012). Relationships between the properties of an urban street canyon and its radiant environment: Introduction of appropriate urban heat island mitigation technologies. *Solar Energy*, *86*(9), 2255–2262.

Yan, X., Chen, L., You, Q., & Fu, Q. (2019). Experimental analysis of thermal conductivity of semi-rigid base asphalt pavement. *Road Materials and Pavement Design*, *20*(5), 1215–1227.

5th International Conference on Countermeasures to Urban Heat Islands

In Situ **Assessment of the Cooling Effects of Pavement-Watering: Application to** *Cool and Low Noise Asphalt* **Roads**

In Situ Assessment of the Cooling Effects of Pavement-Watering: Application to *Cool & Low Noise Asphalt* Roads

Sophie Parison[1],
Paris City Hall, Water and Sanitation & Roads and Traffic Divisions (France)
Univ Paris Diderot, Sorbonne Paris Cité, LIED, UMR 8236, CNRS (France)

Martin Hendel,
Univ Paris Diderot, Sorbonne Paris Cité, LIED, UMR 8236, CNRS (France)
Université Paris-Est, ESIEE Paris, département SEN, (France)

Laurent Royon,
Univ Paris Diderot, Sorbonne Paris Cité, LIED, UMR 8236 (France)

ABSTRACT

As part of the *Life Cool & Low Noise Asphalt project*, the City of Paris will test the effectiveness of three innovative pavements and the cooling effects of their watering using non-potable water as soon as the summer of 2019, in order to mitigate the effect of heat on the population during heat waves. We propose a brief presentation of the project framework and preliminary results of micro-climatic measures conducted prior to the implementation of the new pavements. Further field campaigns will be used to determine the cooling effects of the method expected to be improved by the innovative structures, designed to favor water retention.

Introduction

As a direct consequence of climate change, a growing number of cities are expected to face more and more frequent, intense and long lasting heat-waves by the end of the 21st century, (Lemonsu et el. 2013). In response to this public health threat, various urban heat island (UHI) mitigation techniques are currently being implemented in cities, such as reintroducing evapotranspiration and water into the urban environment, or the use of cool materials, i.e. highly reflective pavements either in the visible and/or infrared spectrum, or permeable pavements, beneficial for both thermal stress and underground life (Akbari, Pomerantz and Taha 2001, Bowler et al. 2010, Santamouris 2013).

In this context, since 2013, the City of Paris has implemented experimental pavement-watering campaigns of public spaces using the city's non potable water network during heat-waves. This method has already proven to reduce the UTCI (Universal Thermal Climate Index) equivalent temperature by up to 2-3°C during the day (Hendel et al. 2016).

More recently, the EU LIFE project *Cool & Low Noise Asphalt* (Life 2017), launched in July 2017, aims to implement three experimental sites in Paris to test for the thermal and acoustic efficiency of innovative alternative pavements, although we will only take interest in the microclimatic aspect in this paper. The project includes an in situ evaluation to quantify the cooling potential of the new innovative materials with regard to traditional pavements. Their composition

---

[1] Corresponding Author: sophie.parison@univ-paris-diderot.fr.

is expected to allow them to remain cooler than standard asphalt and thus lessen the effect of heat on the population and also to help reduce road traffic noise. Following up on the previous watering campaigns, watering at each site is also performed during the summer. Two of the proposed pavements present light-colour aggregates and higher surface roughness while the last one incorporates small clay spheres, making it slightly permeable. Many studies in the literature have shown that reducing pavement surface temperatures lead to air temperature cooling at pedestrian height in the order of 1°C (Taleghani et al., 2019; Synnefa et al., 2011; Kyriakodis and Santamouris, 2018).

Anticipating the beginning of the summer 2019 watering campaign, we present the sites dedicated to the project and briefly discuss the impact assessment methodology. To evaluate the microclimatic impact of the innovative materials and their watering, each site was instrumented with weather stations, measuring air temperature, relative humidity and black globe temperature at pedestrian height (1.5 m) as well as wind speed and net radiation at 4 meters above ground level. These were placed in front of the "innovative" area and a "reference" area for which the pavement was replaced with a standard material (case stations) as well as a "control" area for which the implemented pavement was not replaced (control station). Preliminary results, obtained from measurements conducted in 2018 prior to the implementation of the new pavements, are also presented.

Sites characteristics

For the purposes of the project, three experimental sites were deployed in Paris, France, between July 2017 and August 2018 and equipped with weather to perform microclimatic measurements. Two of them are located in the South-West of Paris in the 15th Arrondissement, one on rue Frémicourt near the northern edge of the district, and the other one in the center on rue Lecourbe. The last site is located in the North-West of Paris near the edge of the 8th Arrondissement on rue de Courcelles. All three sites are respectively referred to as Frémicourt, Lecourbe and Courcelles hereafter. Site positions are illustrated in Figure 1.
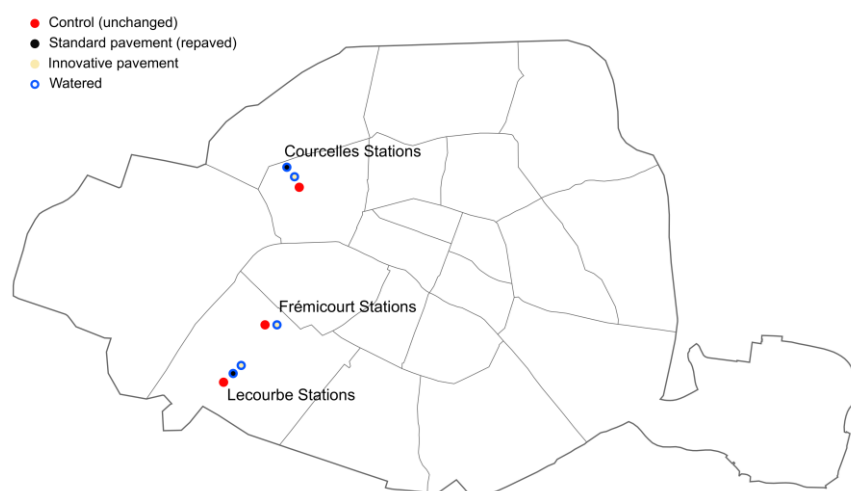

Figure 1. Position of each experimental site in Paris, France. Weather stations are illustrated with a circle which color depends on the type of countermeasure implemented. Control stations are depicted in red.

Sites were selected following several acoustic and thermal criteria in order to maximize the effects of the new pavements. These factors included streets with: high traffic noise (>68 dBA), little or no vegetation, high exposure to direct insolation with limited shading, identical street orientation, canyon aspect ratio and street width as much as possible, and streets relatively distant from the Seine river or parks and direct proximity to the non-potable water network. Due to further operational factors, these criteria could not all be met simultaneously, although the final choice of sites is globally satisfactory. The presence of the Monceau park relatively close to Courcelles is to be noted.

Rue Frémicourt has a E-W orientation, rue Lecourbe a NE-SW orientation, while rue de Courcelles is oriented in a N NW-S SE direction. Their canyon aspect ratios (H/W) are approximately equal to 0.7, 1.3 and 1, respectively. Each site was equipped with a minimum of two weather stations on the Northern sidewalk of the street, one case (watered) and one control (dry) spaced by at least 10 street widths (i.e. ~200m). Station positions are depicted in Figure 2 for each site.
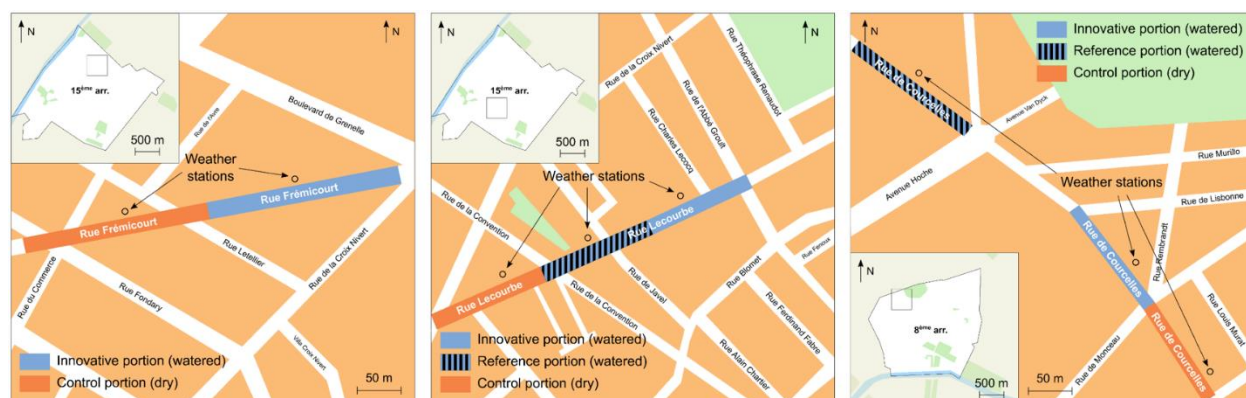
Figure 2. Station positions at Frémicourt (left), Lecourbe (center) and Courcelles (right) sites.

For the Lecourbe and Courcelles sites, three different pavement portions are monitored with weather stations, referred to as the innovative, reference and control portions. The control portion remains dry throughout the study period and is not repaved during the monitoring period. The other two will be watered under certain conditions, in addition to being repaved. The innovative portion is repaved with the new material, while the reference portion is repaved with the standard material, namely asphalt concrete for Lecourbe and asphalt otherwise. This approach is used to isolate the effects of the innovative materials on their own, without watering as well as aging effects. Micro-climatic measurements will thus also include the assessment of the impact the material and the effects of watering on both new traditional asphalt and on an innovative pavement. The Frémicourt site has only two weather stations, since the control area had recently been repaved (less than 2 years).

Two of the proposed alternative pavements, BBphon+ (innovative asphalt concrete) and SMAphon (alternative stone mastic asphalt), respectively installed at the Courcelles and Frémicourt innovative portions, include brighter-coloured aggregates and macro-surface roughness. The formulation implemented at Lecourbe, PUMA asphalt, incorporates small clay spheres, making it slightly permeable on its surface only, an interesting aspect in case of watering. These particular characteristics (higher albedo, surface roughness favoring the surface retention of

water) have been selected to improve the thermal and acoustic performance compared to so-called "traditional" asphalt pavements while maintaining their mechanical properties and limiting additional manufacturing and installation costs.

Instrumentation

Photographs of the weather stations are presented in Figure 3.

Figure 3. Photographs of watered and control weather stations *in situ*. From left to right: control stations at Frémicourt and Lecourbe, and innovative station at Courcelles.

Each station measures a number of microclimatic parameters either at pedestrian height, 4 m above ground level or both, including air temperature, relative humidity, black globe temperature, wind speed and net radiation. In addition, the innovative portions as well as the reference portions were equipped with a thermofluxmeter placed 5 cm deep below the surface of the pavement to measure pavement heat-flux and temperature. Instruments were placed inside white-painted cylindrical cages to prevent them from being vandalized. All measured parameters are listed in Table 1 below.

Table 1: Instrument type, measurement height and accuracy.

Parameter	Instrument	Height	Symbol	Accuracy
Air temperature	Sheltered Pt100 1/3 DIN B	1.5m 4m	T_a $T_{a,4m}$	0.1°C
Relative humidity	Sheltered capacitive hygrometer	1.5m 4m	RH RH_{4m}	1.5% RH
Black globe temperature	Pt100 1/2 DIN A - ISO 7726	1.5m	T_g	0.15°C
Wind speed	2D ultrasonic anemometer	4 m	v	2%
Pavement heat flux	Taylor-made flowmeter	-5cm	V_{-5cm}	5%
Pavement temperature	Type T Thermocouple	-5cm	T_{-5cm}	1°C
Net solar radiation	Net radiometer with thermopile	4m	R_n	5% daily

Watering criteria

For pavement-watering to be activated with a cleaning truck and manual operator, certain meteorological conditions must be met. Those, as well as the heat-wave criteria for Paris, are summarized in, based on Météo-France's 3-day forecast for the "Parc Montsouris" station.

Table 2: Weather conditions required for pavement-watering and heat wave warnings (Hendel et al. 2016)

Parameter	Pavement-watering	Heat-wave warning level
BMI_{Min}	$\geq 16°C$	$\geq 21°C$
BMI_{Max}	$\geq 25°C$	$\geq 31°C$
Wind speed	≤ 10 km/h	-
Sky conditions	Sunny (less than 3 oktas cloud cover)	-

The sky and wind speed conditions automatically filter for days of Pasquill Stability Class A or A-B (Pasquill 1961), while the three-day mean condition imposed on maximum and minimum air temperature entails that observations in the days leading up to or following pavement-watering are often also of Pasquill Stability Class A or A-B and are also used as reference observations when watering was not enabled.

Preliminary results

Preliminary lab tests helped discriminate asphalt formulations according to their thermal behaviour with and without watering (Parison et al. 2019).

Concerning field campaigns, the assessment method is based on the BACI design (Before-After-Contro-Impact) (Hendel et al. 2016, Parison, Hendel and Royon 2019). Thus, instead of taking interest in the measurement of one relevant parameter in particular, the method tests whether the difference between parameters at control and impact sites changes once the countermeasure is implemented, i.e. are the reference and watered interstation profiles different from each other (Hurlbert 1984, Stewart-Oaten, Murdoch and Parker 1986), as shown in Eq. (1):

$$\Delta M_{i,counter} - \Delta M_{i,ref} = I_{i,x2} \tag{1}$$

with $\Delta M_{i,counter}$ and $\Delta M_{i,ref}$, respectively, the interstation profiles between case and control areas for a given weather type i either during the countermeasure period or the reference period, and $I_{i,x2}$ the impact of the countermeasure under weather type i implemented at the case area x_2.

Determining the impact of pavement-watering is then equivalent to comparing the means of both reference and watered interstation profiles ($\Delta M_{i,counter}$ and $\Delta M_{i,ref}$). To that aim, suited statistical procedures, such as a linear mixed model, must be applied to isolate the effect of the countermeasure. The interested reader is invited to read previous work by the authors where the methodology is presented in greater details (Hendel et al. 2016).

In order to evaluate both the impact of pavement-watering and the impact of the new pavement itself, "initial-state" microclimatic measures were performed simultaneously at control, reference and innovative sites prior to the implementation of the new pavements. Unfortunately, these measurements are only available for the Courcelles site due to poor weather conditions during the summer of 2017 for Frémicourt and also because construction work began as soon as the stations were installed at Lecourbe and Frémicourt in 2018. An example of interstation profiles during the reference period, $\Delta M_{i,ref}$, is provided in Figure 4 for air temperature 1.5 m height at Courcelles for the summer of 2018.
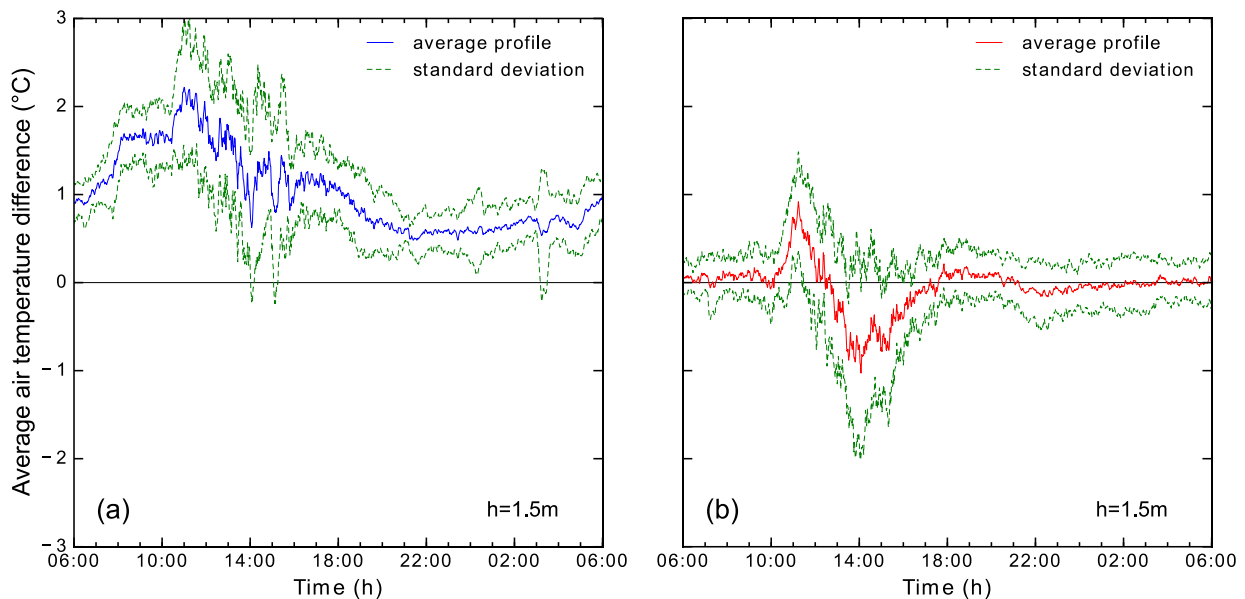
Figure 4. Average interstation profiles $\Delta M_{i,ref}$ for 1.5 m air temperature at Courcelles during the summer of 2018 (reference period): (a): difference between the innovative and control stations (using 18 reference days); and (b): difference between reference and control stations (using 23 reference days).

In Figure 4 (a), we can observe the air temperature difference between the innovative and the control station at Courcelles, averaged for all the reference days recorded during the summer of 2018, that is 18 days. In Figure 4 (b) the same quantity is illustrated except the difference is calculated between the reference and control stations at Courcelles, averaged on 23 days. Note that fewer reference days were recorded for fig. 4 (a) due to battery failure in the innovative station.

As can be seen in fig. 4 (a), the innovative station is always roughly 1 to 2°C warmer than the control station while the difference between reference and control stations (fig. 4 (b)) oscillates around zero although with high variability during the day under direct insolation.

The first watering campaign, launched during the summer of 2019, will allow the determination of the interstation profiles during the countermeasure period, denoted $\Delta M_{i,counter}$. Comparing those profiles to the summer 2019 interstation profiles will allow the determination of:

- The effects of both the new pavement compared to the preexisting one and the cooling effects of watering if only 2019-watering days are used for the further analyses.
- The sole effect of the new pavements if only 2019-reference days are used.

Nevertheless, if the variability of the profiles presented in Figure 4 is too important, further analyses won't provide statistically significant effects and will therefore not be able to isolate the effects of the material itself. For this reason, in the case of definitive UHI-countermeasures, the characterization period before its implementation is essential and must not be neglected.

Fortunately, here, since pavement-watering is a fully reversible UHI countermeasure, reference and watered observations will continue to be obtained every summer that the weather stations continue recording and that pavement-watering is tested. This means that at least the cooling effects of watering on the different pavements will be assessed. These effects are expected to be slightly greater than those measured since 2013 at another experimental site (Hendel et al. 2016, Parison et al. 2017) thanks to the innovative pavements. A comparison of those field campaigns will also help conclude on the thermal efficiency of the pavements.

Conclusion

In this paper, we presented the framework of the *Cool & Low Noise Asphalt* project currently being underway in Paris, France. Three field sites were deployed in Paris to test the efficiency of new alternative pavements in terms of heat stress reduction for the pedestrians during heat-waves.

The methodological framework allowing the assessment of the cooling effects of watering these innovative structures includes carrying out micro-climatic measures prior to the implementation of any definitive UHI-countermeasure to be able to isolate and quantify its effects.

In this regard, the interstation micro-climatic measures carried out during the early stage reference period of the project were presented. Maximum and average impacts in terms of temperature and heat stress reductions will be estimated and discussed as soon as the first watering campaign yields its first results, that is at the end of the summer of 2019.

Acknowledgments

References

Akbari, H., Pomerantz, M., & Taha, H. (2001). Cool surfaces and shade trees to reduce energy use and improve air quality in urban areas. Solar energy, 70(3), 295-310.

Bowler, D. E., Buyung-Ali, L., Knight, T. M., & Pullin, A. S. (2010). Urban greening to cool towns and cities: A systematic review of the empirical evidence. Landscape and urban planning, 97(3), 147-155.

Hendel, M., Gutierrez, P., Colombert, M., Diab, Y., & Royon, L. (2016). Measuring the effects of urban heat island mitigation techniques in the field: Application to the case of pavement-watering in Paris. Urban Climate, 16, 43-58.

Hurlbert, S. H. (1984). Pseudoreplication and the design of ecological field experiments. Ecological monographs, 54(2), 187-211.

Kyriakodis, G.-E. and Santamouris, M. (2018) 'Using reflective pavements to mitigate urban heat island in warm climates - Results from a large scale urban mitigation project', *Urban Climate*. Elsevier B.V., 24, pp. 326–339. doi: 10.1016/j.uclim.2017.02.002.

Lemonsu, A., Kounkou-Arnaud, R., Desplat, J., Salagnac, J. L., & Masson, V. (2013). Evolution of the Parisian urban climate under a global changing climate. Climatic change, 116(3-4), 679-692.

Life *Cool & Low Noise Asphalt* Project official website (July 2017): https://www.life-asphalt.eu/

Parison, S., Hendel, M., Jurski, K., & Royon, L. (2017) The Impact of Different Watering Strategies on the Cooling Effects of Pavement-Watering during Heat-Waves. in PLEA 2017 Proceedings - Design to Thrive. pp. 120–127.

Parison, S., Hendel, M., Grados, A., & Royon, L. (2019). Comportement thermique de revêtements innovants à Paris pour le projet Cool & Low Noise Asphalt. Colloque Interuniversitaire Franco-Québécois, Baie Saint-Paul.

Parison, S., Hendel, & Royon, L. (2019). Quantifying the Field Effects of Urban Heat Island Mitigation Techniques. 10th International Conference on Urban Climate, Special Issue, New York.

Pasquill, F. (1961). The estimation of the dispersion of windborne material. Met. Mag., 90, 33.

Santamouris, M. (2013). Using cool pavements as a mitigation strategy to fight urban heat island—A review of the actual developments. Renewable and Sustainable Energy Reviews, 26, 224-240.

Stewart-Oaten, A., Murdoch, W. W., & Parker, K. R. (1986). Environmental impact assessment:" Pseudoreplication" in time?. Ecology, 67(4), 929-940.

Synnefa, A. *et al.* (2011) 'Experimental testing of cool colored thin layer asphalt and estimation of its potential to improve the urban microclimate', *Building and Environment*. Elsevier Ltd, 46(1), pp. 38–44. doi: 10.1016/j.buildenv.2010.06.014.

Taleghani, M. *et al.* (2019) 'The impact of heat mitigation strategies on the energy balance of a neighborhood in Los Angeles', *Solar Energy*. Elsevier, 177(November 2018), pp. 604–611. doi: 10.1016/j.solener.2018.11.041

33ème Colloque Annuel de l'Association Internationale de Climatologie

"Tièrce Forêt": Greening a Parking Lot

"TIERCE FORET": GREENING A PARKING LOT

Sophie Parison (1), Maxime Chaumont (1), Raphaëlle Kounkou-Arnaud (3), Frédéric Long (3), Andrej Bernik (4), Marcos Da Silva (4), Martin Hendel (1,5)*

*martin.hendel@univ-paris-diderot.fr
(1) Université de Paris, LIED, UMR 8236, CNRS, F-75013, Paris, France
(2) Paris City Hall, Paris, France
(3) Météo-France, Direction des Services Météorologiques, Saint-Mandé, France
(4) Fieldwork Architecture, F-75020, Paris, France
(5) Université Gustave Eiffel, ESIEE Paris, département SEN, F-93162 Noisy-le-Grand, France

Résumé: *Un espace extérieur privatif situé à Aubervilliers (93) est en cours de transformation d'un parking recouvert d'enrobé bitumineux vers un revêtement en béton perméable avec plantations dense d'arbres. Le présent article s'intéressera à la présentation de résultats préliminaires portant sur l'évaluation de l'impact rafraîchissant, notamment sur le stress thermique d'un piéton, grâce à des mesures fixes et mobiles. Des effets bénéfiques pour le stress thermique sont observés suite notamment à la création d'ombrage par les nouveaux arbres se traduisant par une réduction de la température de l'air et de la température moyenne de rayonnement.*

Keywords: *rafraîchissement urbain, béton perméable, végétalisation.*

Summary: *A parking lot in the city of Aubervilliers (Paris metropolitan area) is under conversion from an asphalt-concrete paved area to an open green space with permeable pavement as an urban heat island countermeasure. In this paper, we present preliminary results of the impact of the site's partial conversion on pedestrian heat stress, with fixed and mobile measurement campaigns. Significant improvements of pedestrian heat stress are reported, following the creation of shade from trees resulting in reductions in air temperature and mean radiant temperature.*

Keywords: *urban heat island countermeasure, permeable concrete, urban greening*

Introduction

Urban greening is among the best-known countermeasures to the urban heat island (UHI) phenomenon (Akbari, Pomerantz, and Taha 2001). Parks in particular have been the focus of many studies, but many studies only conduct measurements after park construction (Bowler et al. 2010). However, identifying sites sufficiently ahead of time to prepare a measurement campaign before and after park construction can be difficult.

In the Paris Metropolitan Area, a site in the municipality of Aubervilliers is under study for conversion into an urban green area. The zone under study is currently used as a parking lot for the occupants of a home for young workers. It currently offers no urban amenities for pedestrians and inhabitants and its dark-colored asphalt concrete strongly absorbs solar radiation. The conversion will create a green open space with new functionality for pedestrians and inhabitants, including several trees and permeable concrete paving.

This site and its construction work schedule offer an opportunity to study the site before and after greening. Microclimatic measurements are under way to determine the site's microclimatic characteristics before and after site conversion.

This paper presents results following the partial conversion of the site, i.e. after trees are planted, most of the asphalt concrete is removed and a pervious concrete pavement is laid underneath the case measurement station.

1. Materials and Methods

1.1. Site Description

The site chosen for the study is a parking lot of about 1,200 m² for the occupants of a home for young workers in the municipality of Aubervilliers, located in the Parisian northern periphery.

The site is located in a heterogeneous urban area. The site's vicinity can be classified as LCZ 4 (open high rise), but adjacent areas vary from LCZ 2, B or D (resp. dense mid-rise, scattered trees and low plants). It is currently surrounded by tall buildings and offers no amenities for pedestrians, such as benches, shade or footpaths. The ground is made of a worn out dark-coloured impervious asphalt with an albedo of 0.13. Furthermore, the site offers little vegetation apart from peripheral flowerbeds and sparsely-planted trees. A photograph of the parking lot in its initial state (left) is provided in Figure 1.

Figure 1: Photograph of the site. Left: before conversion, right: after partial conversion in 2019. Bottom: site map and weather station positions.

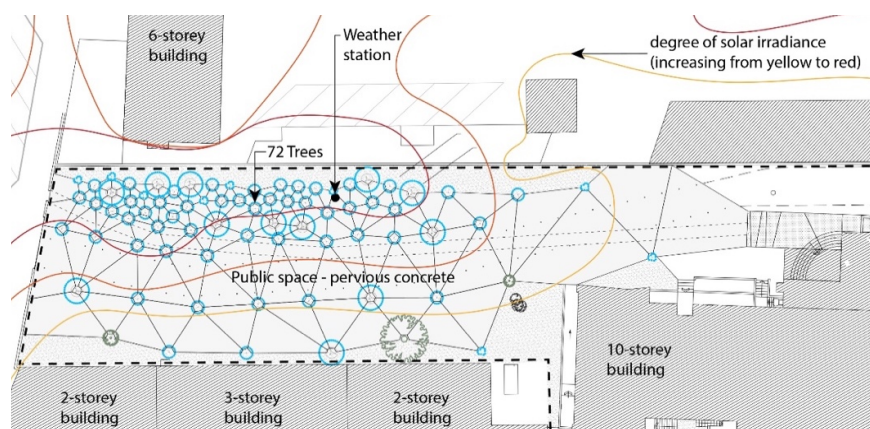Figure 2: Project plan

Considering those characteristics, the site is a good candidate for conversion to an open green area as an urban cooling measure. The projected conversion completely rethinks this area. It will create a friendly pedestrian space for local inhabitants, no longer accessible to vehicles. As illustrated in Figure 2, trees are planted with an increased density in the sunniest areas will

create a "tertiary forest", and the asphalt concrete pavement will be replaced entirely with light-colored permeable concrete in order to retain rainwater in the sub-layers, thus allowing the trees to grow properly and the soil to be fertile.

The microclimatic impact of the project is evaluated by conducting measurements before and after transformation. The site and its construction schedule offer a unique opportunity to monitor the site sufficiently ahead of time. Microclimatic measurements are conducted with two weather stations installed by Météo-France. The case station is placed in the parking lot in an area where trees will be planted, while the control station is located on the rooftop approximately 30 m above the parking lot, outside of the project's area of influence.

Trees were planted and most of the asphalt concrete was removed after partial conversion in time for measurements during summer 2019. In addition, only the area below the case station is paved with pervious concrete (see Figure 1, right), the rest of the soil remained bare.

1.2. Instrumentation

The weather stations monitor several microclimatic parameters at screen height, including those relevant to pedestrian heat stress: air temperature, relative humidity, black globe temperature, wind speed and long and shortwave upward and downward radiation fluxes, as well as a rain gauge near the control (rooftop) station. In addition, mobile measurements were conducted with a mobile weather station. The position of the stations is indicated in Figure 1 (bottom) and a photograph is shown in Figure 3.

Figure 3: Rooftop (left) and parking lot (center) fixed and mobile (right) weather stations (before conversion).

1.3. Data analysis

The cooling impact created by the site's transformation is evaluated using the protocol described by Parison et al. (2020), based on the BACI method combined with the Lowry approach (Lowry 1977). Succinctly, the interstation difference between the case (parking lot) and control (rooftop) stations is monitored before (reference period) and after (countermeasure period) conversion on days presenting radiative conditions (clear skies and wind speed < 3 m/s) with daily minimum and maximum temperatures exceeding 16° and 25°C, respectively.

By comparing the interstation profiles, preexisting differences between stations are filtered out. By comparing the interstation profile during the reference ΔM_{ref} (before) and the countermeasure $\Delta M_{counter}$ (after) periods, the impact of the conversion I can be isolated. The procedure is summarized in equation (1), noting M as the measured meteorological parameter:

$$\Delta M_{counter} - \Delta M_{ref} = \left(M_{case,counter} - M_{ctrl,counter}\right) - \left(M_{case,ref} - M_{ctrl,ref}\right) = I \qquad (1)$$

Results are tested for statistical significance.

2. Results and discussions

2.1. Fixed Measurements
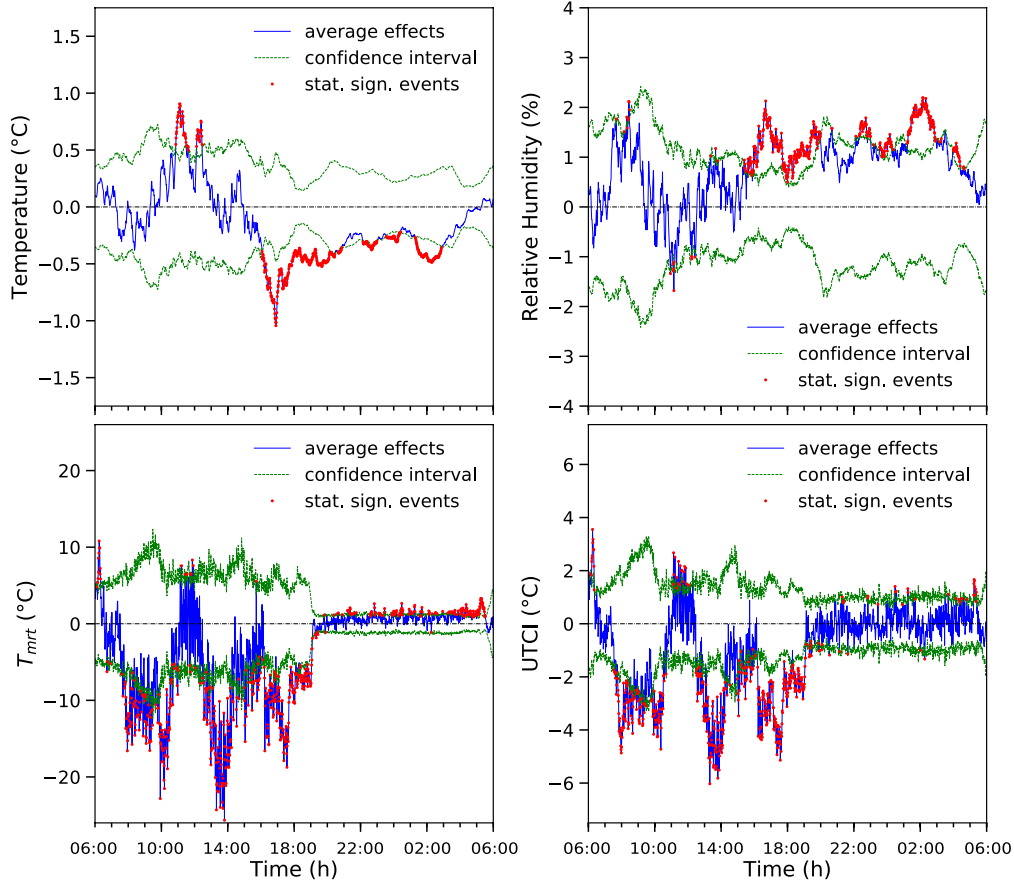
Figure 4: Microclimatic impacts of the site's partial renovation. Assessment based on 18 observation days before and 16 after conversion.

Figure 4 illustrates the microclimatic impacts of the site's partial transformation following the removal of the (partial) asphalt concrete pavement and the planting of trees. The impacts on air temperature, relative humidity and mean radiant temperature (MRT) are reported as well as their combined impact on the Universal Thermal Climate Index (UTCI). Maximum and mean effects are summarized in Table 1.

Table 1: Maximum and mean microclimatic effects

	Air temperature	Relative humidity	MRT	UTCI
Max	-1.0°C	+2.2%	-25.7°C	-6.0°C
Mean	-0.3°C	+1.3%	-7.5°C	-2.5°C
Time of max effect	4:54 pm	11:09 am	1:47 pm	1:18 pm

As can be seen, the microclimatic impacts of the site's partial transformation are quite significant, with three peak cooling effects visible with UTCI, the maximum effect reaching -6.0°C. These are principally attributable to morning and afternoon shade, causing a max reduction in MRT of 25.7°C. Air temperature is reduced up to 1.0°C at the end of the afternoon, while it is briefly increased by 0.9°C around noon. Finally, only minor increases in relative humidity of up to +2.2% are observed during the evening and night. In addition, the observed change is statistically significant for all parameters at least 35% of the day.

Looking at the details, it is clear from the observations that the shade provided by the trees planted in the immediate vicinity of the weather station has a very significant impact in the morning from 8-11 am, 1-3:30 pm and from 5-6 pm on MRT and UTCI. However, conditions seem to have marginally worsened around noon, perhaps due to the reduced thermal inertia of the unsealed soil. In addition, unsealing the soils around the station appears to have increased relative humidity, although climatic differences between 2018 and 2019 also contribute to this. It should be noted that the increase in RH does not have a significant detrimental impact on pedestrian heat stress given how dry conditions are to start with.

2.2. Mobile Measurements

Prior to site transformation, mobile measurements were conducted in June 2018 to estimate the microclimatic spatial distribution before conversion. These were performed on a typical summer day, i.e. with low wind speeds (<3m/s), clear sky and minimum and maximum daily air temperatures respectively greater than 16° and 25°C. These weather conditions match for days of Pasquill Stability Class A or A-B (Pasquill 1961). From these measurements, the Universal Thermal Climate Index (UTCI) equivalent temperature was calculated at several points, as indicated in Figure 5.

Figure 5: Thermal stress indicator (UTCI) on site before conversion measured on eight different locations on June the 26th of 2018, from 1 pm to 3 pm (local time)

As can be seen, strong microclimatic variations are observed between shaded and insolated areas. All measurements performed under trees or building shading exhibit no thermal stress. On the other hand, measurements conducted under direct insolation (indicated with a red dot) show a high level of thermal stress, exceeding 35°C equivalent temperature.

A new mobile measurement campaign will be conducted during summer 2020 to assess the change obtained with the complete transformation.

Conclusion

The partial conversion of a parking lot into a green space with 72 trees and pervious concrete pavement was studied as an UHI countermeasure in the Paris metropolitan area. The site was

monitored with fixed and mobile weather stations in order to determine the impact of the conversion on the site's microclimate. The impacts of partial conversion, following the removal of most of the asphalt concrete and the plantation of 72 trees were assessed.

A significant improvement of pedestrian heat stress is observed thanks to the shading provided by the trees with reductions of MRT and UTCI of up to 27.5°C and 8.1°C, respectively. Air temperature is also positively affected with a maximum reduction of up to 1.4°C. Finally, unsealing the soil led to an increase in relative humidity by up to 5%.

In addition, a preliminary mobile measurement campaign was conducted to investigate the spatial distribution of heat stress before conversion at eight different locations. Results show that no thermal stress is observed in the shade and high heat stress in the sun.

Mobile measurements will be conducted during summer 2020 after site conversion is completed, with the new pervious pavement in place over the entire site.

Acknowledgements

References

Akbari, H, M Pomerantz, and H Taha. 2001. "Cool Surfaces and Shade Trees to Reduce Energy Use and Improve Air Quality in Urban Areas." *Solar Energy* 70 (3): 295–310. https://doi.org/10.1016/S0038-092X(00)00089-X.

Bowler, Diana E., Lisette Buyung-Ali, Teri M. Knight, and Andrew S. Pullin. 2010. "Urban Greening to Cool Towns and Cities: A Systematic Review of the Empirical Evidence." *Landscape and Urban Planning* 97 (3): 147–55. https://doi.org/10.1016/j.landurbplan.2010.05.006.

Lowry, W. P. 1977. "Empirical Estimation of Urban Effects on Climate: A Problem Analysis." *Journal of Applied Meteorology.* https://doi.org/10.1175/1520-0450(1977)016<0129:EEOUEO>2.0.CO;2.

Parison, Sophie, Martin Hendel, and Laurent Royon. 2020. "An Updated Method for Quantifying the Field Effects of Urban Heat Island Mitigation Techniques." *Urban Climate*, (under review).

Pasquill, F. 1961. "The Estimation of the Dispersion of Windborne Material." *The Meteorological Magazine* 90 (1063): 33–49.

Résumé détaillé en français

Introduction

Le travail présenté s'inscrit dans le cadre du volet adaptation au changement climatique du Plan Climat de la Ville de Paris et notamment dans la lutte contre la chaleur urbaine et les îlots de chaleur urbains. L'îlot de chaleur urbain (ICU) est un phénomène de réchauffement local des villes par rapport à leur périphérie, d'autant plus important que la ville en question est dense et étendue. Le cœur de Paris est ainsi plus chaud de 3°C environ en moyenne annuelle que sa périphérie. Cette différence s'explique du fait de l'action combinée de plusieurs mécanismes physiques : le piégeage du rayonnement solaire du fait de la forme urbaine et de la nature minérale des villes (forte inertie thermique), la faible présence de végétation, la faible circulation du vent et les rejets de chaleur anthropique. Qui plus est, en période de canicule, les conditions météorologiques sont propices à l'augmentation de l'intensité de l'îlot de chaleur. Ce phénomène, combiné à une canicule, génère un fort inconfort durant l'été et engendre des problèmes sanitaires importants. Le changement climatique est amené à rendre les vagues de chaleur plus fréquentes, intenses et durables. En réponse à cela, la Ville de Paris étudie dès à présent les moyens d'adaptation à mettre en œuvre pour limiter les conséquences du réchauffement climatique et réduire la chaleur en ville.

Afin d'en réduire l'intensité, les mesures anti-ICU s'adressent à un ou plusieurs des mécanismes responsables de leur formation, par exemple, en utilisant de l'ombrage, des revêtements réfléchissants ou perméables, de la végétation, ou encore de l'arrosage urbain. C'est sur ce dernier aspect que se focalise ce manuscrit.

L'arrosage urbain est une technique qui vise à rafraîchir l'espace public par arrosage des surfaces au sol, et qui est mise en œuvre à titre d'expérimentation à Paris depuis 2013, grâce à son réseau d'eau non potable. L'arrosage urbain permet de générer des flux latent et sensible non atmosphériques. Ces flux sont générés par l'évaporation d'un film d'eau et par son absorption de chaleur sensible. En conséquence, le sol est refroidi, ce qui entraîne une réduction de la convection atmosphérique, du flux thermique de conduction dans le sol, mais également de la radiosité de ce dernier. Outre la légère augmentation de l'humidité, l'arrosage urbain est donc bénéfique en tout point pour l'abaissement du stress thermique des piétons.

Que ce soit pour l'arrosage urbain ou pour d'autres mesures de rafraîchissement, les villes ont besoin de lignes directrices afin de mettre en œuvre leur stratégie de rafraîchissement de l'espace public à l'échelle territoriale, tout en tenant compte des spécificités de chaque site et en utilisant des outils d'évaluation adaptés. L'objectif principal de ce mémoire est de fournir des éléments de réponse aux décideurs sur la procédure à suivre, avec un accent particulier sur l'arrosage urbain et sur les revêtements de voirie arrosés. Notre question de recherche est la suivante : comment adapter opérationnellement l'arrosage urbain aux caractéristiques d'un site donné, en particulier aux différents revêtements qui composent le tissu urbain ainsi qu'à la surface disponible pour arrosage ? Avec quels outils peut-on évaluer les effets microclimatiques correspondants ?

Afin d'apporter des éléments de réponse à notre problématique, nous nous tournons vers l'état de l'art sur l'arrosage urbain. Un certain nombre d'études s'intéressant aux effets thermiques et microclimatiques de la méthode peut être trouvé dans la littérature scientifique. Pour cet état de l'art, nous accordons une attention particulière à la méthode d'estimation des effets microclimatiques, à l'optimisation éventuelle de la stratégie d'arrosage, ainsi qu'au matériau de revêtement arrosé. Les lacunes identifiées dans notre état de l'art nous conduisent à formuler les questions de recherche suivantes :

- Quels outils statistiques peuvent être utilisés afin d'évaluer les effets microclimatiques de mesures anti-ICU sur le terrain ?

- Comment sont affectés les effets de l'arrosage par la portion de rue arrosée ?

- Quelle est l'efficacité de l'arrosage urbain sur des revêtements traditionnels et "frais", et de quoi dépendent les débits d'arrosage optimaux correspondants ?

- Pour des revêtements traditionnels et innovants secs ou arrosés, comment se partitionne l'énergie incidente entre les différents termes du bilan thermique de surface ?

Nous cherchons par la suite à répondre à ces questions. Les résultats obtenus fourniront des informations à la communauté scientifique et aux décideurs qui cherchent à employer l'arrosage urbain comme stratégie de rafraîchissement.

Evaluation des effets microclimatiques de l'arrosage urbain

Méthodologie

Afin de répondre aux questions soulevées, un cadre méthodologique adapté à l'évaluation des effets de mesures anti-ICU est proposé. Ce cadre méthodologique repose sur la méthode BACI ("Before-After-Control-Impact", en français "Avant-Après-Témoin-Etude"), qui consiste à effectuer des mesures de terrain en deux zones : l'une dite "témoin" et l'autre dite "d'étude", cette dernière faisant l'objet d'une transformation en vue d'améliorer sa situation microclimatique. Les mesures doivent être prises simultanément sur ces deux zones, avant et après transformation de la zone d'étude. La méthodologie BACI permet de s'affranchir des différences

préexistantes de comportement microclimatique entre les deux zones sélectionnées, ce qui est essentiel afin d'isoler correctement l'impact la mesure de rafraîchissement déployée.

Pour ce faire, la différence entre les stations d'étude et témoin (nommée "profil interstations") avant transformation est comparée directement à cette même différence après transformation. Chacun de ces profils est moyenné sur plusieurs journées présentant des conditions météorologiques similaires, définies selon des critères stricts. En se servant du formalisme développé par Lowry (1977) servant à décrire empiriquement les effets de l'urbanisation sur le microclimat, on démontre que les profils interstations avant et après travaux sont linéairement dépendants. Afin d'évaluer la significativité statistique de l'impact de la transformation, un modèle linéaire à effets mixtes est utilisé. Ce modèle exprime les profils interstations en fonction d'effets fixes pour un paramètre météorologique donné. Ici, ces effets fixes correspondent à l'installation ou non de la mesure de rafraîchissement. Par ce modèle, des ensembles de données asymétriques peuvent être traités et subdivisés en sous-groupes correspondant à des facteurs aléatoires connus qui influencent les observations. Cet outil méthodologique est essentiel pour évaluer l'efficacité des politiques publiques visant à atténuer la chaleur en ville.

La méthode d'analyse proposée est appliquée à des données recueillies lors d'une expérimentation d'arrosage urbain à l'eau non potable réalisée à la rue du Louvre à Paris entre 2013 et 2018. Les données météorologiques ont été mesurées par deux stations météorologiques situées sur des zones témoin (non arrosée) et d'étude (arrosée) suivant une configuration BACI. Les stations météorologiques situées sur chacune des zones mesurent les paramètres suivants : à hauteur d'homme (1,5 m de haut), température de l'air et humidité relative sous abri et température de globe noir, ainsi qu'à 4 mètres de hauteur, température de l'air et humidité relative sous abri, vitesse de vent et rayonnement solaire net .

Deux protocoles distincts d'arrosage ont été mis en œuvre. Entre 2013 et 2015, la totalité de la largeur de rue est arrosée (chaussée et trottoir). La fréquence d'arrosage correspond à un arrosage toutes les 1 à 2 heures le matin entre 6h30 et 12h, pour un arrosage toutes les 30 minutes l'après-midi entre 14h et 18h20.

Entre 2016 et 2018, seule la chaussée est arrosée (environ 66% de la largeur de rue). La fréquence l'arrosage correspond à un arrosage toutes les 1h30 entre 7h et 11h30, pour un arrosage toutes les 30 minutes l'après-midi entre 14h et 18h20. La rue étant ombragée le matin, la fréquence d'arrosage est plus faible que dans l'après-midi, sous ensoleillement direct. L'arrosage est réalisé grâce au passage d'une laveuse et d'un opérateur manuel pour le trottoir, sous certaines conditions météorologiques qui correspondent à un assouplissement des conditions de canicule à Paris. Ces critères correspondent à des jours de la classe de stabilité atmosphérique A ou A-B.

Résultats

De 2013 à 2015, toute la largeur de la rue est arrosée (trottoir et chaussée). Les résultats montrent que les jours arrosés sont plus frais et plus humides que les jours de référence (sans arrosage) et que l'arrosage permet de réduire le stress thermique des piétons. En particulier, à 1,5 et 4 m de hauteur, respectivement, l'arrosage permet de réduire au maximum la température de l'air de 1,02°C et 0,76°C et d'augmenter au maximum l'humidité relative de 4,08% et

2,61%. La température moyenne radiante et la température équivalente-UTCI sont réduites au maximum de 6,07°C et 1,93°C, respectivement, à hauteur de piéton. De 2013 à 2015, à 1,5 m et 4 m respectivement, des effets quotidiens moyens de -0,34°C et -0,31°C pour la température de l'air et de +1,53% et +1,00% pour l'humidité relative sont observés. A 1,5 m de hauteur, des effets moyens pour la température moyenne radiante et la température équivalente-UTCI de -0,70°C et -0,38°C, respectivement, sont mesurés. Les effets statistiquement significatifs les plus importants sont observés l'après-midi. Alors que l'arrosage n'est effectué que durant 9 heures dans la journée, ses effets perdurent de façon marginale jusqu'à 6 heures du matin le lendemain.

De 2016 à 2018, seule 66% de la largeur de la rue est arrosée (trottoir uniquement). Sans surprise, cette stratégie s'avère moins efficace que la précédente, bien que des effets similaires soient observés, avec des réductions respectives maximale et moyenne à hauteur de piéton de 0,97°C et 0,36°C pour la température de l'air, et de 3,42°C et 0,46°C pour la température équivalente-UTCI. En revanche, une diminution significative de la durée des effets statistiquement significatifs est constatée, qui sont deux à trois fois plus courts selon le paramètre considéré. La température équivalente-UTCI est le paramètre pour lequel la plus forte diminution de la durée des effets statistiquement significatifs est obtenue, ces derniers ne se produisant plus que le matin, principalement.

Enfin, afin de tester la robustesse des effets, une analyse de l'arrosage moyenné sur 24h est réalisée. Celle-ci révèle que l'arrosage de 100% de la largeur de rue produit des effets moyens sur 24h statistiquement significatifs pour la température de l'air, moyenne radiante et équivalente-UTCI ainsi que sur l'humidité relative. A l'inverse, aucun effet statistiquement significatif n'est trouvé pour les températures de l'air et équivalente-UTCI lorsque seule la chaussée est arrosée. Ces deux analyses conjointes permettent de déterminer l'efficacité et la robustesse des différentes stratégies d'arrosage, afin de guider le choix opérationnel de la mise en œuvre de l'arrosage.

Optimisation de l'arrosage sur des revêtements parisiens

Méthodologie expérimentale

Dans la partie précédente, les effets microclimatiques de l'arrosage ont été étudiés grâce à une méthode adaptée. A présent, on s'intéresse à l'optimisation de l'arrosage dépendamment de la structure de voirie ciblée. Afin de limiter la consommation d'eau du procédé, les critères d'optimisation suivants sont adoptés :

- Maximisation du flux rafraîchissant d'arrosage

- Minimisation du débit d'arrosage

Pour ce faire, une expérimentation de laboratoire est développée. Les structures de voirie considérées sont soumises à des conditions climatiques similaires à une canicule parisienne

à l'intérieur d'une enceinte climatique. Le protocole consiste à soumettre les échantillons de revêtement à un cycle de 24h découpé en une période diurne de 8h avec ensoleillement artificiel assuré par une lampe halogène et une période nocturne de 16h sans ensoleillement. Dans l'enceinte, en période diurne, la température est fixée à 35°C pour une humidité relative de 35%. La nuit, elles sont de 25°C et 70%, respectivement. Au préalable, les matériaux sont stabilisés à une température de 25°C environ avant le début des essais. Une tête d'arrosage d'eau pressurisée permet d'humidifier la surface à une fréquence fixe durant la phase d'ensoleillement.

Echantillons de revêtement

Douze structures de revêtement mises en œuvre dans l'espace public sont testées dans l'enceinte : six "traditionnelles" (chaussée classique, trottoir asphalte, stabilisé, trottoir granit, pavés et gazon) et six innovantes (deux peintures réfléchissantes sur le trottoir asphalte, une chaussée perméable, deux bétons perméables et un béton au ciment de laitier). Les échantillons perméables testés comportent environ 15% de vide. Parmi les deux peintures testées sur le trottoir asphalte, l'une est thermochromique : noire à température ambiante, et réfléchissante au-delà de 29°C. L'autre est absorbante dans le spectre visible, mais réfléchissante dans le proche infrarouge. Le béton au ciment de laitier, comme son nom l'indique, incorpore une grande part de ciment au laitier (un sous-produit de l'industrie métallurgique). Cette particularité le rend plus réfléchissant et plus isolant thermiquement qu'un béton traditionnel.

Des thermocouples et fluxmètres disposés en surface et à différentes profondeurs permettent de suivre le comportement thermique des échantillons. Cette instrumentation permet, grâce à un bilan thermique de surface, de déterminer le flux rafraîchissant généré par l'arrosage, ainsi que les différents flux de chaleur en jeu (flux convectif, flux de conduction, rayonnement net, etc.). Enfin, des mesures de l'albédo tenant compte du spectre de la lampe halogène ainsi que de l'émissivité sont réalisées en laboratoire pour les surfaces sèches et arrosées.

Résultats : essais sans arrosage

Le tracé des températures de surface des échantillons secs lors du cycle climatique de 24h permet de mettre en évidence une très forte discrimination des valeurs maximales atteintes au bout de 8h d'ensoleillement artificiel. Une relation empirique entre l'augmentation des températures de surface et leur albédo met en évidence qu'une diminution relative de l'albédo de 10% provoque une augmentation de la température de surface de 3°C.

Les structures les moins échauffées en journée se trouvent être le béton au ciment de laitier (48,4°C) et le stabilisé (51,6°C), qui possèdent les albédos les plus élevés (respectivement 0,41 et 0,44). A l'inverse, les structures les plus chaudes sont les structures bitumineuses, à savoir la chaussée classique (61,5°C), le trottoir asphalte (59,7°C) et la chaussée perméable (58,6°C). Par application de peintures thermochromique et réfléchissante dans le proche infrarouge, respectivement, des réductions maximales de température de 5,7°C et 8,9°C en surface sont observées par rapport au trottoir asphalte traditionnel. Enfin, alors que gazon abondamment arrosé reste largement plus frais que les autres structures (40°C au maximum) du fait de sa très forte évapotranspiration, le gazon non arrosé au préalable se dessèche rapidement et s'échauffe autant

qu'une structure minérale sombre en journée. Cela est dû d'une part à la faible conductivité thermique de la terre végétale sèche, propice à de fortes montées de températures en surface, et d'autre part à son faible albédo. En revanche, la nuit, le gazon se refroidit bien plus vite que les structures minérales du fait de sa plus faible inertie thermique.

Résultats : essais avec arrosage

La seconde partie de l'étude concerne la réalisation des tests avec arrosage à intervalles réguliers. L'objectif final est l'optimisation du procédé pour ce qui est de la quantité d'eau aspergée pour chacun des revêtements de voirie. Des débits d'arrosage allant de de 0,1 mm/h (soit 0,1 litre par m²/h) à 3 mm/h ont été testés.

L'impact de l'arrosage se manifeste par la présence de fortes fluctuations sur la température de surface dues à l'alternance des processus d'aspersion et de séchage. La présence de ces pics montre que la fréquence d'arrosage peut être optimisée. Ces essais ont montré qu'une différence de température maximale de 22°C est obtenue pour la chaussée classique par rapport à son comportement sec. La plus faible différence de température, de 10°C environ, est obtenue pour le béton au ciment de laitier du fait de sa température sans arrosage relativement faible par rapport aux autres échantillons en phase diurne.

Optimisation de l'arrosage

L'instrumentation en surface et en profondeur des échantillons permet de déterminer de façon précise, et pour chaque essai (sec ou arrosé) les termes intervenant dans le bilan thermique d'une surface. En particulier, elle permet d'évaluer le flux rafraîchissant généré par arrosage. Ce terme inclut un terme d'évaporation ainsi qu'un terme sensible (négligeable) qui correspond à l'échauffement du film d'eau avant évaporation. Le flux rafraîchissant est calculé en régime permanent pour toutes les structures et pour tous les débits d'arrosage testés. Le rafraîchissement obtenu est d'autant plus grand que la réduction de température de surface entre un essai sec et arrosé l'est. Les structures les plus sombres sont concernées en premier lieu. Egalement, les échantillons fortement conducteurs de chaleur (comme par exemple le granit) et celles pour lesquelles une grande réduction de l'albédo entre une surface sèche et arrosée est observée (comme les bétons perméables par exemple) sont également fortement rafraîchis.

En traçant ce flux en fonction du débit d'arrosage, deux régimes de rafraîchissement sont observés : le premier correspond à l'augmentation du rafraîchissement par évaporation avec l'augmentation du débit. Le second correspond à l'augmentation marginale du rafraîchissement une fois l'évaporation maximale atteinte. L'intersection des deux régimes correspond au débit optimal d'arrosage recherché, c'est-à-dire celui pour lequel la consommation d'eau est minimisée alors que l'efficacité de la méthode est maximisée.

Une relation empirique est ainsi obtenue entre le débit optimal d'arrosage et l'albédo de la surface ou son indice d'absorptivité. Cet indice tient compte de l'albédo, de l'émissivité ainsi que des proportions respectives de rayonnements visible et infrarouge de la lampe halogène de l'enceinte. Le débit maximal d'arrosage est de 0,83 mm/h pour une surface d'absorptivité valant théoriquement 1. Il est de -0.22 mm/h pour une surface d'absorptivité théorique nulle.

Ce résultat prédit l'existence potentielle d'un domaine de froid radiatif en laboratoire en deçà d'une certaine valeur d'absorptivité.

La confrontation des résultats de laboratoire aux résultats de terrain obtenus dans les deux cas sur une structure de chaussée classique montre que le rafraîchissement observé en laboratoire est deux fois plus élevé que sur le terrain. Il en va de même pour le débit optimal. Ceci s'explique principalement en raison de la quantité de rayonnement net absorbée dans la journée, double également en laboratoire, toutes choses égales par ailleurs.

Répartition de l'irradiance

On s'intéresse enfin à la façon dont le rayonnement incident se répartit sur les différents flux sortants du bilan thermique (radiosité, flux convectif, flux conductif et flux rafraîchissant) pour des surfaces sèche et arrosée avec un débit optimal uniquement. La proportion de chacun de ces flux par rapport à l'irradiance est caractérisée en fonction de l'absorptivité de la surface des échantillons. Ceci permet d'obtenir des informations sur l'impact potentiel de chaque revêtement, arrosé et sec, sur le stress thermique d'un piéton. Par exemple, la radiosité élevée permet indirectement de limiter l'échauffement de la structure (favorable car freinant le réchauffement de l'air) mais est néfaste au bilan radiatif du piéton. Les apports transmis en profondeur n'ont pas d'impact direct significatif sur le piéton. Enfin, les échanges convectifs sont à limiter au maximum dans le but de réduire le stress thermique en journée.

Des revêtements les plus absorbants (structures bitumineuses) aux moins absorbants (stabilisé et béton au ciment de laitier), respectivement, cette analyse montre que la radiosité représente 56% à 74% du rayonnement incident. Ces valeurs chutent respectivement à 42% et 64% pour un arrosage optimisé. La conduction représente entre 26% et 15% de l'irradiance sans arrosage, et entre 18% et 12% pour un arrosage optimisé. Ces valeurs sont de 18% à 11% pour la convection sans arrosage, et chutent entre 5% et 2% pour un arrosage optimisé. Enfin, pour des essais arrosés de façon optimale, le flux rafraîchissant prélève entre 35% et 22% de l'irradiance, ce qui se traduit par une baisse de la conduction, de la convection et de la radiosité.

Enfin, la constitution du flux rafraîchissant est étudiée pour chaque revêtement. Le flux rafraîchissant puise différemment dans les différentes composantes du bilan thermique de la surface, de sorte que les variations de convection, conduction et de rayonnement net entre un essai sec et un essai arrosé se retrouvent dans la valeur du flux rafraîchissant. Il ressort de cette analyse que les parts de chacune de ces composantes diffèrent selon les échantillons. Par exemple, la part de réduction de la conduction par arrosage est plus importante pour les revêtements avec une conductivité thermique élevée (comme le trottoir granit par exemple). Les revêtements changeant significativement d'albédo avec l'arrosage comportent quant à eux une proportion plus importante dans leur flux rafraîchissant de la variation du rayonnement visible réfléchi.

Conclusion et discussion

Des éléments de réponses aux questions de recherche proposées en introduction ont été apportés. Dans un premier temps, une méthodologie d'analyse a été proposée afin d'évaluer les effets microclimatiques de mesures anti-ICU, tout en tenant compte des spécificités du microclimat urbain. La méthode a été appliquée à des essais d'arrosage urbain pour deux stratégies d'arrosage différentes. Les résultats montrent que l'arrosage de la totalité de la largeur de rue permet de réduire la température ressentie par un piéton d'environ 2°C au maximum. Bien que des effets similaires soient obtenus pour l'arrosage de la chaussée uniquement, la durée de ces effets est réduite de plus de moitié.

Dans un second temps, un protocole de laboratoire a été mis au point afin d'étudier le comportement thermique de 12 revêtements parisiens traditionnels et innovants, avec et sans arrosage de leur surface. Le procédé d'arrosage a été optimisé en utilisant deux régimes de rafraîchissement ainsi que le bilan thermique de la surface, dans le but de maximiser l'efficacité de l'arrosage tout en minimisant sa consommation d'eau. Ce faisant, une relation empirique entre le débit optimal et l'absorptivité de la surface a été obtenue. En tenant compte des différences d'ensoleillement cumulé entre le terrain et le laboratoire, un bon accord entre les débits optimaux est obtenu par les deux approches. La répartition de l'irradiance a également pu être étudiée pour chaque revêtement en fonction de son absorptivité. Ceci a montré que les structures les moins absorbantes sont le stabilisé et le béton au ciment de laitier. Enfin, nos analyses ont montré que la valeur du flux rafraîchissant puisait différemment dans les composantes du bilan thermique de surface dépendamment des propriétés des matériaux.

Notre recherche permet d'améliorer la connaissance des effets rafraîchissants de l'arrosage et des paramètres influençant son optimisation. Ces informations permettront de guider les villes choisissant de déployer l'arrosage urbain comme stratégie de rafraîchissement de l'espace public. Néanmoins, certains aspects mériteraient d'être étudiés plus amplement. En particulier, les analyses de laboratoire soulèvent les questions suivantes :

- Comment adapter le protocole expérimental à des matériaux perméables ?

- Comment mieux décrire les conditions du terrain en laboratoire ?

- Peut-on étudier des matériaux permettant d'observer du refroidissement radiatif ?

En l'état, le protocole expérimental ne permet pas d'étudier les effets de la perméabilité d'un matériau par rapport à un revêtement imperméable, du fait de de l'absence de ruissellement en laboratoire. Sur le terrain, les matériaux perméables permettent de réduire la fréquence d'arrosage et le ruissellement par rapport à un matériau imperméable. Les améliorations futures du protocole pourront investiguer cet aspect, par exemple en permettant le ruissellement d'eau sur les bords des échantillons.

Egalement, le protocole pourra faire l'objet d'améliorations afin d'être plus fidèle à des conditions réalistes, par exemple, par le biais de rampes dynamiques de température, d'humidité et d'ensoleillement artificiel. Des lampes possédant un spectre plus proche du spectre solaire

AM 1,5 pourraient être utilisées. Cependant, quelles que soient les améliorations considérées, une expérience en laboratoire ne pourra jamais reproduire pleinement la complexité de conditions réelles de terrain.

Enfin, les résultats de laboratoire suggèrent qu'un régime de refroidissement radiatif dans l'enceinte pourrait être observé. L'observation d'un tel phénomène est néanmoins complexe car les matériaux nécessaires doivent présenter des propriétés optiques sélectives très performantes. Sous ensoleillement direct, le froid radiatif permettrait aux surfaces de maintenir une température inférieure à celle de l'air, ce qui est donc particulièrement intéressant dans le cadre de rafraîchissement urbain.

En ce qui concerne la méthode d'analyse de terrain, nos recherches soulèvent les questions suivantes :

- Quels effets aléatoires peuvent être identifiés et inclus dans l'analyse ?

- Quels seraient les effets microclimatiques de l'arrosage sur des revêtements innovants ?

- Dans l'ensemble, comment améliorer la méthode d'analyse ?

Les pistes d'amélioration futures de l'analyse concernent principalement la prise en compte de facteurs aléatoires dans un modèle linéaire à effets mixtes. Les conditions météorologiques sont par exemple susceptibles d'influencer des mesures microclimatiques et pourraient à ce titre être traités comme des effets aléatoires dans l'analyse. Toutefois, pour que l'analyse soit robuste, un suivi approprié avant et après transformation du site est requis, avec un nombre important d'observations dans chaque jeu de données des effets aléatoires sélectionnés.

Par ailleurs, bien que les effets thermiques de l'arrosage aient été étudiés en laboratoire sur de nombreux revêtements traditionnels et innovants, les effets microclimatiques de ces matériaux et de leur arrosage doivent encore être évalués. En l'état, dans le cadre de nos recherche, seule la chaussée classique a été étudiée sur le terrain. Certains projets portés par la Ville de Paris (par exemple, le projet *Life Cool & Low Noise Asphalt*, ou le projet FEDER UIA *OASIS* de la Stratégie de résilience de la Ville de Paris) pourraient apporter des éléments de réponse à cet aspect.

Enfin, la méthode d'analyse pourrait faire l'objet d'améliorations supplémentaires. Les limitations de la méthode BACI ont été discutées dans ce manuscrit. Par exemple, dans un environnement urbain en constante évolution, les observations les plus anciennes sont susceptibles de devenir incomparables aux observations les plus récentes. Aussi, dans le cas où les zones témoin et d'étude seraient trop proches l'une de l'autre, la transformation de la zone témoin serait susceptible d'influencer également la zone témoin, ce qui entraînerait une sous-estimation de l'impact de la transformation. Pour pallier cela, une méthode BACI "multiple" (MBACI) peut être déployée, c'est-à-dire en impliquant un réseau de stations témoin réparties dans le voisinage direct de la station d'étude. À l'avenir, il sera possible d'examiner tous ces aspects plus en détail grâce à la récente installation de nombreuses stations météorologiques pour les besoins de divers projets de rafraîchissement, dont les projets susmentionnés. Ces stations offriront une couverture microclimatique étendue de Paris.

Bien que brièvement évoqué, le transfert des résultats et des connaissances scientifiques aux décideurs et opérationnels n'a pas été formellement abordé dans ce manuscrit. La question de la mise en œuvre pratique de solutions de rafraîchissement urbain ainsi que celle de leur arbitrage par les décideurs reste à explorer. L'utilisation d'un outil SIG peut aider à répondre à cette question, en intégrant des données pertinentes au sein d'un outil utile aux acteurs urbains. Qui plus est, notre recherche s'est principalement focalisée sur les effets microclimatiques et thermiques de l'arrosage, sur la base de mesures physiques. Toutefois, d'autres dimensions importantes ont été omises, telles que la pollution de l'air, les coûts énergétiques et financiers, la résistance mécanique et les propriétés de dérapage des chaussées, ou encore la perception sociale des solutions proposées. Ce dernier aspect pourrait être exploré par le biais d'enquêtes, afin d'apprécier le rafraîchissement réellement perçu par les piétons, d'une part, ainsi que de la perception sociale d'une technique de rafraîchissement spécifique, par exemple. Compte tenu des politiques actuelles d'économies d'eau en France et en Europe, la perception sociale de techniques nécessitant l'emploi d'eau est tout aussi cruciale que l'optimisation de leur consommation d'eau aux yeux des décideurs et des élus.